TECHNISCHE UNIVERSITÄT MÜNCHEN

TUM School of Engineering and Design

Aerodynamic Influences of Non-Parallel Ground Effect, Rotor-Rotor Interference, and Dynamic Actuation on Rotors in Hover

Stefan Platzer

Vollständiger Abdruck der von der TUM School of Engineering and Design der Technischen Universität München zur Erlangung des akademischen Grades eines Doktors der Ingenieurwissenschaften (Dr.-Ing.) genehmigten Dissertation.

Vorsitz:	Prof. Dr.-Ing. Hartmut Spliethoff
Prüfende der Dissertation:	1. Prof. Dr.-Ing. Manfred Hajek
	2. Prof. Jayant Sirohi, Ph.D.

Die Dissertation wurde am 23.06.2021 bei der Technischen Universität München eingereicht und durch die Fakultät für Maschinenwesen am 30.09.2021 angenommen.

Kurzfassung

Die Untersuchung der Strömungsfelder von Drehflüglern im Schwebeflug und deren Modellierung wurde in der Vergangenheit meist im stationären Schwebeflug mit Einzelrotoren durchgeführt. In der vorliegenden Arbeit wurde die Rotoraerodynamik bei anderen Rotorkonfigurationen und in abweichenden Flugzuständen betrachtet. Hierbei wurden drei verschiedene Forschungsfragen adressiert: der Einfluss von nicht parallelem Bodeneffekt auf das Strömungsfeld, die Ähnlichkeiten und Unterschiede zwischen koaxial gleichläufigen (stacked) und gegenläufigen (CCR) Rotoren und die aerodynamische Reaktion von Rotoren auf dynamische Anstellwinkel- und Rotordrehzahländerungen.

Instationäre Reynolds-gemittelte Navier–Stokes Simulationen wurden durchgeführt, um Einblicke in die zugrunde liegende Strömungsphysik zu gewinnen und die Einflüsse mehrerer Turbulenzmodelle auf die Simulationsergebnisse zu untersuchen. Experimentelle Daten wurden von Forschungspartnern bereitgestellt um die Güte der Simulationen zu beurteilen. Die Aerodynamik wurde unter anderem anhand von instantanen, phasengemittelten und zeitgemittelten Geschwindigkeitsverteilungen (Inflow), Blattspitzenwirbeltrajektorien, Schnittkraftverteilungen und der Schubaufteilung auf die obere und untere Rotorebene untersucht.

Der Einfluss des nicht parallelen Bodeneffekts auf das Strömungsfeld und die Rotoranströmung (Inflow) wurde anhand eines zweiblättrigen Rotors mit 0.8 m-Durchmesser untersucht. Darüber hinaus wurden die Ergebnisse mit Schwebeflugdaten außerhalb des Bodeneffekts verglichen. Es wurde festgestellt, dass die geneigte Grundebene sowohl die zeitgemittelten, als auch die phasengemittelten Strömungsfelder beeinflusst. Die Blattspitzenwirbel hoben auf der hangabwärtigen Seite vom Boden ab und der Staupunkt auf dem Boden verlagerte sich hangaufwärts. Dadurch wurde das Strömungsfeld stark asymmetrisch. Die Simulationsergebnisse zeigen, dass die axiale Geschwindigkeitsverteilung in der Rotorebene beim Schweben im nicht parallelem Bodeneffekt hauptsächlich in der Nähe der Rotorblattspitzen auf der hangaufwärtigen Seite und in der Nähe des Rotorkopfes beeinflusst wurde.

Die aerodynamischen Wechselwirkungen zwischen den Rotorebenen von Koaxialrotoren wurden anhand zweier Rotorkonfigurationen mit je 2 m Durchmesser untersucht. Eine erhöhte Komplexität des Strömungsfelds nahe der unteren Rotorebene wurde durch den Abwind des oberen Rotors und zusätzlich durch Luft, welche von außerhalb des oberen Rotorabwinds nahe der Blattspitzen in die untere Rotorebene gesaugt wurde, verursacht. Die Auswertung der Wirbeltrajektorien des gegenläufigen Rotors ergab, dass sich die Wirbelbahnen der oberen und unteren Blätter nicht schneiden und weitestgehend parallel verlaufen, sowie eine geringe Abhängigkeit von der Blattbelastung aufweisen. Der gleichläufige Rotor zeigte eine starke Abhängigkeit der Trajektorien von der Blattbelastung und dem eingestellten Indexwinkel zwischen den Rotorebenen. Abhängig von

deren Kombination zeigten Analysen der Simulationsergebnisse direkte Blattwirbelinteraktionen, Wirbelverschmelzung, bzw. quasi parallele oder sich kreuzende Wirbelbahnen. Insgesamt war die erhöhte axiale Konvektion der oberen Rotorblattspitzenwirbel bei Koaxialrotoren, und somit deren Distanz zu den Rotorblättern, einer der wichtigsten Einflüsse auf die Rotorströmung. Darüber hinaus zeigte sich, dass zeitgemittelte Strömungsfelder, Wirbeltrajektorien, axiale Geschwindigkeitsverteilungen und die Aufteilung des Gesamtschubs auf die Rotorebenen sowie deren Abhängigkeit zum eingestellten Indexwinkel beim gleichläufigen Rotor generell gut vorhergesagt wurden.

Die transiente aerodynamische Reaktion schwebender Rotoren auf kollektive Einstellwinkel- und Rotordrehzahländerungen, wurde anhand der gleichen Rotorkonfigurationen untersucht. Numerische Ergebnisse zeigten Schubüberhöhungen für Einstellwinkeländerungen von 1° und 2°, die über 0.5 und eine Rotorumdrehung eingesteuert wurden, sowie für eine Rotordrehzahlerhöhung von 20%, welche über eine Rotorumdrehung eingesteuert wurde. Die Überhöhungen wurden durch den zeitlichen Verzug zwischen den Steuereingaben und dem Aufbau des Inflow hervorgerufen. Relative Schubüberhöhungen waren im Innenbereich der Rotorblätter am größten, was darauf hindeutete, dass sich der Inflow zunächst in der Nähe der Blattspitzen und nachfolgend in der Nähe der Blattwurzeln aufbaute. Für längere Eingabedauern ergab sich eine gute Übereinstimmung zwischen Simulation und Experiment, jedoch ohne Schubüberhöhungen hervorzurufen. Darüber hinaus stimmten die transienten axialen Geschwindigkeitsverteilungen an fixen räumlichen Punkten gut überein. Die Strömungsgeschwindigkeit nahmen während der Einsteuerung kontinuierlich zu, was darauf schließen ließ, dass sich der Inflow dort im vergleichbaren Maß zu den Einsteuerungen veränderte.

Abstract

The investigation of flow fields of rotorcraft in hover and their modeling has so far mostly been conducted in stationary hover flight. In order to promote hovering rotor research the aerodynamics of other flight conditions and rotor configurations, which have received significantly less attention so far, were investigated in the thesis at hand. Three different research objectives were addressed: the influences of non-parallel ground effect on the flow field and inflow, similarities and differences between the aerodynamics of coaxial co-rotating (stacked) and counter-rotating (CCR) rotors, and the aerodynamic response of rotors to dynamic collective pitch and rotor rotational speed step inputs.

Unsteady Reynolds-averaged Navier–Stokes simulations were conducted to gain insights into the underlying flow physics and to study the influences of multiple turbulence models on the simulation results. Experimental data were provided by research partners and correlated to the numerical results to assess the accuracy of the simulations. The aerodynamics were investigated, inter alia, based on instantaneous, phase-averaged, and time-averaged velocity (inflow) distributions, vortex trajectories, sectional force distributions, and thrust sharing.

The influence of inclined ground planes on the flow field and inflow was studied based on a two-bladed 0.8 m-diameter rotor. In addition, data was compared to hover out of ground effect. It was found that the inclined ground plane affected the time-averaged and phase-averaged flow fields. The rotor slipstream lifted off the ground on the downhill side and the stagnation point on the ground plane shifted uphill, i.e., the flow field got asymmetric. Computations revealed that the axial velocity distribution in the rotor plane was mostly affected near the blade tips on the uphill side and near the rotor head when hovering over inclined ground planes.

Rotor-rotor interference was studied based on two two-by-two-bladed 2 m-diameter rotors. In general, a higher complexity of the flow field near the lower rotor was seen, which was affected by the upper rotor downwash and fluid that was entrained from outside the upper rotor slipstream boundary near the blade tips. For the CCR rotor it was found that tip vortex trajectories (slipstream boundaries) kept their separate paths and showed little dependence on blade loading. For the stacked rotor a strong dependency on blade loading and index angle was seen. Depending on their combination, blade-vortex interactions, vortex pairing, parallel or intersecting of vortex trajectories were observed. It was found that the increased axial convection of the upper rotor tip vortices for coaxial rotor designs and thus, the miss-distance between the upper rotor tip vortices and the rotor blades, was one of the most important influences on the rotor flow fields. Correlations with available experimental data showed that time-averaged flow fields, tip vortex trajectories, axial velocity distributions, as well as thrust sharing and overall thrust variations when varying the index angles for the stacked rotor, were accurately predicted.

The transient aerodynamic responses of hovering rotors caused by collective pitch and rotor rotation speed inputs were studied using the same rotor configurations. Numerical results revealed thrust overshoots for collective pitch inputs of 1° and 2° commanded over 0.5 and one rotor revolution, as well as for a rotor rotational speed increase of 20% commanded over one rotor revolution. Results showed that the overshoot at the end of the inputs was linked to the time required for the inflow to build up. Moreover, the relative sectional thrust overshoot was largest at inboard sections. It was concluded that inflow built up first towards the tip and then progressed further inboard. Good agreement between simulation and experiment was observed for increased input durations, though without showing thrust overshoots. Transient axial velocity distributions were in good agreement and were continuously increasing during the inputs, indicating that the inflow built up at similar rates compared to the commanded inputs at fixed points in space.

Acknowledgments

I was fortunate to be able to work with and learn from many outstanding people during my dissertation. They were all making essential contributions to the success of my research and to the joy that my work brings me. I am grateful to each and every one of them.

I want to thank my doctoral supervisor Manfred Hajek for his support and appreciation during the last years. I am thankful for his unreserved trust and the chance to work independently under his guidance. I would also like to thank him very much for always offering a sympathetic ear and good advice in difficult situations.

Additionally, I would like to thank my mentor Jürgen Rauleder. In particular his commitment, the intensive exchange of expertise and ideas, and his guidance were extremely valuable and a continuing source of encouragement and inspiration to my work.

Moreover, it was a great pleasure working with Martina Thieme, the heart of our institute. Thank you for all you have done to help me navigate the jungle of TUM's special regulations, all the laughs, and the many good and cheerful conversations we have had over the years.

I want to thank Joseph Milluzzo for sharing his experimental data and expertise. Furthermore, I would like to thank Jayant Sirohi, Patrick Mortimer, Chloe Johnson, and Daiju Uehara for hosting me during my research visit at the University of Texas at Austin as well as for the excellent cooperation during our joint research projects. It was a great pleasure working with all of you.

Furthermore, my colleagues deserve a huge thank you for all the fruitful discussions, continuous encouragement to pursue my research in hard times and the magnificent working environment. I particularly want to mention my office-mates Aaron Barth, Markus Rinker, Roland Feil and Lukas Maier, as well as Willem Rex and Bastian Horvat who always made time for a professional exchange and a good chat. Likewise, I want to thank our institute's team of system administrators for the excellent cooperation and all you taught me.

I also want to thank the team at Leibniz Supercomputing Centre and the TAU developers at Deutsches Zentrum für Luft- und Raumfahrt for their quick, friendly, extremely helpful and highly professional support, whenever it was needed.

Finally, I would like to thank my family and friends for their continuous moral support and encouragement during the last years. This is especially true for my partner Magdalena Schwojer, who has gone through all the ups and downs of my work with me and has shown a lot of understanding, encouragement, patience, indulgence, support, and love. Thanks!

Contents

Abbreviations and Symbols

Acronyms

2D-2C	two-dimensional, two-component
BVI	Blade Vortex Interaction
C	Chimera airfoil grid
CCR	Coaxial-Counter Rotating
CFD	Computational Fluid Dynamics
CFL	Courant–Friedrichs–Lewy
DES	Detached Eddy Simulation
DLR	German Aerospace Center (*Deutsches Zentrum für Luft- und Raumfahrt*)
DNS	Direct Numerical Simulation
EARSM	Explicit algebraic Reynolds stress models
FOV	Field of View
G	Airfoil grid
IGE	In Ground Effect
LEA	Linearized Explicit Algebraic Stress Model
LES	Large Eddy Simulation
LRR	Launder-Reece-Rodi model
LU-SGS	Lower-Upper Symmetric Gauss–Seidel
NS	Navier–Stokes
OGE	Out of Ground Effect
PIV	Particle Image Velocimetry
RANS	Reynolds-Averaged Navier–Stokes
RC	Rotation/Curvature Correction

ROI	Region of Interest
RPM	Revolutions per Minute
RQEVM	Realizable Quadratic Eddy Viscosity Model
RSM	Reynolds stress model
SA-neg-RC	Negative Spalart–Allmaras One-Equation Model with Rotation/Curvature Correction
SAS	Scale-Adaptive Simulation
SSG	Speziale-Sarkar-Gatski model
SSG-LRR-ω	Speziale–Sarkar–Gatski/Launder–Reece–Rodi differential Reynolds-stress model + ω equation
SST	Menter Shear Stress Transport Model
SST-RC	Shear Stress Transport Model with Rotation/Curvature Correction
SST-SAS	Menter Shear Stress Transport Model with Scale-Adaptive Simulation
SST-SAS-RC	Menter Shear Stress Transport Model with Scale-Adaptive Simulation and Rotation/Curvature Correction
T	Transfer grid
URANS	Unsteady Reynolds-Averaged Navier–Stokes
USNA	United States Naval Academy
UTA	University of Texas at Austin

List of symbols

Greek

Symbol	Description	Unit	Formula
α	Angle of Attack	deg.	
α_0	Zero-lift Angle of Attack	deg.	
β_p	Precone angle	deg.	
δ_{ij}	Kronecker delta	-	
Δ	Difference	-	
Δs	Grid spacing	% c	
Δz_r	Inter-rotor spacing	% R	$= z_r / R$
		c	$= z_r / c$
ϵ	Turbulent dissipation rate	$\mathrm{m^2\,s^{-3}}$	$= 2\nu\overline{S_{ij}S_{ij}}$
Γ	Circulation	$\mathrm{m^2\,s^{-1}}$	$= \iint_S \omega \cdot \mathrm{d}S$
Γ_1	Non-dimensional scalar quantity	-	see Appendix C equation C.1
ζ	Wake age of the tip vortex	deg.	$= \Omega t$
Θ	Pitch angle	deg.	
Θ_0	Blade collective pitch angle	deg.	
$\Theta_{1\mathrm{c}}$	Blade longitudinal cyclic pitch angle	deg.	
$\Theta_{1\mathrm{s}}$	Blade lateral cyclic pitch angle	deg.	
Θ_{GP}	Ground plane inclination angle	deg.	
Θ_{TR}	Tail rotor collective pitch angle	deg.	
Θ_M	Angle between velocity vector and radius vector	deg.	
μ	Dynamic viscosity	$\mathrm{kg\,m^{-1}\,s^{-1}}$	
μ_t	Eddy viscosity	$\mathrm{N\,s\,m^2}$	
ν	Kinematic viscosity	$\mathrm{m^2\,s^{-1}}$	$= \mu / \rho$
ν_t	Eddy viscosity	$\mathrm{m^2\,s^{-1}}$	$= \mu_t / \rho$
ξ	Azimuthal angle of plane of data extraction	deg.	
$\tilde{\nu}$	Spalart–Allmaras viscosity	$\mathrm{m^2\,s^{-1}}$	see [2]
ρ	Air density	$\mathrm{kg\,m^{-3}}$	
σ	Rotor solidity	-	$= N_b c / (\pi R)$
σ	Standard deviation	m	
τ_w	Wall shear stress		$= \rho\nu \left(\frac{\partial V_x}{\partial y}\right)_{\mathrm{y=0}}$
ϕ	Rotor index angle	deg.	
ψ_b	Rotor blade azimuth angle	deg.	

Symbol	Description	Unit	Formula
ω	Turbulence frequency / rate of dissipation per unit turbulent kinetic energy	s^{-1}	$= \epsilon / k$
ω	Vorticity	s^{-1}	$= \nabla \times \mathbf{U}$
Ω	Rotational frequency of the rotor	Hz	
Ω	Rotation rate tensor	s^{-1}	$= \frac{1}{2}\left(\frac{\partial U_i}{\partial x_j} - \frac{\partial U_j}{\partial x_i}\right)$

Roman

Symbol	Description	Unit	Formula
a	Speed of sound	$m\,s^{-1}$	$= \sqrt{\kappa \frac{p}{\rho}}$
A	Rotor disk area	m^2	$= \pi R^2$
c	Rotor blade chord length	m	
c_l	Section lift coefficient	-	$= L/0.5\rho V^2 c$
c_d	Section drag coefficient	-	$= D/0.5\rho V^2 c$
c_{my}	Airfoil pitching moment coefficient	-	$= M/0.5\rho V^2 c^2$
c_p	Pressure coefficient	-	$= (p - p_r ef)/q_\infty$
C_P	Rotor power coefficient	-	$= P/\rho A(\Omega R)^3$
C_T	Rotor thrust coefficient	-	$= T/\rho A(\Omega R)^2$
C_Q	Rotor torque coefficient	-	$= Q/\rho A(\Omega R)^2 R$
D	Diameter	m	
dF	Section force per unit span	$N\,m^{-1}$	
dM_z	Section torque coefficient per unit span	$Nm\,m^{-1}$	$= dF_x r$
g_{bl}	Boundary layer growth rate	-	
I	Rotor moment of inertia	$kg\,m^2$	
k	Turbulent kinetic energy	$m^2\,s^{-2}$	$= \frac{1}{2}\overline{V_i' V_i'}$
L	Section lift per unit span	$N\,m^{-1}$	
M	Moment per unit span	$Nm\,m^{-1}$	
M	Mach number	-	$= V/a$
N	Number of points	-	
N	Number of revolutions	-	
N_b	Number of rotor blades	-	
p	Pressure	$N\,m^{-2}$	
P	Point in data set	-	
P	Power	W	
$\mathbf{P}$	Radius vector	m	
q_0	Dynamic pressure with simulation reference variables	$N\,m^{-2}$	$= \frac{1}{2}\rho_{\mathrm{ref}} V_{\mathrm{tip}}^2$

Symbol	Description	Unit	Formula
Q	Rotor torque	Nm	
Q	Q-criterion	s^{-2}	$= \frac{1}{2}\left(\|\Omega\|^2 - \|S\|^2\right)$
r	Radial coordinate in cylindrical coordinates	-	
r	Radial distance from rotational axis	c	
r	Radial distance from rotational axis	m	
r_a	Blade root cut out	% R	$= y_a/R$
R	Rotor radius	m	
Re	Reynolds number	-	$= Vc\rho/\mu$
R_{rho}	Scaled density residual	-	
S	Area	m^2	
S	Strain rate tensor	s^{-1}	$= \frac{1}{2}\left(\frac{\partial U_i}{\partial x_j} + \frac{\partial U_j}{\partial x_i}\right) - \frac{1}{3}\nabla \cdot \mathbf{U}\delta_{ij}$
t	time	s	
T	Rotor thrust	N	
u_τ	Friction velocity	$m\,s^{-1}$	$= \sqrt{\tau_w/\rho}$
$\mathbf{U}$	Velocity vector	$m\,s^{-1}$	
v_h	Theoretical hover induced velocity	$m\,s^{-1}$	$= \sqrt{T/(2\rho A)}$
v_z	Vertical velocity component	$m\,s^{-1}$	
V	Velocity	$m\,s^{-1}$	
V_{tip}	Rotor tip speed	$m\,s^{-1}$	$= \Omega R$
x,y,z	Distance in Cartesian coordinate system	m	
X,Y,Z	Cartesian coordinate system	-	
y	Wall normal coordinate	m	
y_a	Begin aerodynamic section	m	
y^+	Dimensionless wall distance	-	$= u_\tau y/\nu$
$\mathbf{z}$	Unit vector normal to plane	-	

Subscripts

Symbol	Description
2b	Two-bladed single rotor
aer	Aerodynamic
az	Azimuthal direction
b	Blade
bl	Boundary layer
c	Vortex core

Symbol	Description
coax	Coaxial rotor
eff	Effective
equiv	Equivalent
exp	Experiment
GP	Ground plane
hpp	Half peak-to-peak
i,j,k	Direction in computational space
i	inertial
l	Lower rotor
mag	Magnitude
max	Maximum
r	Radial direction
ref	Reference
sim	Simulation
T	Turbulent
tip	Blade tip
tot	Total
u	Upper rotor
x,y,z	Coordinate directions

Superscripts

Symbol	Description
$\bar{}$	Average
$'$	Fluctuating part

Symbols

Symbol	Description
∇	Gradient operator

List of Figures

List of Tables

1. Introduction

Recently there has been a resurgence of interest in the aeromechanics of coaxial rotor systems. These rotors have gained popularity in the field of Urban Air Mobility as they are a compact, highly efficient way to produce thrust. Moreover, to increase rotorcraft cruise flight speed Coaxial-Counter Rotating (CCR) rotor systems with closely-spaced, rigid-hub rotors have received increased attention. However, due to the close proximity of the two coaxial rotor planes, the flow field of coaxial rotors is considerably more complex than that of an isolated single rotor, especially in hover. In addition, as the range of applications of unmanned aerial systems is ever-increasing, engineers and researchers need to be able to accurately model all possible flight conditions, including operations near obstacles and the ground. Furthermore, due to advances in electric motor technology the design space for new aircraft configurations has been significantly increased. A possible design choice are distributed electric propulsion systems, for which rotorcraft control can be achieved by differential collective blade pitch angle changes or without complex swashplate mechanisms by fixed-pitch, variable rotational speed rotors.

In order to design control systems and to model arbitrary flight conditions of vertical lift aircraft employing any of the aforementioned ideas and technologies, computationally efficient mathematical models are required, which are capable of simulating the rotor inflow in these complex flow environments. Existing dynamic inflow-type models could fulfill that need. However, a prerequisite for developing such models further is an understanding of the complex three-dimensional fluid dynamics of the problem, which does not fully exist to date.

So far, a vast variety of different mathematical methods has been developed to compute and analyze the flow fields of rotors in hover, ranging from, e.g., integral approaches such as momentum theory, over blade element theory used in combination with a variety of inflow models, to high fidelity three-dimensional Computational Fluid Dynamics (CFD) approaches solving different forms of the Navier–Stokes (NS) equations. Even though the physical modeling depth and accuracy has been increasing continuously, the accurate computation of rotor inflow in hover is still a challenge, even for modern computational tools. The already high physical complexity of the aerodynamic environment in hover is further complicated when rotors are operating In Ground Effect (IGE), by the presence of rotor-rotor-interference for coaxial rotor configurations, or if the transient responses due to control inputs need to be considered.

Therefore, a research cooperation was established between Technical University of Munich (TUM) and two partner universities (United States Naval Academy (USNA) and University of Texas at Austin (UTA)) to promote hovering rotor research in the aforementioned areas. Three research questions were posed to help close existing knowledge gaps. First, hovering rotors over inclined, i.e., non-parallel, ground planes were investigated as a first step to a better understanding of the

aerodynamics of rotors operating over arbitrary oriented or moving surfaces (e.g., ship decks). Second, the flow fields of coaxial co-rotating (stacked) and CCR rotors were investigated to help understand the similarities and differences between the two coaxial rotor concepts. Third, the transient aerodynamic effects caused by commanding collective pitch and rotor Revolutions per Minute (RPM) inputs were studied.

Combined experimental and numerical studies were conduced for all three research objectives to investigate the underlying fundamental aerodynamic characteristics of the different rotor concepts and operating conditions. The studies focused on describing and understanding the (transient) rotor flow fields, rotor loads, rotor inflow and wake in response to inclining the ground plane, rotor-rotor interactions, and changing pitch and RPM commands. In particular, the experimental data provided by the project partners was correlated to the finite-volume Unsteady Reynolds-Averaged Navier–Stokes (URANS) CFD simulations performed by the author to assess the accuracy and applicability of the chosen modeling strategy for the posed research questions.

2. Current Status of Research and Objective of Work

The numerical simulation and experimental investigation of the flow field characteristics of rotorcraft in hover are ongoing research topics; see, e.g., the AIAA Rotorcraft Hover Prediction Workshop and the associated rotor tests[1]. In the past, most studies were conducted in stationary hover flight using single rotors, i.e, rotors operated at constant thrust with all blades located in the same rotor plane. For these rotor designs the associated flow field characteristics are relatively well known. However, other rotor concepts or flight conditions received significantly less attention. In order to promote hovering rotor research, such flight conditions (non-parallel ground effect) and rotor configurations (stacked and CCR rotors) were investigated in this thesis. Moreover, the research was expanded towards the transient behavior of rotors and their associated flow fields when commanding dynamic pitch angle ($\Delta\Theta_0$) and RPM step inputs. Compared to isolated single rotors, these flight conditions and configurations are characterized by asymmetries in the flow fields, time-dependent inflow variations, and increased inter- and intra-rotor vortex interactions. Open research questions were identified based on a literature research, which also served as a foundation for data evaluation and baseline for the creation of the numerical simulations. Consequently, the subsequent sections of this chapter focus on previous experimental and numerical work, including computational results generated by other numerical approaches than the URANS CFD approach used in this study (see chapters 2.1 to 2.3), and the scientific approach and methodology used in this thesis; see chapter 2.4.

2.1. Rotors in Ground Effect

Aerodynamic interactions between rotors and the ground have always been of great concern for rotorcraft. Especially during take-off and landing the well documented performance benefits for hovering IGE can be used to reduce power requirements at a given rotorcraft weight, or increase the lift capability over the amount possible Out of Ground Effect (OGE)[68, 20, 35, 44, 85]. Moreover, multiple research activities investigated the flow topology of a hovering rotor above a parallel ground plane[144, 78, 141, 98]. Early attempts used, e.g., balsa-dust[144] or the wide-field shadowgraph method[85] to visualize the effect of ground proximity on the rotor flow field and compared it to hover OGE. More recent studies performed flow visualization by illuminating tracer particles with a laser and flow field measurements using Particle Image Velocimetry (PIV)[78, 141, 98]. The latter not only allowed to gain qualitative but also quantitative insights into the behavior of tip vortices and trailed vortex sheets for hover IGE. In comparison to hover OGE, "the rotor wake initially contracts below the rotor but then rapidly turns and expands outward in a direction that is

nearly parallel to the ground plane"[141]. Due to the stretching of the tip vortices, a reintensification could be observed which increases the persistence of the tip vortices for hover IGE compared to OGE. The final decay of the vortices is caused by viscous interaction (shearing) with the ground plane.[97, 141] The general effect on the flow topology is illustrated, e.g., in Figs. 5.2 and 5.23.

Besides the beneficial aspects of ground effect, the interaction between the rotor downwash and the ground can also cause detrimental effects such as brownout or whiteout. Here, particles from the ground (dust, snow) are picked up and dense clouds form around the rotorcraft. These clouds reduce visibility levels significantly and can lead to losses of aircraft as the pilots ability to safely operate the rotorcraft is drastically reduced[124]. Therefore, these dual-phase flows (air and sediment) were investigated experimentally by means of flow visualization, PIV and particle tracking in the past[141, 124]. The focus of these studies was on the mechanisms causing particle pickup and the extend to which the dual-phase flow altered the flow field in comparison to a single-phase flow, i.e., air. It was found that at least six fundamental uplift and sediment transport effects exist[141], with the dominant feature being the tip vortices[141, 124]. Also, the turbulence characteristics were measurably affected by the presence of the second flow phase[124].

More recent experiments using a model scale helicopter in ground effect were reported in [156]. Hereby, in contrast to the previously cited studies, volumetric flow field measurements were performed using helium-filled soap bubbles, and the focus of this study was to experimentally measure secondary vortex structures known from high-resolution numerical simulations. These were identified and appeared to "entangle the primary tip vortices in an 'S'-shaped layout"[156]. The used helium-filled soap bubbles resulted in a void in the tip vortex centers, and therefore, no information on tip vortex core-related information was given. Hence, the focus was not on rotors in ground effect per se, but rather the experimental setup built to measure the secondary vortex structures required IGE rotor operation.

Most flow visualization experiments use model scale rotors. One of the exceptions was reported in [72], where the flow field of a Hughes 300C was investigated in hover to track the tip vortices and gain a general understanding of the flow topology. Moreover, thrust trimmed numerical simulations (Reynolds-Averaged Navier–Stokes (RANS)) of the isolated rotor were correlated to the experimental results. It was found that the tip vortex trajectories correlated well with the experimental data up to the first blade passage ($\zeta = 120°$). However, due to the relatively coarse mesh, the tip vortices could not be properly preserved and transported to the ground.

Another relatively exotic full scale configuration was investigated in [38] and was motivated by the Sikorsky Human Powered Helicopter Challenge to build a rotorcraft powered solely by one or more humans. In this configuration the rotor operated in extreme ground effect ($z/R \approx 0.1$) and at extremely low RPM (RPM ≤ 20). The experimental performance results were used to validate a blade element aerodynamics model with rigid prescribed wake (with a mirror image rotor representing the ground) and a finite-element structural model, which allowed parametric studies to find the optimal parameter combination for the tasks envisioned.

Besides experimental investigations different mathematical / numerical methods have been developed and used to investigate the aerodynamics of rotors in ground effect. The simplest mathematical tools are empirical correlations which relate power and thrust IGE to the respective OGE

values based on experimental results; see, e.g., [20, 44].

More detailed analysis are possible by using wake models. For example, in [49] a rigid wake model was used to compute the rotor flow field. This model neglected the aforementioned physically required wake distortion in ground effect. The impact of the ground on the wake system was modeled by different means, such as a truncation of the wake, deflection of the wake on the ground or a mirror boundary condition. In [126] variations in rotor thrust near the ground or ceiling were investigated using arrays of concentric vortex cylinders with a mirror technique. The methodology was improved by "semiempirical"[126] corrections, which modified the axial distance of the image rotor system above the ceiling. Using this correction worked well as long as the ground or the ceiling were not to close to the rotor. These methods require problem dependent assumptions and modifications, and hence, more generic tools are desirable.

A more physical approach towards rotor in ground effect computations can be made by using free wake analysis. Multiple attempts have been pursued to properly model the influence of the ground on the rotor wake such as, e.g., using a mirror image of the wake [85], or a combination with a panel method to simulate the ground [54]. In [85] it was found that the vortex trajectory could adequately be represented, while considerable differences were observed for the variations of thrust and figure of merit with the distance to the ground. In particular, the reduction of hovering power closer to the ground ($z/R < 1$) was not accurately reproduced. In [54] panels were used to compute the non-penetration boundary condition on the ground. This enhanced the free wake solver capabilities as any relative orientation between the rotor and the ground could be included in the analysis.

To overcome some of the empiricism of wake methods and to further increase the physical modeling depth the Euler or NS equations can be applied. The Euler equations were, for example, solved in [142, 143] on a fourth-order accurate Cartesian background grid. Due to neglecting viscosity in the simulations the method is less diffusive compared to viscous simulations. However, the relatively coarse background mesh caused the tip vortices to diffuse too quickly and thus, they were not properly transported down to the ground plane. Nevertheless, the reduction of power IGE showed similar trends when compared to empirical correlations based on experimental data[20, 44]. The results showed in an exemplary way that spacial resolution is of crucial importance when solving the Euler or NS equations to properly resolve the tip vortices, especially for hover IGE.

Extensive numerical studies using URANS simulations have been made at the University of Maryland for hover IGE over parallel ground planes[60, 61, 62, 75, 63]. Within the course of their investigations, a main focus of the work was put on improving the numerical tools to properly preserve the tip vortices and compute the interaction with the viscous ground plane. They found that a system of overset/chimera meshes showed excellent correlation to numerical results. In particular, vortex tracking grids were used along with a higher-order accurate spacial discretization. It was observed that the rotor performance was little affected by the ability to transport the tip vortices to the ground plane, i.e., by using vortex tracking grids, as long as the overall flow topology was computed correctly[75]. In [63] the effect of turbulence modeling on the simulation results was described. The Spalart–Allmaras One-Equation Model (SA) turbulence model results were compared to laminar computations and Detached Eddy Simulation (DES) simulations. The laminar computation, neglecting the physically relevant effects of turbulence in the flow field, showed

best correlation to experimental data. DES simulations did not per se improve the simulation results. Only when adapting the length scale function to take the grid stretching in the rotationally symmetric background grid into account, the DES simulation showed superior performance compared to the simpler approaches.

A numerical study simulating the flow field of a model scale helicopter in ground effect with significantly increased spacial resolution (more than 950 million grid points in the background mesh) was described in [14]. The focus of this study was to assess effects of sub-iteration convergence on the creation of secondary vortex structures. In addition, a qualitative comparison to the experiments described in [156] was made. The ground plane was modeled as a frictionless impermeable wall because the flow field on the ground was not of concern in this study (it was a specification by the experiment). It was found that the development of secondary vortex structures was only independent of the used grid setup if a sufficient spacial resolution and convergence of the inner iterations was achieved. The derived thresholds for inner iterations counts were found to be solver dependent and thus, no general guideline could be given for other solvers to accurately compute secondary vortex structures in rotor wakes.

An extension of the parallel ground plane case is hover over obstacles (e.g., over buildings) or in confined areas (e.g., next to buildings, urban canyons). Experiments have been performed by different research groups. In [53] hub load measurements were used to assess the performance of rotorcraft in confined areas. It was found that rotorcraft can enter the vortex ring state in confined areas and experience recirculation. In [37, 109] pressure measurements on the obstacles, PIV and hub load measurements were made to investigate the flow field of hovering rotorcraft over obstacles. It was found that the amount of ground effect was highly affected by the fraction of the rotor area which was above the obstacle and could even reverse the beneficial effects of ground effect when hovering in front of the obstacle. Large recirculation regions formed next to the building with the highest unsteadiness in the flow field when hovering over the edge of the obstacle. The experimental results published in [37] were, for example, used to validate URANS simulations of varying modeling fidelity[22]. Hereby, fully resolved blades and (unsteady) actuator disk computations were made in hover and with side wind. Moreover, it was investigated to what extend a superposition of the rotor flow field and the flow around the building is justified. It was found that the actuator disk was sufficient to model the average flow at one rotor diameter away from the obstacle, but that resolving the tip vortices was required to capture the unsteady effects. Furthermore, the superposition method proved to be inaccurate if the rotor was in close proximity to the obstacle.

An area of research for rotorcraft IGE, where only a very limited amount of work has been done in the past, is hovering in non-parallel ground effect and the associated changes in flow topology and inflow. Non-parallel ground effect plays a role when hovering over sloped terrain, or can be regarded as the simplified case of hovering over a moving ship deck. Experiments and evaluations of experimental data on this topic have been published, e.g., in [35, 51, 52, 69, 99, 112, 146, 90]. In [51, 52] a two-bladed articulated rotor was investigated in hover over inclined surfaces in full and partial ground effect. Hub load and blade flapping measurements were performed. It was found that the effects on rotor torque were small when inclining the ground plane. The coning angle showed no significant changes for low to moderate ground plane inclination angles ($\Theta_{GP} = 0°$, ..., $15°$). The cyclic blade flapping did show a response to changing ground plane inclination angles, how-

ever, for moderate Θ_{GP} the flapping amplitudes were comparable to the parallel ground plane. The differences mostly manifested as a phase shift.[51] For the partial ground effect investigations a strong dependency of the flapping angle on the center-to-edge distance from the rotor hub to the ground plane edge was observed. Moreover, the partial ground effect got stronger for reduced hovering heights above the ground plane.[52] Similarly, in [35] results indicated that the thrust augmentation IGE was only slightly reduced when hovering over inclined ground planes.

Another experimental study on hover over inclined ground planes was described in [69]. Flow visualization and Laser Doppler Anemometry (LDA) measurements were made to examine a rotor hovering above an inclined ground plane at $\Theta_{GP} = 10°$. This study documented a change in the mean induced velocity between the uphill and downhill sides of the rotor, but only the outboard region near the blade tip was examined. A drawback of the study was the relatively coarse measurement grid for the LDA measurements. Furthermore, because of the qualitative nature of flow visualization, the wake could not be investigated quantitatively.

A detailed investigation of the flow fields of hovering rotors above inclined ground planes was made in [99] and further assessed by the author of the present thesis along with the experimenter in [112]. PIV and hub load measurements were conducted on a model scale rotor to assess the effect of ground plane inclination on the flow field and vortex trajectories. It was found that at low thrust, as profile power dominates, the ground plane angle had little effect on the rotor. The Figure of merit was at a maximum when hovering over a parallel ground plane.[99] A description of the rotor setup is given in chapter 3.1 and the effects on the flow field for hover OGE, and over a parallel and inclined ground plane ($\Theta_{GP} = 15°$) are described in chapter 5. The experimental work was extended in [90] for dynamic ground plane movements (heaving and pitching). The heaving motion mostly affected thrust and was most pronounced for low thrust conditions, large heaving amplitudes and low mean rotor heights above ground. Ground plane pitching resulted mainly in a rotor pitching moment response. In contrast to the heaving motion, the tested magnitudes of ground plane pitching did not affect the rotor pitching moment response significantly, and the effect was more pronounced under high thrust conditions.

Full scale flight tests over sloped terrain were made in [146] using a UH-72A helicopter. Different flight conditions (thrust/power), hub heights above ground, slope angles and aircraft orientations were tested. It was found that the "performance for hover over sloped terrain are both nonintuitive and operationally significant"[146]. The tests revealed that hover in parallel ground effect is not just a matter of rotor head height above ground. Rotor thrust and power settings were also crucial parameters. Moreover, performance effects were significant enough in the flight tests to not be masked by the general measurement uncertainty. For sloped terrain, the aircraft orientation was considered of minor importance, i.e., the main rotor is the dominant quantity of interest. Furthermore, over sloped terrain, the power requirements of the full scale helicopter can exceed OGE or fall below classical IGE correlations over level terrain, while laboratory data results showed higher power requirements over sloped terrain compared to hover flight over level ground[146].

Numerically, hover over sloped terrain was investigated with different computational tools. In [54] a free wake panel method using a single trailer wake model was used. The model showed a qualitative agreement with the flow topology measured in [99], i.e., streamline patterns showed a comparable shift of the stagnation point on the ground plane towards the uphill side. Note that

in [99] a different two-bladed rotor with smaller radius was used and hence, the results are not directly comparable. A drawback of this method was that the wake became highly distorted and attached closely to the ground plane, a flow feature that was not seen in the detailed analysis of the wake structure by the author of the current thesis[112] and chapter 5. In [112] URANS results were correlated to the experimental results first published in [99]. A detailed assessment of the correlation and the detailed analysis of the flow topology is given in chapter 5. The same experiment was used to correlate results of a potential based three dimensional free-wake aerodynamic solver, where the ground plane was modeled by a mirror plane[108]. The effect of the ground on the vortex trajectories was underestimated in this study for the inclined ground plane as the rotor slip stream attached to closely to the ground on the downhill side. Axial velocity distributions close to the rotor blades showed large deviations from the experimental results. However, the overall flow topology was in good agreement with the measurements and performance correlated well.

If the flow field on the ground plane is of lesser importance and the primary goal is to compute the inflow in the rotor plane, e.g., for flight simulations or controller development, the aforementioned mathematical / numerical procedures are either not generic enough (semi-empirical correlations) or too cost intensive (e.g., URANS). Therefore, over the past decades, considerable amounts of research projects were started to development finite state dynamic wake inflow models capable of modeling static and dynamic ground effect[161, 162, 163, 158, 159, 160, 45, 168]. In the most widely used approach these models are based on the Peters-He finite state dynamic wake interference model[48, 47]. The Peters-He model is based on solving the equations for incompressible potential flow in the limit of small perturbations, while fulfilling the continuity and momentum equations. Model variants can take rotor wake distortion effects into account and allow to compute aerodynamic interaction velocities at points in the flow field, e.g., the rotorcraft stabilizers[47]. Further developments include wake decay and and expansion[45].

The extensions of the model for ground effect computations use source like pressure perturbations on the ground plane to satisfy the no penetration boundary condition[161, 163]. The inflow field at the rotor is computed by superposition of the rotor and ground flow field. The model has been used to numerically show the effects of ground motion on the rotor, e.g., during shipboard operations[161, 162, 163]. It was found that the superposition is superior to the image rotor method[162] and that it can be extended to partial ground effect[158, 160], or interactions between multiple rotorcraft[45]. The methods have been correlated with static (partial and inclined) test data[159, 45], but the lack of experimental data for inclined and dynamic ground effect conditions limited the ability for validation. A similar model was derived in [168] where the ground effect was modeled by a ground rotor, i.e., a second rotor in the fluid domain. The model uses a velocity potential and skewed cylindrical wake assumption. The ground rotor is represented as a mass source with exit pressure equal to the main rotor force exerted on the ground. Using a ground pressure correction was required to improve the results.

More recently, a two-way based coupling of a blade element based flight dynamcis code with a Lattice-Boltzmann based fluid dynamics solver was proposed to simulate the effects of arbitrary objects in the vicinity of a rotorcraft in real-time[13]. The influence of objects and their airwakes is transported to the rotor by the fluid simulation. This approach allows capturing changes in the inflow and hence, enables the computation of the changed rotorcraft dynamics. Compared to the established Pitt-Peters dynamic inflow model the proposed model showed good agreement

in terms of power required and control inputs in trimmed forward flight. Moreover, the effects of ground on power required were "adequately"[13] represented.

2.1.1. Objective – Rotors in Ground Effect

In the past, a vast variety of experiments and computations were made for rotors operating in ground effect. However, a gap in research could be identified for inclined ground planes. Comparisons between full scale and experimental data for hovering rotors over inclined ground planes gave inconclusive results in terms of power requirements[146]. Also, numerical methods could not thoroughly be validated by experimental data. A great dependency of the solution of RANS-based computations on the chosen turbulence model[63] and grid resolution / grid topology[75] could be shown for parallel ground planes. Such data were not available for inclined ground planes. Therefore, this thesis aims to quantify the effects caused by hovering over inclined ground planes on the rotor flow field. For one thing, this shall be achieved by an in-depth analysis of experimental data to provide a better understanding of the complex flow field of hovering rotors over inclined ground planes[99, 112]; see chapter 5. From a numerical point of view, an extensive study on the effects of grid and temporal resolution (chapter 4.5.1.7), and turbulence models (chapter 5) on the computed flow fields was made, as the literature review showed that such data were not yet available. Furthermore, experimental and numerical data were correlated to assess the validity and accuracy of the numerical simulations and to identify further research potential.

2.2. Coaxial Rotors

Inter- and intra-rotor interaction phenomena were investigated based on two different coaxial rotor configurations, namely a CCR and a stacked (co-rotating) rotor. Despite their inherent differences due to the different rotation directions of the lower rotor plane, the flow fields of both rotors are characterized by Blade Vortex Interaction (BVI) and vortex-vortex interactions. Hence, studying both designs can give valuable insight into the dominant fluid dynamic phenomena.

2.2.1. Coaxial-Counter Rotating

Research towards a better understanding of CCR rotor configurations has been conducted since the early days of rotorcraft development. An excellent survey of experimental and analytical research up to the year 1997 can be found in [23]. In this publication, aspects like rotor separation distance, load sharing, wake structure, solidity, swirl recovery, and the benefits of not requiring a tail rotor for torque balance were discussed. In [23] it was also pointed out that a lot of research was conducted in Russia that was never published. Results included an increase in rotor efficiency (Figure of Merit (FM)) compared to a single rotor with equivalent solidity; see e.g. [21]. One of the exceptions is [6] where a general overview of CCR rotor configuration aspects, including the sizing of control surfaces or effects on the drag characteristics of fuselages, was presented. General

characteristics of the rotor flow field were observed early on, such as that for CCR rotors in hover the upper rotor tip vortex contraction and downward convection is increased compared to the lower rotor; see, e.g., [21]. This feature of the flow field was used to explain the increased FM of CCR rotor configurations compared to the equivalent single rotor configurations with identical solidity σ. The wake contraction of the upper rotor allows clean air to be sucked in by the lower rotor. As a result this effectively increased the rotor disc area of a CCR rotor and hence, reduced the effective disc loading and therefore, the induced power. Also in forward flight CCR rotors can require less power if hub drag is not dominant. Furthermore, it was pointed out that "a detailed experimental study of the induced velocity flow field of a coaxial rotor system is required in order to advance the sophistication of current theoretical models"[23]. A statement which is still true at the time of writing this thesis. The overview is complemented by [123], where an extensive list of CCR rotor hover performance measurements conducted before 2010 is provided, and by [7] which lists multiple numerical studies for CCR rotors in hover and forward flight in the years 2006 to 2016 including the experimental data sources used for validation. In the remainder of the section, the focus will be placed on hover conditions only and the reader is referred to the cited overview papers for further information on CCR rotors in forward flight.

An early detailed investigations of the flow field of CCR rotors was performed using balsa-dust for flow visualization[144]. In this study a two-bladed teetering rotor was used in CCR and single rotor configuration. It was found that the vortex filaments of the two rotor planes interacted but did not cancel or merge, i.e., that the upper and lower rotor tip vortices kept their separate paths.

Rotor performance and blade motion measurements were performed in [43] with the so called *Harrington rotor*. The experiments were performed for a range of blade pitch angles and tip speeds on a 25 ft diameter teetering rotor. It was demonstrated that torque balanced CCR rotors had the lowest power requirements, i.e., when neither of the rotors dominated the flow field. Also, by varying rotor rotational speeds it was found that scale effects need to be considered, i.e., variations in rotor efficiency with Reynolds number were observed.

An early study measuring the induced downwash (hot wire anemometers and total pressure transducers) in addition to the rotor performance was made in [5]. It was found that the induced power was reduced by up to 5% for CCR rotors compared to single rotors at equivalent thrust potential, i.e., solidity. Moreover, measurements of the induced velocities showed that the equivalent single rotor induced a higher total downwash at each blade compared with the averaged downwash of the CCR upper rotor.

A study concerning the effects of tip vortex wandering, i.e., the "scatter in the instantaneous positions of a vortex due to the inherent unsteadiness of a rotor wake"[106], was performed on a 1 m diameter two-by-two bladed rotor in hover in [106]. The experimental data revealed that vortex wandering increased with wake age for the upper and lower rotor. The measured fluctuations in the vortex positions were higher for the lower rotor compared to the upper rotor. Furthermore, for the upper rotor, the amount of vortex wandering increased faster with wake age compared to the lower rotor. Moreover, the lower rotor vortex cores appeared to be more asymmetric compared to the upper rotor vortices at identical wake ages, i.e., they were more influenced by the superimposed axial velocity field produced by the CCR rotor configuration.

In addition to particularities in the flow fields, unsteady forces are of practical concern for CCR rotors. For example in [16] a two-by-two bladed rotor was tested at UTA, with the same test stand used for the CCR reference experiments in this thesis. It was found that the unsteady vibratory loads significantly increased compared to an isolated rotor, with the highest contribution at the blade passing frequency. Vibrations were recorded to be up to 11% of the mean thrust for the lower rotor at this frequency. In a second publication push rod loads were measured as well and the results were compared to momentum theory results and free wake analysis[17]. The upper rotor contributed 54% of the total system thrust at torque balance. The overall rotor performance was not affected by an unbalanced torque of up to 5%.

The same test stand was operated in a one-by-one bladed CCR rotor configuration[18]. Blade deformations were measured in the lower rotor plane using digital image correlation and results were compared to comprehensive rotorcraft analysis results computed with CAMRAD II. It was found that blade passage resulted in a flapping response of the rotor blades. Significant axial displacements were measured (deformations at the blade tip were in the order of the blade chord length). The computed two-per-revolution displacements and vibratory thrust correlated well with the experimental data. However, it was noted that the simulation could not capture thickness effects which produce thrust variations that could influence the higher harmonic content seen in the experimental data; see e.g. [73] for a discussion of the thickness induced impulsive loading of CCR rotors in hover. In [148] this study was extended. The two-per-revolution displacements due to blade passage in the lower rotor were reported to be up two 6% of the mean flapping displacements at the tested inter-rotor spacing and blade loading. Moreover, the study showed that the upper rotor experienced higher mean displacements due to the larger thrust share, while the lower rotor had larger fluctuations in the displacements. The free wake results presented in [148] showed that maximum angle of attack variations were found during blade crossing. The aerodynamic angles of attack at the blades reached a maximum in the simulation 15° before blade crossing, and a minimum 15° after the blade crossing, in line with blade loads, deformations and inflow variations. However, as a time step size of $\Delta\psi_b = 15°$ was used, these values should not necessarily be considered as precise quantities, rather as an indication of the location of maximum aerodynamic fluctuations. While the same test stand used for the reference experiments cited in this thesis was used (see chapter 3.2.2), the blades had a significantly reduced bending stiffness, which resulted in increased flap bending. Good performance correlations with the stiffer blades used in this thesis were published in [34] using CAMRAD II.

An extensive attempt to study the effects of CCR, stacked, tandem and tilt rotors in hover was made in [123]. In this publication, a wide range of thrusts, tip speeds, axial separation distances and number of blades were investigated. The individual rotors of the stacked and the CCR rotor planes were not mechanically coupled. Simple aerodynamic models based on momentum theory and Blade Element Momentum Theory (BEMT) were used to explain and understand performance differences. It was found that the CCR rotor's FM was increased by 9% compared to the single rotor at equivalent solidity. This was attributed to swirl recovery and axial separation effects. If the two rotor planes of the CCR rotor were compared to two isolated rotors with the same combined solidity, the CCR rotor required 20% more induced power (the effect was also shown numerically, e.g., in [150]). Hence, it could be concluded that it was important to compare rotors with the same thrust potential. To quantify the effect of swirl recovery, the same rotor setup was used with both rotors spinning in the same direction (stacked rotor). It was found that the CCR rotor required 5%

less power compared to the stacked rotor in this particular setup without mechanically coupled rotors. The benefits were attributed to swirl recovery. It has to be noted, that the stacked rotor self-synchronized with the upper rotor leading the lower rotor. Moreover, the performance of the CCR rotor was independent of the axial separation distance between the rotor planes for $z/D > 0.15$.

A further study into swirl recovery of CCR rotors was reported in [147]. A comparison between CCR and stacked rotors was made with each rotor plane producing the same torque as in the torque trimmed CCR rotor setup. At an index angle of $\phi = 90°$, where the upper rotor thrust coefficient of the stacked rotor was almost identical to the CCR rotor, the swirl recovery was estimated to be 4%. Moreover, it was found that if the lower rotor trails the upper rotor by $\phi = 10°$ a 4% performance gain was achievable compared to the CCR rotor. At other index angles of $\phi = 0°$ and $\phi = -10°$ no performance differences between the two configurations were observed.

Investigations of the flow fields of a one-by-one bladed and two-by-two bladed, 2 m diameter CCR rotor at a blade loading of $C_T/\sigma = 0.085$ were conducted by the experimenter and the author of this thesis in [101]. In this study flow field measurements were made using PIV and the focus was put on vortex trajectories and inflow variations. It was found that the flow topology was independent of the number of blades in each rotor plane. This configuration was also used in the study at hand. A description of the rotor setup is given in chapter 3.2.2.

Another study on the near wake of a CCR rotor was presented in [135]. The axial separation distance of the mechanically uncoupled three-bladed rotors ($R = 0.395$ m, $Re \approx 64{,}000$, $C_T/\sigma \approx 0.0345$) was varied in the experiment ($\Delta z_r = 3.5,\ 6,\ 8.8\ \%R$). PIV was used to measure the velocity distribution near the rotor. The measurements revealed that for small axial separation distances between the rotors, inter-rotor vortex interactions were observed. On the contrary, for increased separation distances, vortex interactions were only observed between the lower rotor tip vortices (intra-rotor vortex interactions).

Different from the previously mentioned experimental investigations of CCR rotors which were performed in air, the stability of helical vortex filaments of a 0.26 m diameter rotor was investigated in water by means of flow visualization and PIV in [71]. It was found that for low axial separation distances, the lower rotor tip vortices develop instabilities quicker compared to the upper rotor tip vortices. This tendency reduced with increasing separation distance. Moreover, upper and lower tip vortices were observed to rotate around each other, i.e., pairing of tip vortices was present in the experiment. A further study in a water tank was presented in [88]. The flow fields of a two-by-two-bladed model scale CCR rotor and a two-bladed single rotor were investigated using PIV. It was found that vortex wandering was increased for older wake ages, equivalent to experiments performed in air. Moreover, for the single rotor and the lower rotor plane of the CCR rotor an upwash was observed near the blade tip. This feature was not observed for the upper rotor plane. Effects on inflow velocities were also measured. It was found that the upper rotor inflow peak velocity was about 19% lower compared to the lower rotor.

Full scale flight test results of an ultralight rotorcraft in two-by-two bladed CCR rotor configuration and corresponding correlations to CAMRAD II simulations were reported in [33, 34]. Power required, control angles, tail boom and hubs loads, as well as teeter angles were measured. It was found that a two-per-revolution interaction was visible in the experimental data that could not be

seen in the numerical simulation. This was attributed to rotor fuselage interactions. However, no definite answer could be given to what extend deviations in the center of gravity position, download on the tail surface, or other control inputs required to keep the rotor in hover were influencing this finding. Forward flight conditions were also measured and correlated to the free wake simulations and are reported in the cited papers.

Besides experimental campaigns a lot of research has gone into developing suitable numerical tools and theoretical approaches for CCR rotors. Such a theoretical approach was, e.g., proposed in [79] in which a new definition of the FM for CCR rotors was described. In particular, this definition accounts for the effect of thrust sharing. Moreover, from a theoretical standpoint, it was derived that maximum efficiency is achieved if the lower rotor was operated in the fully developed wake of the upper rotor. According to [79] this was supported by experimental data which showed similar results. Moreover, based on BEMT a theoretically optimal hovering rotor was derived in [82]. As for single rotors the upper rotor twist should be hyperbolic, while for the lower rotor a multipart hyperbolic twist with a break point at the average impingement point of the upper rotor wake would be required.

More detailed numerical analysis of CCR rotors are possible when using free-wake analysis. In [86], a free-wake analysis (CAMRAD II) was used and compared to experimental data. According to the authors, "a free wake model enabled satisfactory performance correlation of the coaxial rotors"[86]. Moreover, it was pointed out that Reynolds number corrections were required to accurately account for variations in airfoil characteristics when changing the rotor RPM. In addition, this study was extended to hover IGE.

In [150] a free wake method combined with lifting lines for the rotor blades was used for extensive code validation of the comprehensive rotorcraft code CHARM. A vortex rollup model was included in the simulations, which allows computing the rollup rate and the tip vortex core radii of the consolidated vortex based on first principles, rather than empirical factors. Moreover, for convergence improvement, rather than accuracy reasons, a diffusion model was added with different parameters for the upper and lower rotor wake and the minimum vortex core radius was increased compared to the standard settings used in CHARM. Computed rotor performance and tip vortex trajectories were compared to several experimental data sets. Overall good correlation of the computed and measured power and vortex trajectories was shown. In addition, multiple of the statements in the previously cited overview paper on CCR rotors[23] could numerically be confirmed, such as optimal hover performance at torque balance, changes in power requirements when comparing single to CCR rotors, and that increasing the axial separation distance to values larger than $\Delta z_r = 10\%$ R showed little effect on hover performance.

The RCAS free wake model was validated in [50] based on two full-scale and two model-scale experiments. Moreover, for one of the full-scale rotors, CFD predictions were compared to the free wake results. The study showed that RCAS was mostly showing good agreement with experimental data (thrust sharing, induced power, FM) and CFD, including trends in all performed parameter sweeps (e.g., separation distance).

Based on the code validation in [50], a free wake study looking into co- and counter-rotating rotor performance and swirl recovery was described in [11]. The rotor was modeled as a lifting line

and the far-wake was composed of a tip, a root, and a third vortex representing the inboard wake sheet. It was claimed that "while induced swirl losses and recovery may play a small role in performance of coaxial rotors, the main driver for the performance differences between co-rotating and counter-rotating coaxial rotors appears to be the underlying wake interactions and the resulting induced inflow"[11]. This gave a different perspective on where the performance benefits from CCR rotors stem from. It was stated that for coaxial rotors "the upper rotor experiences a net benefit from the rotor-to-rotor interactions"[11]. This was caused by an increased transport velocity of the upper rotor vortices which reduce the self-induced inflow. This effect was larger compared to the increased inflow caused by the lower rotor plane. For CCR rotors, this effect is time-dependent ($2 \cdot N_b$ blade crossings per revolution). Thus, the performance gains of CCR rotors over single rotors with the same solidity, are time-dependent and a net benefit can be achieved averaged over one rotor revolution.

A different vorticity conserving way of simulating CCR rotors in hover was described in [15] were the incompressible and inviscid NS equations were solved in vorticity conserving form. The method computed valid wake structures for hovering rotors and was intended for flight mechanics simulations. The model was extended in [66, 67]. In these studies profile drag was modeled as either constant or a function of the aerodynamic angle of attack. The required rotor power was underpredicted for the examined CCR rotor despite good agreement for the single rotor. Moreover, at higher wake ages, vortex trajectories showed noticeable deviations from empirical models, despite good agreement for low wake ages.

A different vorticity preserving methodology is the viscous vortex particle method, which was, e.g., used in [136]. The method was applied to the corresponding two-dimensional problem first, i.e., airfoil passages, to study the interactions effects on a simplified problem. This study showed impulsive load changes caused by blade passage. For the three-dimensional rotor simulations a strong sensitivity on the chosen airfoil drag coefficients was observed. Furthermore, qualitative agreement of the computed trajectories with experimental data was seen. For unsteady loads, the method was extended by using an unsteady aerodynamics model, which showed promising results for rotor thrust and torque computations.

To avoid the usage of airfoil drag coefficients the method was coupled with CFD in [121]. Here, the rotor blade aerodynamics were computed with a RANS method, while the farfield aerodynamics were modeled using particles. In combination with CFD a better agreement with experimental data was achieved compared to a lifting line representation of the rotor blades. Differences were highlighted by time-averaged axial velocity distributions above and below the rotor planes, which showed good agreement with experimental data.

To further increase the potential physical modeling depth, the URANS equations can be solved in the complete flow domain. This was, e.g., done in [7]. In this study the rotor was modeled as actuator disk or lifting line. For the investigated two-by-two bladed rotor, good performance correlation was achieved using the actuator disk. The chosen grid dimensions along with the lifting line blade representation were, however, not capable of preserving the tip vortices.

To better preserve the dominant flow features, fully resolved blades were used in [73]. The computed performance showed excellent agreement with the experimental data for an isolated rotor

plane, with slightly degraded predictive capability for the CCR rotor. Periodic variations in rotor forces and moments were attributed to loading and thickness effects, which decreased with increased inter-rotor spacing. The thickness effect was further investigated at $C_T = 0$. It was explained that the Venturi effect, which leads to a reduction of pressure between the blades, caused a response in the individual rotor thrust and torque signals (spikes), despite the average thrust being zero; see also [120]. Moreover, variations in sectional thrust distributions along the blade span were plotted, quantifying the unsteadiness in the flow field. Furthermore, in [107] it was shown that CFD methods are required to capture impulsive forces due to blade crossing. These fluctuations are required for the correct computation of rotor vibrations, which could not accurately be computed using free wake models. In this study the free wake model was considered sufficient for performance estimates.

A quantification of the effect of using turbulence models in the off body grid was described in [164]. In this study the Spalart–Allmaras turbulence model was used with and without a modification in the off body grid. The modification consisted of switching the turbulence model off outside the chimera blade grids (called laminar off-body model). Hereby, eddy viscosity is only generated in the rotor blade mesh, and allowed to convect downward unchanged until entering into the lower rotor blade mesh. This "engineering approach"[164] allowed for reduced computing times compared to, e.g., DES simulations while keeping the eddy viscosity levels low. In the study the CCR rotor was not torque balanced. Compared to DES the laminar off-body approach showed a wider spread of the wake, but compared otherwise "favorably"[164] to DES and showed better results compared to RANS simulation in the off-body mesh. It should be noted that the RANS simulation were performed without Rotation/Curvature Correction (RC) terms and that the off body grid was comparatively coarse (Δ_s = 10% c). An attempt to quantify the effects of torque balance based on the first study was subsequently made in [166]. Torque balancing was found to have a negligible effect on the overall rotor flow field characteristics based on inspecting Q-criterion isosurfaces and axial velocity contours, i.e., "the effects of torque balancing on the wake structures visually appear to be relatively small"[166]. Slight variations in the change of lower rotor thrust when decreasing the inter-rotor spacing were observed compared to not torque trimmed simulations.

A different approach to CCR rotor aerodynamics is provided by finite state inflow models. In [118] two generalized CCR rotor inflow models were developed for hover; one being an extension of the Peters–He model[48] by superimposing two pressure fields, the other one being based on the inflow theory developed in [100], which is based on Galerkin weighted residuals. To better account for inter-rotor interactions, viscous effects and wake contraction had to be considered in the models. Comparisons to PIV measurements showed good agreement for time-averaged velocities near and below the rotors. When considering inflow dynamics, i.e., the transient response of a rotor, it was found that velocity potential based solvers were capable of computing the finite time required for wake changes to reach the lower rotor[119].

2.2.2. Stacked Rotor

The idea of stacked rotors dates back decades. For example, in 1974 a study of variable-geometry model-scale rotors was published[76]. A six-bladed single rotor was taken as baseline configuration, out of which a three-by-three-bladed stacked rotor was derived. It was found that a performance gain could be achieved by axially and azimuthally spacing the rotor blades. An axial spacing variation resulted in a 5% increase in thrust at constant power, or a 10% torque reduction at identical thrust, if the rotors were at a distance of $\Delta z_r = 2$ c. At $\Delta z_r = 1$ c only slight performance gains were achieved at high thrust levels. Highest performance increase was observed at $\Delta z_r = 2$ c and an index angle of $\phi = 30°$, i.e., with the upper rotor blade leading. The maximum increase in FM was 0.07, from 0.55 for the six-bladed single rotor to 0.62 for the stacked rotor at one operating condition ($C_T/\sigma = 0.08$). Differential collective pitch in the two rotor planes appeared to have a negligible or slightly detrimental effect on hover performance. A corresponding study using a full scale test rig[125] showed thrust increases of up to 6% at constant power for the stacked rotor. In contrast to the model scale rotor, higher pitch settings in the upper rotor plane gave a net performance benefit. According to the authors the performance of the full scale tests showed reasonably well agreement with the model scale tests. However, no clear trends for performance improvements could be derived, as vortex trajectories seemed to be the most influential factors, i.e., a quantity which is influenced by thrust levels and geometrical details to a great extend.

In [127] tail rotors in stacked configuration were the primary focus. Hence, power requirements were subordinate. By using stacked rotors ($\Delta z_r = 10$ %R) and index angles in the order of $\phi = -35° \ldots -55°$ thrust was increased by up to 10% at constant collective. In addition, the highest FM was observed to be in the range of optimum thrust and could be increased by up to 0.03. A spacing larger than $\Delta z_r = 10\,\%R$ was found to not increase FM further.

An extensive attempt to study the effects of CCR, stacked, tandem and tilt rotors in hover was made in [123]. A wide range of thrusts, tip speeds, axial separation distances and number of blades were investigated. The individual rotor planes of the stacked rotor and the CCR rotor were not mechanically coupled in this study. Momentum theory and BEMT were used to explain and understand performance differences. It was found that CCR and stacked rotors were more efficient than the corresponding single rotor with equivalent thrust potential. In addition, the CCR rotor required 5% less power compared to the stacked rotor in this particular setup. The additional benefits of CCR rotors over stacked configurations were attributed to swirl recovery. As he stacked rotor self synchronized as "biplanes" with the upper rotor leading the lower one the resulting azimuthal separation was considered optimal in terms of power required. However, this could not be shown experimentally as the azimuthal spacing could not be controlled directly.

Also, research was conducted at UTA to gain insight into swirl recovery for CCR rotors[147, 149]. Measurements showed that a stacked rotor with the lower rotor trailing the upper rotor by $\phi = 10°$ had a performance benefit of up to 4% over the corresponding CCR rotor. At index angles $\phi = 0°$ and $\phi = -10°$ no performance differences between the two rotor concepts were observed. Only the torque levels in the individual rotor planes changed. Performance increase was attributed to the increased vortex convection in the upper rotor plane which resulted in a net reduction of induced velocity[149]; see also [11].

Further studies at UTA revealed that not only the thrust could be increased by up to 5% at constant power compared to a single rotor with identical solidity (Δz_r = 1.75 c; ϕ = 90°), but also that variations of the index angle can be used to control rotor thrust (up to 20% thrust variation for $\Delta\phi$ = 39°)[58]. The experimental data suggested that blade vortex interactions were the main driver for performance and thrust characteristics of stacked rotors, as no consistent trend was observed in the experimental data. In a subsequently published study, it could be shown that FM could be increased by up to 4.6% for small axial spacings (Δz_r = 0.5 c; ϕ = 90°)[57].

Similarly in a joint numerical and experimental study a ≈ 7% power reduction was measured on a three-by-three-bladed rotor compared to the equivalent single rotor with the lower rotor leading the upper rotor by $\phi = -40°$, dependent on the thrust condition[154]. It was pointed out that using other blades and collective pitch settings for the two rotor planes could entail further benefits.

Compared to CCR rotors, considerably less numerical work has been done with the focus on stacked rotors. A main driver of these studies was the hoped for better understanding of CCR rotor configurations. This was, e.g., done in [11] where CCR and stacked rotor performance was investigated. A lifting line representation was used in conjunction with a free wake solver, modeling three discrete vortices: a tip, a root, and an inboard vortex representing the trailing vortex sheet. The study showed that averaged vortex trajectories of the two configurations were well comparable. In particular, the best and worst performance of the stacked rotor (based on index angle ϕ) bounded the CCR trajectories. Therefore, it was stated that performance benefits of stacked and CCR rotors were a result of changed induced inflow distributions in the two rotor planes. Depending on the thrust condition, varying index angles would therefore be required to achieve 'optimal' performance for stacked rotors, i.e., lower the net induced inflow in the rotor planes due to an increased axial transport of the tip vortices. The induced power savings can therefore be larger than the increased inflow due to adding a second rotor plane (inter-rotor influences), at specific index angles.

A viscous vortex particle method coupled with a lifting line representation of the rotor was used in [56] and compared to DES simulations. To account for blades in close proximity (low Δz_r and ϕ) blade bound circulation effects were included in the particle simulation. Both methods showed consistent trends with experimental data. The particle method underestimated the thrust variations in the rotor planes when varying ϕ at fixed collective, whereas the DES simulation gave better predictions. Thrust differences in an index angle range of $-5.625° \leq \phi \leq 5.625°$ were within 2% of the experimental results using DES, but only half of the experimental variation was seen in the particle method. In addition, angle of attack (α) distributions and wake trajectories were shown to highlight the effect of index angle variations on the flow field. At low index angles ϕ the leading (lower) rotor blades α distribution along the blade span was altered such that it was close to its optimal lift-to-drag ratio over the entire blade radius. On the contrary, for the trailing (upper) blade, α was significantly reduced compared to the blades operated at $\phi = 90°$. Wake trajectories revealed that different index angles changed the tip vortex paths significantly. For $\phi = 90°$ the tip vortices of both rotors follow essentially the same paths and remain evenly spaced. For $\phi = 45°$ tip vortices from the two rotor planes only initially follow the same paths. At a wake age of $\zeta = 45°$ the upper rotor tip vortex was convected downwards faster. An extension of this study focusing on rotor acoustic was published in [55].

The aerodynamic interactions of stacked rotors were investigated using two-dimensional CFD analysis in [24]. It was found that stacked symmetric airfoils at $\alpha = 0°$ could produce non-zero thrust. Conventional airfoil tables consider each blade section as an isolated two-dimensional airfoil. Hence, if all aerodynamic sections were operated at α_0 neither of the rotor planes would produce thrust. Consequently, no bound, or shed circulation would exist in the flow field and thus no inflow would build up. Conventional lifting line analysis does not include the effect of non-zero lift when all aerodynamic sections are operated at α_0. It was concluded that adding further quantities to conventional airfoil tables, such as vertical and axial spacing, were required to accurately compute stacked rotors using, e.g., free-wake analysis.

Further CFD studies were conducted in [128], where model scale drone rotor blades were used in CCR and stacked rotor configuration. The time-dependent NS equations were solved using a finite differences solver. All simulations were made with a Delayed Detached Eddy Simulation (DDES) approach employing the SA turbulence model. Stacked rotors were investigated at three different index angles ($\phi = -30°$, $0°$, $30°$). Depending on the index angle BVI was observed. Moreover, all tested index angles resulted in lower performance (C_T/C_P) compared to the CCR rotor configuration. Furthermore, benefits of using ducts were investigated and qualitative conclusions were drawn towards noise.

2.2.3. Objective – Coaxial Rotors

Research activities related to CCR[5, 123] and stacked (co-rotating) rotors[76, 125, 127] have been performed for several decades. It has been shown for both configurations that performance benefits can be achieved over conventional single rotor configurations with the same thrust potential, i.e., same blade loading with identical (number of) blades[123, 147]. Recently, increased interest in Urban Air Mobility (UAM), a new paradigm for transportation in congested cities using 'air taxis', has resulted in a plethora of different new rotorcraft designs and CCR rotor systems with closely-spaced, rigid-hub rotors are considered potential game changers in the rotorcraft industry. Therefore, experimental and numerical studies concerning the compact, highly efficient rotor designs were resumed to look at potential pros and cons of either of these two configurations.

Previous studies on CCR and stacked rotors revealed large variations in performance depending on the number of blades, rotor radius, thrust conditions, and configuration. In [123], experimental results showed that the tested CCR rotor's figure of merit was increased by up to 9% compared to a single rotor with equivalent solidity, and 5% less induced power was required compared to the corresponding stacked rotor. Other studies showed opposite trends. In [147], a stacked rotor with the lower rotor trailing the upper by $\phi = 10°$ required 4% less power compared to the corresponding CCR rotor. A general observation for stacked rotor configurations is that optimum performance is dependent on the locations of tip vortices and blade vortex interactions. As a result, 'optimum' configurations with respect to performance showed azimuthal offsets of $\phi \approx -40°$[127], $\phi = 10°$[147], or $\phi = 30°$[76]. It was hypothesized [123, 147] that swirl recovery was responsible for performance improvements in CCR rotors. However, in [11] the underlying changes in wake interaction characteristics, and thus, induced velocities, were regarded as the main factors influencing stacked and CCR rotor performance. In addition, two-dimensional numerical simulations showed

that not only wake interactions play a significant role for stacked rotor designs, but also mutual influences of the bound circulation on the individual rotor blades[24]. Overall, currently available data are inconclusive with regard to which coaxial rotor design showed superior performance and which index angle ranges gave best results for stacked rotors.

Therefore, the current study aims to give insights into the aerodynamic interactions of CCR and stacked rotors beyond the current state of the art. In particular, this shall be achieved through an in-depth investigation and comparison of the flow fields of single and coaxial rotors to assess differences and similarities between the two coaxial configurations and to study the effects of adding a second rotor plane. Hereby, a focus will be put on inflow, loading, and vortex trajectory variations caused by changes in blade loading (C_T/σ) and index angles (ϕ). Moreover, the developed simulation models and results from investigating the flow physics of coaxial rotor configurations in hover will be used as reference cases for the investigation of the effects of dynamic actuation; see chapter 2.3.

2.3. Dynamic Actuation

For rotorcraft, rapid changes in the blade pitch controls are required in maneuvering flight, such as, e.g., pull up in high speed forward flight[9, 10, 145]. However, it is difficult to compute and measure the response of complete rotorcraft configurations. Moreover, the dynamic response to control inputs is of particular interest for UAM, as they require high control authorities in hover for the successful application of distributed propulsion systems for multicopters. As the focus of this thesis is on hover flight conditions, only the state of the art of research concerning changes in Θ_0 or RPM in hover is described below.

In the past few experiments have been performed for rotors in hover with dynamic actuation. In an early attempt, qualitative information on the wake evolution during rapid acceleration of the rotor from rest at fixed Θ_0 was gained using balsa-dust for flow visualization[144]. It was found that the flow patterns of the single rotor were "strikingly similar to those obtained in a similar investigation [...] in which smoke streamers were used [...] and in which the sudden thrust increase was obtained by rapid change of pitch"[144]. Using a coaxial rotor system showed that the vortices of the upper and lower rotor merged to form one starting vortex similar to the single-rotor case.

Rapid increase in blade pitch was measured in [19]. The goal of this study was to gain insight into the flow phenomena that are responsible for the thrust overshoot when performing jump take offs. Smoke visualization was used to gain qualitative information on the overall flow field. Moreover, RPM, thrust, blade pitch, flap angles, and induced velocities beneath the rotor were measured. For the latter windmill anemometers were used to measure the steady state, while drag changes of balsa wood panels were recorded to measure the transient states. At the highest pitch rates tested, thrust overshoots in the order of the steady thrust after the input were seen, with a rapid decrease ($\approx -80\%$) in the first rotor revolution after the input. The flow visualizations suggested that the induced inflow built up first towards the tip and later towards the root. However, this appeared to be a second-order effect compared to the overall build up of inflow along the blade span. As the

rotor was operated at zero thrust before the pitch input a starting vortex formed.

Changes of the induced flow due to continuous pitch input variations at various frequencies were measured on a four bladed rotor in [32]. Hot wire probes and a LDA measurements were used at various radial and axial points in space to measure the flow velocities. It was found that the response was highly dependent on the measurement location, as well as the frequency of excitation. Moreover, it was stated that the wake structure and shed vorticity seemed to be important for the correct computation of the inflow. A similar study with continuous pitch excitation was reported in [87]. LDA measurements revealed that substantial variations in the inflow were even caused by low oscillation amplitudes ($\Delta\Theta_0 = 1°$). In addition, the inflow variations included substantial hysteresis effects. Furthermore, a combined momentum and blade element theory model with apparent mass term was developed and correlated to the experimental data. The calculated thrust-coefficient showed an overshoot of $C_T \approx 10\%$ compared to the measured data.

A more recent attempt focusing on potential advantages of variable pitch rotors over variable RPM rotors for quadrocopters was made in [117]. It was found that changing blade pitch rather than rotational speed gave faster responses and "that variable collective-pitch rotors are more efficient in terms of energy consumption than comparable fixed-pitch rotors"[117].

Experimental data based on the single rotor configurations of both UTA rotor setups (see chapter 3.2) were published by the experimenters and the author of this thesis[113, 102, 103]. Step collective pitch and RPM inputs were commanded, the rotor thrust and torque response were recorded, and the flow field was measured using PIV. Also numerical data were correlated to the results and the numerical simulation were used to expand the test matrix. A discussion of the simulation results and correlation to experimental data is given in chapter 7.

A similar study correlating experimental data to CFD, free-wake, and dynamic inflow results was presented in [157]. A pitch amplitude of $\Delta\Theta_0 = 4°$ was commanded over two revolutions. Fair agreement between the different numerical methods and the experimental data was seen.

Further attempts to model the dynamic response using free-vortex wake methods can be found in [8, 4]. In both studies the experimental results published in [19] were used as references. In contrast to most other free-wake analysis which assume periodicity, a time-accurate free-wake method was used. In [8] it was concluded that the primary driver for the transient buildup of inflow was the transient evolution of the trailed rotor wake. Moreover, tip vortices and the trailed wake dominated the flow field and the shed wake circulation was less important. The same test case[19] was investigated using a viscous vortex particle method in [46]. Good correlation was observed for the thrust coefficient and temporal evolution of the mean inflow.

A comparison of different computational methods was made in [29]. Based on the experimental setup described in [19] a test case was constructed based on the *Caradonna and Tung* rotor. URANS computations with the SA turbulence model, a vorticity transport method combined with a lifting line to represent the rotor blades, and a single-state dynamic inflow model (variation of the inflow model proposed in [19]) was used. It was found that all models showed similar behavior, as long as the blades did not stall.

2.3.1. Objective – Dynamic Actuation

A key aspect of modeling and simulating flight dynamics is understanding the temporal evolution of rotor loads, inflow, and wake in response to dynamic control inputs. Although several models, numerical as well as theoretical, have been developed to predict dynamic inflow and wake evolution, there is only limited experimental data to validate these predictive methods for non-oscillatory inputs in hover, i.e., ramp/step inputs[144, 19, 117, 113, 102, 103, 157]. Moreover, high fidelity numerical solutions with dynamic actuation are scarce for single rotor designs[8, 29, 46, 113, 102, 103]. This is even more true for coaxial configurations. Therefore, the evolution of the rotor wake and the response of the rotor system to step inputs requires further investigation. Within this thesis, collective pitch (Θ_0) step inputs were commanded using the UTA CCR rotor test rig; see chapter 3.2.2. Computations were made with the two-by-two-bladed CCR configuration and the two-bladed single rotor. Step RPM inputs were commanded for the stacked rotor setup (see chapter 3.2.3), and the corresponding four-bladed and two-bladed single rotors. All step inputs were modeled as '1 − Cosine' functions. For the two-bladed configurations, the numerical simulations could also be correlated to measurements performed at UTA[113, 102, 103].

Hence, the third objective of this thesis is to investigate the temporal evolution of inflow, and rotor forces and moments caused by step collective pitch and RPM inputs, as well as the temporal evolution of sectional forces. Differences and similarities between single and coaxial rotors will be highlighted.

2.4. Scientific Approach and Methodology

The findings from the literature review described in the previous subsections showed that many questions concerning hovering rotors have not yet been answered completely. Consequently, the identified knowledge gaps shall be reduced or closed wherever possible in this thesis. To do so, combined experimental and numerical studies were conducted to be able to provide a deep insight into the relevant flow physics. The combination allowed connecting the strengths of both approaches. Correlating the results made it possible to identify potential shortcomings in the numerical modeling as well as in the design of the experiment, or data evaluation. Moreover, the verified numerical models could be used to investigate regions of the flow field or quantities, which could not be measured.

All experimental data were provided by the research partners at the United States Naval Academy (USNA) and the University of Texas at Austin (UTA) and were shared with the author for the joint research undertaking[112, 101, 113, 102, 103, 114]. This included, among other things, geometrical data of the rotor test rigs, (raw) velocity vector fields from PIV measurements, inflow distributions, tip vortex trajectories and characteristics, and transient integral rotor data (thrust and torque). The test rigs are described in chapters 3.1 and 3.2. Details on the flow field measurements are given in chapters 3.1.2, 3.2.2.2, and 3.2.3.2.

The numerical part of the work was done using URANS CFD simulations based on the following reasoning. The questions to be answered shall ultimately be used to validate or refine other, less computationally expensive tools such as finite-state inflow models of free wake analysis. Therefore, these or similar numerical methods were not used in this study, especially as they require empirical corrections or assumptions and thus, a sound understanding of the flow physics prior to their application which did not exist. Moreover, vorticity conserving methods (e.g., vortex particle methods) did show similar performance compared to URANS methods in previous studies. Hence, using them would not enable deeper insights into the relevant flow physics and would also prevent the investigation of the effects of using different turbulence models for the investigated test cases.

Computationally more advanced methods, such as DES, showed superior performance in previous studies over most URANS-based simulations. However, properly resolving the relevant vortical flow structures in time and space requires very dense grids and low time steps and thus long computing times. Therefore, URANS-based simulations will be a viable tool whenever computational effort is a limiting factor in the foreseeable future. Hence, providing further insights into the predictive performance of this modeling approach by investigating unconventional configurations is expected to be well received by the community.

In summary, it was decided to use an URANS-based finite-volume CFD solver (German Aerospace Center (*Deutsches Zentrum für Luft- und Raumfahrt*) (DLR) TAU code; see chapter 4.1) with a variety of different turbulence models (chapter 4.4) to assess the different rotor configurations and operating conditions. To gain confidence in the simulation results and allow for comparisons between the setups, similar grid generation strategies were used along with, where possible, identical numerical settings; see chapter 4. Moreover, system elasticities were not considered (i.e., infinitely rigid blades, an infinitely rigid control system, and an idealized motor controller to keep the RPM at the prescribed level throughout all dynamic inputs were assumed) to be able to study purely aerodynamic influences without superimposed test rig specific particularities.

The present study was made to gain insights into rotor configurations and flight states which did not receive significant attention in the past. So far, these flight states have not been studied extensively either experimentally or numerically. Moreover, the experimental data have not yet been used, at least not extensively, by other researchers for correlation with numerical URANS finite-volume CFD data. Therefore, the present work must be regarded as a first step towards a deeper understanding of the underlying flow physics and the results shall be seen as a first building block for a fundamental understanding of the involved flow physics. Consequently, further experimental studies and correlations with (other) numerical procedures are required to substantiate the findings and to achieve fully validated results.

3. Reference Experiments

The thesis focused on investigating the flow fields of rotors in hover in multiple non-standard configurations and/or operating conditions. These were (non-parallel) ground effect, rotor-rotor interference for CCR and stacked rotors, the influences of step collective pitch changes, and the effects of dynamic variations of rotor rotational frequencies. To assess the accuracy of the simulations, numerical results were correlated to experimental data wherever possible. As a consequence of the variety of rotor designs to be discussed, multiple reference experiments were required. These were performed by project partners at the United States Naval Academy (USNA) and University of Texas at Austin (UTA). The IGE test stand was built and operated at USNA and is described in chapter 3.1. The other experiments were performed on two different test rigs built and operated at UTA. These differed in their design but used the same rotor blades. The blade and the test rig details are given in chapter 3.2.

3.1. US Naval Academy – Rotor In-Ground Effect Test Rig

The IGE and corresponding OGE experiments were performed by USNA. Loads, performance, and flow field measurements were made by researchers at USNA. First experimental results were published by them [99] and the processed PIV velocity vector fields were shared with the author for further data processing in a joint research project [112] and the thesis at hand.

3.1.1. Rotor Configuration

At USNA a test stand is operated to perform experiments on a two-bladed model scale teetering/seesaw rotor. The experimental setup used in this thesis was previously described in [99] and also in a former study by the author[112]. A photograph showing the rotor assembly with the ground plane is shown in Fig. 3.1a.

The stiff rotor blades had a radius of $R = 0.408$ m, were untwisted and had a constant chord length of $c = 44.45$ mm. The NACA 0012 profile was used along the entire aerodynamic section. The rotor was operated at a rotational frequency of $\Omega = 35$ Hz, which yielded a blade tip velocity of $V_{\text{tip}} = 89.7$ m s^{-1}. The rotor test stand characteristics are summarized in Table 3.1. The rotor thrust was controlled by setting the collective blade pitch angle Θ_0 to a predefined value prior to spinning up the rotor. A six-axis load cell was used to measure the rotor torque and thrust.

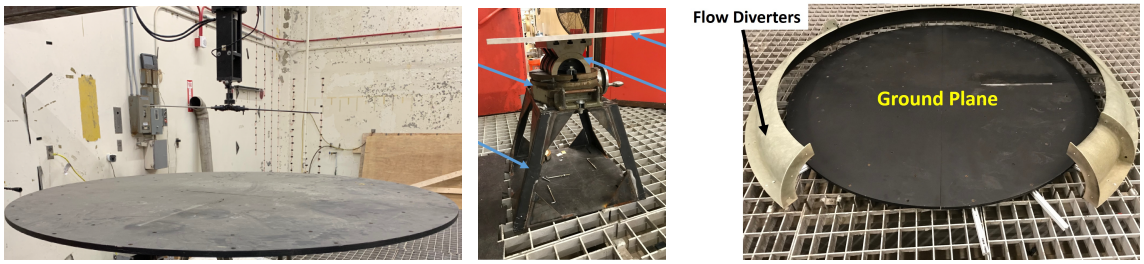

(a) Rotor test rig without flow diverter.[90]

(b) Ground plane stand.[99]

(c) Photograph of the ground plane with flow diverter.[99]

Figure 3.1.: Photographs showing the USNA rotor test rig, the ground plane stand, and the ground plane equipped with flow diverter to reduce recirculation in the test facility.

Table 3.1.: Summary of rotor parameters for the USNA rotor test rig.

Rotor		
Number of blades, N_b	2	-
Airfoil	NACA 0012	-
Rotor radius, R	0.408	m
Chord, c	0.0445	m
Root cutout, r_a	13.7	% R
Solidity, σ	0.069	-
Ground Plane		
Ground plane diameter, D_{GP}	$4 \cdot R = 1.632$	m
Operating Conditions		
Rotor rotational frequency, Ω	35	Hz
Rotor blade tip speed, V_{tip}	89.7	$m\,s^{-1}$
Rotor blade tip mach number, M_{tip}	0.27	-
Rotor blade tip Reynolds number, Re_{tip}	280,000	-

The rotor plane was located at a height of z/R = 1.0 above the ground plane pivot point for all IGE simulations made in this thesis; see Fig. 3.2. This means that the rotor head remained fixed relative to the pivot point. The ground plane had a diameter of four rotor radii and was mounted on a stand which allowed to change the ground plane angles; see Fig. 3.1b. Due to the teetering rotor head, the rotor could freely respond to changing ground plane inclination angles by a flapping motion. However, the possible flapping response of the rotor due to a changed ground plane angle could not be measured experimentally using the current setup.

Flow field and performance measurements were made for ground plane inclination angles of $\Theta_{GP} = 0°, ..., 30°$[99]. To reduce flow recirculation in the test facility, a flow diverter was mounted along the circumference of the ground plane; see Fig. 3.1c.

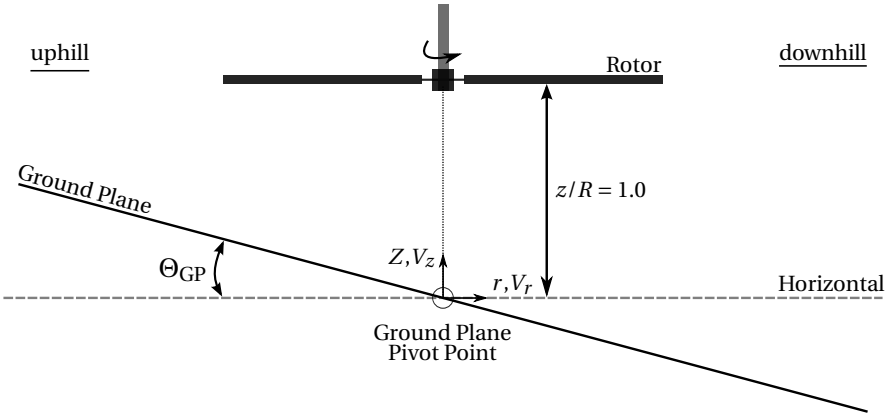

Figure 3.2.: Schematic showing the rotor-ground plane orientation at a rotor azimuth angle of $\psi_b = 0°$ for the USNA rotor test rig.

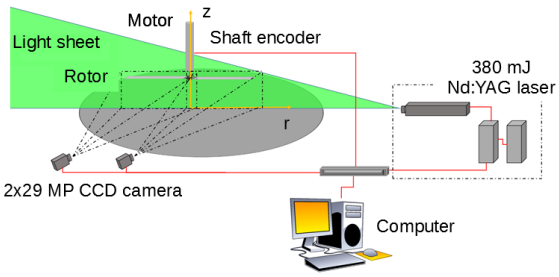

Figure 3.3.: Schematic showing the the USNA rotor test rig with the two-bladed rotor and the experimental setup with the laser and the cameras used for PIV.[112]

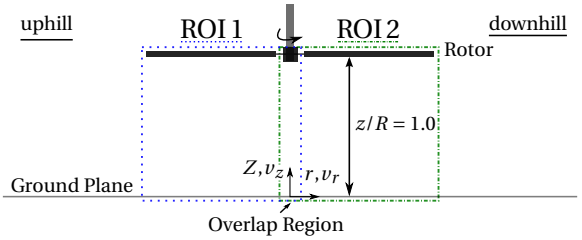

Figure 3.4.: Schematic showing the definition of the coordinate system and the ROI used for flow field measurements of the USNA rotor test rig.[112]

3.1.2. Flow Field Measurements

Flow field measurements were made using phase-resolved two-dimensional, two-component (2D-2C) PIV[99]. The flow field measurements were previously described by the experimenter [99] and the author [112] and are subsequently given for the sake of completeness based on [112].

The cameras were aligned orthogonal to the measurement plane illuminated by the laser; see Fig. 3.3. The laser light sheet was focused on the desired Region of Interest (ROI) defined in Fig. 3.4, and was aligned with the trailing edge of the downhill facing blade at $\psi_b = 0°$; see Figs 3.2 and 3.5. Therefore, the measurements were made in front of the leading edge of the uphill side blade and behind the trailing edge of the downhill blade. The ROI was chosen such that the rotor wake could be examined from the rotor plane downstream to the ground plane for parallel and non-parallel IGE operation. A digital synchronization was used between the cameras and the laser, such that the laser pulses triggered the camera images.

Data was recorded with two 29 mega pixel CCD cameras (6600-by-4400 pixel) and a Nd:YAG laser capable of 380 mJ/pulse when operated at frequencies below 10 Hz. The maximum imaging rate

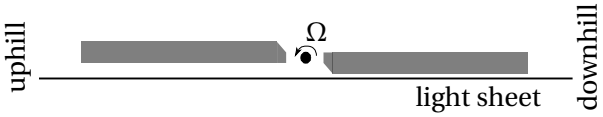

Figure 3.5.: Schematic showing a top view of the USNA rotor test rig with the laser light sheet at a rotor azimuth angle of $\psi_b = 0°$.[112]

of the cameras (1.8 Hz) was lower than the rotor rotational frequency ($\Omega = 35$ Hz). Thus the imaging system and rotor rotational frequency were synchronized. This synchronization resulted in PIV images being acquired at sub-integer multiples of the rotor frequency (i.e., one image approximately every 35 rotor revolutions).

To provide the necessary spatial resolution and image size multiple ROI were required; see Fig. 3.4. Therefore, the cameras were positioned adjacent to each other with an overlap in their field of view. The images were stitched together during the postprocessing to increase the effective field of view without degrading the spatial resolution. The high resolution of the cameras allowed for a large ROI while maintaining the necessary measurement resolution (inter-vector spacing of ≈ 1.72 mm). The measurements were performed with each camera focusing on an initial ROI of approximately 470 x 700 mm (1.15 x 1.72 R) with a 55 mm overlap in their fields of view, resulting in a total mosaiced field of view of 890 x 700 mm (2.18 x 1.72 R). Further details are given in [112].

3.2. University of Texas at Austin – Rotor Test Rigs

A CCR and a stacked rotor test rig were built and are operated at UTA; see Fig. 3.6. Loads, performance, and flow field measurements were made by researchers at UTA. Processed experimental data, including PIV velocity vector fields, were shared with the author during joint research projects[101, 113, 102, 103]. The following description of the test rigs and measurements is based on the previously published information in these articles. It is repeated here for the sake of completeness.

Both test rigs were operated indoors in a large test chamber (50 × 33 × 60 ft. / 15.2 x 10.1 x 18.3 m)[58, 102]. The experiments used to correlate numerical data in this thesis were performed with the rotor shaft oriented horizontally. Particularly, with regard to the flow field measurements this installation facilitated the optical access; see chapters 3.2.2.2 and 3.2.3.2. In addition, by directing the thrust towards the support column the wake was unobstructed. The distance to the closest wall downstream was greater than four rotor radii and the distance from the rotor shaft to the closest wall to the sides was more than five rotor radii. Both test rigs used identical rotor blades; see chapter 3.2.1. However, as the rotor hubs have different diameters, the rotor radii differ between the two test stands; compare Tables 3.2 and 3.3.

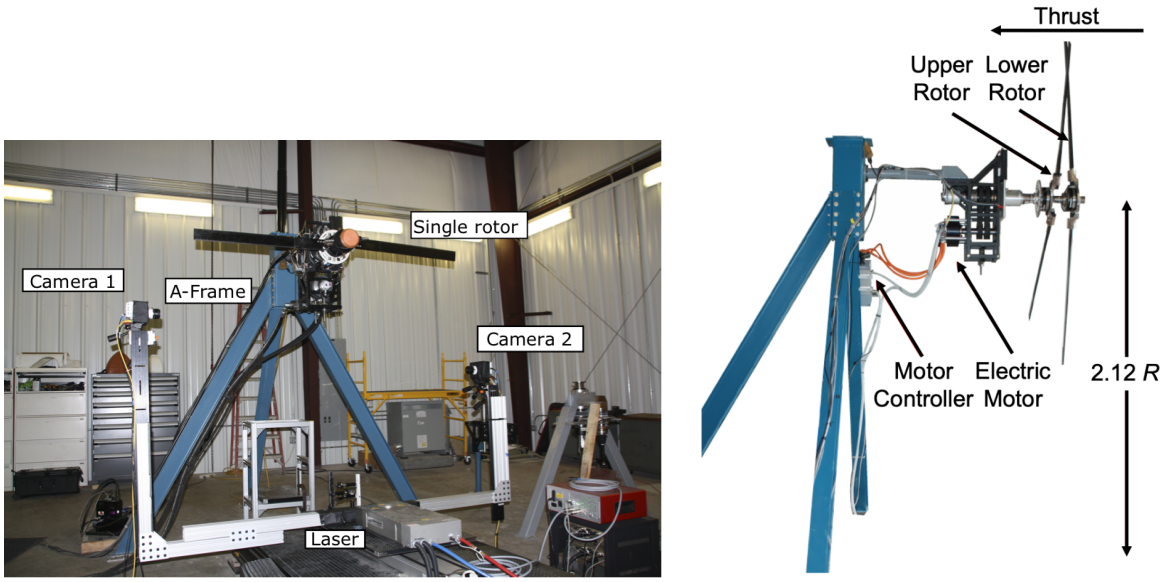

(a) CCR rotor test rig in single rotor configuration.

(b) Stacked rotor test rig[58].

Figure 3.6.: Photograph and schematic of UTA rotor experiments, showing the horizontal rotor shaft alignment.

3.2.1. Rotor Blade

Identical rotor blades were used for both rotor configurations. The stiff carbon fiber rotor blades used modified VR-12 airfoils including tabs for all aerodynamics sections; see Fig. 3.7. The blades were untwisted, untapered and had a chord length of $c = 0.080$ m. The blade tip and vertical face of the trailing edge were not rounded or chamfered, i.e., had sharp 90° corners.

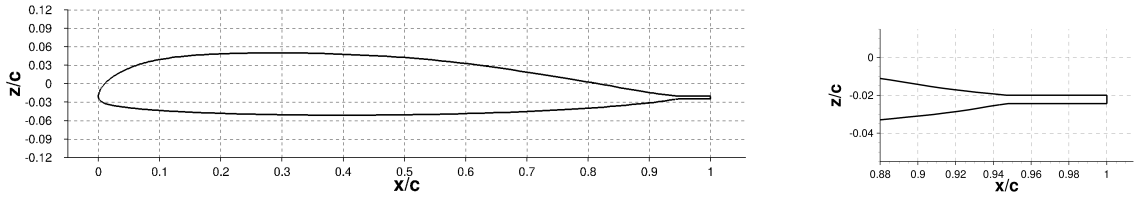

(a) VR-12 airfoil.

(b) VR-12 trailing edge.

Figure 3.7.: Schematic showing the geometry of the VR-12 airfoil (a) and the tab at the trailing edge (b).

Carbon fiber blade cuffs were added inside $r/R = 0.322$ ($r/R = 0.412$ for the stacked rotor) to increase the blades bending stiffness; see Figs. 4.19a and 4.20. These were made of additional layers of carbon composite and had a thickness of approximately 0.5 mm. Conformal layers were added to the VR-12 airfoil at the outboard end of the cuff on the suction and pressure side of the blades. No layers were added to the vertical part of the tab, i.e., the chord length was not altered by adding the cuffs. Towards the blade root, the cuff increased the blade thickness to approximately 21.5 mm at the quarter chord line. Therefore, the airfoil was not comprised of a VR-12 like airfoil in the cuffed region of the blade.

3.2.2. Coaxial Counter-Rotating Rotor Test Rig

3.2.2.1. Rotor Configuration

The CCR rotor test rig had a diameter of 2.032 m and was operated at a rotational frequency of $\Omega = 15$ Hz. This resulted in a tip Mach number of $M_{\text{tip}} = 0.28$ and a Reynolds number at the blade tip of $Re_{\text{tip}} = 524,000$. The rotational axis was installed horizontally at a height of 2.350 m from the ground, with a blade tip clearance of 1.334 m[113]. Further details are given in Table 3.2 and the test stand in single rotor configuration is shown in Fig. 3.6a.

Tests referenced in this thesis were made with a two-by-two-bladed CCR and a two-bladed single rotor configuration. For the latter, the upper rotor of the CCR setup was used; see Fig. 3.9. The blades (see chapter 3.2.1) were attached to a rigid rotor hub without dedicated flap and lead-lag hinges. The hub was mounted on a six component load cell to measure hub loads in the rotating-frame with a resolution of 0.5 N and 0.0125 Nm, and a bias uncertainty of 8 N and 4.8 N/m, respectively.

The test stand is powered by a hydraulic motor with belt driven transmission assembly[16]. A 1024 count optical encoder mounted to the drive shaft (motor axis) was used to measure the rotor rotational speed. Magnetic sensors mounted on the blade grips were used to measure the blade pitch angles with a resolution of 0.1° and a bias uncertainty of 0.05°. All measurements were made at a sampling frequency of 10 kHz.[113]

For the dynamic pitch input tests, the rotor was equipped with a high bandwidth hydraulic swash-plate. Three hydraulic actuators were used to control the orientation. Each actuator consisted of a hydraulic servo valve, a micro-controller, and magnetic position sensor for feedback control.[113]

A schematic showing the used angle definitions for the UTA CCR rotor test rig is shown in Fig. 3.8. More information on the test rig is given in [16, 17, 101, 113, 103].

3.2.2.2. Flow Field Measurements

PIV flow field measurements were made for the single and CCR rotor setup. To illuminate the measurement plane a Photonics dual-pulsed Nd:YLF DM-30 model laser (527 nm wavelength with 30 mJ per pulse) was used. Data was extracted in a radial slice of the rotor flow field at an azimuth angle of $\psi_b = 0°$. The PIV plane remained fixed in space for all measurements.[101, 113, 103].

Single rotor configuration[113, 103] Time-resolved 2D-2C measurements were made for the single rotor setup at blade loadings of $C_T/\sigma = 0.06$, 0.08, and 0.10. The recording frequency was 44/rev ($\Delta\psi_b = 8.2°$) and images were captured over 67 continuous rotor revolutions. In total 3015 image pairs (per camera) per test run were taken[113]. The two 4 MP high-speed Phantom VEO-640 cameras encompassed a Field of View (FOV) of 60% of the rotor radius. Each camera

Table 3.2.: Summary of rotor parameters for the UTA CCR rotor test rig.

Rotor			
	Single Rotor	Coaxial Rotor	
Number of blades per rotor, N_b	2		-
Precone angle, β_p	3		deg.
Airfoil	VR-12		-
Rotor radius, R	1.016		m
Chord, c	0.08		m
Root cutout, r_a	12		% R
Solidity, σ	0.050	0.010	-
Inter-rotor spacing, Δz_r	-	13.8	% R
	-	1.75	c
Nominal Operating Conditions			
Rotor rotational frequency, Ω	15		Hz
Rotor blade tip speed, V_{tip}	95.76		m s^{-1}
Rotor blade tip mach number, M_{tip}	0.28		-
Rotor blade tip Reynolds number, Re_{tip}	524,000		-

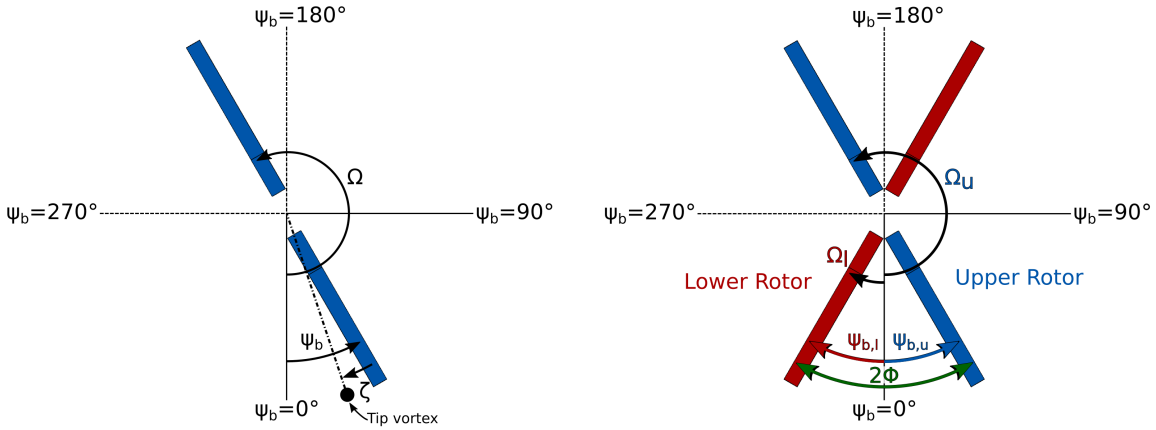

(a) Single rotor configuration.

(b) CCR rotor configuration.

Figure 3.8.: Top view showing the index angle ϕ, blade azimuth angle ψ, and wake age ζ definitions used for the UTA CCR rotor test rig in single and in CCR rotor configuration.

viewed an independent region of interest, one capturing the inboard region of the blade, while the other captured the tip region. The two regions were stitched together to give a single vector field; see Fig. 3.9a. The calculated uncertainty for each of the velocity components was found to be 0.081 m s^{-1} and 0.076 m s^{-1} for the radial and axial component of the velocity vector, respectively.[113]

Flow field measurements were made at fixed collective pitch and with pitch step inputs. To ensure converged statistics at fixed blade pitch a total of 670 rotor revolutions were recorded (ten runs). Ten runs per pitch angle step were recorded. For further details see [113, 103].

The grid size for the captured images measured $617x397$ mm in the x and z-directions, respectively, with a scale factor of 4.219 pixel/mm. The resulting spatial resolution was 3.793 mm with a total of 29,503 calculated vectors.[113]

CCR rotor configuration[101] Time-resolved measurements were made for the CCR rotor at a blade loading of $C_T/\sigma = 0.085$. The laser was triggered continuously at 64/rev (960 Hz). Stereoscopic PIV was made with two 1 MP (1,280×800 pixel) Miro 310 cameras. About 50% of the rotor radius were part of the FOV with both rotor planes captured by each camera; see Fig. 3.9b. The temporal resolution allowed capturing images every $\Delta\psi_b = 5.625°$ over 65 continuous rotor revolutions per test run. In total eight test runs were performed, resulting in a total of 520 rotor revolutions for time averaging.[101]

The grid size for the captured images measured $710x443$ mm with a scale factor of 1.80 pixel/mm. The resulting spacial resolution was 3.730 mm with a total of 6,042 vectors calculated per frame. Further details are given in [101].

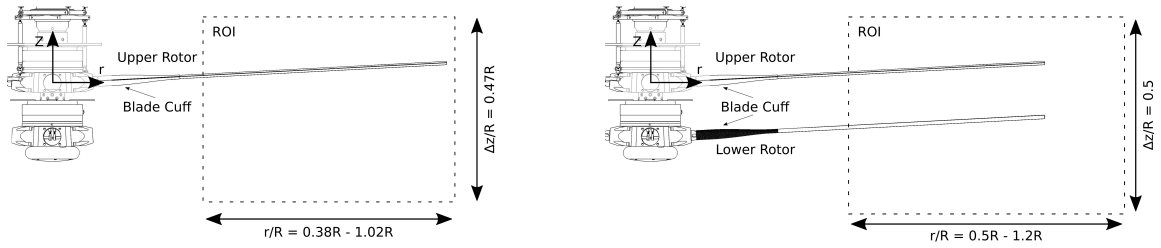

(a) Single rotor configuration.

(b) CCR rotor configuration.

Figure 3.9.: Schematic showing the UTA CCR rotor test rig in single and in CCR rotor configuration, including the ROI used for PIV measurements.

3.2.3. Stacked Rotor Test Rig

3.2.3.1. Rotor Configuration

The stacked rotor test rig had a diameter of 2.216 m and was operated at a nominal rotational frequency of $\Omega = 15$ Hz. This resulted in a tip Mach number of $M_{tip} = 0.30$ and a Reynolds number at the blade tip of $Re_{tip} = 571,000$. The rotational axis was installed horizontally at a height of 2.350 m from the ground, with a blade tip clearance of 1.241 m. Further details are given in Table 3.3 and the test stand in single rotor configuration is shown in Fig. 3.6b.

Tests referenced in this thesis were made with a two-bladed single rotor[102] and a two-by-two-bladed stacked rotor[114] configuration. The upper rotor of the stacked rotor setup was used for

the single rotor experiments; see Fig. 3.10. The blades (see chapter 3.2.1) were attached to a rigid rotor hub without dedicated flap and lead-lag hinges. The hub was mounted on a six component load cell to measure hub loads in the rotating-frame with a bias uncertainty 8 N and 4.8 N/m. The blade pitch angles could be varied for each blade individually using servo actuators mounted on the hub.[58]

The test stand is powered by an electric motor, which drives a transmission consisting of synchronized toothed belts and pulleys[58]. A 1024 count optical encoder mounted to the drive shaft (motor axis) was used to measure the rotor rotational speed. All measurements were made at a sampling frequency of 10 kHz.[102]

The index angle (ϕ) definition is shown in Fig. 3.11. At positive index angles, the upper rotor is leading the lower rotor. Hence, the blade azimuth angle of the lower rotor can be computed as $\psi_{b,l} = \psi_{b,u} - \phi$. More information on the test rig is given in [58, 102].

Table 3.3.: Summary of rotor parameters for the UTA stacked rotor test rig.

Rotor			
	Single Rotor	Coaxial Rotor	
Number of blades per rotor, N_b	2		-
Precone angle, β_p	3		deg.
Airfoil	VR-12		-
Rotor radius, R	1.108		m
Chord, c	0.08		m
Root cutout, r_a	19		% R
Solidity, σ	0.046	0.092	-
Inter-rotor spacing[1], Δz_r	-	12.7	% R
	-	1.75	c
Nominal Operating Conditions			
Rotor rotational frequency, Ω	15		Hz
Rotor blade tip speed, V_{tip}	104.43		m s^{-1}
Rotor blade tip mach number, M_{tip}	0.30		-
Rotor blade tip Reynolds number, Re_{tip}	571,000		-

[1] Absolute distance between rotor planes chosen identical to CCR rotor; see Table 3.2.

3.2.3.2. Flow Field Measurements

Flow field measurements were made for a two-bladed single rotor[102]. The cameras, the laser and the general setup were identical to the previously described tests for the CCR rotor test rig in single rotor configuration; see chapter 3.2.2.2. Due to the different rotor radii of the setups, the FOV was smaller with about 50% of the rotor radius; see Fig. 3.10. Images were recorded at

41/rev corresponding ($\Delta\psi_b$ = 8.8°) over 73 continuous rotor revolutions. The tests were made to investigate the influence of step RPM variations on the rotor flow field, forces and moments. In total eight runs were made at constant speed over a total of 584 rotor revolutions, and eight runs were made with RPM ramps; see chapter 7.2. Three blade loadings $C_T/\sigma = 0.08, 0.10, 0.12$ (at nominal RPM) were investigated. The uncertainties in the velocity measurements were calculated to be 0.132 m s^{-1} and 0.105 m s^{-1} for the component and axial component of velocity vector, respectively.

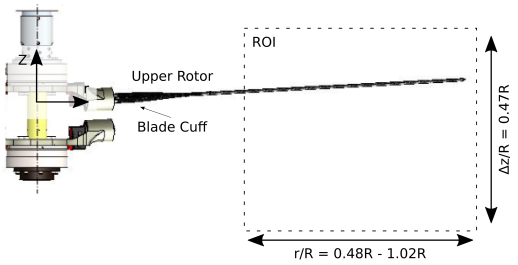

Figure 3.10.: Schematic showing the UTA stacked rotor test rig in single rotor configuration, including the ROI used for PIV measurements.

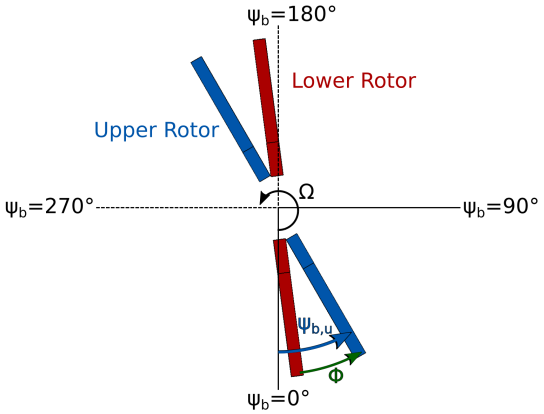

Figure 3.11.: Top view of rotor showing the index angle ϕ, blade azimuth angle ψ, and sense of rotation Ω for the UTA stacked rotor test rig.

The grid size of the captured images measured 592x487 mm in the r- and z-direction, respectively, with a scale factor of 5.316 pixel/mm. The resulting vector-to-vector spacing was 3.009 mm with a total of 31,979 calculated vectors in the ROI after merging of the two camera images.[102] Further details are given in [102].

4. Numerical Method – Finite-Volume Computational Fluid Dynamics

Within the subsequent chapters all relevant assumptions, simplifications, models, and parameters used in the simulations are summarized. Special attention was given to provide the reader with all required information to ensure reproducibility of the numerical results. The main focus was put on the description of the modeling of the geometric domain and the discretization of the modeled domain by a suitable mesh system. Both steps in the simulation process are not universally describable and a large number of differing solutions has been published. Moreover, a strong dependence of the solution on these aspects is known. For the numerical discretization of the partial differential equations, turbulence closure and the solution of the set of algebraic equations a more universal description is possible as only well established methods were used. Therefore, a comprehensive presentation of these methods is not provided, but the most important aspects were described and relevant literature for further reading is linked.

4.1. Solver

In the present study the finite volume CFD code TAU[1] [36, 131, 132], developed and maintained by DLR, was used. The software system TAU consists of multiple modules and libraries (preprocessor, solver, grid deformation, ...) and can be used standalone or within a python scripting environment. Grid generation and postprocessing of results were made using other software packages[2]. The solver is based on the compressible Navier–Stokes (NS) equations. To compute quasi incompressible flows low Mach number preconditioning can be used. Parallelization is achieved by domain decomposition and the message passing concept using MPI, which allows for efficient computations of large grids (several ten million grid points) [132].

The governing equations are solved based on a vortex-centered unstructured dual mesh approach, which is well suited for hybrid grids (mixed element meshes) or a cell-centered discretization which shows improved convergence behavior for grids with sharp edges[153]. Volume meshes can be composed of tetrahedrons, pyramids, prisms, and hexahedrons, to employ the best suited cell type for individual flow regimes. Arbitrary grid motions can be simulated by considering whirl fluxes in the flux balance[36] and grid deformation can be included in the simulations as the geometric conservation law is fulfilled[132]. Relative motions of individual grid blocks are possible when using chimera boundary conditions.

[1] TAU code version 2018.1.0

[2] Pointwise V18.3R1 was used for grid generation. Tecplot and Python were used for data extraction and visualization.

For the time integration Runge–Kutta based methods or implicit backward Euler methods are available. For the latter, the linear equation system is solved by using the Lower-Upper Symmetric Gauss–Seidel (LU-SGS) scheme. The solver has up to third order accuracy in time. Time accurate solutions are computed using the dual time stepping method proposed by Jameson or global time stepping. Geometric multigrid can be used along with local time stepping to improve the rate of convergence of the simulation. For the explicit time stepping scheme, residual smoothing can be used to further stabilize the convergence rate.

Fluxes can either be computed by one of several upwind schemes or a central scheme[36]. To stabilize the solution when using a central scheme, artificial dissipation can be added (scalar or matrix dissipation)[131]. Up to second order accuracy can be achieved.

The solver is capable of computing inviscid, laminar and turbulent flows. For the latter, a vast variety of turbulence models is available. Modeling approaches for turbulent flows included in the software range from one-equation models to Large Eddy Simulation (LES). If vortex dominated flows are to be computed, the solution accuracy can be improved by using Rotation/Curvature Correction (RC) terms in several of the available turbulence models.

The software was used successfully in a vast variety of flow problems, ranging from 2D airfoils to 3D space vehicles, rockets and hypersonic flows[131]. In the field of rotorcraft aerodynamics it had, for example, been used to compute the drag of rotorcraft fuselages[133] and rotor hubs [65, 115], the formation of tip vortices [40], and dynamic stall [83].

Based on the aforementioned specification of the software and the successful application to numerous different problems in rotorcraft aerodynamics, it was decided to use TAU with a cell-vertex scheme and second order accuracy in time and space. Though in hover most people rely on structured solvers with higher than second order accuracy [70], no final answer to how good a second-order solver can perform for such kinds of flow is given yet[28]. Moreover, the numerous available turbulence models enable the investigation of the performance of such models in the flow conditions investigated in this thesis. In addition, the (unstructured) solver allows extending the simulations by including more detailed hub geometries, elastic rotor blades, fuselages, actuator disks, and/or installation effects (e.g., the geometry of a hover test chamber or the rotor mount) easily in future investigations.

4.2. Spacial and Temporal Discretization

In the present study the inviscid convective fluxes were approximated with a second-order accurate central scheme. Hereby, the meanflow flux was computed as the analytic flux of the centrally averaged conservative variables on the cell face (*flux of average*). Matrix dissipation was chosen as dissipation scheme. Turbulent convection was computed using a second-order accurate Roe scheme. The reconstruction of gradients for higher order accuracy was computed with the Gauss divergence theorem or a least square approach depending on the simulation.

The temporal discretization was done using an implicit second-order backward Euler scheme. In the simulations every physical time step was transformed into a pseudo-stationary problem using the dual-time-stepping approach proposed by Jameson. Hence, acceleration techniques for steady problems can be used (e.g., local time stepping). The resulting equation system is solved by a LU-SGS method. In contrast to explicit schemes, the implicit scheme allows using larger time steps, at the cost of increased computational effort per iteration. The physical time step was chosen as a result of a temporal sensitivity study (see chapters 4.5.1.7 and 4.5.2.6) or was based on previous publications by the author[112, 113, 102, 103]. To further increase the convergence rate, a two stage V-cycle multigrid scheme was used with an additional step on the coarser grid level, except for the simulations using full Reynolds stress models where multigrid was not used; see chapter 4.5.1.7. On all grid levels a Courant–Friedrichs–Lewy (CFL) number of eight was set. Further details are given in the respective subsections.

4.3. Boundary Conditions

TAU offers a vast variety of boundary conditions, which reflect the wide spectrum of tasks it is used for in industry, research, and academia[131, 132]. In the context of this doctoral thesis only a small subset was used. Throughout this thesis boundary parameters were not modified between simulations and rotor configurations, unless necessary due to, e.g., the usage of different turbulence models; see chapter 4.4. A complete overview of all available boundary conditions, their respective parameters, and further implementation details is given in the TAU user [26] and technical documentation [27].

Farfield An inflow and outflow boundary condition at the outer boundary of the computational domain (*farfield*) was chosen, which sets all gradients to zero and does not take viscous effects into account [26]. Hence, the boundary condition was placed far away from the simulated object. At the boundary condition a virtual exterior point outside the computational domain holds the farfield state. "The farfield fluxes are evaluated via a characteristic method that is in line with the interior face-flux computation"[26]. For the simulations the velocity was set to $V = 0\,\mathrm{m\,s^{-1}}$ at the boundary condition and therefore, for all interior points in the fluid domain were initialized with this value.

Viscous turbulent wall Viscous surfaces were used for the rotor blades. Here, transition was neither prescribed nor computed and the boundary condition was set to be turbulent. The boundary layer was resolved ($y+ < 1$) and wall functions were not used.

Frictionless wall Walls without viscous effects were used for the generic rotor hub and a part of the rotor blade surface in the UTA rotor simulation (see chapter 4.5.2.2), as well as for the ground plane in the USNA rotor IGE simulations (see chapter 4.5.1.5). A correction was employed which modified "the wall pressure to the value required to bring any wall-normal velocity component to zero"[26].

Chimera To enable relative motions of grid parts and to be able to build optimized grid blocks for different regions in the flow field, the chimera/overset grid methodology, which is implemented in TAU, was used. This method defines artificial boundaries inside the computational domain. Hence, an overlap or a common region is required to interpolate the conservative variables across the boundary interfaces. Inherent drawbacks of the method are a loss of conservation, extra cost due to interpolation and a reduced accuracy in the overlap region due to different cell sizes between the individual blocks. These are outweighed by the ability to enable relative grid motion, required for rotor simulations.

Appropriate donor cells for the transfer of information between the grid blocks are searched around the interpolation points and the transfer of information is done by linear interpolation. To reduce interpolation errors, the "smallest among all valid donor cell is associated to an interpolation point, based on the assumption that the smallest cell shows the best representation of the local flow features and leads to the smallest interpolation error"[26]. To further reduce interpolation errors in the current study, all grids were built such that the size and orientation of cells in the overlap region matched where possible and that all required donor cells could be found without extending the search range outside the overlap region; see chapters 4.5.1 for the USNA test case and 4.5.2 for the UTA test cases. Cell sizes were reduced in regions where the tip vortex rollup was not yet completed, i.e., behind the trailing edge of the rotor blades, to better resolve gradients in the interpolation region.

To define the chimera boundary in the background grids hole cutting was performed based on predefined hole grid blocks, or interpolation zones were directly defined in the generated grid blocks. Automatic hole cutting was not used. Details can be found in chapters 4.5.1 and 4.5.2.

To reduce interpolation errors at the generic rotor head of the USNA rotor, wall projection was applied. This avoided problems in the boundary layer where the two blade blocks overlap; see chapter 4.5.1.2. The wall projection ensures an identical wall distance of the interpolation point and the interpolated data to "minimize interpolation errors close to curved surfaces"[26].

Rotational symmetry The flow field of isolated rotors in hover without crosswind can in good approximation be considered rotationally symmetric, if only collective pitch inputs (Θ_0) are commanded. Therefore, simulating only a fraction of the overall domain can significantly reduce the required computational time. For an equally spaced N_b-bladed rotor only a $1/N_b$-fraction of the domain needs to be simulated, e.g., for a four-bladed rotor only a quarter of the domain. In this thesis this was exploited for the single and stacked rotor simulations of the UTA rotor test stands. The implementation of the boundary condition assumes that pairs of points exist on periodic planes which are identified during preprocessing. Therefore, building rotationally symmetric grids by rotating a vertical slice can be used to fulfill this requirement. A description of this grid generation approach is given in chapters 4.5.2.4 and 4.5.2.4.

4.4. Turbulence Models

Most aerodynamic flows in nature are turbulent and thus, in comparison to laminar flows, the transport and mixing of matter, heat and momentum is greatly enhanced by turbulence[116]. Moreover, this increased transfer of momentum and energy increases the skin friction on walls compared to laminar flows. The probably most accepted theory of turbulence was developed by Kolmogorov and is based on the energy cascade concept[104]. The theory assumed that turbulent flows are composed of eddies of different sizes with each one possessing a certain amount of energy based on its dimensions. Energy is transferred from larger eddies to smaller eddies in a chain process as they break up. The newly formed eddies undergo a similar process. This is continued until the smallest eddies reach a size where molecular viscosity is dissipating kinetic energy as heat.[104, 116] These smallest structures have very short time scales and are independent of the slow dynamics of the large energy bearing eddies[155]. As a consequence, fluid velocity fields vary significantly and irregularly in both position and time[116].

Computing this process requires the exact solution of the non-simplified NS equations, and is usually referred to as Direct Numerical Simulation (DNS). This requires resolving all spacial and temporal scales of the flow field, from the largest energy carrying eddies in space to the smallest scales where dissipation occurs in time[155]. Moreover, as flows are chaotic in nature, small changes in the initial and boundary conditions can lead to different solutions[116, 12]. Hence, each DNS simulation represents one possible realization of a flow field[116].

However, due to limited computational resources this process is not feasible for the problems investigated in this thesis and other ways to account for turbulence effects are required. For a full description of the physics of turbulence[116] or an introduction into modeling[155] or implementing models in numerical simulation programs[12, 104] detailed information can, for example, be found in the referenced text books. The information provided in the following sections is given for the sake of completeness and reproducibility of the numerical results.

4.4.1. Turbulence Modeling and Closure Problem

To overcome the limitations given by the computational requirements of DNS simulations, statistical analysis is required to simplify the simulation of turbulent flows, i.e., approximate the effects of the random fluctuations. Such a mathematically sound description of the governing equations is, for example, possible by splitting the transported quantities in a mean and fluctuating part. This results in the RANS equations to describe the flow field without resolving all scales[116]. Hence, the scales of turbulent flows are modeled using turbulence models, which drastically reduces mesh size and time step limitations[104]. However, this process leads to the so called closure problem, as averaging results in new unknowns, the components of the Reynolds stress tensor (symmetric tensor with six unknowns)[155].

Dependent on the field of application a vast variety of turbulence models have been developed with different levels of complexity. A general classification is, for example, given in [12] where

models for non-laminar viscous flows are classified as first order closure (algebraic / zero-equation, one-equation, multiple-equation), second-order closures (Reynolds stress model (RSM)), or LES.

First order closures are mostly based on the eddy-viscosity hypothesis of Boussinesq[116, 12]. The hypothesis assumes that the turbulent stress tensor can be expressed in terms of the mean rate of strain, just as the viscous stress for Newtonian isotropic fluids. Only the coefficient of the molecular viscosity is replaced by the eddy viscosity. This leads to the same form of the transport equations as for laminar flows, except that the molecular exchange coefficients are replaced by their effective values (e.g., $\mu_{\text{eff}} = \mu + \mu_t$). Therefore, the closure problem can be solved when providing the eddy viscosity and diffusivity coefficients.[42] The eddy viscosity μ_t, however, is not a physical characteristic of the fluid but a function of the local flow condition and strongly affected by flow history effects[12].

Assuming that the turbulent flux of momentum, heat and species are directly related to the mean flow field poses limitations on the applicability of these models. Among other aspects, eddy viscosity models are not able to account for extra strain caused by e.g. streamline curvature, skewing, or rotation.[42] These are, however, particularly important aspects for the simulations of rotors. Hence, additional correction terms can be used to improve simulation results[12].

Further improvements can be expected by extending the linear relationship between strain rate and turbulence by using higher-order products of strain and rotation tensors. These non-linear eddy-viscosity models are only slightly more computationally expensive but can provide better predictions.[12] However, a generally valid non-linear eddy-viscosity model is not yet available[155].

A different way to compute the Reynolds stress tensor can be achieved with second-order closures, which are the most straight forward way of closing the turbulent flow equations within the framework of Reynolds averaging. Compared to eddy viscosity models, they have the sounder physical basis and the stress generation is treated in its exact form[42]. "This allows better reproduction of the evolution of the turbulent stress field and its anisotropy, effects of streamline curvature, flow and system rotation and flow three-dimensionality"[42]. For second-moment closures, moments of the NS equations are taken before averaging, which allows for solving one differential equation per unknown in the Reynolds stress tensor, i.e., six new equations. As a result of this process 22 new unknowns are created which need to be modeled. New unknowns are a general problem which cannot be overcome by taking higher moments of the equations. Using these models allows for taking history effects of the flow field into account, as the shortcoming of the Boussinesq hypothesis is overcome: the instantaneous return to isotropy.[155] The modeling effort is shifted from modeling the second moments to unknown higher-order correlations (usually third and fourth order correlations with diminishing effect on the mean flow properties). However, it has to be noted that these models are not per se superior over eddy-viscosity models, as the greater potential of modeling more terms comes at the risk of modeling them wrong.[42]

Another way of simulating turbulent flows is provided by LES and DES. In LES computations large scale turbulent structures are directly simulated, whereas small turbulent scales are modeled using sub-grid scale models[12]. However, LES is very often too costly for complex engineering configurations as the boundary layer has to be resolved. Therefore, DES methods were invented, a hybrid between URANS and LES. The former is used to resolve attached boundary layers, while

LES is used outside the wall region to capture the detached three-dimensional eddies[12]. Despite reaching a relatively high level of maturity, DES methods are not the focus of the current work.

All turbulence models have in common that they are not universally applicable. No single turbulence model exists which can be used for all types of flows to reliably predict the quantities of interest[12]. Despite ongoing efforts to develop new turbulence models, the usage of rotational corrections along with common one- and two-equation turbulence models will continue to be the most widely used way of simulating rotor flows[84]. Therefore, providing numerical results for flow fields which had not created substantial interest in the past and correlating these with experimental measurements continues to be a valuable contribution to the CFD and rotorcraft community. Hence, in addition to describing the underlying flow physical phenomena of the investigated configurations and flight conditions, the performance of different turbulence models was tested.

4.4.2. Spalart–Allmaras Model

The Spalart–Allmaras one-equation turbulence model is one of the most widely used turbulence closures in RANS simulations. According to the model developers, "the transport equation for turbulent viscosity is assembled using empiricism and arguments of dimensional analysis, Galilean invariance, and selective dependence on molecular viscosity"[138]. It was built from scratch and not derived from other models by simplification. The idea of the developers was to construct a transport equation for the eddy viscosity ν_t which relates the Reynolds stress tensor to the strain-rate tensor. Moreover, the model is local, meaning that one point in the computational domain does not depend on solutions at other points.[138]

The model was calibrated on three basic flow fields: a two-dimensional mixing layer, wakes, and flat-plate boundary layers. Moreover, a wall distance dependent non-viscous destruction term was included in the model.[138] Despite these relatively simple calibration cases the model found great interest in research and industry due to its simple form, good-natured numerical behavior, and moderate requirements of grid resolution in the near wall region[12].

Many variants were developed based on the original model. Out of these the *Negative Spalart–Allmaras One-Equation Model* was selected in the present work and "is generally recommended because of its more robust numerical behavior"[2]. This variant includes a modification of the original model in cases where the transport variable $\tilde{\nu}$ becomes negative. This avoids clipping updates to eliminate negative (non-physical) solution values.[3]

When used for external aerodynamic flows, for which it is intended, the model has proven to be "quite successful"[116]. Among other aspects, especially when looking at the computational expense required, it is reasonably accurate for flows with adverse pressure gradients and could smoothly transfer from laminar to turbulent flow at user defined positions[12]. A drawback is that the model requires the distance to the closest viscous surface at every grid point[155]. This was considered in the simulations by computing the distances every physical time step based on the current geometry which changed due to grid movement. Moreover, it is for example inca-

pable of accurately computing the decay of eddy viscosity far from solid boundaries in a uniform stream[155], the decay of ν_t in isotropic turbulence, or correctly computing jet spreading rates[116].

The previously described Spalart–Allmaras turbulence model performs well for attached or mildly separated turbulent boundary layers. However, system rotation, strong streamline curvature, and three-dimensional effects are difficult to compute with these models. This can lead to excessive amounts of turbulence which diffuse, for example, rotor tip vortices by far to quickly. To overcome these difficulties, a RC correction was developed for the Spalart–Allmaras turbulence model[139, 134]. This extension enhances the accuracy of the model for flow fields where the streamlines show high curvature and rotation plays a dominant role. It is implemented in the model equations by multiplying the production term with a "rotation function"[134]. Previous research has shown, that this modification significantly improves vortex preservation for rotors in hover[84].

In the present thesis the Spalart–Allmaras model was used with Rotation/Curvature Correction (RC). The turbulent boundary layer was resolved, wall functions were not used, and transition was not prescribed or computed. The turbulence equations were coupled with the mean flow equations and solved on each multigrid level. The model will subsequently be referred to as Negative Spalart–Allmaras One-Equation Model with Rotation/Curvature Correction (SA-neg-RC). A complete description of the model is given in [3], further details on the RC can be found in [139, 134] and other variants of the model and implementation details are described in [3, 2].

4.4.3. Menter Shear Stress Transport (SST) Model

A variety of two-equation models has been developed in the past. Most of these models use the exact transport equation for the turbulent kinetic energy k as a starting point. This equation poses little challenges and only the turbulent diffusion needs to be modeled.[155, 93] For the second equation a variety of formulations have been proposed, where mostly dimensional arguments lead to the exact formulation[155]. The second equation is used for the required length or time scale of the flow[95]. Two popular choices for the second variable are the turbulent dissipation rate ϵ, or the turbulence frequency ω.

For ϵ, an exact transport equation can be derived. However, this equation is extremely complex with double and triple correlations which cannot be measured and hence, not validated[155]. Therefore, the equation is usually modeled in analogy with the k-equation using mostly intuitive and dimensional arguments[116, 93]. Models based on ϵ as second transport variable found great attention and are used very successfully. However, usually they have deficiencies for adverse pressure flows and separated flows[155] as separation may be delayed (or prevented)[95]. In addition, the equation is numerically stiff, requires a damping function to stay valid through the viscous sublayer to the wall[95, 12] and ϵ does not go to zero at nonslip surfaces[95].

For ω a transport equation is modeled in analogy with the k-equation[93]. In comparison to using ϵ based equations, it performs better in adverse pressure gradient regions and no damping function is required. Besides, a Dirichlet type boundary condition is sufficient. The downside of the

models is its strong dependence on freestream values and too low spreading rates for free shear flows.[95]

A blending of the two models has been proposed to reduce their downsides and make use of their favorable properties. Hereby, a $k-\omega$ model is used from the wall to the inner region of the boundary layer and a $k-\epsilon$ in the outer region. Moreover, the transport effects of the principal turbulent shear-stress are accounted for by limiting the eddy-viscosity. This property gave the model its name: Menter Shear Stress Transport Model (SST). The results obtained with this model are similar to the original $k-\omega$ model.[95] Hence, the model combines the robustness of the $k-\omega$ model near walls (no damping function is required[12]) with the superior performance of the $k-\epsilon$ model at boundary layer edges and far of the surface (insensitivity to freestream values)[104]. Overall, it shows improved performance in adverse pressure gradient regions and for pressure-induced boundary layer separation predictions[12].

As all other models based on the Boussinesq hypothesis, the model has problems with secondary flows/motions, system rotation, and flows over curved surfaces. Moreover, there is no reason why μ_t should only depend on the turbulence parameters such as k, ϵ, and ω. Hence, the equations are no more likely than one-equation models to apply universally, despite their greater complexity.[155]

In the current study, a version of the model published in 2003 was used. A complete description of the model was given in [92, 2]. The turbulent boundary layer was resolved and wall functions were not used. This allowed using the same numerical settings for all investigated rotor configurations, including BVI where generic wall functions are not applicable. Transition was not prescribed or computed. The turbulence equations were coupled with the mean flow equations. For the USNA rotor test case the turbulence equations were solved on each multigrid level, whereas for the UTA cases the multigrid operators were disabled. Limitation of the transport variables was done by clipping for k ($k \geq 1e-05$). The lower limit for ω was derived from the Schwarz inequality for the Reynolds stresses that is implied by the realizability conditions. Realizability means in this context that by physical considerations the eigenvalues of the Reynolds stress tensor must be all non-negative[27].

4.4.3.1. SST with Rotation/Curvature Correction – SST-RC

To improve the SST predictions when rotation and streamline curvature play an important role, a RC was developed for the model. It is based on the correction for the SA turbulence model. The correction for SST differs from the correction for SA in the model constants. The correction is applied to both equations in the model.[137] Details on the correction, including model constants, can be found in [137, 2]. Simulation results computed with the combination of SST and RC are named Shear Stress Transport Model with Rotation/Curvature Correction (SST-RC) in subsequent chapters.

4.4.3.2. Scale Adaptive Simulation – SST-SAS

A Scale-Adaptive Simulation (SAS)[3] model can be considered as an advanced URANS model with the capability to produce spectral content for unstable flows. This means that SAS based models can, under certain conditions, automatically balance the contributions of modeled and resolved parts of the turbulent stress. The model behaves similar to DES for unstable flows. In contrast to DES, the explicit influence from grid spacing on the RANS part of the simulation is removed.[93] "For unstable flows, the model changes smoothly from an LES model through various stages of eddy-resolution back to a steady RANS model, based on the specified time step"[93].

This behavior is achieved by introducing the von Karman length scale in the scale-determining equation of the RANS turbulence model. The length scale "allows the turbulence model to recognize resolved scales in unstable flows and to adjust the eddy-viscosity to a level, which allows the formation of a turbulent spectrum. At the same time, attached boundary layers are automatically treated in RANS mode"[30].

The SAS modification is realized by introduction an additional production term, sensitive to resolved fluctuations, in the ω equation. The task of the additional term is to increase ω in regions where the flow is at the margin of becoming unsteady.[25] "The result is that k and ν_t are reduced so that the dissipating (damping) effect of the turbulent viscosity on the resolved fluctuations is reduced, thereby promoting the momentum equations to switch from steady to unsteady mode"[25]. This transition to unsteady mode requires a sufficiently fine grid resolution[25]. In general the idea behind SAS can be applied for other turbulence models as well, such as Explicit algebraic Reynolds stress models (EARSM) or RSM.[93]

Simulation results computed with the combination of SST and the SAS formulation are named Menter Shear Stress Transport Model with Scale-Adaptive Simulation (SST-SAS) in subsequent chapters. Despite the fact that the overall spacial resolution in the computations made here is insufficient for a DES or LES simulation, previous research by other researchers showed that improved results can be achieved by using DES simulations on comparable grids[63]. These results did not benefit from resolving small scale turbulence, but rather by limiting the amount of eddy-viscosity in the tip vortices, and consequently, improved vortex preservation. Therefore, using SST-SAS may improve simulation results significantly compared to other eddy-viscosity models and can reduce computation time compared to second-order closures.

4.4.3.3. SST-SAS-RC

In addition to the aforementioned two SST variants, the combination of SAS and RC was used in conjunction with the SST formulation. The idea was to benefit from both corrections to obtain better numerical flow solutions for the investigated case. This turbulence model is referred to as Menter Shear Stress Transport Model with Scale-Adaptive Simulation and Rotation/Curvature

[3] The model is not yet included in the release version of TAU 2018.1.0. It is only available in development mode.

Correction (SST-SAS-RC) in subsequent chapters. Details on the individual components of the model are given in the previous sections of chapter 4.4.3.

4.4.4. SSG/LRR-ω Full Reynolds Stress Model

A widely used RSM is the Speziale–Sarkar–Gatski/Launder–Reece–Rodi differential Reynolds-stress model + ω equation (SSG-LRR-ω) model. It is a blend between the Speziale-Sarkar-Gatski model (SSG)[140] and the Launder-Reece-Rodi model (LRR)[77] for the pressure-strain correlation, combined with Menter's baseline ω-equation[95]. The latter is used to provide the length scale. The model can be integrated down to the wall (low-Re model). In the combined model LRR is used near walls and SSG further off the wall. As with SST the second part of the combined turbulence model (SSG) is ϵ-based. The F1 blending function of Menter's k-omega based models[95] is used to combine the two models. "Thus the SSG/LRR-omega model consequently transfers the principles of Menter's k-omega models into the framework of Reynolds stress transport equations"[26].

For RSM a closed form for the mean-flow convection and production terms can be used. Modeling is required for the dissipation, Reynolds stress fluxes and the pressure rate of strain tensor.[116] The latter part is of prime importance, as it allows for a redistribution of energy among the stress components, which results in stress anisotropy[116, 42]. This is achieved as fluctuations in one velocity component can excite fluctuations in all other components, thus re-distributing the kinetic energy to the different fluctuating velocity components[27].

Overall, rotation and curvature terms are inherently included in the model, which is considered a tremendous advantage of full Reynolds stress models over simpler eddy-viscosity based models[139]. This is achieved by using exact production terms in the stress equations[42]. Hence, no further model to correct for rotation and curvature is required (in contrast to simpler Bousinesq hypothesis based models) to be used for applications such as rotors in hover.

The pressure-strain correlation is based on the two baseline models of SSG-LRR-ω. Diffusion was modeled with the generalized gradient diffusion hypothesis. The model constants are given in [31][4]. For the dissipation the isotropic dissipation tensor defined by Rotta was used. The length scale was provided by Menter's baseline ω-equation. Turbulent diffusion was accounted for in the energy equation, turbulent kinetic energy was accounted for in the total energy and a simple strain rate tensor was used in the re-distribution term. The wall boundary condition was implemented as a smooth wall.

This turbulence model is referred to as SSG-LRR-ω in subsequent chapters. Due to increased numerical complexity compared to the other turbulence models investigated in this thesis, parts of the time stepping scheme (see chapter 4.2) and findings from the temporal sensitivity study (see chapter 4.5.1.7) had to be adapted compared to the other models. As a consequence, no multigrid was used and the inner iteration count was increased; see chapter 4.5.1.7.

[4] According to [31] the model is listed as SSG-LRR-ω2012 on [2]. However, coefficients differ between [31] and [2]. In TAU the model is named SSG-LLW-ω.2010.

4.4.5. Realizable Quadratic Eddy Viscosity Model (RQEVM)

Simple turbulence models based on the Boussinesq hypothesis showed insufficient capabilities to correctly predict complex flow problems. On the other hand RSM have not yet reached the state of maturity required for every day use. Therefore, non-linear eddy viscosity models and EARSM have been developed, with the latter being a rational approximation to RSM.[26] For these models the transport terms in the RSM equations are approximated to reduce the set of six coupled transport equations to six algebraic relations. Therefore, they are less general and accurate compared to RSM, but simpler. The Reynolds stresses can then be computed locally as a function of k, ϵ or ω and the mean velocity gradients.[116] In general, these models are numerically robust with little overhead compared to their background two-equation models, which provide the velocity and length scale[151]. The derived models can be regarded as non-linear two-equation models that can be a good approximation of the full second-moment closure[129].

In this thesis, the Realizable Quadratic Eddy Viscosity Model (RQEVM) developed by Rung[129] was used. The background model applied was the Wilcox $k-\omega$ model[27]. The model "stems from an explicit solution to the second-moment closure in the limit of equilibrium turbulence"[26]. Due to its non-linearity, the models allows for a non-alignment between the principal axes of the viscous and the Reynolds stress tensor. This can be regarded as an extended Boussinesq hypothesis.[27]

Rotation and curvature corrections, which can be developed for these models[152], have not been applied and the model is used in standard form. Using this model allowed to investigate possible benefits of the non-linearity of the model compared to standard eddy-viscosity models.

4.4.6. Linearized Explicit Algebraic Stress Model (LEA)

The Linearized Explicit Algebraic Stress Model (LEA) turbulence closure stems from an explicit solution of the second-moment closure in the limit of equilibrium turbulence. It can be regarded as a non-linear, generalized two-parameter model which retains the predictive benefits of second-moment closure models. The previously described RQEVM model is the corresponding quadratic model.[26]

As for the RQEVM the Wilcox $k-\omega$ model forms the basis. It is derived from the linear eddy-viscosity part of RQEVM[129]. It differs from the Wilcox 1988 model only in the eddy-viscosity. The required coefficients are identical to the Wilcox 1988 model, including modifications that stem from[94]. This turbulence model is referred to as LEA in subsequent chapters and shall highlight differences to the quadratic model RQEVM.

4.5. Geometry and Computational Grid

Despite the fact that the hovering rotor configurations treated in this thesis were different (see chapter 3), the simulation strategies were similar. Therefore, the baseline grid structure was identical for all rotor configurations and was only adapted to the individual requirements of the experimental setups. All rotor simulations were performed using chimera / overset grids, to allow for blade pitch angle changes and relative motions between grid blocks, if required.

To best resolve the dominant flow features (tip vortices and trailed vortex sheets) structured grids were created for the blades and in the path of these flow features. Due to the known, predominant rotational symmetry of the flow fields, i.e., the spiral tip vortex trajectories in hover, the background grids were created rotationally symmetric as well. This enabled a high spacial resolution perpendicular to the tip vortex core ($\Delta s \approx 2\%$ c) in order to resolve the large velocity gradients in the tip vortices properly, while keeping the overall cell count low due to a larger grid spacing in azimuthal direction (Δs_{az}).

Each of the computational grids consisted of three basic building blocks: a blade grid block, a background grid block, and a transfer grid block; see Figs. 4.1, 4.11, and 4.23. The latter was used to locally increase the grid resolution near the blades and to create a smooth transition from the cuboid blade grid to the rotational symmetric background grid. A similar strategy was previously used by other researchers[73] and was adapted and refined. Details of the grids and required geometrical simplifications for the simulations are given in sections 4.5.1 for the USNA IGE rotor test rig and 4.5.2 for the UTA rotor test rigs.

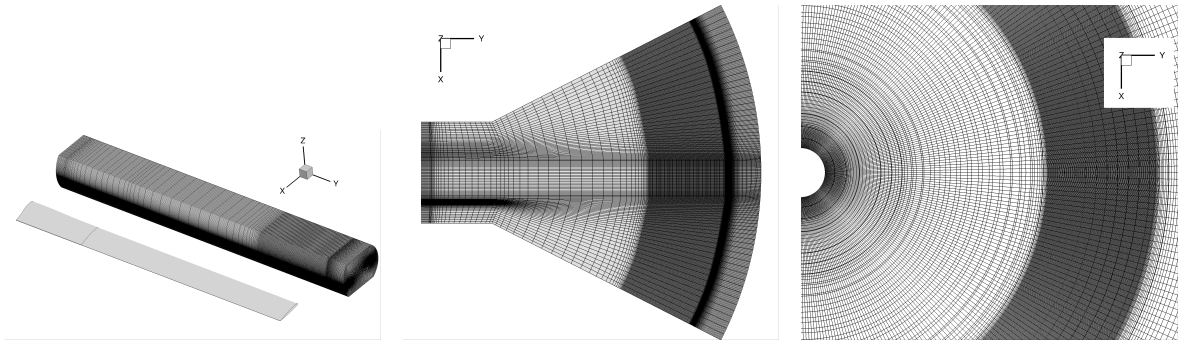

(a) Blade surface (bottom) and chimera interpolation zone (top).

(b) Top view of generic transfer grid showing transition from rectangular blade grid to rotational symmetric background grid.

(c) Enlarged top view on cut through a generic rotational symmetric background grid.

Figure 4.1.: Illustration of the three generic chimera grid building blocks used for CFD simulations. High grid resolution perpendicular to tip vortex path visible by compression of grid points (dark regions) in images.

4.5.1. US Naval Academy Rotor In-Ground-Effect Test Rig

4.5.1.1. NACA 0012 Airfoil

The NACA 0012 profile was used for the aerodynamic sections of the USNA rotor blades. Contrary to the original airfoil definition with a blunt or a sharp trailing edge, the rotor blades were manufactured with a rounded trailing edge tab (see Fig. 4.2). To reduce numerical errors in the numerical simulations of the rotor test stand, a grid convergence study was performed for the modified airfoil. To exclude possible effects from chimera interpolation, results were first computed for a structured O-grid type body fitted grid. Chimera results were subsequently compared to affirm the chosen grid resolution and chimera interpolation strategy. As no experimental or computational aerodynamic data was available for this particular shape in the literature, a validation of the aerodynamic data based on experimental data or a code-to-code comparison could not be conducted.

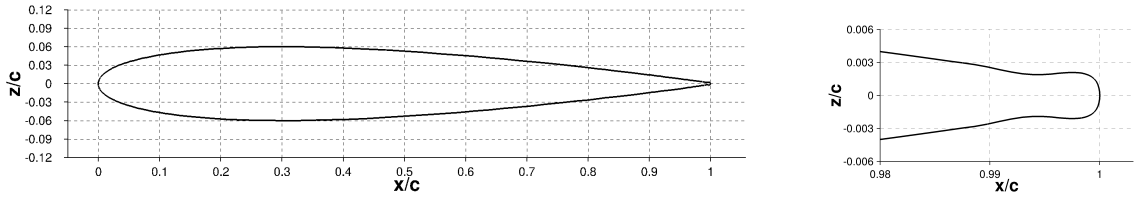

(a) NACA 0012 airfoil.

(b) Trailing edge.

Figure 4.2.: Schematic showing the geometry of the modified NACA 0012 airfoil (a) and the tab at the trailing edge (b).

Three different levels of refinement with a doubling of nodes between them, two different heights of the first cell height above the surface (Δs_{bl}), and three different boundary layer growth rates (g_{bl}) were used in the grid convergence study of the single body fitted airfoil grid. The farfield boundary condition was placed at a distance of $r = 100$ c. A schematic of the NACA 0012 airfoil grid, including node counts and grid spacings is shown in Fig. 4.3. Spacing constraints and node counts were placed symmetrically on the upper and lower surface at five locations ($x/c = 0$, $x/c = 0.004$, $x/c = 0.500$, $x/c = 0.989$, and $x/c = 0.998$).

The chimera airfoil grid and the transfer grid are shown in Fig. 4.4. A pitch angle of $\Theta = 6°$ was geometrically built in the grid to improve interpolation in the pitch angle regime of interest for the subsequent studies. The airfoil chimera boundary was placed at a distance of $r = 1.46$ c from the quarter chord point at the leading edge, and $r = 1.24$ c at the trailing edge. The height of the airfoil block was 1.5 c. An identical chimera interpolation zone was created between the airfoil and the transfer grid. It had a width of four cells spanning a distance of 0.11 c; see blue zone in Fig. 4.4.

Information on the surface node distribution of the finest grid resolution and the chimera grid is given in Table 4.1. A complete overview of the used surface grids, and their specific settings is given in Table D.1. Further details of the chimera specific dimensions are listed in Tables 4.2 and 4.3.

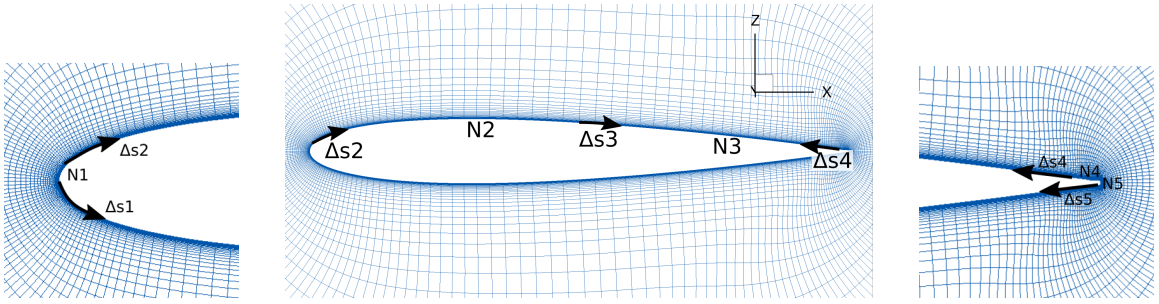

(a) Leading edge. **(b)** NACA 0012 airfoil grid. **(c)** Trailing edge.

Figure 4.3.: Schematic of the NACA 0012 airfoil grid, including grid spacing and node count definitions used in Table 4.8. Node count N4 is on the tab surface, whereas N5 is at the trailing edge.

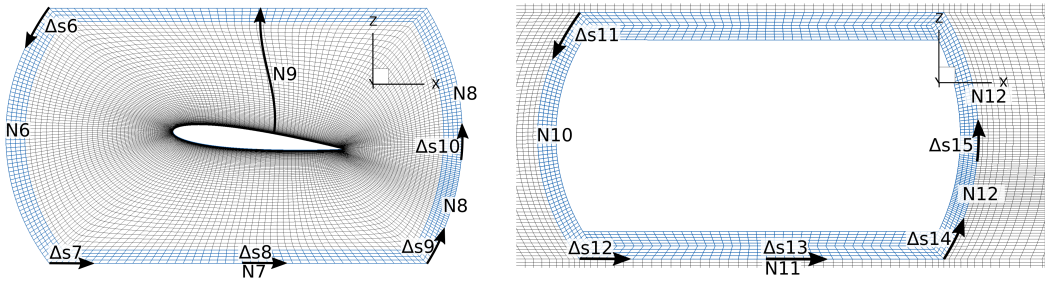

(a) Airfoil grid. **(b)** Transfer grid.

Figure 4.4.: Schematic of the chimera airfoil and transfer grid for the NACA 0012 grid convergence study. Chimera interpolation zones are marked in blue. Grid spacings and node counts are given in Tables 4.2 and 4.3.

Computations were made for six different angles of attack in the range of $\alpha = -2°$, $0°$, ... $8°$ at $V = V_{\text{tip}} = 89.72\ \text{m s}^{-1}$. The SA-neg-RC turbulence model was used (see chapter 4.4.2) along with the numerical settings specified in chapter 4. Angle of attack changes for the chimera grid were achieved by rotating the airfoil grid around the quarter chord axis, whereas in the single grid cases the freestream velocity vector was rotated. The grid setup with chimera interpolation boundaries in the airfoil and transfer grid allowed blade pitch angle changes in the range of $\Theta = 1.9°$, ..., $10.9°$ without extending the valid chimera nearest neighbors.

It was found that for the single grids (**G1** to **G18**) the differences in c_l were less than 0.45%, in c_d were less than 1.01%, and in $c_{\text{m}y}$ were less than 6.9% for all angles of attack $\alpha \neq 0°$ when compared to the finest grid **G4**. For the chimera grid **C1** in combination with the transfer grid **T1**, the difference in c_l was less than 0.11%, in c_d was less than 1.26%, and in $c_{\text{m}y}$ was less than 2.23% for all angles of attack $\alpha \neq 0°$ when compared to the finest grid **G4**. A comparison between the aerodynamic coefficients of grids **G4** and **C1** is shown in Fig. 4.5. These differences were considered to be adequate for the subsequent investigations, in particular as the blades were assumed to be stiff and consequently, the airfoil pitching moment was not of interest. Therefore, the grid resolution of the chimera grid **C1** and transfer grid **T1** were used for all further investigations of the three-dimensional flow fields.

Table 4.1.: Overview of mesh spacings (Δs) node counts (N) for the airfoil grids used in the grid convergence study for the NACA 0012 airfoil. Definitions of spacings for the airfoil grid G and the chimera airfoil grid C are shown in Fig. 4.3.

NACA 0012 - single grid												
	Δs1 [%c]	Δs2 [%c]	Δs3 [%c]	Δs4 [%c]	Δs5 [%c]	N1	N2	N3	N4	N5	Δs_{bl} [%c]	g_{bl}
G4	0.025	0.05	0.5	0.05	0.025	34	258	251	27	14	0.0009	1.05
NACA 0012 - chimera airfoil grid												
C1	0.1	0.1	3	0.1143	0.0337	13	47	47	13	11	0.0018	1.175

Table 4.2.: Overview of mesh spacings (Δs) node counts (N) for the chimera airfoil grid (C) used in the grid convergence study for the NACA 0012 airfoil. Definitions of spacings are shown in Fig. 4.4a.

NACA 0012 - chimera airfoil grid									
	Δs6 [%c]	Δs7 [%c]	Δs8 [%c]	Δs9 [%c]	Δs10 [%c]	N6	N7	N8	N9
C1	2.39	3.15	5.00	2.30	1.43	69	48	46	90

Table 4.3.: Overview of mesh spacings (Δs) node counts (N) for the transfer grid (T) used in the grid convergence study for the NACA 0012 airfoil. Definitions of spacings are shown in Fig. 4.4b.

NACA 0012 - chimera transfer grid								
	Δs11 [%c]	Δs12 [%c]	Δs13 [%c]	Δs14 [%c]	Δs15 [%c]	N10	N11	N12
T1	2.39	3.15	5.90	2.30	1.43	69	42	46

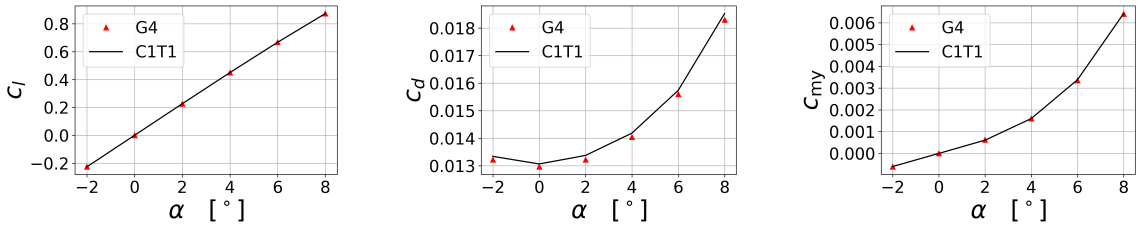

(a) c_l. **(b)** c_d. **(c)** c_{my}.

Figure 4.5.: Comparison between NACA0012 grids **G4** and **C1T1** airfoil characteristics as result of grid convergence study.

4.5.1.2. Rotor Blade and Rotor Hub

The rotor blade was meshed based on the results of the NACA 0012 grid convergence study (see chapter 4.5.1.1). The two-bladed rotor with the teetering rotor head, rotor shaft and rotor mount used in the experiments performed by USNA is shown in Fig. 4.6a.

For the numerical simulations a number of simplifications were made for the rotor hub. The rotor mount and shaft were not included in the numerical simulations. Furthermore, the rotor head was simplified when compared to the experimental geometry. It was modeled as a circular tube with a diameter of 25% c and a length of 8 mm. This surface was also used for chimera interpolation between the two rotor blades. Blade attachment bolts and blade clamps were also not included in the numerical simulations. For the untwisted, rectangular blades in hover, inflow and lift are highly biased towards the blade tips. Therefore, the aforementioned simplifications were expected to cause negligible effects along the rotor blades, as their primary range of influence is localized close to the rotor center. Similar modeling strategies were used by other researchers and the computed performance[73], thrust, and vortex characteristics at young wake ages (i.e., before the turbulence models lead to excessive tip vortex dissipation)[62] were in good agreement with experimental data. Note that in [62] a rotor with blades of equivalent radius was tested in parallel ground effect. A smooth surface was modeled from the simplified hub geometry to the original tapered blade root. The simplified rotor head is shown in Fig. 4.6b. It was decided to keep a generic rotor head in the simulation setup, rather than leaving a finite distance between the rotor blades, to avoid excessive flow in the upwards direction between the rotor blades.

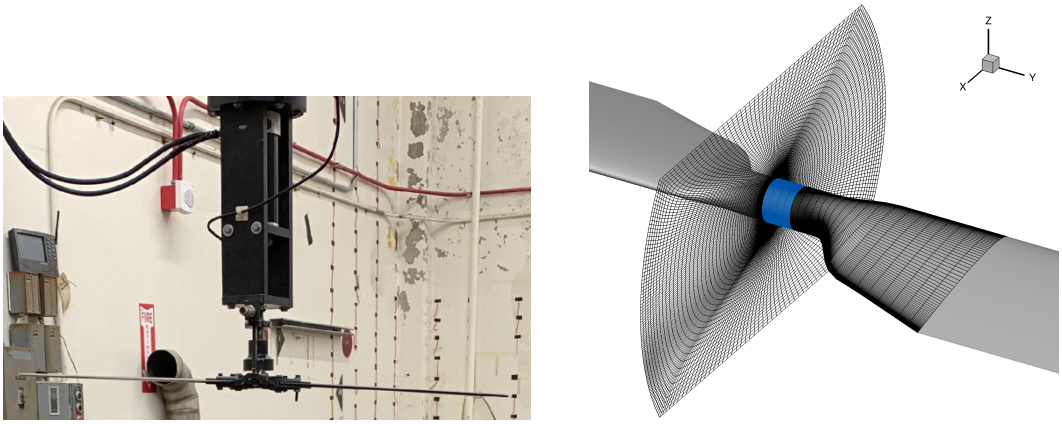

(a) Experimental rotor hub configuration.[90]

(b) Modeled rotor head and blade attachment. Blade-to-blade chimera interpolation zone marked in blue.

Figure 4.6.: Comparison between experimental rotor hub and simplified rotor head used in the numerical simulations for the USNA rotor.

In addition, the rotor blade tip was rounded compared to the square blade tip in the experimental setup; see Fig. 4.7b. To do so, the symmetric airfoil was rotated around the chord line, and subsequently scaled radially by a factor of 0.25 around its center of rotation. This was done to create a smooth surface (i.e., no sharp edge at the blade tip), while keeping the differences to the original shape minimal. Similar strategies have been pursued by other researchers for various blade tip

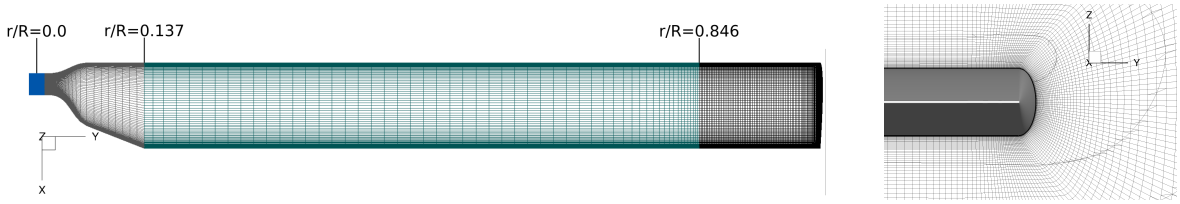

(a) USNA rotor blade. Blade-to-blade chimera interpolation zone marked in blue ($r/R \leq 0.0$). Refined tip mesh shown in black ($r/R \geq 0.946$.)

(b) Enlarged view on the rounded blade tip.

Figure 4.7.: Schematic showing the blade surface grid of the USNA rotor blade (a) and the modeled rotor blade blade tip and grid (b).

shapes and gave good correlation to experimental data[62].

The rotor blade was meshed with an O-O type grid topology. At the generic rotor hub, the mesh was extruded inwards along the blade axis. An O-grid topology was used for the airfoil sections and at the blade tip; see Figs. 4.4a and 4.7b. A dense clustering of grid points was used at the trailing edge chimera interpolation zone to assure that the tip vortex formation was not significantly influenced by the widening of grid cells due to the O-grid topology.

The airfoil was meshed according to the chimera grid **C1**, shown in Fig. 4.4a and described in Tables 4.1 and 4.2. As for the airfoil chimera block, the blade chimera block had a height of 1.5 c. The chimera interpolation zone at the blade tip was placed at a radial distance of $r/R = 0.083$ from the blade tip; see Fig. 4.8b.

Along the blade axis, 4 cells were used for the generic rotor hub (Δs = 4.5% c), 19 cells were distributed inside r/R = 0.137, 55 cells were used up to the beginning of the refined tip region ($r/R \leq 0.846$) with a maximum spacing of Δs_{max} = 15.3% c, and 99 cells were placed in the refined region at the tip. For the latter, a maximum grid spacing of Δs_{max} = 2% c was used, which decreased to about Δs = 0.05% c at the tip. The radial extension was chosen such that the first tip vortex passage took place in the refined region and that the spacing matched the resolution of the background mesh; see chapter 4.5.1.4. A schematic of the blade mesh is shown in Fig. 4.7. The tip face was meshed using a O-grid topology with 15 nodes in the circular grid region. The boundary layer was extruded such that a dimensionless wall distance of $y+ \leq 1$ is assured for all simulations. Overall, the blade grid consisted of $4.569 \cdot 10^6$ points.

4.5.1.3. Transfer Block

The transfer grid block enabled a smooth transition from the cuboid blade grid to the rotationally symmetric background grid. A similar grid strategy was used by other researchers[73] and was expanded here. Not only was the transfer block used to locally increase the grid resolution close to the rotor blade, but also to improve the chimera interpolation between the blade and the background by having identical interpolation regions in the grid blocks; compare Figs. 4.4 and 4.8. To further reduce influences from chimera interpolation, the transfer block was sized such that the tip vortex was entering and leaving the transfer block through vertical side faces during the first

blade passage; see extension of transfer block in negative z-direction in Fig 4.8c. Therefore, the tip vortex was only interpolated in planes perpendicular to the vortex axis, which improved vortex conservation. The transfer block dimensions are given in Fig. 4.8.

The radial node distribution was taken over from the rotor blade grid; see chapter 4.5.1.2. The chimera interpolation between the rotor blade and the transfer block was identical to the definition of **T1**; see Table. 4.3. All other chimera interpolation zones had a width of 4 cells, except in the azimuthal direction. Here, the cell count was altered to match the azimuthal background grid resolution; see Fig. 4.8b. A maximum grid spacing of $\Delta s = 2\%$ c was used in the vertical direction. Transfer grid dimensions for the different azimuthal background grid spacings (Δs_{az}) are given in Table 4.4.

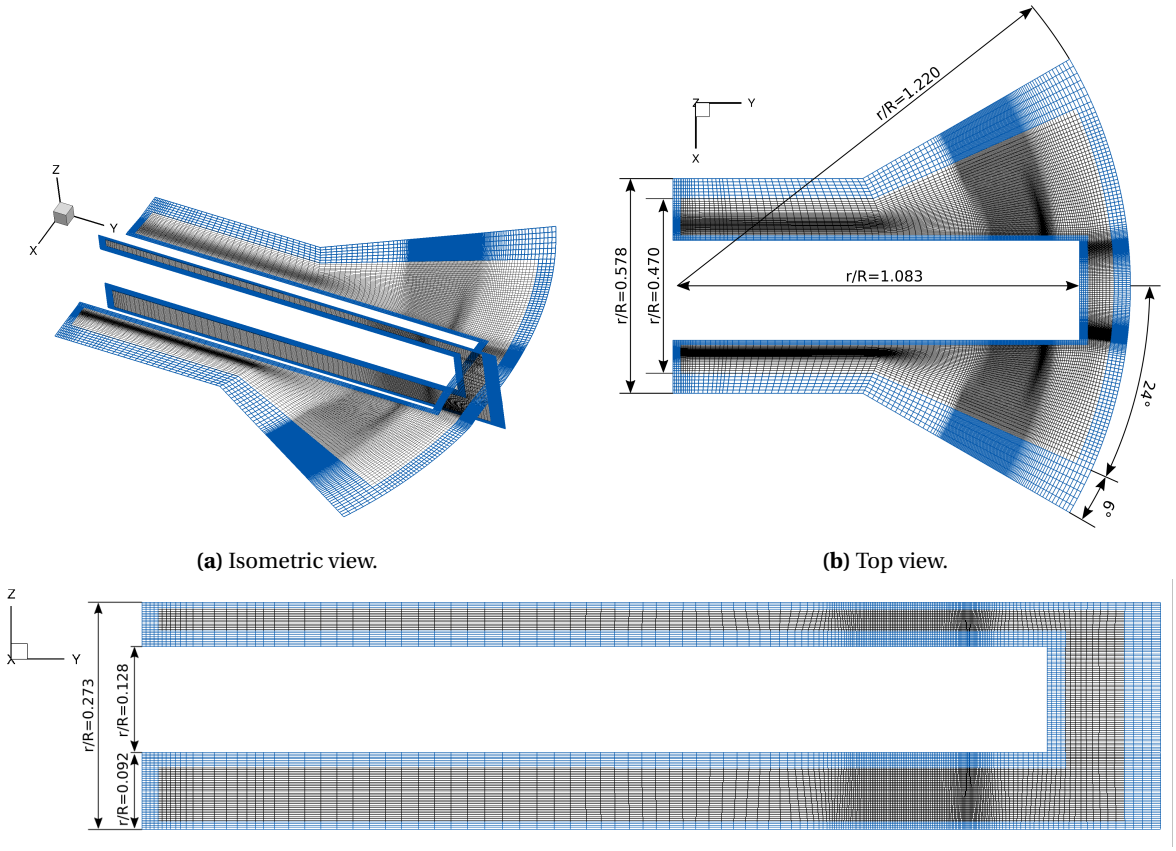

(a) Isometric view.

(b) Top view.

(c) Side view.

Figure 4.8.: Schematic showing sectional cuts through the transfer volume grid of the USNA rotor. Chimera interpolation zones are marked in blue.

4.5.1.4. Background

Two fundamentally different background grids were created for the USNA rotor test rig; one for the OGE simulations and one for the IGE simulations. The latter allowed tilting the ground plane in a

Table 4.4.: Transfer grid sizes for the USNA rotor simulations.

Background grid resolution Δs_{az}	Grid points
1°	$2.828 \cdot 10^6$
2/3°	$2.973 \cdot 10^6$
0.5°	$3.167 \cdot 10^6$

range of $-15° \leq \Theta_{GP} \leq 15°$ around the X and Y-axis. Using one grid for all IGE simulations allowed using the parallel ground plane simulation result as a restart solution for the inclined ground plane case, and hence, to save computational time (see also chapter 4.5.1.7). However, this advantage came at the cost of increasing the region of highest grid resolutions (i.e., the grid point count) into regions not required for a particular ground plane inclination angle; see Figs. 4.9b, 4.11b, and 4.11c.

A cut through the rotationally symmetric background grid created in the path of the tip vortices is shown in Fig. 4.9. To avoid a singularity at the center of rotation, a quad dominant prismatic mesh was created inside of $r/R = 0.578$ with a target grid spacing of $\Delta s = 10\%$ c and extruded in Z-direction. Outside of the rotationally symmetric grid, the volume was filled with unstructured cells up to a distance of $r = 30$ R from the rotor head. By using a gradual transition from the structured to the unstructured grid region, abrupt changes in the cell sizes were avoided. Moreover, using an unstructured background grid enabled placing the farfield boundary far away from the rotor without significantly increasing the cell count. The distance chosen exceeded that used by most other researchers. For example in [84] a distance of $r = 20$ R was used, in [14] the farfield was located at $r = 15$ R, or in [61, 63] the farfield was placed $r = 10$ R.

To improve vortex preservation a maximum cell size of $\Delta s = 2\%$ c was used in the path of the tip vortices (see blue region in Fig. 4.9), comparable to grid sizes used by other researchers[63]. For the OGE background grid, this region was adapted to the vortex trajectory, showing the typical contraction of the tip vortex helix. Outside this region a smooth transition to the unstructured background grid was created using structured grids. Background grid dimensions for the different azimuthal background grid spacings (Δs_{az}) are given in Table 4.5. The azimuthal grid spacings tested resemble those used by other researchers[60, 61, 62].

Table 4.5.: Background grid sizes for the USNA rotor simulations.

Background grid resolution Δs_{az}	Grid points IGE	Grid points OGE
1°	$80.695 \cdot 10^6$	$43.688 \cdot 10^6$
2/3°	$118.545 \cdot 10^6$	-
0.5°	$156.001 \cdot 10^6$	-

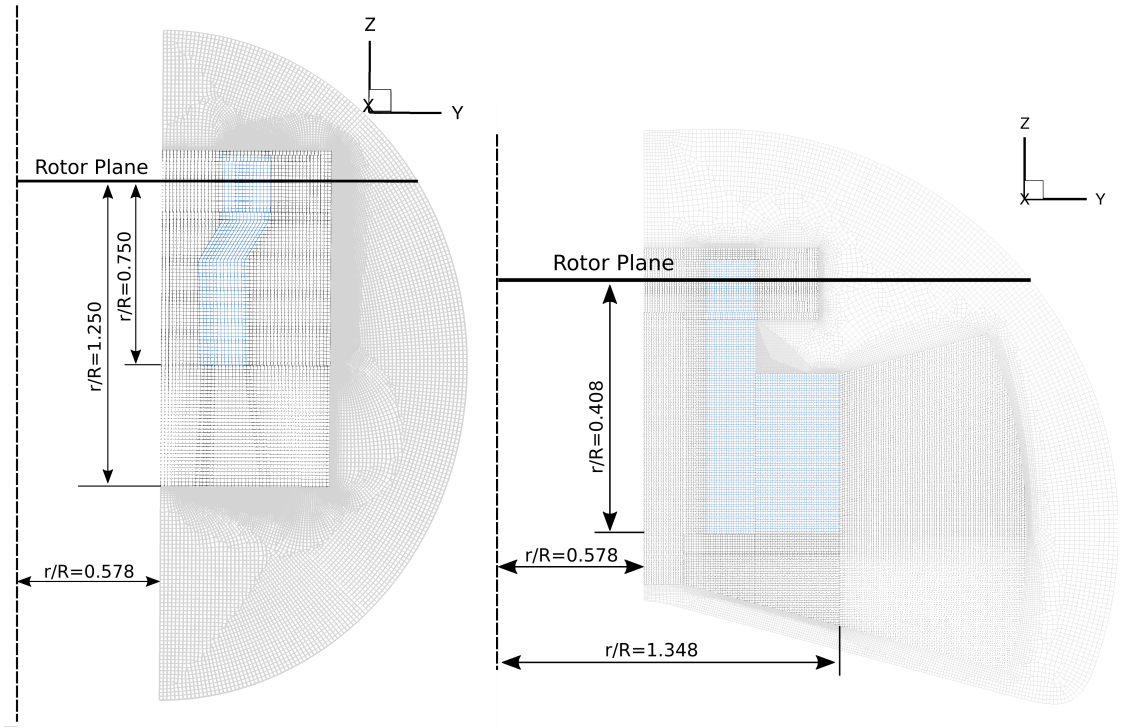

(a) OGE. **(b)** IGE.

Figure 4.9.: Schematic showing sectional cuts through the rotationally symmetric parts of the USNA rotor background grids used for the (a) OGE and (b) IGE simulations. High resolution grid regions ($\Delta s = 2\%$ c) for improved tip vortex preservation are shown in blue, structured regions in black, and unstructured regions in gray.

4.5.1.5. Ground Plane

A comparison between the ground plane ($D = 4$ R) used in the experiments and the modeled geometry is shown in Fig. 4.10. To simplify the geometry, the flow diverter used in the experiment were not modeled.

A rotationally symmetric structured grid was created outside of $r/R = 0.578$, equivalent to the background grid. A grid spacing of $\Delta s = 2\%$ c was chosen in the region of grid refinement for improved tip vortex preservation (see blue parts of the grid in Fig. 4.9b). The ground plane mesh had a height of 0.07; R with 33 cells of size $\Delta s = 2\%$ c perpendicular to the upper surface. As the ground plane was modeled as a frictionless wall, no wall boundary layer refinement was created. This assumption was also used by other researchers who were primarily interested in the flow field near the rotor[14]. To avoid a singularity caused by a purely rotationally symmetric grid, an unstructured, quad dominant prismatic mesh with a maximum grid size of $\Delta s = 10\%$ c on the ground plane surface was created inside of $r/R = 0.578$. Grid dimensions are given in Table 4.6.

(a) Photograph of the ground plane with flow diverters[99].

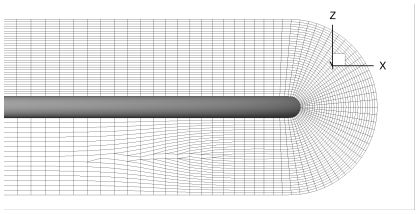

(b) Schematic of the ground plane grid. Radial cut through mesh showing the outer 14% of the ground plane.

Figure 4.10.: Comparison between the ground plane used in the experiments and the modeled geometry in the numerical simulations.

Table 4.6.: Ground plane grid sizes for the USNA rotor simulations.

Background grid resolution Δs_{az}	Grid points
1°	$6.311 \cdot 10^6$
2/3°	$9.401 \cdot 10^6$
0.5°	$12.225 \cdot 10^6$

4.5.1.6. Grid Assembly

Schematics of the assembled grids for the OGE and IGE simulations based on the USNA rotor test stand are shown in Fig. 4.11. The required differences in the background grids caused by adding a ground plane in the simulations can clearly be seen. The overall grid dimensions are listed in Table 4.7.

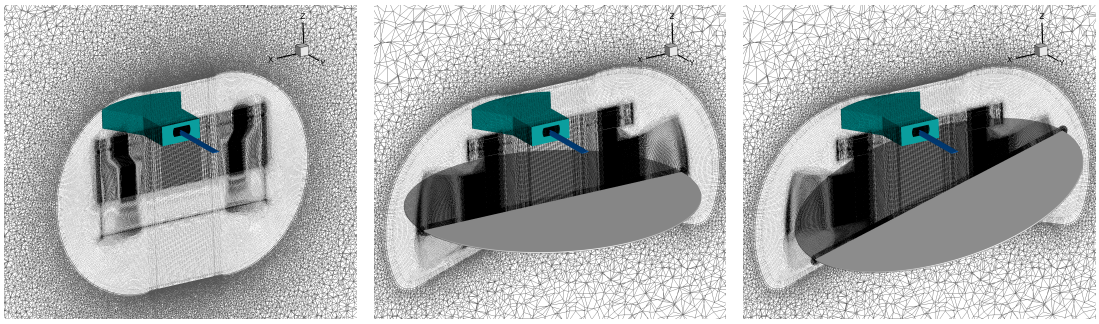

(a) OGE. **(b)** IGE $\Theta_{GP} = 0°$. **(c)** IGE $\Theta_{GP} = 15°$.

Figure 4.11.: Schematic showing sectional cuts through the assembled grids for the USNA rotor: (a) OGE, (b) IGE with parallel ground plane ($\Theta_{GP} = 0°$), and (c) IGE with inclined ground plane ($\Theta_{GP} = 15°$). The transfer block outer chimera boundary is shown in green, the rotor blade is shown in blue.

Table 4.7.: Overview of grid sizes for the USNA rotor simulations.

Grid name	Test condition	Δs_{az}	Grid points
GIGE1	IGE	1°	$101.800 \cdot 10^6$
GIGE2	IGE	2/3°	$143.030 \cdot 10^6$
GIGE3	IGE	0.5°	$183.697 \cdot 10^6$
GOGE1	OGE	1°	$69.559 \cdot 10^6$

4.5.1.7. Grid and Temporal Sensitivity Study

To assess temporal and grid discretization effects for the USNA rotor simulations, a sensitivity study was made at a ground plane inclination angle of $\Theta_{GP} = 15°$ with the SA-neg-RC turbulence model. The numerical setup and the turbulence model are described in sections 4.1 to 4.4.2.

All simulations were started in parallel ground effect with a time step size of $\Delta\psi_b = 45°$ and were run for 15 revolutions to convect the starting vortex off the ground plane. Afterwards, the ground plane inclination angle was increased to $\Theta_{GP} = 15°$ within four revolutions and 360 time steps per period with 25 inner iterations. Subsequently the simulation was run for another two to three revolutions with the corresponding time step size and inner iteration settings investigated. The rotor was trimmed to the experimental thrust of $C_T = 0.003565$ (≈ 18.717 N) at $\Theta_{GP} = 15°$ as described in chapter 4.6. This resulted in an identical collective pitch of $\Theta_0 = 6.8°$ for all simulations.

Multiple combinations of time step sizes ($\Delta\psi_b = 0.5°$, $0.6\overline{6}°$, $1.0°$) and inner iteration counts (25,50) were investigated. The temporal resolution was chosen chosen in accordance with the azimuthal grid spacing (Δs_{az}) of the tested background grids; see chapter 4.5.1.4. These values were comparable to investigations made by other researchers dealing with similar problems[61].

The temporal resolution study showed that time step size and inner iteration counts mostly affected the residual and had negligible effects on the rotor forces and moments; see Figs. 4.12 and 4.14. Also the background grid resolution did not show any significant differences; see Figs. 4.13 and 4.15. Therefore, it was decided to run all subsequent simulation with grid **GIGE1**, a time step size of $\Delta\psi_b = 1.0°$ and 25 inner iterations. The only difference being the SSG-LRR-ω model. Here, no multigrid scheme could be used due to numerical stability issues and therefore, the inner iteration count was increased to 100 while keeping the time step size identical. For hover OGE and IGE at $\Theta_{GP} = 0°$ using **GIGE1** and **GOGE1** the normalized density residual dropped to about $\approx 1.2 \cdot 10^{-6}$ compared to the density residual in the first iteration. At $\Theta_{GP} = 15°$ the scaled density residual was $\approx 1.7 \cdot 10^{-5}$. Both quantities were in good agreement with the values reached in the temporal sensitivity study using the SA-neg-RC model; see Fig.4.12c.

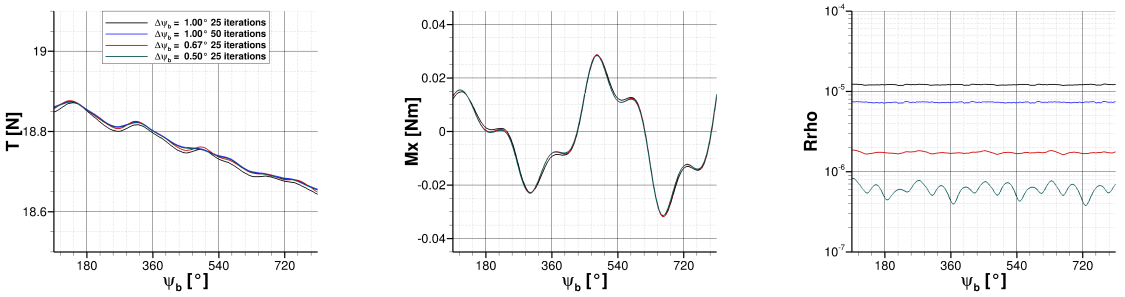

(a) Rotor thrust.

(b) Rotor hub moment in rotating frame.

(c) Normalized density residual.

Figure 4.12.: Evaluation of effect of time step size ψ_b and inner iteration count per time step on the numerical simulation results for the USNA rotor at $\Theta_{GP} = 15°$ with background grid **GIGE2**. Data shown over two rotor revolutions, beginning after one rotor revolutions at constant ground plane inclination angle $\Theta_{GP} = 15°$ (in total 22 rotor revolutions).

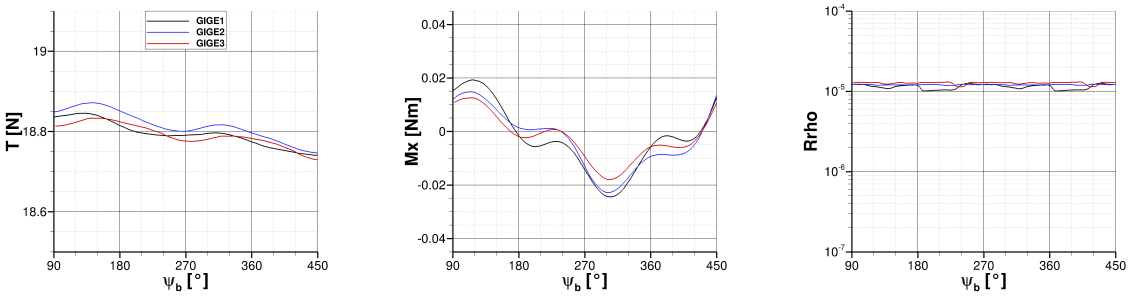

(a) Rotor thrust.

(b) Rotor hub moment in rotating frame.

(c) Normalized density residual.

Figure 4.13.: Evaluation of effect of background grid resolution on the numerical simulation for the USNA rotor at $\Theta_{GP} = 15°$ with three different background grid resolutions at $\Delta\psi_b = 1.00°$ and 25 inner iterations per time step. Data shown over one rotor revolution, beginning after one rotor revolution at constant ground plane inclination angle $\Theta_{GP} = 15°$ (in total 21 rotor revolutions).

4.5.2. University of Texas at Austin Rotor Test Rigs

4.5.2.1. VR-12 Airfoil

The VR-12 profile was used for the aerodynamic sections of the UTA rotor blades. Contrary to the original airfoil definition with a blunt or a sharp trailing edge a modified geometry was used. The carbon fiber rotor blades were manufactured with a trailing edge tab; see Fig. 3.7. As for the NACA 0012 airfoil (see chapter 4.5.1.1) a grid convergence study was made for the modified airfoil. To exclude possible effects from chimera interpolation, results were first computed for a structured O-grid type body fitted grid. Chimera results were subsequently compared to affirm the chosen grid resolution and chimera interpolation strategy.

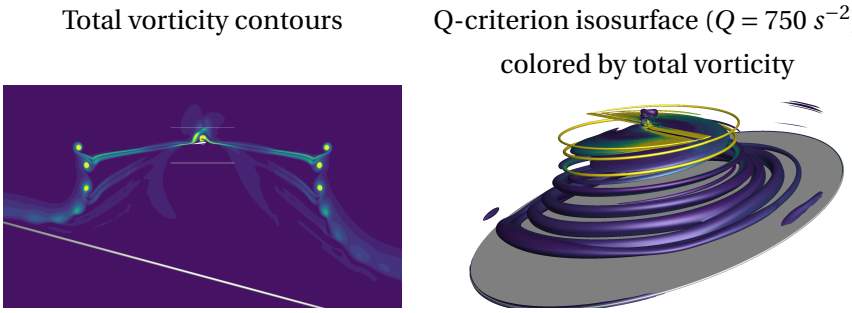

(a) $\Delta\psi_b = 1.0°$, 25 inner iterations.

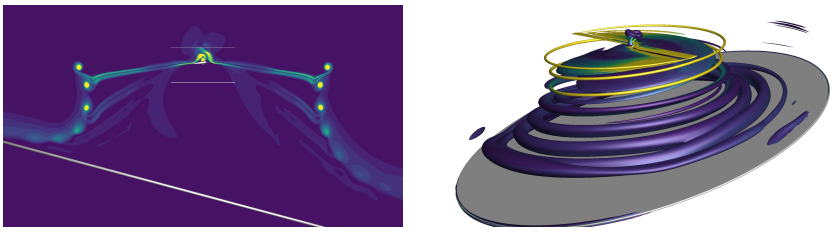

(b) $\Delta\psi_b = 1.0°$, 50 inner iterations.

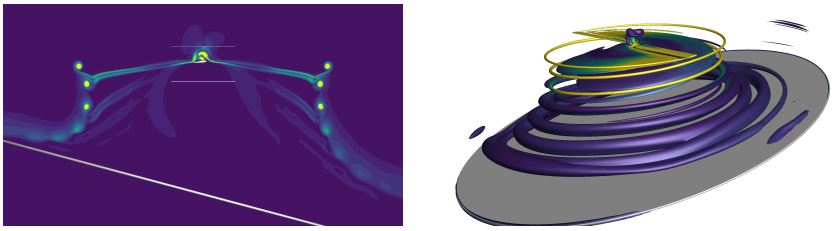

(c) $\Delta\psi_b = 0.67°$, 25 inner iterations.

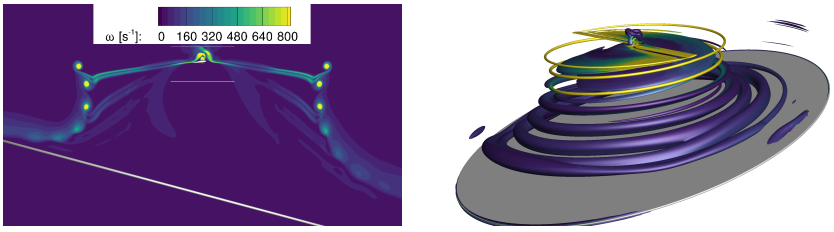

(d) $\Delta\psi_b = 0.5°$, 25 inner iterations.

Figure 4.14.: Visualization of the effects of temporal resolution on the computed flow field of the USNA rotor at $\Theta_{GP} = 15°$. Flow solution computed with grid **GIGE2**. Images extracted at $\psi_b = 90°$ after three rotor revolutions at constant ground plane inclination angle $\Theta_{GP} = 15°$ (in total 22 rotor revolutions). Isosurfaces visualized over the ground plane.

Three different levels of refinement with a doubling of nodes between them, two different heights of the first cell height above the surface (Δs_{bl}), and three different boundary layer growth rates (g_{bl}) were used in the grid convergence study of the single body fitted airfoil grid. The farfield boundary condition was placed at a distance of $r = 100$ c. A schematic of the VR-12 airfoil grid, including

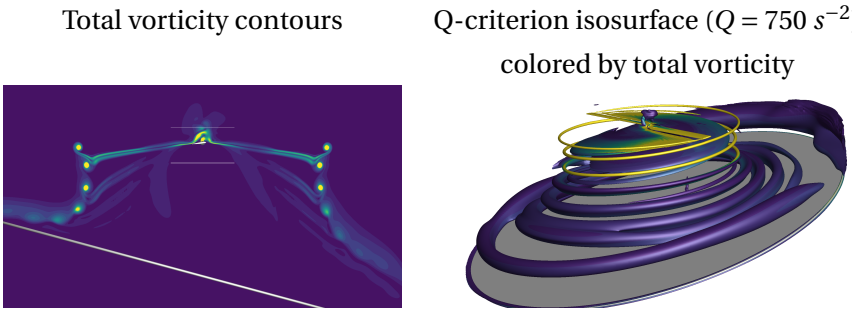

(a) GIGE1.

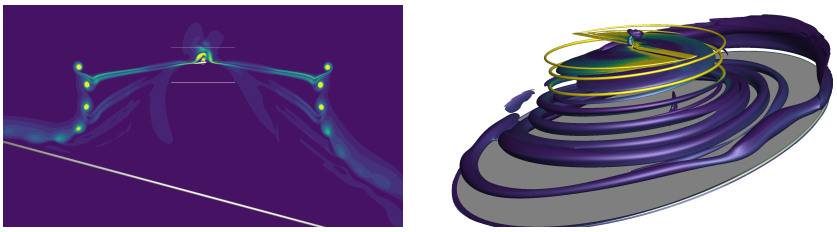

(b) GIGE2.

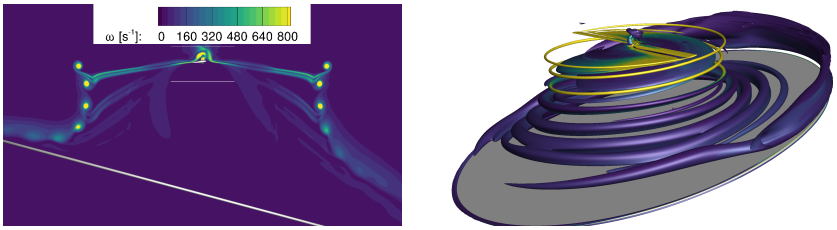

(c) GIGE3.

Figure 4.15.: Visualization of the effects of grid resolution on the computed flow field of the USNA rotor at $\Theta_{GP} = 15°$. Flow solution computed with a time step size of $\Delta\psi_b = 1.00°$ and 25 inner iterations. Images extracted at $\psi_b = 90°$ after two rotor revolutions at constant ground plane inclination angle $\Theta_{GP} = 15°$ (in total 21 rotor revolutions). Isosurfaces visualized over the ground plane.

node counts and grid spacings is shown in Fig. 4.16. Spacing constraints and node counts were placed symmetrically on the upper and lower surface for at four locations (N1 to N4 at $x/c = 0$, $x/c = 0.125$, $x/c = 0.500$, and $x/c = 0.947$).

A schematic of the chimera airfoil grid and the transfer grid is shown in Fig. 4.17. A pitch angle of $\Theta = 6°$ was geometrically built in the grid to improve interpolation in the pitch angle regime of interest for the subsequent studies. The airfoil chimera boundary was placed at a distance of $r = 0.8125$ c at the leading edge, and $r = 1.125$ c at the trailing edge from the quarter chord point. The height of the airfoil block was 1.3225 c, limited by the inter-rotor spacing of the CCR rotor setup; see chapter 3.2.2. An identical chimera interpolation zone was created between the airfoil and the transfer grid, with a width of four cells spanning a distance of 0.084 c; see blue zone in Fig. 4.17. For the transfer grid, this region was further extended inward by four additional layers.

An overview of the used grids, and their specific settings is given in Tables D.2, D.3, and D.4. Information on the finest grid resolution and the selected chimera grid block specifications is in addition shown in Table 4.8, 4.9, and 4.10.

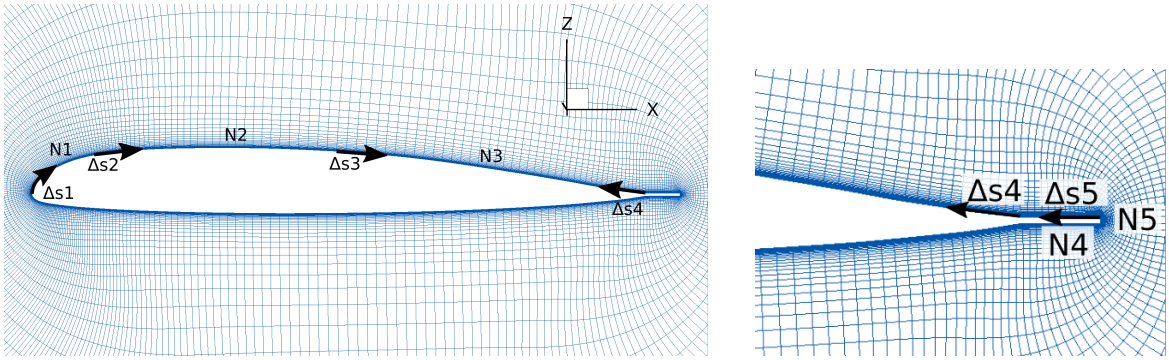

(a) VR-12 airfoil grid.

(b) VR-12 airfoil trailing edge.

Figure 4.16.: Schematic of the VR-12 airfoil grid, including grid spacing and node count definitions used in Table 4.8. Node count N4 is on the tab surface, whereas N5 is at the trailing edge.

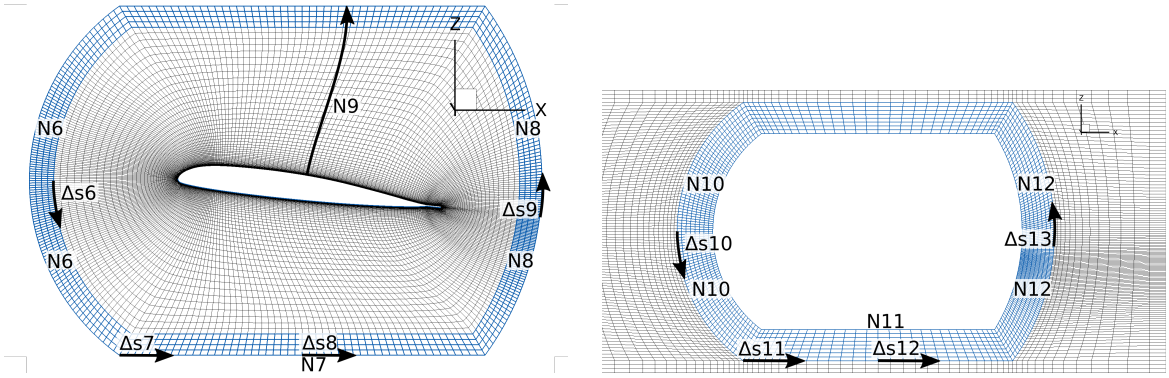

(a) VR-12 airfoil grid.

(b) VR-12 transfer grid.

Figure 4.17.: Schematic of the VR-12 airfoil and transfer grid for the VR-12 grid convergence study. Chimera interpolation zones are marked in blue. Grid spacing and node count for the transfer grid are given in Table 4.8.

Table 4.8.: Overview of mesh spacings (Δs) node counts (N) for the airfoil grids used in the grid convergence study for the VR-12 airfoil. Definition of spacings for the airfoil grid G and the chimera airfoil grid C are shown in Fig. 4.16.

VR-12 - single grid												
	Δs1 [%c]	Δs2 [%c]	Δs3 [%c]	Δs4 [%c]	Δs5 [%c]	N1	N2	N3	N4	N5	Δs_{bl} [%c]	g_{bl}
G4	0.025	0.125	0.5	0.125	0.025	239	139	167	86	19	0.00044	1.05
VR-12 - chimera airfoil grid												
C4	0.075	0.375	1.875	0.1875	0.025	63	31	40	27	17	0.00069	1.15

Table 4.9.: Overview of mesh spacings (Δs) node counts (N) for the transfer grid (T) used in the grid convergence study for the VR-12 airfoil. Definition of spacings is shown in Fig. 4.17a.

VR-12 - chimera airfoil grid								
	Δs6 [%c]	Δs7 [%c]	Δs8 [%c]	Δs9 [%c]	N6	N7	N8	N9
C4	0.898	2.764	2.764	0.554	58	51	59	84

Table 4.10.: Overview of mesh spacings (Δs) node counts (N) for the transfer grid (T) used in the grid convergence study for the VR-12 airfoil. Definition of spacings is shown in Fig. 4.17b.

VR-12 - chimera transfer grid							
	Δs10 [%c]	Δs11 [%c]	Δs12 [%c]	Δs13 [%c]	N10	N11	N12
T3	1.110	2.764	5.950	0.516	51	31	58

Computations were made for seven different angles of attack in the range of $\alpha = -2°$, $0°$, ... $10°$ at $V = V_{\text{tip,coax}} = 95.76\ \text{m s}^{-1}$. The Spalart-Allmaras turbulence model (see chapter 4.4.2) and numerical settings specified in chapter 4 were used. Angle of attack changes for the chimera grids were achieved by rotating the airfoil grid around the quarter chord axis, whereas the freestream velocity vector was rotated for the single grids. The grid setup with chimera interpolation boundaries in the airfoil and transfer grid blocks allowed blade pitch angle changes in the range of $\Theta = -1.5°, \ldots + 13.5°$ without extending the valid chimera nearest neighbors.

It was found that for the single grids (**G1** to **G18**) the differences in c_l were less than 0.34%, in c_d were less than 1.47%, and in $c_{\text{m}y}$ were less than 2.27% for all angles of attack when compared to the finest grid **G4**. Hence, all grid resolutions were considered adequate.

For the chimera grid **C4** in combination with transfer grid **T3**, the difference in c_l was less than 0.12%, in c_d was less than 1.49%, and in $c_{\text{m}y}$ was less than 1.88% for all angles of attack when compared to the grid **G4**. The results were most influenced by the vertical extension of transfer grid block above the interpolation zone (z-direction), followed by the resolution in the wake of the airfoil (x-direction). The node count in x-direction in the transfer grid block (N11) did not influence the results significantly. Hence, for the three-dimensional computations, the transfer grid block should be extended in z-direction as much as possible. However, it is limited by the inter-rotor spacing of the CCR rotor. A comparison between the aerodynamic coefficients of grids **G4** and **C4** is shown in Fig. 4.18.

The differences were considered to be adequate for the subsequent investigations, in particular as the blades were assumed to be stiff and consequently, the airfoil pitching moment was not of interest. Therefore, the grid resolution of the chimera grid **C4** and transfer grid **T3** were used for all further investigations.

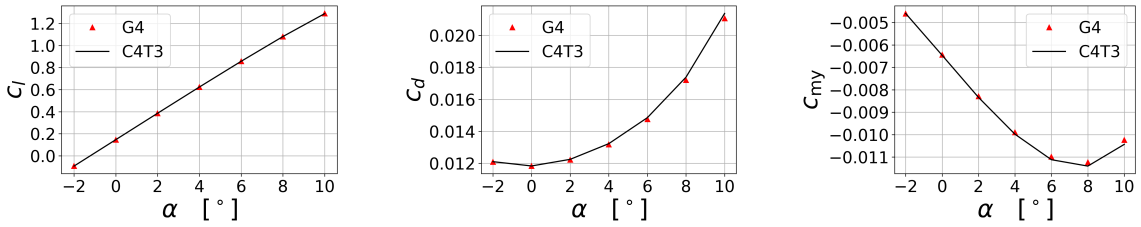

(a) c_l. **(b)** c_d. **(c)** c_{my}.

Figure 4.18.: Comparison between VR-12 grids **G4** and **C4T3** airfoil characteristics as result of grid convergence study.

4.5.2.2. Rotor Blade and Rotor Hub

Both of the UTA rotor test rigs were using the same rotor blades, despite having different rotor hub designs; compare Figs. 4.19a and 4.19b. This resulted in different rotor radii despite the blades being identical; see chapter 3.2 for further details on the rotor test rigs.

For the numerical simulations the rotor head assembly was simplified. A cylindrical structure was used to replace the complex design consisting of the blade grips, bolts to attach the blades, pitch links, wiring for the experimental instrumentation, and load cells; see Figs. 3.6, 3.9, 4.19, and [58]. The cylinder diameter was selected such that it was equal to the load cell diameter (R = 97.5% c). As explained previously for the USNA rotor test rig (see chapter 4.5.1.2), for rotors with untwisted, rectangular blades in hover, inflow and lift are highly biased towards the blade tips. Therefore, the aforementioned simplifications were expected to cause negligible effects along the rotor blades, as their primary range of influence was localized close to the rotor center. Similar modeling strategies were used by other researchers and the computed performance[73], thrust, and vortex characteristics at young wake ages (i.e., before the turbulence models lead to excessive tip vortex dissipation)[62] were in good agreement with experimental data. Moreover, note that in [73] a CCR rotor was investigated. The simplified rotor head was included in the background grid; see Fig 4.22a. The modeled rotor head assembly is compared to the experimental setups in Fig. 4.19.

The geometrical shape of the rotor blades, including the blade cuff used to increase the blade flap bending stiffness in the experiments (see Fig.4.19a), was not altered for the numerical simulations. A H-O-O type grid topology was used to mesh the blade. The airfoil was meshed according to grid **C4**; see Fig. 4.17 and Tables 4.8 and 4.9. Scaled spacing distributions were used for the cuff. The airfoil mesh and an unstructured mesh on the blade root were extruded inwards (Δy = 0.027 R) creating an H-topology at the blade root. The square blade tip was meshed using an O-grid type topology; see Fig. 4.20b. The radial distance to the chimera interpolation zone at the blade tip was r/R = 0.039.

In total 228 cells were distributed along the blade axis. The blade cuff was meshed using 18 cells with a cell size of Δs = 2.5% c at the root, Δs = 15.6% c at the end of the cuff, and a maximum cells size of Δs = 25.0% c in between. Between the cuff and the refined tip region 24 cells were placed

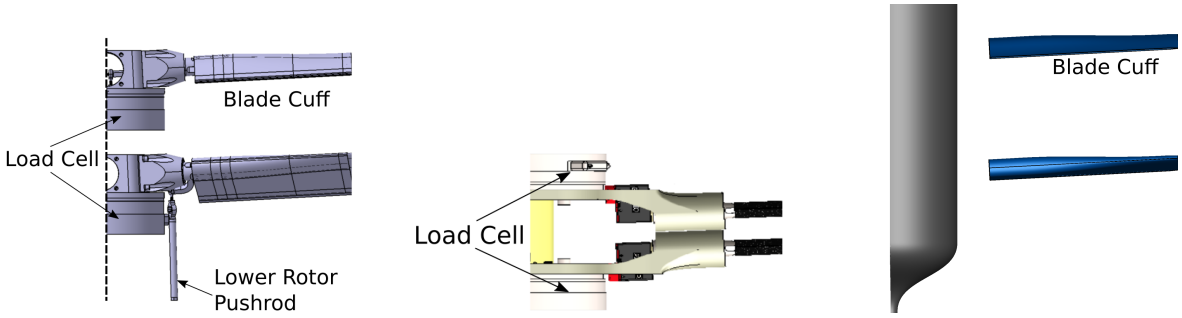

(a) Experimental CCR rotor head configuration.

(b) Experimental stacked rotor head configuration.

(c) Modeled rotor head. CCR rotor head shown.

Figure 4.19.: Comparison between experimental rotor head configurations and simplified cylindrical rotor head used in the numerical simulations for the UTA rotor setups.

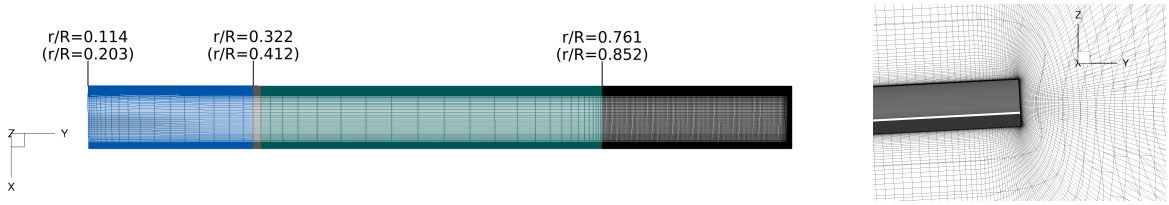

(a) UTA rotor blade. Blade cuff marked in blue, refined tip mesh shown in black. Reference lengths are given for the CCR rotor and in brackets for the stacked rotor.

(b) Enlarged view on the blade tip with precone.

Figure 4.20.: Schematic showing the blade surface grid of the UTA rotor blade (a) and the rotor blade tip grid (b).

with a maximum cells size of $\Delta s = 42\%$ c and matching cell sizes to the adjacent surface meshes. The refined tip region was meshed using 186 cells with a maximum cell size of $\Delta s = 2.0\%$ c. At the tip, it was decreased to $\Delta s = 0.0003125\%$ c to properly resolve the squared tip. On the blade tip face an O-grid topology was used with 20 cells in peripheral direction. Overall, the blade grid consisted of $7.493 \cdot 10^6$ points.

4.5.2.3. Transfer block

The basic structure of the transfer block was identical with the one described for the USNA test case; see chapter 4.5.1.3. Therefore, only aspects specific to the UTA setup are described here. As the transfer grids for the UTA rotor setups were used in the context of stacked and CCR rotors it was not possible to avoid non-perpendicular interpolations of the tip vortices. Therefore, in contrast to the USNA transfer grid, no additional extraction in z-direction was made for this purpose. The block dimensions are shown in Fig. 4.21.

Based on the results of the VR-12 airfoil grid convergence study, the chimera interpolation to the rotor blade was meshed according to grid **T3**; see Table 4.10. The radial node distribution was taken over from the rotor blade grid; see chapter 4.5.2.2. Towards the rotor hub the interpolation

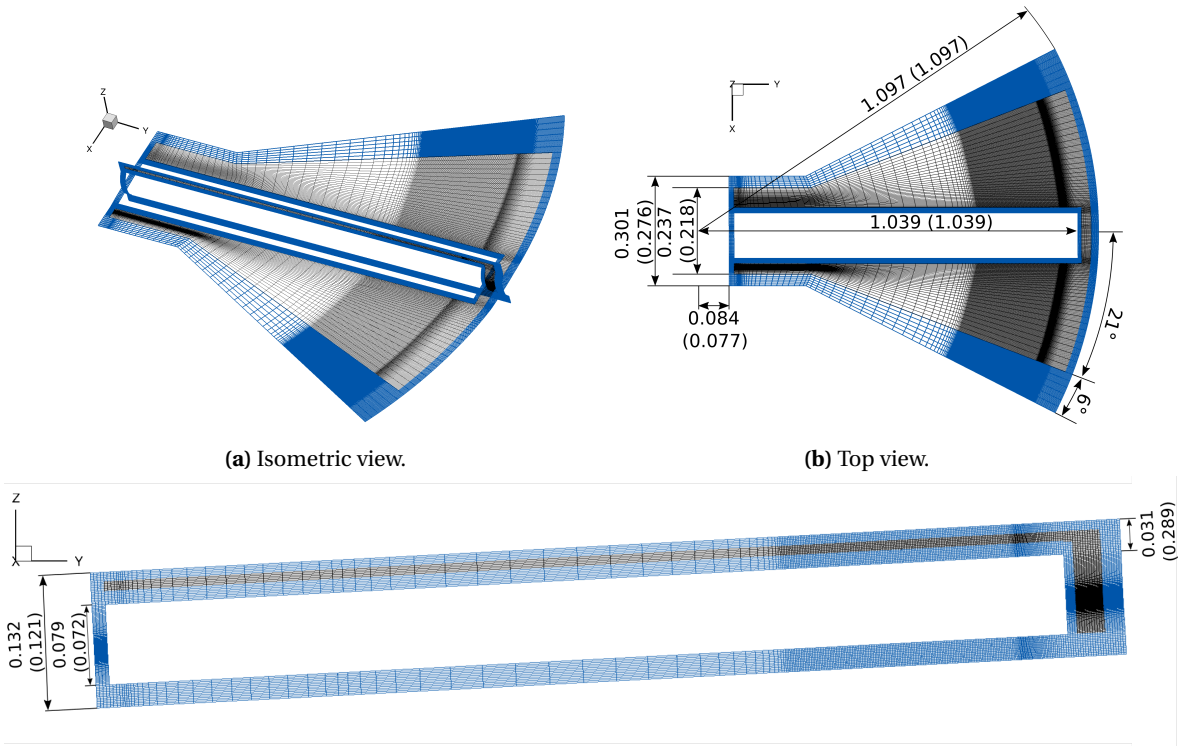

(a) Isometric view.

(b) Top view.

(c) Side view with precone of $\beta_p = 3°$.

Figure 4.21.: Schematic showing sectional cuts through the transfer volume grid of the UTA rotors. Chimera interpolation zones are marked in blue. Reference lengths are given for the CCR rotor and in brackets for the stacked rotor as fraction of the rotor blade radius (r/R). Block used for single rotor simulations and the upper rotor plane of the CCR and stacked rotor.

zone was meshed with four cells ($\Delta s = 4.2\%$ c), whereas outboard interpolation zone had a width of eight cells ($\Delta s = 3.0\%$ c). The top and bottom interpolation zones were six cells wide ($\Delta s = 2.0\%$ c). In azimuthal direction the grid spacing was adapted to match the background grid spacing in the interpolation zone. The upper rotor transfer block size, which was also used for the single rotor computations, was increased by six cells in vertical direction ($\Delta s = 2.0\%$ c); see black grid region between the blade and background interpolation zones in Fig. 4.21c.

Grid dimensions are given in Table 4.11. Note that the lower rotor transfer grid blocks had a reduced size due to the lower vertical extension compared to the upper transfer grid blocks.

Table 4.11.: Transfer grid sizes for the UTA rotor simulations.

Background grid resolution Δs_{az}	Upper/Single rotor	Lower rotor
1°	$3.423 \cdot 10^6$	$3.256 \cdot 10^6$
2/3°	$4.118 \cdot 10^6$	$3.918 \cdot 10^6$

4.5.2.4. Background

The UTA setups only differed in the rotor radius R. Therefore, the basic background grid structure was identical. As all numerical results were computed in hover, purely rotationally symmetric background grids were created. The radial node distribution used for the transfer grid was applied; see chapter 4.5.2.3. In the path of the tip vortices the grid was refined perpendicular to the vortex axis (Δs = 2.0% c); see blue region in Fig. 4.22. In addition, a structured grid was used in the rotor plane(s) and below the rotor to better resolve the trailed vortex sheets. Outside of these structured parts a mix of triangles and quads was employed. The farfield boundary was placed at a distance of r = 30 R from the rotor head of the upper rotor. Geometric grid dimensions are given in Fig. 4.22.

In contrast to the USNA background grid, the singularity at the center of rotation (i.e., the rotor shaft axis) was avoided by extending the cylindrical rotor hub structure to the farfield boundary above the rotor and a scaled down version to the lower farfield boundary; see Fig. 4.22 and chapter 4.5.2.2. Similar strategies have been pursued by other researchers [60, 62, 64, 73, 74, 75, 121]. The complete domain was only simulated for the CCR rotor; see Fig. 4.23b. To reduce the computational expense, symmetry boundary conditions were used for the two-bladed, and four-bladed single rotors and the stacked rotor computations, see Figs. 4.23a and 4.23c. In [157] it was shown that "no significant differences are observed demonstrating the validity of using single-bladed, periodic domain simulations"[157], even for simulating dynamic collective pitch actuation with a two-bladed rotor.

To test the influence of the extension of the refined vortex grid below the rotor, two different vertical extensions were created; compare Fig. 4.22a and 4.22b. The corresponding grid point counts are given in Table 4.12.

Table 4.12.: Background grid sizes for the UTA rotor simulations.

Rotor test rig	Rotor configuration	Δs_{az}	Vortex tracking	Grid points
CCR	2-by-2	1°	small	$49.062 \cdot 10^6$
CCR	2-by-2	$\frac{2}{3}$°	small	$73.592 \cdot 10^6$
CCR	2-by-2	1°	large	$61.197 \cdot 10^6$
CCR	2-bladed single	1°	small	$24.978 \cdot 10^6$
Stacked	2-by-2	$\frac{2}{3}$°	small	$39.155 \cdot 10^6$
Stacked	2-bladed single	1°	small	$26.151 \cdot 10^6$
Stacked	4-bladed single	1°	small	$13.148 \cdot 10^6$

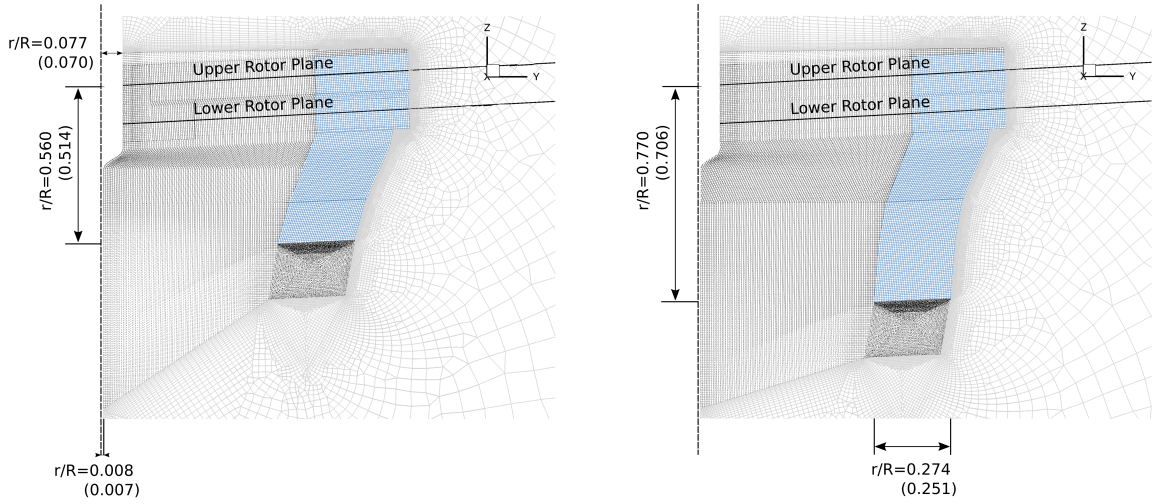

(a) Small vortex tracking grid.

(b) Large vortex tracking grid.

Figure 4.22.: Schematic showing sectional cuts through the UTA rotor background grids, for different vortex tracking grid sizes. High resolution grid regions ($\Delta s = 2\%$ c) for improved tip vortex preservation are shown in blue, structured regions in black, and unstructured regions in gray. Reference lengths are given for the CCR rotor and in brackets for the stacked rotor.

4.5.2.5. Grid Assembly

Schematics of the assembled grids for the single rotor, stacked rotor, and CCR rotor simulations based on the UTA rotor test stands are shown in Fig. 4.23. The differences caused by adding a second rotor plane (stacked and CCR rotor) and using symmetry boundary conditions (two-bladed single and stacked rotor) are illustrated. The overall grid dimensions are listed in Table 4.13.

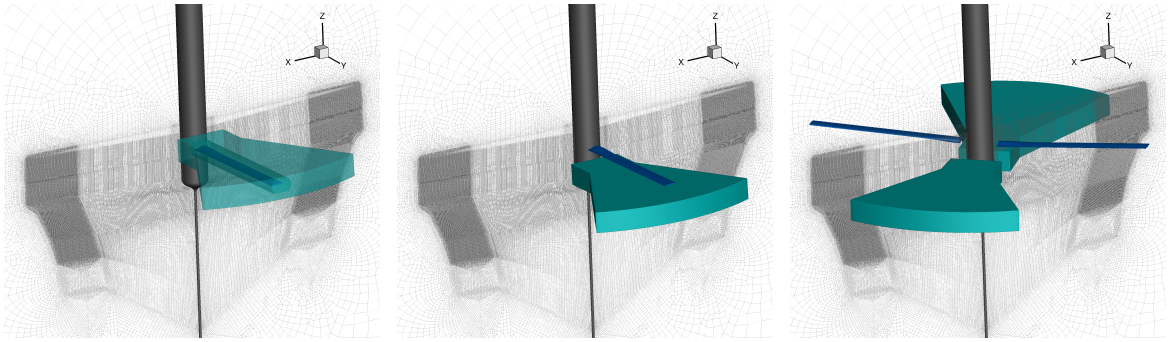

(a) Two-bladed single rotor. Grid on symmetry boundary condition shown in gray.

(b) Stacked rotor at index angle $\phi = 0°$. Grid on symmetry boundary condition shown in gray.

(c) CCR rotor at index angle $\phi = 45°$. Grid in vertical cut through background grid shown in gray.

Figure 4.23.: Schematic showing the assembled grids for the UTA rotor configurations: (a) two-bladed single rotor, (b) stacked rotor, and (c) CCR rotor. The transfer block outer chimera boundary is shown in green, the rotor blade is shown in blue, and the cylindrical rotor hub in black.

Table 4.13.: Overview of grid sizes for the UTA rotor simulations.

Grid name	Rotor test rig	Rotor configuration	Δs_{az}	Vortex tracking	Grid points
GCCR1	CCR	2-by-2	1°	small	$92.390 \cdot 10^6$
GCCR2	CCR	2-by-2	$\frac{2}{3}$°	small	$119.635 \cdot 10^6$
GCCR3	CCR	2-by-2	1°	large	$104.526 \cdot 10^6$
GCCRS	CCR	2-bladed single	1°	small	$35.894 \cdot 10^6$
GSta1	Stacked	2-by-2	$\frac{2}{3}$°	small	$62.176 \cdot 10^6$
GStaS2	Stacked	2-bladed single	1°	small	$37.067 \cdot 10^6$
GStaS4	Stacked	4-bladed single	1°	small	$24.064 \cdot 10^6$

4.5.2.6. Grid and Temporal Sensitivity Study

Based on the grids described in chapters 4.5.1.1 to 4.5.2.4 a grid and temporal sensitivity study was made[5]. The viscous flow calculations were performed with the one-equation SA-neg-RC turbulence model. A detailed description of the numerical setup is given in chapters 4.1 to 4.4.2. The numerically most challenging rotor configuration (i.e., the two-by-two-bladed CCR rotor with inter-rotor vortex interactions, blade passage, and short duration BVI events) was chosen. It was expected that these results could be transferred best to the other, less challenging, configurations. This assumption was primarily based on the fact that short duration BVI events are most challenging for temporal convergence and require the highest spacial resolution to resolve the interaction properly. Moreover, the flow fields of CCR rotors also showed most vortex interactions below the lower rotor plane compared to all other rotor configurations simulated in this thesis; compare Figs. 6.11 and F.4 with Figs. 6.33 and G.2. The rotor was trimmed to $C_T/\sigma = 0.085$. See chapter 4.6 for a description of the trim process.

Different temporal resolutions ($\Delta\psi_b = 0.125°$, $0.25°$, $0.5°$, $0.6\overline{6}°$, $1.0°$) were tested in combination with different inner iteration counts (25, 50, 100). The higher temporal resolutions ($\Delta\psi_b \leq 0.25°$) agreed with established time-step sizes in the literature; $\Delta\psi_b = 0.5°$ [120], $\Delta\psi_b = 0.3\overline{3}°$ [39], $\Delta\psi_b = 0.25°$ [130, 59, 165, 166], $\Delta\psi_b = 0.125°$ [73, 74]. The same was true for the inner iteration count. While the time-step size is driven by the requirement to resolve flow physical phenomena, the inner iteration count is dependent on the flow solver settings.

All simulations were trimmed using a large initial time-step of $\Delta\psi_b = 1.5°$, and were subsequently run for one revolution with the fine time-step and inner iteration count, i.e., for four blade crossings and BVI events. Trimming resulted in identical collective pitch angle settings for all simulations; $\Theta_{0,u} = 9.30°$ and $\Theta_{0,l} = 9.56°$. The sensitivity of the solutions to the different parameter combinations were assessed based on thrust, torque and Normalized Density Residual (Rrho) time histories. Furthermore, the conservation of vorticity, the effects on Q-criterion isosurfaces during BVI, and the evolution of tip vortex swirl velocity profiles were considered; see Figs. 4.24 to 4.28.

[5] In the grid and temporal sensitivity study an inter-rotor spacing of $\Delta z_r = 14.0\%$ R instead of the $\Delta z_r = 13.8\%$ R was used; see chapter 3.2.2. It was assumed that the validity of the study was not affected by this difference. The correct value of $\Delta z_r = 13.8\%$ R was used during the rest of the thesis.

Grid **GCCR2** was used to investigate the effects of time-step size and inner iteration count variations; see Figs. 4.24. A time step of $\Delta\psi_b = 1.0°$ was adequate for trimming the rotor, but proved insufficient in terms of density residual reduction and properly computing blade vortex interactions, regardless of the inner iteration count. It lead to significant vortex deformation during BVI. All other time steps produced comparable results for the thrust and torque time histories; see Figs. 4.24a and 4.24b. Larger influences were observed for the density residual reduction; see Fig. 4.24c. Here, a time-step of $\Delta\psi_b = 0.125°$ with 25 inner iterations was performing best. The azimuthal resolution and size of the vortex tracking grid did not show any significant influences on the three parameters; see Fig. 4.25.

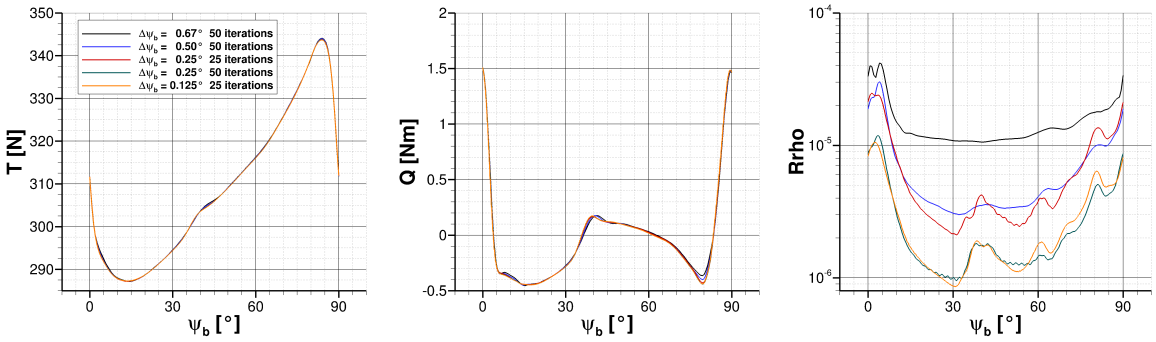

(a) Rotor thrust. **(b)** Rotor torque. **(c)** Normalized density residual.

Figure 4.24.: Evaluation of the effects of time step size ψ_b and inner iteration count per time step on the numerical simulation results for the UTA CCR rotor with background grid **GCCR2**. Data shown over one quarter of a revolution. Blade crossings at $\psi_b = 0°$ and 90°.

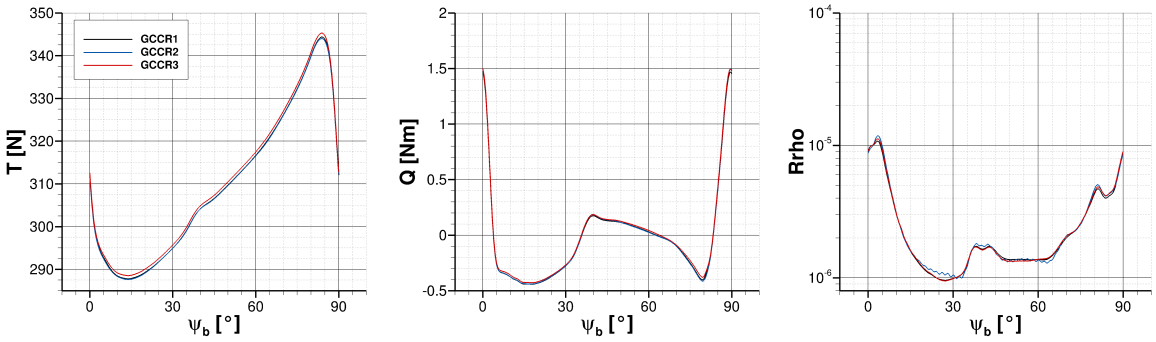

(a) Rotor thrust. **(b)** Rotor torque. **(c)** Normalized density residual.

Figure 4.25.: Evaluation of the effect of background grid resolution on the numerical simulation results for the UTA CCR rotor with three different background grid resolutions at $\Delta\psi_b = 0.25°$ and 50 inner iterations per time step. Data shown over one quarter of a revolution. Blade crossings at $\psi_b = 0°$ and 90°.

When comparing out of plane vorticity contours and Q-criterion isosurfaces during BVI similar conclusions could be drawn. A reduction in time-step size and increase in inner iteration count resulted in improved vorticity conservation. This lead to more distinct vortex cores below the lower rotor plane and more compact vortices during BVI; compare e.g. Figs. 4.26a and 4.26d. The large vortex tracking grid did not prove to be advantageous compared to the smaller grid; compare **GCCR1** and **GCCR3** in Figs. 4.27a and 4.27c. An increased azimuthal resolution did prove to

be advantageous in terms of vortex preservation and during BVI, although the effect was small; compare **GCCR1** and **GCCR2** in Figs. 4.27a and 4.27b.

Moreover, tip vortex swirl velocity profiles were compared at different wake ages; see Fig. 4.28. Data was extracted at an index angle of $\phi = 0°$, i.e., during blade passage, for multiple wake ages of the upper (ζ_u) and lower (ζ_l) rotor. In Fig. 4.28a the effects of various time step settings are shown. Noticeable differences could only be observed for the upper rotor tip vortex at $\zeta_u = 150°$. Converged solutions were found for time step sizes of $\Delta\psi_b = 0.5°$ and $\Delta\psi_b = 0.25°$, while the peak-to-peak velocity amplitude was lower for larger time steps. At the youngest vortex shown ($\zeta_u = 30°$) and for the lower rotor tip vortex ($\zeta_l = 270°$) differences caused by time step settings were considered negligible. Also, the radial location was not affected by variations of $\Delta\psi_b$. The spacial convergence of the solutions was investigated for the same vortex locations in Fig. 4.28b. It was found that the swirl velocity profiles were not influenced by the length of the vortex tracking grid (compare **GCCR1** and **GCCR3**), while the peak-to-peak velocity and radial location differed when increasing Δs_{az} (compare **GCCR1** and **GCCR2** at $\zeta_l = 270°$). This vortex formed during blade passage (four blade passages per revolution for the two-by-two-bladed rotor, i.e., every $\Delta\psi_b = 90°$), and hence, a higher azimuthal resolution did influence the vortex conservation to some extend in a coaxial rotor configuration. To assess the influence of the spacial resolution on the vortex conservation in single-rotor configurations, tip vortices which formed at the maximum distance from blade passage (and approximately from the location of BVI at the particular blade loading; see Figs. 4.26 and 4.27) were investigated; see Fig. 4.28b. It was found that for these vortices, neither the tip vortex strength nor the radial location was influenced by Δs_{az}.

Based on the grid and temporal sensitivity study it could be concluded that noticeable effects were visible during BVI, and were caused by inter-rotor vortex interactions. Therefore, the strictest limitations in terms of azimuthal grid resolution, time-step size, and inner iteration count only applied for the CCR rotor simulations. For single rotor computations, these limits could be lowered, as was shown previously by the author by comparison to experimental data[113, 102]. As result of the sensitivity study, all coaxial rotor simulations were made based on **GCCR2**, i.e., an azimuthal grid resolution of $\Delta s_{az} = 0.66^{\circ}$ along with the small vortex tracking grid; see Table. 4.13 and Fig. 4.22. To properly capture BVI events of the CCR rotor a time step size of $\Delta\psi_b = 0.25°$ along with 25 inner iterations were chosen[6]. For the stacked rotor $\Delta\psi_b = 0.5°$ and 25 inner iterations per time step were selected, as no short duration BVI events occur when both rotors rotate in the same direction. All single rotor simulations were made with an azimuthal spacing of $\Delta s_{az} = 1.0°$, $\Delta\psi_b = 0.5°$ and 25 inner iterations per time step.

[6] In chapter 6.1.2 50 inner iterations were used when comparing different turbulence models for the CCR rotor at $C_T/\sigma = 0.085$.

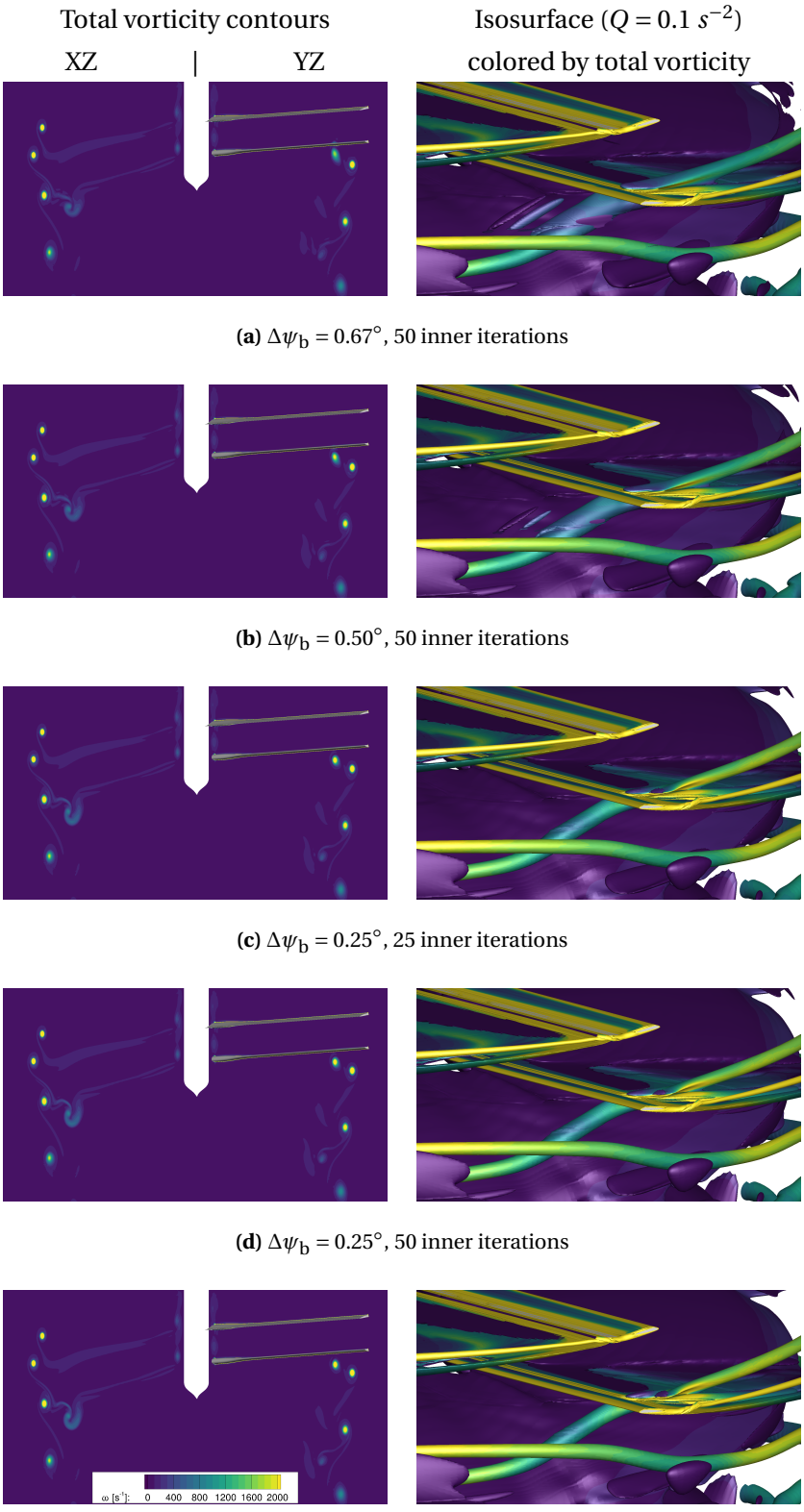

(a) $\Delta\psi_b = 0.67°$, 50 inner iterations

(b) $\Delta\psi_b = 0.50°$, 50 inner iterations

(c) $\Delta\psi_b = 0.25°$, 25 inner iterations

(d) $\Delta\psi_b = 0.25°$, 50 inner iterations

(e) $\Delta\psi_b = 0.125°$, 25 inner iterations

Figure 4.26.: Visualization of the effects of temporal resolution on the computed flow field of the UTA CCR rotor. Flow solution computed with grid **GCCR2**. Images extracted during blade crossing ($\phi = 0°$). Vorticity contours shown in two perpendicular vertical planes through the rotor shaft axis (XZ- and YZ-plane).

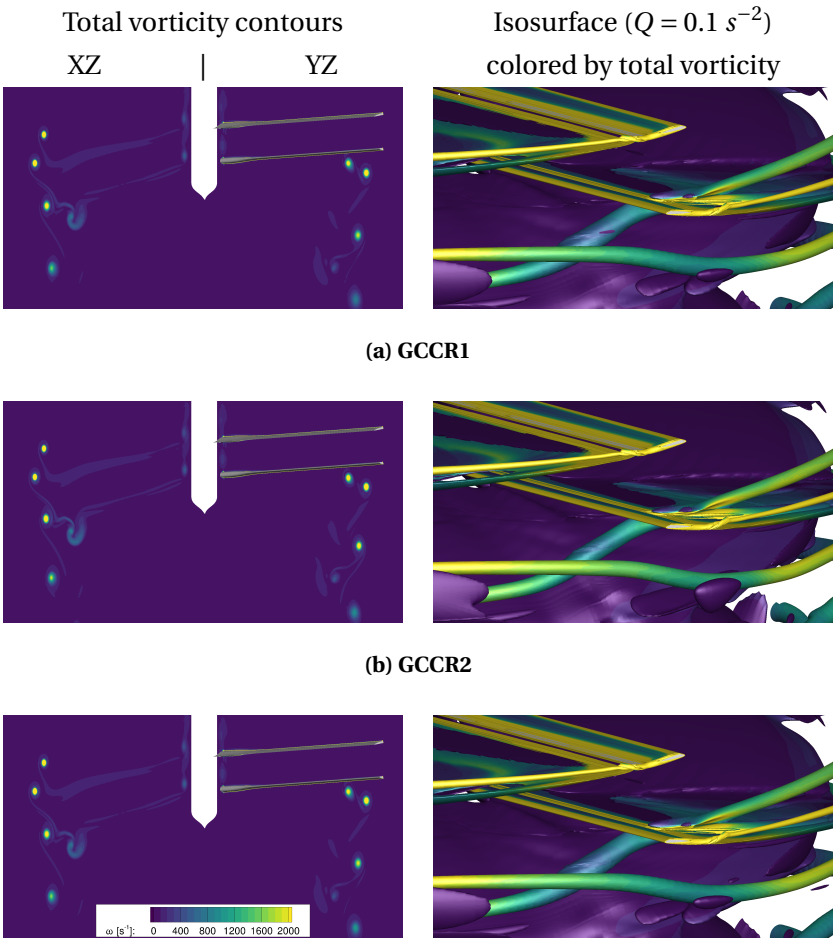

(a) GCCR1

(b) GCCR2

(c) GCCR3

Figure 4.27.: Visualization of the effects of grid resolution on the computed flow field of the UTA CCR rotor. Flow solution computed with a time step size of $\Delta\psi_b = 0.25°$ and 50 inner iterations. Images extracted during blade crossing ($\phi = 0°$). Vorticity contours shown in two perpendicular vertical planes through the rotor shaft axis (XZ- and YZ-plane).

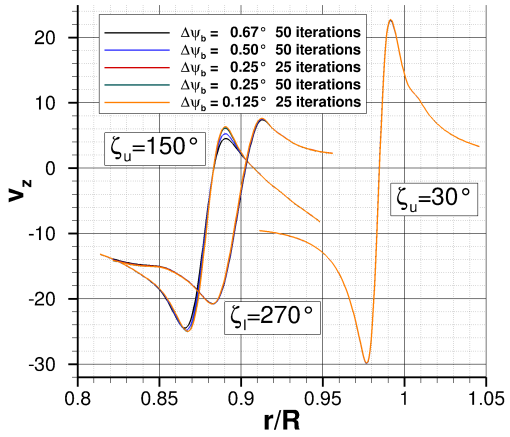

(a) $\Delta\psi_b$ variation, **GCCR2**.

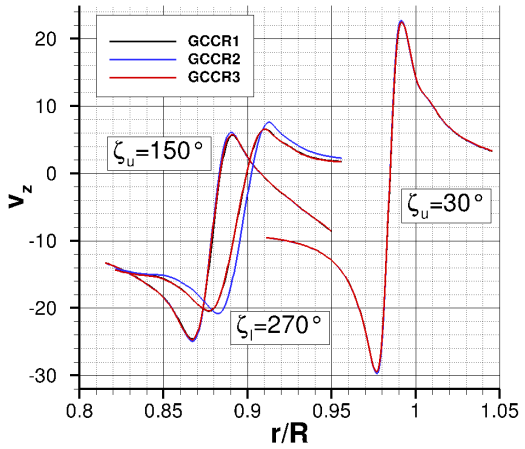

(b) Δs_{az} variation, $\Delta\psi_b = 0.25°$ and 50 inner iterations per time step.

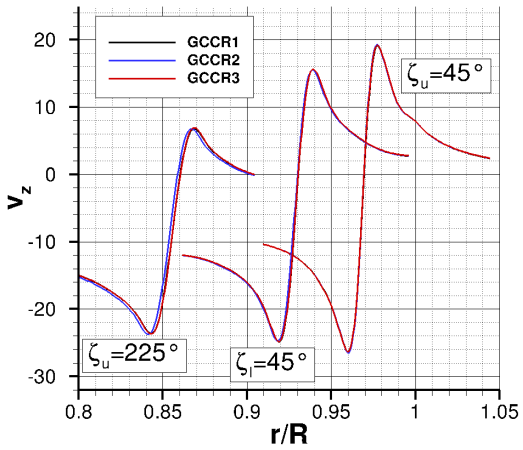

(c) Δs_{az} variation, $\Delta\psi_b = 0.25°$ and 50 inner iterations per time step.

Figure 4.28.: Evaluation of the effects of grid and temporal resolution on the vortex conservation for the UTA CCR rotor simulations. Axial velocity profiles (v_z) are shown over non-dimensional radial distance to rotor shaft (r/R) for different wake ages of the upper (ζ_u) and lower rotor (ζ_l). Data extracted during blade passage, i.e., $\phi = 0°$.

4.6. Trim

Trimming a rotorcraft in numerical simulations requires the calculation of blade pitch controls, blade flapping (rotor disk orientation), rotor or control system elastic deformations, and overall rotorcraft orientation for the flight condition to be computed. In general, it is required to adjust the force and moment components in all three axes. For a conventional helicopter with one main and one tail rotor, four independent controls are used for this purpose: the collective pitch Θ_0, the lateral cyclic pitch Θ_{1c}, the longitudinal cyclic pitch Θ_{1s}, and the tail rotor collective pitch Θ_{TR}. Rotorcraft in general are characterized by strong cross-coupling of the forces and moments when either of the control inputs is applied. Therefore, trimming a rotorcraft is an iterative calculation, until all influences of the involved components are in equilibrium.[81]

In the study at hand the problem was greatly simplified as isolated rotors were investigated. Therefore, it was not required to control the orientation of the rotorcraft. Furthermore, the rotors were investigated in hover with the moment reference points in the rotor hub. The roll and bank moments were set to zero and consequently, the cyclic controls were not used for trimming ($\Theta_{1c} \equiv \Theta_{1s} = 0°$). Only the collective pitch (Θ_0) control input was required. Moreover, the rotor blades were modeled to be infinitely rigid. Hence, the computations of control system or rotor blade elastic deformations were not included in the simulations. Trim targets were blade loading coefficients (C_T/σ), and additionally for the CCR rotor a torque balance between the upper and lower rotor (Q_u and Q_l).

In the subsequent simulations, the rotor thrust trim target was set to be within 1% of the respective target blade loading. This threshold was considered sufficient to be able to compare the numerical simulation results to the available experimental data and to draw conclusions when comparing to other numerical results[73].

Additional aspects with regard to the particular configurations of the UTA rotor setups and the desired conclusions that shall be drawn from the simulations are as follows:

CCR rotor The numerical simulations for the CCR rotor were made prior to a corresponding experimental campaign. Therefore, the threshold value for torque balance used in the experiments was not yet known. Setting the collective pitch angles used in the experiments, as for example done in [59], was not possible. Consequently, results from other researchers were used as an indicator for an appropriate threshold value. In some studies the threshold was not quantified [164, 165], or it was simply stated that the absolute values of the upper rotor and lower rotor torque were equal[123, 66]. More precise definitions could be found in other publications, where relative torque differences of the lower rotor compared to the upper rotor of $\leq 0.1\%$[166], $\leq 1.0\%$[7, 73], up to $\leq 5.0\%$[74, 106] were reported. In [74] a rotor at fixed pitch using RPM variations for torque balancing was investigated. It was found that an increased threshold value for torque balance of $\leq 5.0\%$ affected the simulation accuracy only marginally. Furthermore, an experimental study found that a torque unbalance of up to 5% did not affect the rotor performance[17]. Based on these findings, the following condition was used to define torque balance of the CCR rotor in this thesis:

$$\left| \frac{|Q_l|}{|Q_u|} - 1 \right| \leq 0.01 \tag{4.1}$$

Stacked rotor For stacked rotor configurations both rotor planes are rotating in the same direction. Therefore, no torque balance can be achieved on the rotor assembly level. However, the upper and lower rotor collective pitch angles can be used to change the thrust distribution between the two rotor planes and therefore, a large number of trim targets can be defined based on, e.g., power consumption, vibration, or noise. In the current study, it was decided to set the same collective pitch angles for the upper and lower rotor plane ($\Theta_{0,u} \equiv \Theta_{0,l}$). This allowed examining the effects caused by stacking two rotor planes on top of each other (two-by-two-bladed configuration) in comparison to the equivalent single rotor at identical collective pitch angle (four-bladed configuration). To enable a better comparability to available two-bladed single rotor measurements, the upper rotor thrust at an index angle of $\phi = 0°$ was trimmed to the value of the two-bladed single rotor. The thrust of the lower rotor and the four-bladed rotor was therefore a consequence of the trim strategy and not a trim target. Moreover, to assess the effects of varying the index angle ϕ on thrust, torque and the flow field, the collective pitch angle was not altered for other configurations ($\phi \neq 0°$) compared to the baseline case at $\phi = 0°$.

Dynamic actuation For all cases where dynamic Θ_0 or RPM inputs were commanded, the rotor forces and moments were allowed to freely respond to the inputs. As the hub remained fixed, the rotor assembly did not accelerate. In comparison to a real rotorcraft the test stand was not allowed to respond to the inputs by changing its location, velocity, or orientation in space. Also changes in the torque balance of the CCR rotor were not corrected for by adjusting the control inputs.

5. Rotor Aerodynamics in Non-Parallel Ground Effect

The influence of inclined ground planes on the flow fields of rotors in hover was assessed by investigating two different ground plane inclination angles ($\Theta_{GP} = 0°$ and $\Theta_{GP} = 15°$). To complement the results the rotor was also studied in hover OGE. Throughout the following discussions the same coordinate system was used for all test cases (see Figs. 3.2 and 3.4). The rotor head was located at $z/R = 1.0$ and the ground plane pivot point at $z/R = 0$. To simplify the discussion, the terms *uphill* ($r/R < 0$) and *downhill* ($r/R > 0$) were used for all cases, even though they do not have any significance for the parallel ground plane and OGE; see Fig. 3.2. A first study on this topic was published by the author and the experimenter[112] based on experimental results first published in [99]. The subsequently shown results are an extension of this work, including new computational grids, an assessment of different turbulence models, and a more in depth data evaluation of the experimental results. Details on the used grids are given in chapter 4.5.1, a description of the turbulence models is given in chapter 4.4, and the experimental configuration and flow field measurements are described in chapter 3.1. For all simulations the inverse fourth order dissipation coefficient was 64 and the second order dissipation coefficient was 0.1 (SSG-LRR-ω: 0.5) for the employed matrix dissipation scheme. A least square approach was used for the reconstruction of gradients.

The experiment was not trimmed to specific thrust values, but rather collective pitch angles (Θ_0) were set. This resulted in different thrusts for the three cases. The numerical simulations were trimmed as described in chapter 4.6. Trim results are given in Tables 5.1 and 5.2. The OGE simulations were ran for at least 16 revolutions, the IGE simulations with $\Theta_{GP} = 0°$ for 18 revolutions, and at $\Theta_{GP} = 15°$ for 23 revolutions. These numbers were required to transport the starting vortex out of the rotationally symmetric background grid shown in Fig. 4.9. To reduce computational cost and to reduce detrimental influences of the starting vortex on the simulation results (among other things, excessive tip vortex growth and tip vortex diffusion) the $\Theta_{GP} = 15°$ case was not started from scratch. After 15 initial rotor revolutions in parallel ground effect, the ground plane inclination was increased with a '1 – Cosine' function over four rotor revolutions. The rotor flow fields showed only little variation between consecutive revolutions, as shown for hover IGE at $\Theta_{GP} = 15°$ in Fig. E.1 and variations in rotor thrust between consecutive revolutions were within the desired trim target. It has to be noted however, that vortex preservation degraded when computing additional revolutions after inclining the ground plane, especially for the SA-neg-RC model; see Fig. E.1a. Only the SSG-LRR-ω model showed comparable performance over multiple revolutions; see Fig. E.1d. Moreover, neither of the computed flow solutions IGE at $\Theta_{GP} = 15°$ showed clear periodic behavior in the rotor forces and moments within the number of simulated revolutions; see Fig. 5.21.

Table 5.1.: Comparison of thrust coefficient (C_T) between experiment and CFD for the USNA experiment. Numerical thrust values were averaged over one rotor revolution.

Test case	Experiment*	SA-neg-RC	SST-RC	SST-SAS-RC	SSG-LRR-ω	RQEVM	LEA
OGE	0.00350	0.00349	0.00349	0.00350	0.00347	0.00349	0.00349
IGE $\Theta_{GP} = 00°$	0.003877	0.00384	0.00389	0.00389	0.00385	0.00384	0.00394
IGE $\Theta_{GP} = 15°$	0.003565	0.00355	0.00356	0.00354	0.00356	-	-

* Rotor was tested at constant pitch, therefore, the thrust varied slightly for the different tested configurations (i.e., the rotor was not trimmed to a specific thrust)[99].

Table 5.2.: Comparison of collective pitch angle (Θ_0) between experiment and CFD for the USNA experiment.

Test case	Experiment[1]	SA-neg-RC	SST-RC	SST-SAS-RC	SSG-LRR-ω	RQEVM	LEA
OGE	6.6°	7.205°	7.185°	7.19°	7.14°	7.185°	7.15°
IGE $\Theta_{GP} = 00°$	6.0°	7.00°	7.00°	6.95°	6.95°	6.95°	6.95°
IGE $\Theta_{GP} = 15°$	6.0°	6.80°	6.75°	6.70°	6.75°	-	-

All simulations except for the LEA turbulence model in parallel ground effect reached the desired trim target (rotor thrust was averaged over the last computed revolution). For this particular simulation the thrust started to increase over the last computed revolution, after trimming the simulation before. Moreover, due to the in comparison inferior performance of the RQEVM and LEA turbulence models, they were not used to compute flow solutions at $\Theta_{GP} = 15°$. The effect of using different turbulence models on the required pitch angles was little, despite major differences in the ability to preserve the tip vortices, as will be shown in the subsequent sections. The experimental pitch settings were overpredicted in all simulations. The maximum difference in Θ_0 between turbulence models was observed IGE at $\Theta_{GP} = 15°$ between the SA-neg-RC and SST-SAS-RC turbulence model with $\Delta\Theta_0 = 0.1°$; see Table 5.2. For a definite explanation of the observed deviation between experimental and computational Θ_0 values additional investigations are required. Due to the, in good approximation, constant offset of Θ_0 in the numerical simulations for the individual configurations, it was assumed that a systematic deviation was present. A similar behavior, i.e., an increased collective pitch angle compared to the experiment at a given trim condition, was observed by other researchers using a free-wake aerodynamic solver[108].

5.1. Flow Field

A comparison between the predictive performance of the various turbulence models and the experimental results is shown in Fig. 5.1, where contours of time-averaged in plane velocity magnitude, superimposed by streamlines, are plotted. For the experimental results, images were recorded at increments of $\Delta\psi_b = 10°$. Averaging was made with ten images per azimuth. The numerical results were averaged over one rotor revolution at increments of $\Delta\psi_b = 3°$, as variations between successive revolutions were small. The minor excursions in the slipstream boundary visible in the numerical results were caused by this relatively low sample size. As the plane of data extraction was located behind the trailing edge of the downhill facing blade (see Fig. 3.5) no symmetry in the results can be expected despite the symmetric configurations for OGE and IGE at $\Theta_{GP} = 0°$.

The experimental results showed the well known behavior for OGE (contraction of the rotor slipstream boundary) and the parallel ground plane (expansion of the rotor slipstream after an initial contraction); see Fig. 5.1a. Both results showed the expected, almost symmetrical behavior. For the OGE case, a comparatively small recirculation region formed below the rotor hub. For the parallel ground plane, two large, distinct recirculation regions were visible in the interrogation plane. These extended from the ground plane to the rotor hub.

Inclining the ground plane caused the flow topology to become asymmetric. The stagnation point on the ground plane shifted uphill. As for the other two cases, the slipstream boundary was well defined. As a consequence of inclining the ground plane the downhill slipstream boundary was lifted significantly further off the ground compared to the parallel ground plane. Furthermore, a ground plane parallel flow formed which was strongly biased towards the downhill side[1]. When comparing both IGE cases, differences in the slipstream boundaries were more pronounced on the uphill side. Also, the recirculation region below the rotor hub changed and showed more similarity with the OGE case than the $\Theta_{GP} = 0°$ measurement. A further discussion of the shift of the stagnation point is given in chapter 5.5.1, in which the flow at the ground plane was investigated in more detail based on simulation results.

For the numerical results of the OGE case a comparable recirculation region formed below the rotor hub for all tested turbulence models. Close to the rotor hub ($z/R = 1.0$) the experimental data showed higher velocities compared to the numerical simulations and a larger extension of this region. Hence, the chosen rotor head modeling strategy (Fig. 4.6) along with the numerical settings (discussed in chapter 4) did not fully model the unsteadiness of the flow field here. A more detailed geometrical model of the rotor head could potentially improve the numerical results close to the rotor hub. This was also observed for the IGE simulations. However, the flow field at the rotor hub was not of particular interest in the current study and thus, no further investigations were made with regard to this topic.

[1] The shift in the stagnation point was previously seen using a free-wake solver combined with a panel code[54]. However, based on the published data for a two-bladed rotor operating at $z/R = 1.5$ at $\Theta_{GP} = 25°$ the significantly lifted slipstream boundary on the downhill side was not observed

For the IGE simulations at $\Theta_{GP} = 0°$ two large distinct recirculation regions formed, similar to those experimentally observed. However, they differed in their axial extension. Closest qualitative agreement between experiment and simulation was achieved with the SA-neg-RC and SSG-LRR-ω turbulence models. Furthermore, a smaller additional recirculation regimes formed close to the rotor plane on the uphill side for all turbulence models. This second set of small recirculation regimes was only allusively seen in the experiment.

At $\Theta_{GP} = 15°$ all turbulence models showed a comparable behavior, and were in close agreement with the experimental results. In particular, the observed shift of the stagnation point on the ground was well predicted. Also the location of the slipstream boundary was well comparable to the experimental values. Best qualitative agreement was found for the SA-neg-RC and SSG-LRR-ω turbulence models. Differences in the shape of the recirculation region below the rotor hub were more pronounced for the SST-RC and SST-SAS results.

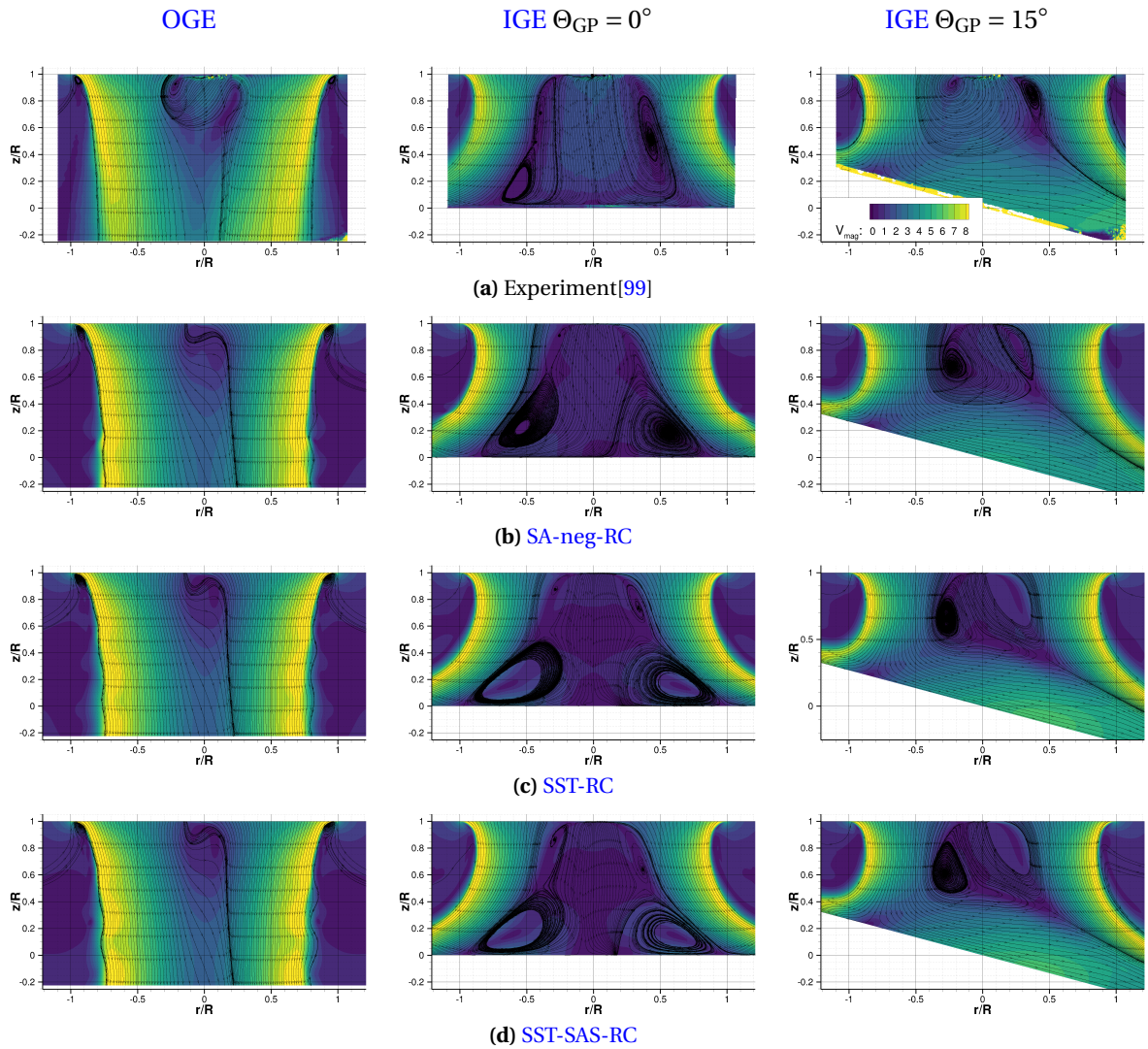

(a) Experiment[99]

(b) SA-neg-RC

(c) SST-RC

(d) SST-SAS-RC

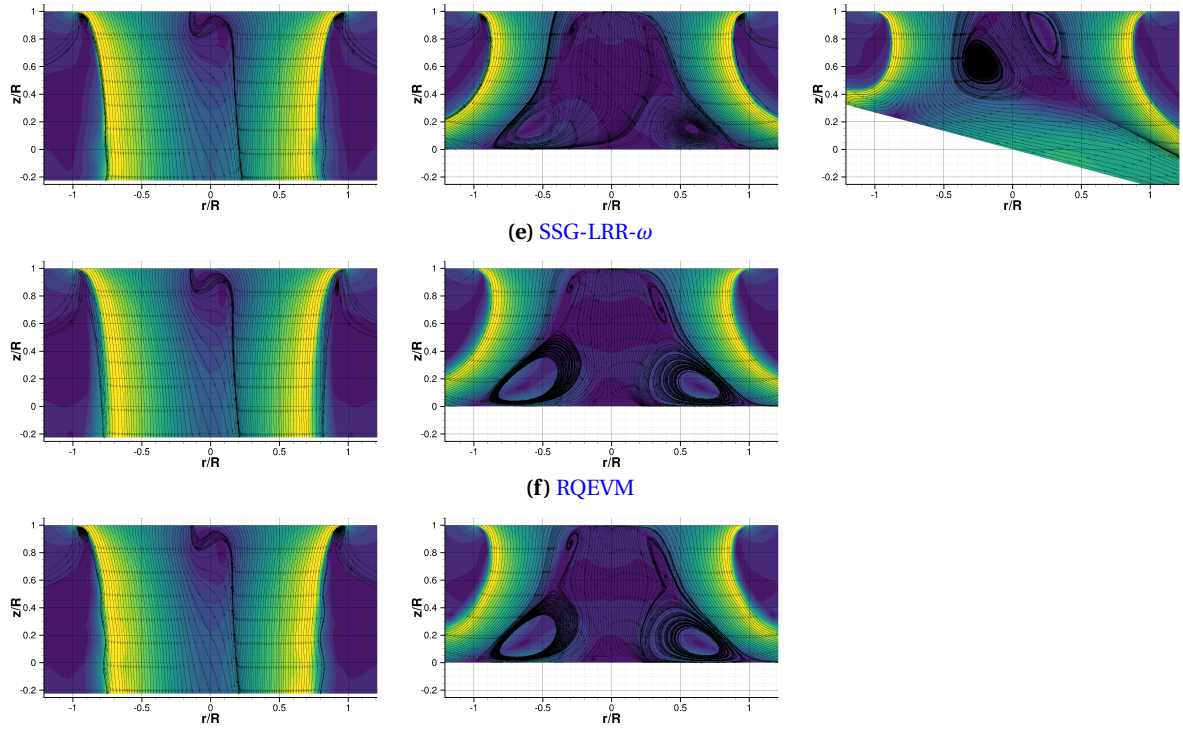

(e) SSG-LRR-ω

(f) RQEVM

(g) LEA

Figure 5.1.: Comparison of time-averaged contours of in-plane velocity magnitude between experiment and simulations for the USNA rotor, superimposed by streamlines of the in-plane velocity field. Experimental results recorded in increments of $\Delta\psi_b = 10°$ (10 images per azimuth). Numerical data averaged over one rotor revolution in increments of $\Delta\psi_b = 3°$ (i.e., 120 slices). Data extracted in PIV plane, i.e., behind the trailing edge of the downhill facing blade; see Fig. 3.5. Note that no simulations were performed for the RQEVM and LEA turbulence models at $\Theta_{GP} = 15°$.

A more detailed visualization of the flow field is given by instantaneous out-of-plane vorticity contours shown in Fig. 5.2. For all assessed cases, the experimental data showed clearly defined vortices which persisted down to the ground plane for hover IGE; see Fig. 5.2a. It has to be noted that as different thrust values were recorded in the experiment for each case, no direct comparison between the strength of the vortices can be made based on vorticity; see Table 5.1. For hover OGE indicators for vortex bundling and wandering could be seen for older wake ages on the downhill side in the instantaneous image shown. A more detailed investigation into these phenomena is given in chapter 5.2.

All tested turbulence models predicted the vortex wake contraction correctly OGE, however, their ability to preserve the tip vortices differed drastically. For the RQEVM and LEA turbulence models a distinct concentrated vortex core was only visible for a wake age of $\zeta = 180°$, i.e., the youngest vortex shown in the contour plots. At older wake ages, the vortices were significantly distorted and dissipated. This was not in agreement with the experimental data. The other tested turbulence models performed significantly better. Using the SAS correction enabled the SST-SAS-RC turbulence model to preserve the tip vortices longer compared to the SST-RC model. Increased diffusion was observed below $z/R = 0.25$ as the region of highest refinement ended here; see Fig 4.9a. The most compact vortices were computed with the SSG-LRR-ω turbulence model, which served as an

indication that the Full Reynolds Stress Model preserved the tip vortices best.

For hover in parallel ground effect, the predictive capability of the various turbulence models were comparable to the OGE case. In particular the RQEVM turbulence model was not capable of preserving the tip vortices long enough, i.e., until they interact with the ground plane. However, the general trajectory (based on regions of increased vorticity) was computed well; see Fig. 5.2f. The LEA model performed better, but still considerably worse compared to the other turbulence models. This indicated that the general shape of the rotor slipstream was defined by the sheer presence of the ground plane, rather than the detailed structure of the wake. Best agreement between experiment and simulation was achieved with the SSG-LRR-ω model followed by the SA-neg-RC model.

The comparison between the experimental and predicted out-of-plane vorticity contours showed greater discrepancies for the inclined ground plane. Vortex preservation was significantly reduced at $\Theta_{GP} = 15°$ compared to $\Theta_{GP} = 0°$ for all tested turbulence models except for the SSG-LRR-ω model, i.e., the vorticity magnitude was lower and the vortices appeared more blurred and dissipated faster. This was not supported by the experimental results; see Fig. 5.2a. However, the vortex trajectories were computed well. The only model that showed comparable performance to OGE and IGE at $\Theta_{GP} = 0°$ was the SSG-LRR-ω model.

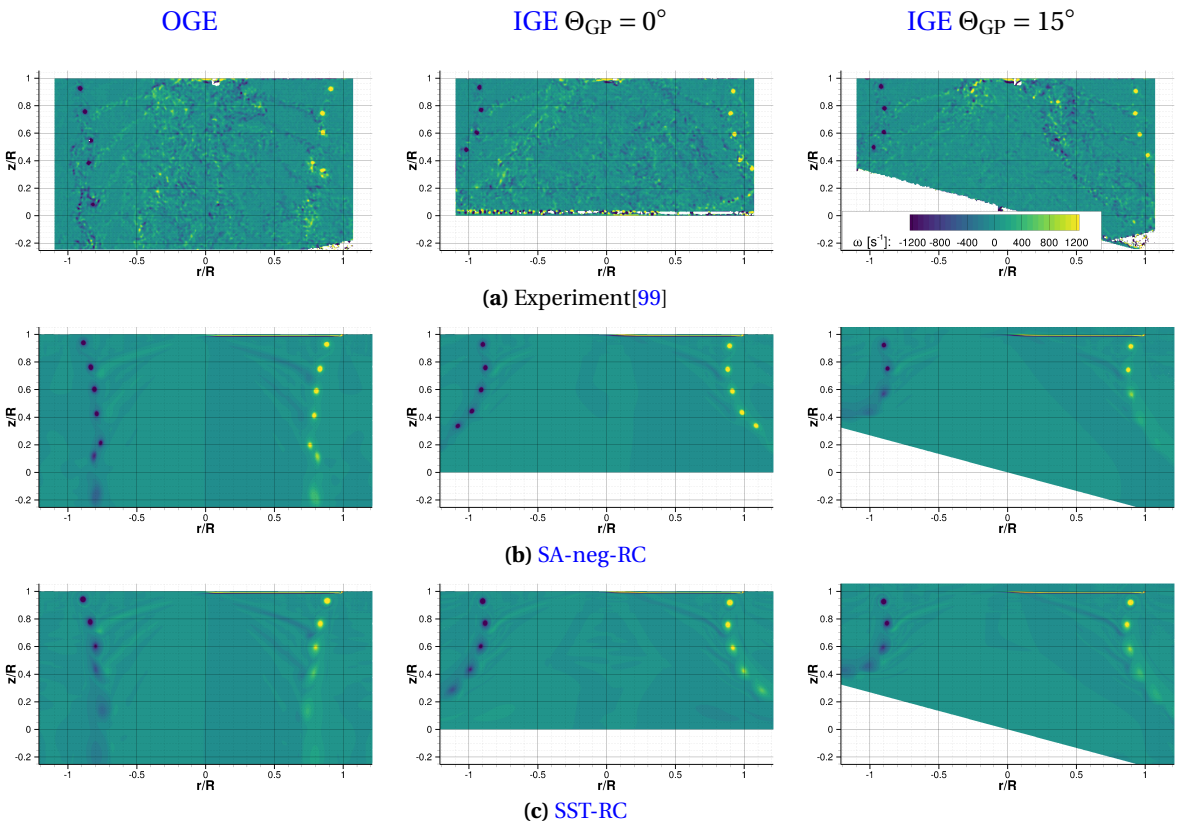

(a) Experiment[99]

(b) SA-neg-RC

(c) SST-RC

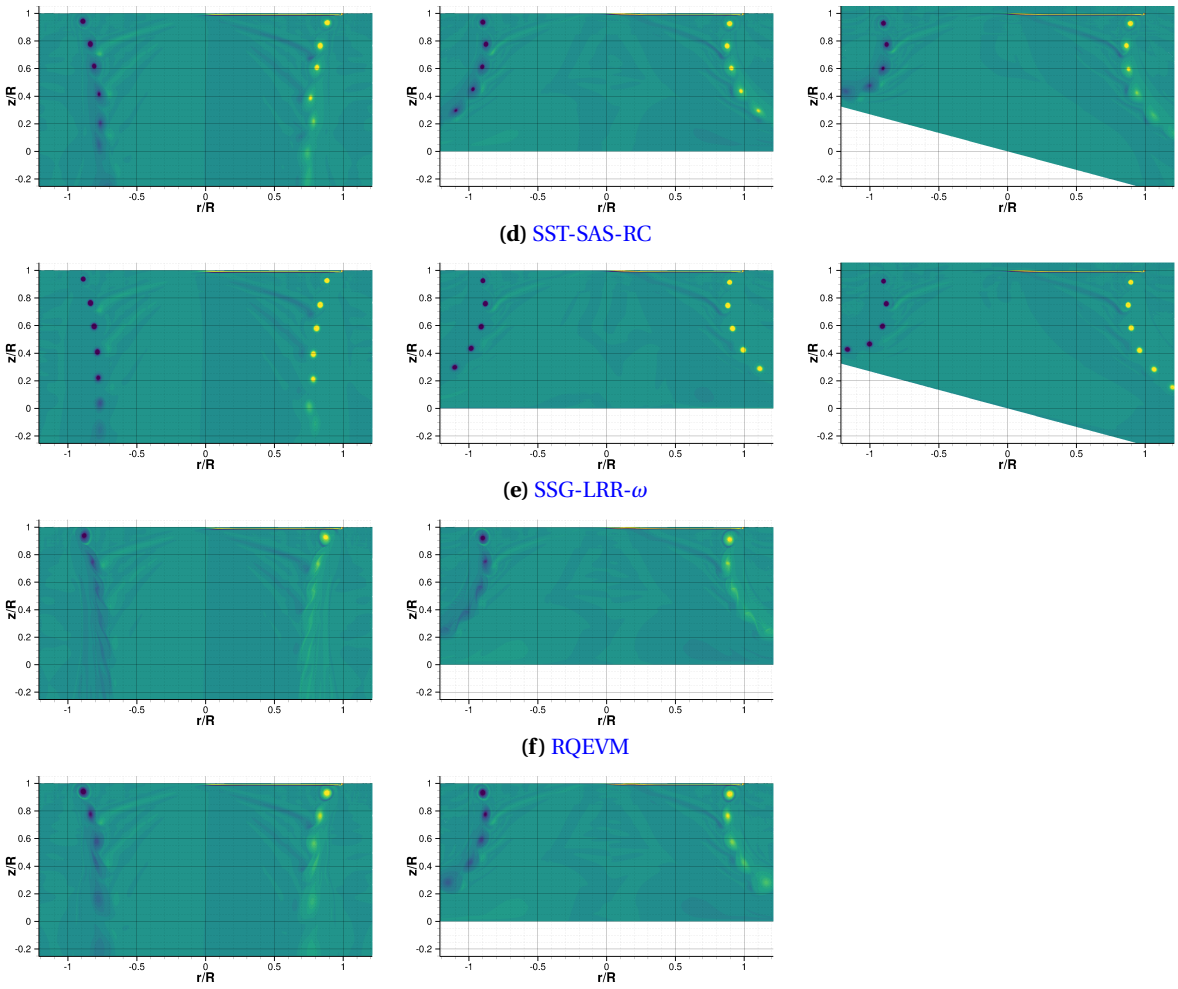

(d) SST-SAS-RC

(e) SSG-LRR-ω

(f) RQEVM

(g) LEA

Figure 5.2.: Comparison of out-of-plane vorticity contours between experiment and CFD simulations for the USNA rotor at $\psi_b = 0°$ of the reference blade. Data extracted in PIV plane, i.e., behind the trailing edge of the downhill facing blade; see Fig. 3.5. Note that no simulations were performed for the RQEVM and LEA turbulence models at $\Theta_{GP} = 15°$.

5.2. Tip Vortex Trajectories and Vortex Wandering

To quantify the qualitative findings from the out-of-plane vorticity contours discussed before, a comparison between the vortex center positions of the instantaneous flow field realizations with the numerically predicted locations was made. A description of the automated vortex center detection algorithm is given in chapter C. It is based on an algorithm first proposed in [96] and was described in [41]. The method looks only at the topology of the flow field and not at the magnitude and computes a dimensionless scalar quantity Γ_1 at each point in the flow field. For a vortex without distortion, e.g., an isolated potential vortex, $\Gamma_1 = 1.0$ is computed in the vortex center. The algorithm was adapted in the current study by using a minimum vorticity threshold to exclude small scale turbulence from the evaluation.

The dimensionless quantity Γ_1 was computed based on a square field around each data point in the data set with an edge length of ≈ 14 mm. A vortex center was detected if $\Gamma_{1,\min} \geq 0.75$ and the average vorticity in the square field was $\overline{\omega}_{\min} \geq 700\,s^{-1}$ for the experimental velocity vector fields. For the numerical simulations the size of the search field was identical, however, the threshold values were set to $\Gamma_{1,\min} \geq 0.70$ and $\overline{\omega}_{\min} \geq 450\,s^{-1}$. The average vorticity threshold could be reduced for the numerical simulations as less small scale fluctuations with large vorticity values were present in the simulation results compared to the experimental data; see Fig. 5.2. Numerical results were interpolated to a Cartesian grid with a resolution of $\Delta s = 1\%$ c before running the algorithm.

In Figs. 5.3 to 5.5 vortex center locations based on the experimental (500 PIV flow field realizations per case) and numerical results are shown in the experimental measurement plane; see Fig. 3.5. Wake ages up to $\zeta = 900°$ were included. If ambiguous vortex ages were detected, the corresponding vortex centers were not displayed. Furthermore, due to vortex wandering (vortex position possibly outside PIV ROI), vortex dissipation or vortex break-up the number of detected vortices for older wake ages was reduced. As the laser sheet was aligned with the trailing edge of the downhill blade, the wake ages of the tip vortices at the uphill blade are only approximate values; see Fig. 3.5. Moreover, on the downhill side, the vortices just passed below the rotor blade (downwash due to bound circulation), whereas on the uphill side the vortices were located in front of the leading edge of the rotor blade (upwash). For OGE and the parallel ground plane, this effect, caused by the location of the used measurement plane, could explain the asymmetry between uphill and downhill vortex center locations at the first blade passe; see Figs. 5.3 and 5.4.

The detected vortex center locations for hover OGE showed the typical characteristic for hovering rotors OGE. At first, a constant contraction of the trajectory was observed, while vortex wandering increased. At older wake ages a widening of the streamtube could be seen. At this stage "the tip vortices have begun to spin-down under the action of viscosity and turbulence. The older vortices in the far wake were also more susceptible to the development of instabilities and the pairing of adjacent turns of the helical wake"[141]. As a result, a turbulent far wake develops which causes the widening of the slipstream boundary. While being a qualitative explanation for the observed behavior of the tip vortices at older wake ages ($\zeta = 720°$), the large asymmetry between the uphill and downhill side could not fully be explained by this phenomenon; see Fig. 5.3. The number of identified vortex center locations as well as the general shape of the cluster of identified vortex centers, visualized by standard deviation ellipsoids in the plot, indicated significant differences. The exact cause of this discrepancy could not be identified based on the available data. Possible reasons could be differences in seeding and/or illumination in the PIV plane or recirculation in the test chamber. However, this statement must not be mistaken for a final conclusion on this topic, but should rather be regarded as a possible starting point for further analysis of the experimental data and future experiments.

Overall a good correlation between the numerical simulations and the experimental data was observed. The detected vortex centers were close to or within the ellipsoids enclosing 95.44% of the experimental instantaneous vortex center positions (2σ). The computed trajectories were therefore comparable to a single flow field realization observed in the experiment. As indicated by the out-of-plane vorticity contours (see Fig. 5.2) the SSG-LRR-ω and SA-neg-RC turbulence models preserved the tip vortices best, followed by the SST-SAS-RC model. As expected, vortex centers

could only be identified for the youngest wake ages with the RQEVM and LEA turbulence models, which further substantiates the finding that these models, along with the numerical settings used in this thesis, were not capable of predicting the flow physics correctly.

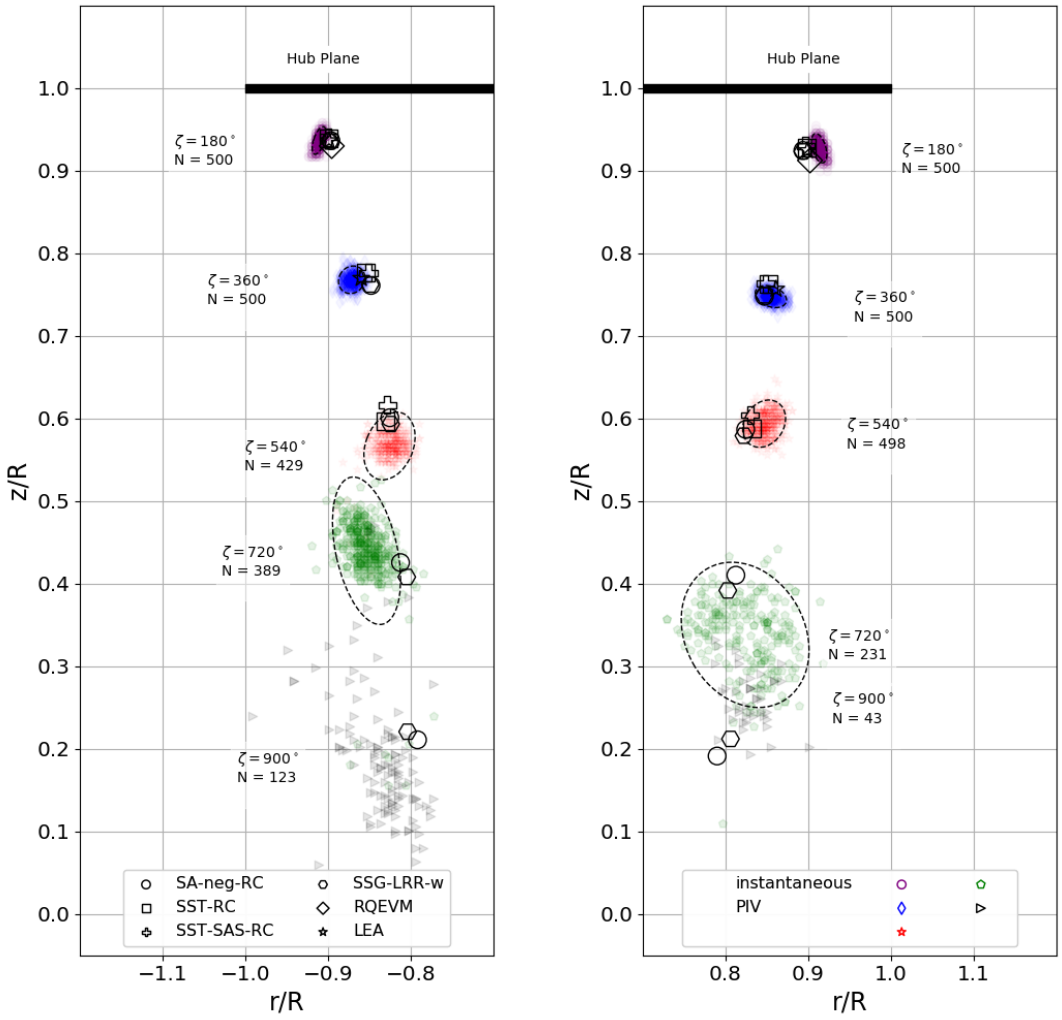

(a) uphill **(b)** downhill

Figure 5.3.: Instantaneous vortex center positions for hover OGE. Standard deviation ellipsoids (2σ) are shown for wake ages up to $\zeta = 720°$. Wake ages at the uphill side are approximate values; see Fig. 3.5. Identified number of vortex centers from experimental data (N) is indicated for each wake age.

For hover IGE at $\Theta_{GP} = 0°$ a clear influence of the ground plane on the vortex trajectories could be seen; see Fig. 5.4. Not only the typical contraction and expansion of the rotor wake IGE was observed, but also the clusters of detected tip vortex center locations were more compact at older wake ages. For younger wake ages the opposite was true, i.e., the presence of the ground plane increased the unsteadiness in the flow field compared to OGE in the experiment. Also, the preferred direction of wandering changed compared to hover OGE. As the motion in vertical direction was restricted by the ground plane, a dominant horizontal component of vortex wandering was found.

Again, at older wake ages, larger differences between the uphill and downhill side were observed in the experimental data. Correlation between the experimental and numerical results was slightly improved over the OGE case. The SSG-LRR-ω and SA-neg-RC turbulence models were able to preserve the tip vortices best (shown up to a wake age of $\zeta = 900°$). Most tip vortices were outside the ROI in the experiment at this wake age and only a limited number of points could be identified based on the available experimental data. For the sake of completeness, these were also plotted in Fig. 5.4 but must not be confused with giving the complete information at this wake age.

Inclining the ground plane to $\Theta_{GP} = 15°$ resulted in a considerable reduction of vortex wandering compared to $\Theta_{GP} = 0°$; compare Figs. 5.4 and 5.5. Here, vortex wandering was also restricted in the horizontal direction by the ground plane. Hence, the inclined ground plane reduced the unsteadiness in the flow field. The areas within which vortex centers were located were more circular for the inclined ground plane compared to $\Theta_{GP} = 0°$. Consequently, no preferred direction of motion of the vortex centers could be found. As seen in the out-of-plane vorticity contours, the ability of the numerical simulations to preserve the tip vortex down to the ground plane was reduced for all but the SSG-LRR-ω turbulence model; compare Figs. 5.2 and 5.5. No vortex could be identified for wake ages of $\zeta = 720°$ with the other turbulence models. In addition, larger discrepancies were observed between the computed and measured vortex center locations, especially at young wake ages where the contraction of the streamtube was overpredicted in the simulations, especially on the downhill side. Overall, the SSG-LRR-ω model showed a tremendously superior predictive capability compared to the other tested models.

A quantification of vortex wandering as a function of wake age is shown in Fig. 5.6 to further substantiate the previous findings on vortex wandering for the experimental data. At the youngest wake age, no significant differences were observed between the three cases. For all wake ages at $\Theta_{GP} = 15°$, the standard deviations in both directions were comparable in magnitude, while a clear preferred direction of wander in the horizontal direction (σ_r) was observed for the parallel ground plane. Furthermore, the variations in the vortex center locations for hover OGE grew drastically between $\zeta = 540°$ and $\zeta = 720°$.[2]

Overall, it could be concluded that the vertical location of the tip vortices was computed correctly for all turbulence models up to the location where the tip vortices were dissipated in the simulations. Correlation was slightly worse for the radial locations as wake contraction was overpredicted. This is summarized in Figs. 5.7 and 5.8, where the computed trajectories were superimposed by box plots of the experimental results. Due the limited amount of experimental data IGE at $\zeta = 900°$ the shown box plot was only based on a fraction of the true vortex center locations (most vortices probably outside the PIV ROI) and does not contain the full statistical data contained at younger wake ages.

[2] See, e.g., [105] for a similar study on the dynamical characteristics of a four-bladed rotor in hover OGE using PIV and various vortex center detection methods including the Γ_1 method used in this thesis.

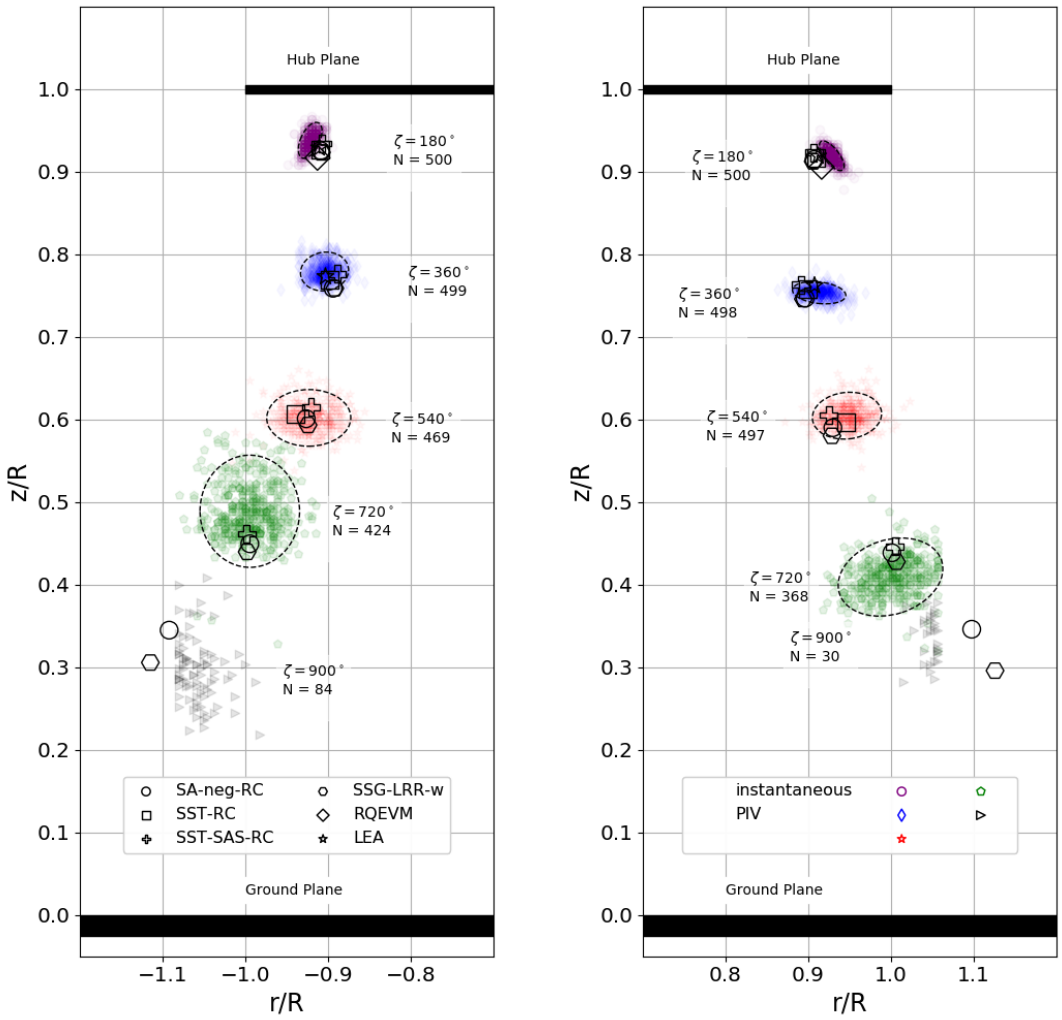

(a) uphill

(b) downhill

Figure 5.4.: Instantaneous vortex center positions for hover IGE and $\Theta_{GP} = 0°$. Standard deviation ellipsoids (2σ) are shown for wake ages up to $\zeta = 720°$. Wake ages at the uphill side are approximate values; see Fig. 3.5. Identified number of vortex centers from experimental data (N) is indicated for each wake age.

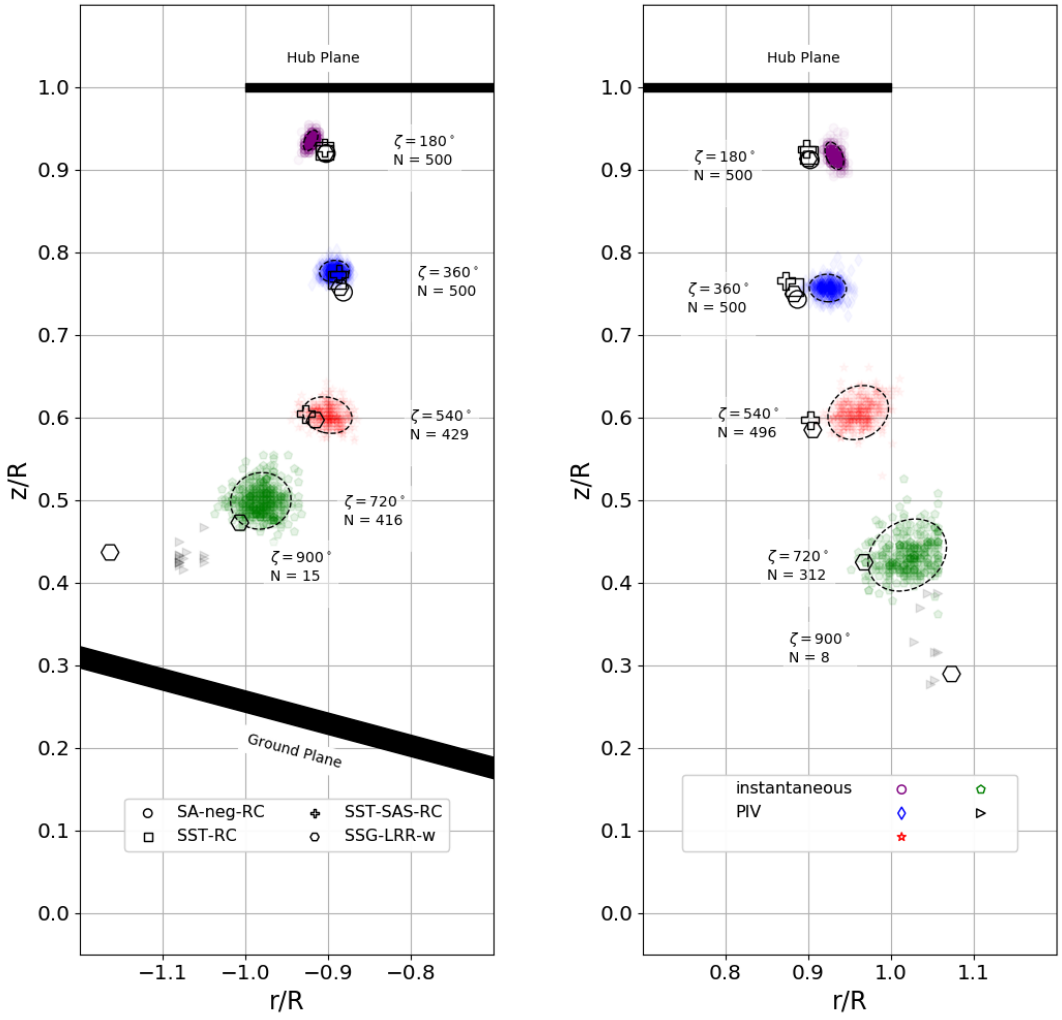

(a) uphill

(b) downhill (ground plane located below shown region)

Figure 5.5.: Instantaneous vortex center positions for hover IGE and $\Theta_{GP} = 15°$. Standard deviation ellipsoids (2σ) are shown for wake ages up to $\zeta = 720°$. Wake ages at the uphill side are approximate values; see Fig. 3.5. Identified number of vortex centers from experimental data (N) is indicated for each wake age. Note that no simulations were performed for the RQEVM and LEA turbulence models at $\Theta_{GP} = 15°$.

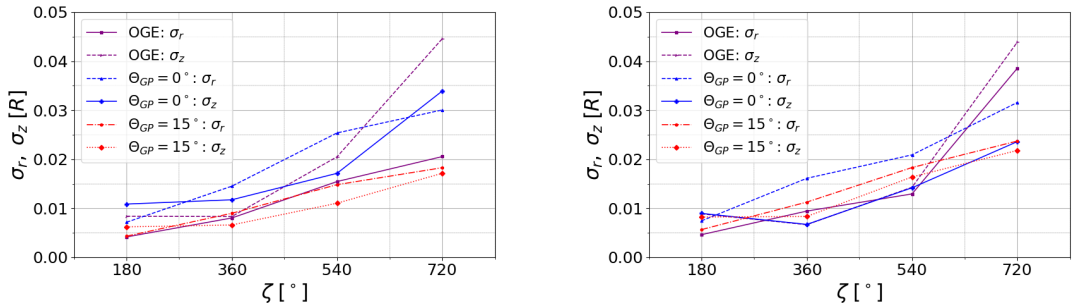

(a) uphill **(b)** downhill

Figure 5.6.: Visualization of the effect of wake age (ζ) on the variation of detected experimental vortex center positions for the USNA rotor. Data represented as standard deviation in horizontal (σ_r) and vertical (σ_z) direction.

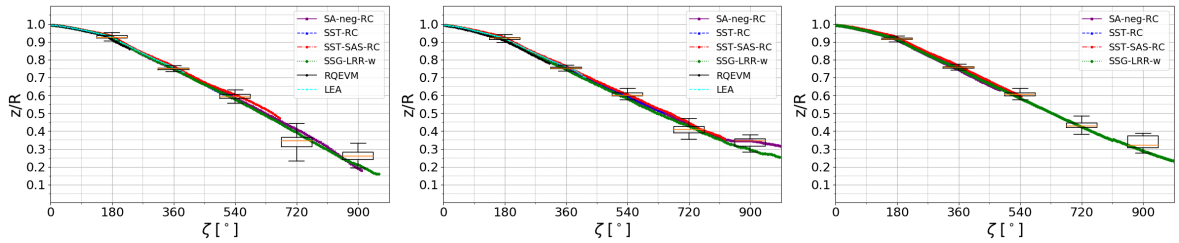

(a) OGE. **(b)** IGE $\Theta_{GP} = 0°$. **(c)** IGE $\Theta_{GP} = 15°$.

Figure 5.7.: Comparison of computed and experimentally measured vertical motion (z/R) of the tip vortices on the downhill side as a function of wake age (ζ). Experimental data shown as boxplots. Median value given by orange line. Box indicating interquartile range, whiskers are ending at last data point inside interval of 1.5 times the interquartile distance measured from the end of the box. Outliers are not shown.

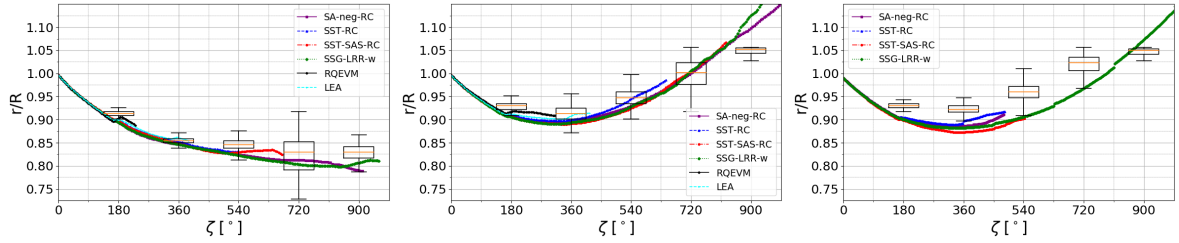

(a) OGE. **(b)** IGE $\Theta_{GP} = 0°$. **(c)** IGE $\Theta_{GP} = 15°$.

Figure 5.8.: Comparison of computed and experimentally measured horizontal motion (r/R) of the tip vortices on the downhill side as a function of wake age (ζ). Experimental data shown as boxplots. Median value given by orange line. Box indicating interquartile range, whiskers are ending at last data point inside interval of 1.5 times the interquartile distance measured from the end of the box. Outliers are not shown.

5.3. Vortex Size and Strength

Not only vortex trajectories are of key importance to understand the flow field of a hovering rotor and to allow for a valid assessment of the numerical results, but also the temporal evolution of vortex quantities needs to be considered. Thus vortex circulation (Γ), core radius (r_c) and swirl velocity were investigated. For the latter the half peak-to-peak velocity is given (V_{hpp}). Circulation was computed based on a square integration region with an edge length of 1 c centered around the detected vortex core, i.e., with a closest distance from center to edge of 0.5 c. Core radius and V_{hpp} were computed based on the averaged quantities from a horizontal and vertical data extraction through the detected vortex cores. Values are shown up to a wake age ζ where a distinct inflection point could be found in the velocity profiles. Due to increased vortex wandering and unsteadiness the observed scatter in the experimental data for hover OGE at a wake age of $\zeta = 720°$ grew significantly compared to $\zeta = 540°$. This could be observed for all three quantities.

Over the complete range of wake ages, the computed circulation was well within the experimental scatter bands, shown as boxplots in Fig. 5.9. Hence, the overall strength of the tip vortex was comparable with the experimental results. As a fixed integration region was used, i.e., for example not scaled with the vortex core radius, not only the circulation in the tip vortex but also the surrounding flow field was entrained in the calculation. It was assumed that this was the best possible comparison despite differences in the ability to preserve the tip vortices by the various tested turbulence models. A consequence of this approach can be seen during the first blade passage ($\zeta = 180°$) marked by the kink in the curve. All turbulence models showed comparable behavior, indicating that the general roll-up process of the tip vortex was comparable, i.e., the same amount of circulation was entrained during the formation of the tip vortex.

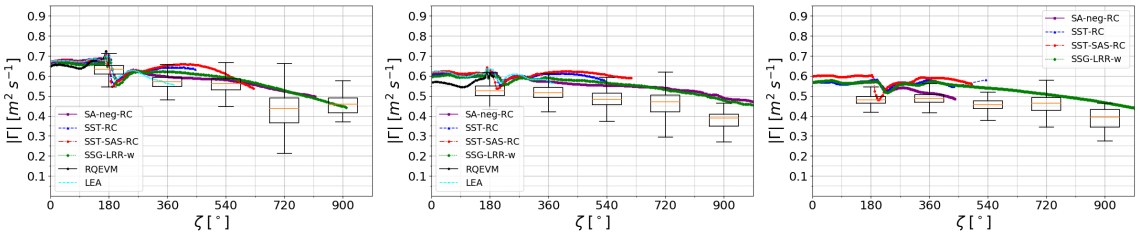

(a) OGE. **(b)** IGE $\Theta_{\mathrm{GP}} = 0°$. **(c)** IGE $\Theta_{\mathrm{GP}} = 15°$.

Figure 5.9.: Comparison of computed and measured tip vortex circulation (Γ) on the downhill side as a function of wake age (ζ). Data was integrated over square region centered around vortex core location with an edge length of 1 c. Experimental data shown as boxplots, without outliers. Median value given by orange line. Box indicating interquartile range, whiskers are ending at last data point inside interval of 1.5 times the interquartile distance measured from the end of the box.

As the circulation was computed away from the large gradients in the velocity field surrounding a tip vortex, this is, however, not an indication whether the detailed structure of the vortex was computed correctly. Therefore, the vortex core radius was considered as second quantity of interest; see Fig. 5.10. Based on the numerical results it could be concluded that tip vortex growth was overestimated in the simulations when compared to the experimental values. Only the SA-neg-RC, SSG-LRR-ω, and SST-SAS-RC turbulence models were able to compute vortex core radii

close to the scatter in the experimental results during the first blade passage. For example a ≈ 20% increased core radius was computed at $\zeta = 360°$ OGE and IGE at $\Theta_{GP} = 0°$.

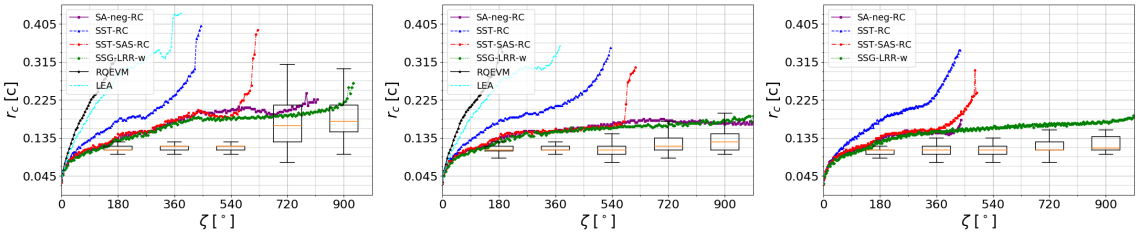

(a) OGE. **(b)** IGE $\Theta_{GP} = 0°$. **(c)** IGE $\Theta_{GP} = 15°$.

Figure 5.10.: Comparison of computed and measured vortex core radii (r_c) of the tip vortices on the downhill side as a function of wake age (ζ). Core radii based on inflection points in velocity profiles through vortex core and averaged from horizontal and vertical data extraction. Experimental data shown as boxplots, without outliers. Median value given by orange line. Box indicating interquartile range, whiskers are ending at last data point inside interval of 1.5 times the interquartile distance measured from the end of the box

In addition to the vortex core size, also the swirl velocities need to be computed correctly. A comparison between experimental and numerical data is given in Fig. 5.11. Due to the resolution of the PIV data the experimental results most likely did not capture the true peak velocities, i.e., due to the grid resolution the peak velocities were on average not recorded due to the limited number of sampling points of the PIV data over the vortex core. In [80], for example, a grid spacing of 0.2 mm was used to characterize the velocity profiles of tip vortices for a blade of comparable chord length ($c = 42.5$ mm), compared to 1.72 mm in the current study ($c = 44.45$ mm). Therefore, the velocities should probably be regarded as a lower bound, which the numerical data should most likely exceed. However, none of the tested turbulence models were capable of doing so with the current numerical settings and grids for all investigated wake ages. The SST-SAS-RC model managed to be within the scatter of experimental results for a wake age of $\zeta = 180°$. Improved predictions of the flow field could be achieved with the SSG-LRR-ω model. The extracted V_{hpp} values significantly exceeded those computed by all other turbulence models. Especially for hover IGE the values were higher or within the experimental scatter band for all wake ages.

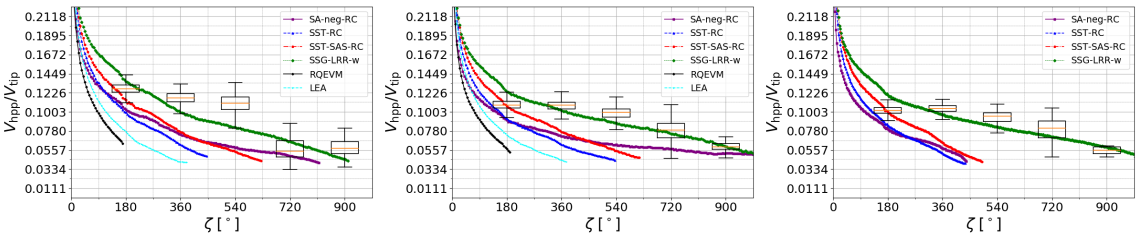

(a) OGE. **(b)** IGE $\Theta_{GP} = 0°$. **(c)** IGE $\Theta_{GP} = 15°$.

Figure 5.11.: Comparison of computed and measured half peak-to-peak velocities (V_{hpp}) of the tip vortices on the downhill side as a function of wake age (ζ). Values normalized by V_{tip}. Data averaged from horizontal and vertical velocity profile through vortex core. Experimental data shown as boxplots, without outliers. Median value given by orange line. Box indicating interquartile range, whiskers are ending at last data point inside interval of 1.5 times the interquartile distance measured from the end of the box.

5.4. Rotor Inflow

The observed changes in the flow field ultimately manifest in changes in the axial velocity (inflow) distribution in the rotor plane, where rotor blade sectional angles of attack are altered and consequently the rotor blade's lift, drag, and pitching moment. Therefore, instantaneous, phase-averaged, and time-averaged experimental axial velocity distributions were compared to the numerical data. The objective was to assess the temporal variations of the axial velocity near the rotor plane to determine the dependency of the axial velocity distribution on the ground plane inclination angle, i.e., what effect the ground plane inclination angle has on the flow field in the rotor plane. Furthermore, numerical data was used to generate a complete picture of how the inflow behaves in planes not included in the experimental data and how different turbulence models behave for hover over non-parallel ground.

5.4.1. Time-averaged Inflow Correlation

In Fig. 5.12 time-averaged axial velocity (v_z) distributions extracted 0.25 c below rotor hub (at $z/R = 0.973$) in the PIV plane (see Fig. 3.5) are shown. The values were normalized by the theoretical hover induced velocity (v_h). For hover OGE slight differences between the uphill and downhill side were found which could be attributed to the non-symmetric recirculation region below the rotor in the measurement plane; compare Figs. 5.1a and 5.12a. Compared to hover IGE the velocity amplitudes were higher. The experimental IGE results differed mainly at the inboard sections; compare Figs. 5.12b and 5.12c. This was again in agreement with differences in the recirculation region below the rotor hub; see Fig. 5.1a.

For all three cases the time-averaged numerical results correlated well with the experimental data. The increased contraction of the rotor wake computed by the numerical method was also seen here close to the blade tips $|r/R| \approx 1$; see also chapter 5.2. The peak amplitudes matched the experimental data well. Only close to the rotor hub, larger differences were observed. The asymmetries seen in the experimental data were not computed by either of the turbulence models for all three cases. These were most likely caused by geometric simplifications of the hub in the numerical simulation; see chapter 4.5.1.2. Differences between the turbulence models were negligible. Overall, the correlation IGE at $\Theta_{GP} = 15°$ was slightly worse compared to the other two cases. As data was extracted in a plane perpendicular to the rotor shaft in all cases and blade flapping was not modeled, this could be an indicator that blade flapping was present in the experiment at this ground plane inclination angle. However, as the correlation was not severely impaired, it is hypothesized that the flapping amplitude was small, a result previously seen in other experiments[54, 51].

5.4.2. Phase-averaged Inflow Correlation

Compared to the time-averaged data correlation (see chapter 5.4.1), a more detailed analysis was possible by looking at the instantaneous axial velocity distributions; see Fig. 5.13. Data was extracted 0.25 c below the rotor hub (at $z/R = 0.973$) in the PIV plane (see Fig. 3.5) at $\psi_b = 0°$ and

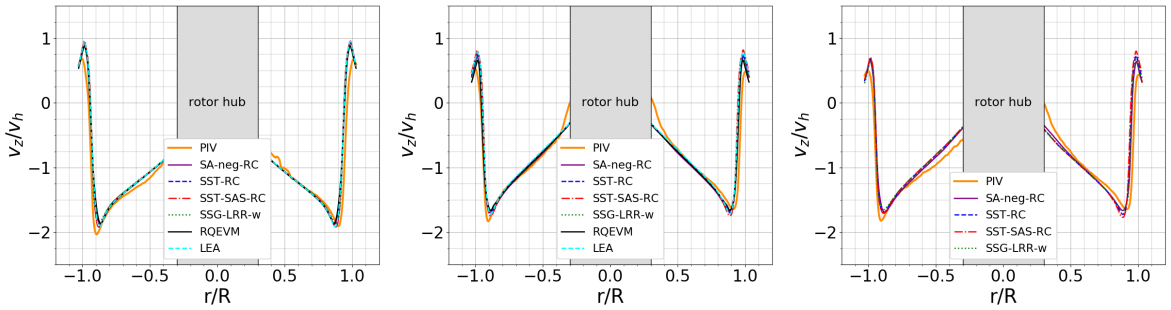

(a) OGE. **(b)** IGE $\Theta_{GP} = 0°$. **(c)** IGE $\Theta_{GP} = 15°$.

Figure 5.12.: Comparison of experimental[99] and computed time-averaged radial distributions of axial velocity (v_z) normalized by the theoretical hover-induced velocity (v_h). Values were extracted 0.25 c below rotor hub (at $z/R = 0.973$) in PIV plane; see Fig. 3.5. Inboard sections blanked due to excessive reflections from the rotor hub. Experimental results recorded in increments of $\Delta\psi_b = 10°$ (10 images per azimuth). Numerical data averaged over one rotor revolution in increments of $\Delta\psi_b = 3°$ (i.e., 120 slices).

normalized by the theoretical hover induced velocity (v_h). For all three cases the largest velocity fluctuations in the experimental data were located close to the rotor hub and near the tip (tip vortex wandering). The unsteadiness was reduced in between. A tendency which could also be discerned when looking at the recirculation regions in Fig. 5.1a and the described tip vortex wandering in chapter 5.2. As the vortex center locations play a significant role for instantaneous data, larger differences were expected in the axial velocity distributions between the uphill and downhill side.

The predominant influence on the downhill side can be attributed to tip vortices at a wake age of $\zeta = 0°$ and the blade bound circulation. Remember that data was extracted in a plane aligned with the trailing edge of the the downhill facing blade; see Fig. 3.5. As data were normalized by the hover induced velocity and the thrust values for the three cases were similar, i.e., the tip vortex strength was of comparable magnitude, the differences in the normalized axial velocities were small.

The computed and measured velocity distributions were in good agreement on the downhill side. In particular the peak-to-peak velocities correlated well. Differences were seen at the inboard sections where all numerical results overestimated the axial velocity magnitude. Close to the rotor hub, best agreement between the simulations and the experimental data was found for hover OGE; see Fig. 5.13a. Moreover, all numerical results coincided on the downhill side over almost the complete span of the rotor blade for each of the cases. At this wake age, the vortex locations were merely identical (rigid blades; only minor differences in Θ_0; see Table 5.2) and vortex diffusion could not yet diminish the tip vortex strength. Hence, an expected result.

On the contrary no agreement between the experimental and numerical values was found on the uphill side. Here, the most influential vortex (because closest to the rotor) was at an approximate wake age of $\zeta \approx 180°$, as the data were extracted in front of the blade. However, differences in the vortex center locations, vortex core size and strength could not fully explain the qualitative and quantitative differences in the velocity profiles throughout all investigated cases.

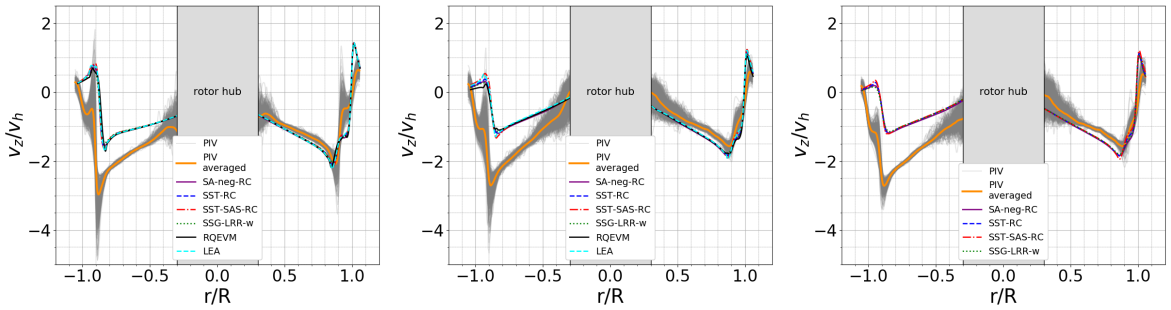

(a) OGE. **(b)** IGE $\Theta_{GP} = 0°$. **(c)** IGE $\Theta_{GP} = 15°$.

Figure 5.13.: Comparison of experimental[99] and computed instantaneous radial distributions of axial velocity (v_z) normalized by the theoretical hover-induced velocity (v_h). Values were extracted 0.25 c below rotor hub (at $z/R = 0.973$) in PIV plane, i.e., behind the trailing edge of the downhill facing blade (see Fig. 3.5) at $\psi_b = 0°$.

In order to find the cause for the striking differences in the axial velocity profiles on the uphill side, the phase-averaged experimental axial velocity v_z was compared to instantaneous numerical result (SA-neg-RC); compare Figs. 5.14a and 5.14b. On the downhill side the data matched well, i.e., the formation of the tip vortex at $r/R \approx 1.0$ and a distinct first passage of the tip vortex at $z/R \approx 0.92$ were seen. On the uphill side significant differences were observed. The experimental data showed a large region of downward flow at $z/R \approx 1.0$. A feature not allusively seen in the numerical result.

As this feature was visible in the phase-averaged flow field, it must have been a fundamental aspect of the measured flow field. Hence, it was suggesting that a systematic difference was present either in the data processing of the numerical simulations or the recording of the experimental data set. Out of the investigated possible differences a potential phase offset in the experimental data resolved the aforementioned issues best. When the numerical data were extracted at an azimuth angle of $\psi_b = 6°$ rather than $\psi_b = 0°$, the numerical results correlated well with the experimental data on the uphill side; compare Figs. 5.14a and 5.14c. The effect of the phase offset on the downhill side was small. A phase offset of $\Delta\psi_b = 6°$ would correspond to a time delay of $\Delta t \approx 4.8 \cdot 10^{-4}$ s in the measurements and cause parts of the rotor blade to intersect the plane of data extraction; see blanked region on uphill side in Fig. 5.14c.

The corresponding numerical axial velocity profiles with phase offset were correlated to the experimental data in Fig. 5.15. On the downhill side, the results were comparable to those without phase offset; see Fig. 5.13. On the uphill side the agreement between the experimental and numerical data was drastically improved. In particular, the peak-to-peak values close to the blade tip were in good agreement. As the phase-offset is only a hypothesis no tuning of parameters was made, i.e., the same offset was used for all three cases. In addition, as the distance to the rotor plane is low, minor variations in the blade position, e.g., caused by the infinitely stiff blade assumption in the simulation compared to the real blade, or blade flapping can have a large influence on the extracted values. Therefore, the proposed cause of the discrepancies does not fully explain the differences. Consequently, the phase offset was not applied to any of the other results shown. A final clarification of the problem would require further experimental results, which were not available

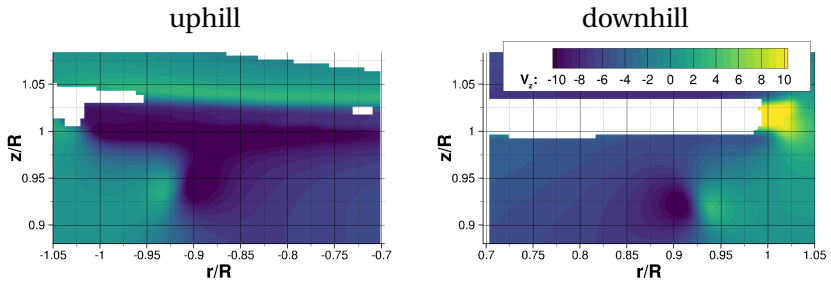

(a) Phase-averaged experiment. Only valid points are shown.

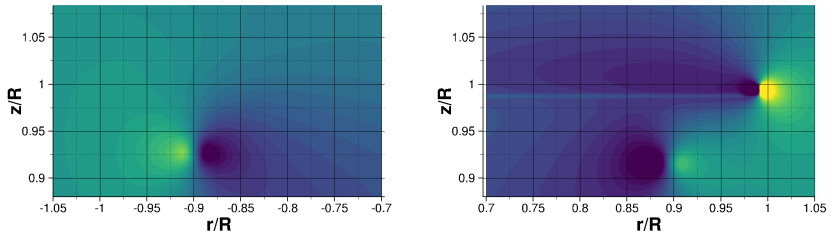

(b) Simulation, $\psi_b = 0°$

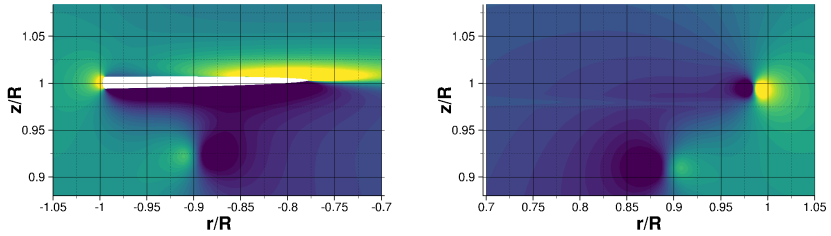

(c) Simulation, $\psi_b = 6°$. White region uphill shows intersection of rotor blade with data extraction plane.

Figure 5.14.: Visualization of the effect of phase offset ($\Delta\psi_b$) during data extraction on the axial velocity close to the rotor blade tips for the USNA rotor IGE at $\Theta_{GP} = 0°$. Values were extracted in PIV plane, i.e., behind the trailing edge of the downhill facing blade; see Fig. 3.5. Phase offset definition according to Fig. 3.2. Numerical results computed with the SA-neg-RC turbulence model.

at the time of writing of the thesis.

5.4.3. Inflow Variations with Rotor Azimuth Angle

Hovering over inclined ground planes affects the axial velocity distribution in the rotor plane. To gain a complete picture of where the effects were most pronounced, differences in the instantaneous inflow 0.25 c above the rotor plane (at $z/R = 1.027$) are shown in Fig. 5.16. Differences were considered to be deviations from the point symmetry usually found for hovering rotors OGE. For the two-bladed rotor investigated here ($\Delta\psi_b = 180°$), values were computed as $\left(v_{z,\zeta} - v_{z,\zeta+180°}\right)/2$, i.e., by half of the subtracted axial velocity of opposing points relative to the rotational axis. Data was normalized by the theoretical hover induced velocity v_h. If the axial velocity was independent of the blade azimuth angle ψ_b the computed quantity would be zero. Hence, the inflow would be time independent and thus the rotor thrust would be constant over the complete revolution. For

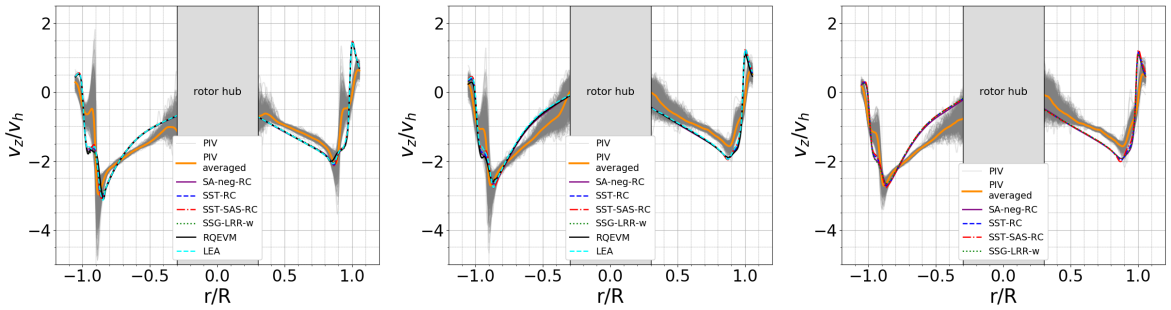

(a) OGE. **(b)** IGE $\Theta_{GP} = 0°$. **(c)** IGE $\Theta_{GP} = 15°$.

Figure 5.15.: Comparison of experimental[99] and computed instantaneous radial distributions of axial velocity (v_z) through the rotor normalized by theoretical hover-induced velocity (v_h). Values extracted 0.25 c below rotor hub (at $z/R = 0.973$) in PIV plane, i.e., behind the trailing edge of the downhill facing blade; see Fig. 3.5. Experimental values were extracted at $\psi_b = 0°$. Numerical values were extracted with phase offset at $\psi_b = 6°$.

this reason data OGE is not shown, as only small portions right at the rotor hub showed values significantly different from zero; i.e., $\left(v_{z,\zeta} - v_{z,\zeta+180°}\right)/2 \neq 0$. For hover IGE at $\Theta_{GP} = 0°$ only minor variations were found over most of the rotor plane. Fluctuations were only seen close to the rotor hub. This was caused by the flow around the rotor head, generated by the large recirculation region below the rotor (see Fig. 5.12) and the root vortices (see Fig. 5.23). Differences between the turbulence models were small. The largest asymmetry was found for the SSG-LRR-ω model; see Fig. 5.16d.

The situation changed when inclining the ground plane. At $\Theta_{GP} = 15°$ a variation of the inflow over larger portions of the rotor disk was found. In particular two distinct regions could be identified; one at the margin of the rotor disk plane and one close to the rotor hub. The first was caused by subtle differences in the tip vortex trajectories between the uphill and downhill side. The second stems from the asymmetric recirculation region below the rotor hub; compare Figs. 5.1 and 5.16. At the two rotor blade azimuth angles shown ($\psi_b = 0°$ and $\psi_b = 90°$, i.e., rotor perpendicular and parallel to the ground plane axis of rotation) the regimes remained relatively fixed in space and showed little variation. This was true for all turbulence models. Hence, based on the numerical instantaneous flow field realizations it could be concluded that the largest asymmetries in the inflow distribution were constrained to distinct regions of the flow field and did not rotate with the swirl in the rotor flow field. A quantification of the results was made in chapter 5.4.4 based on the SSG-LRR-ω results.

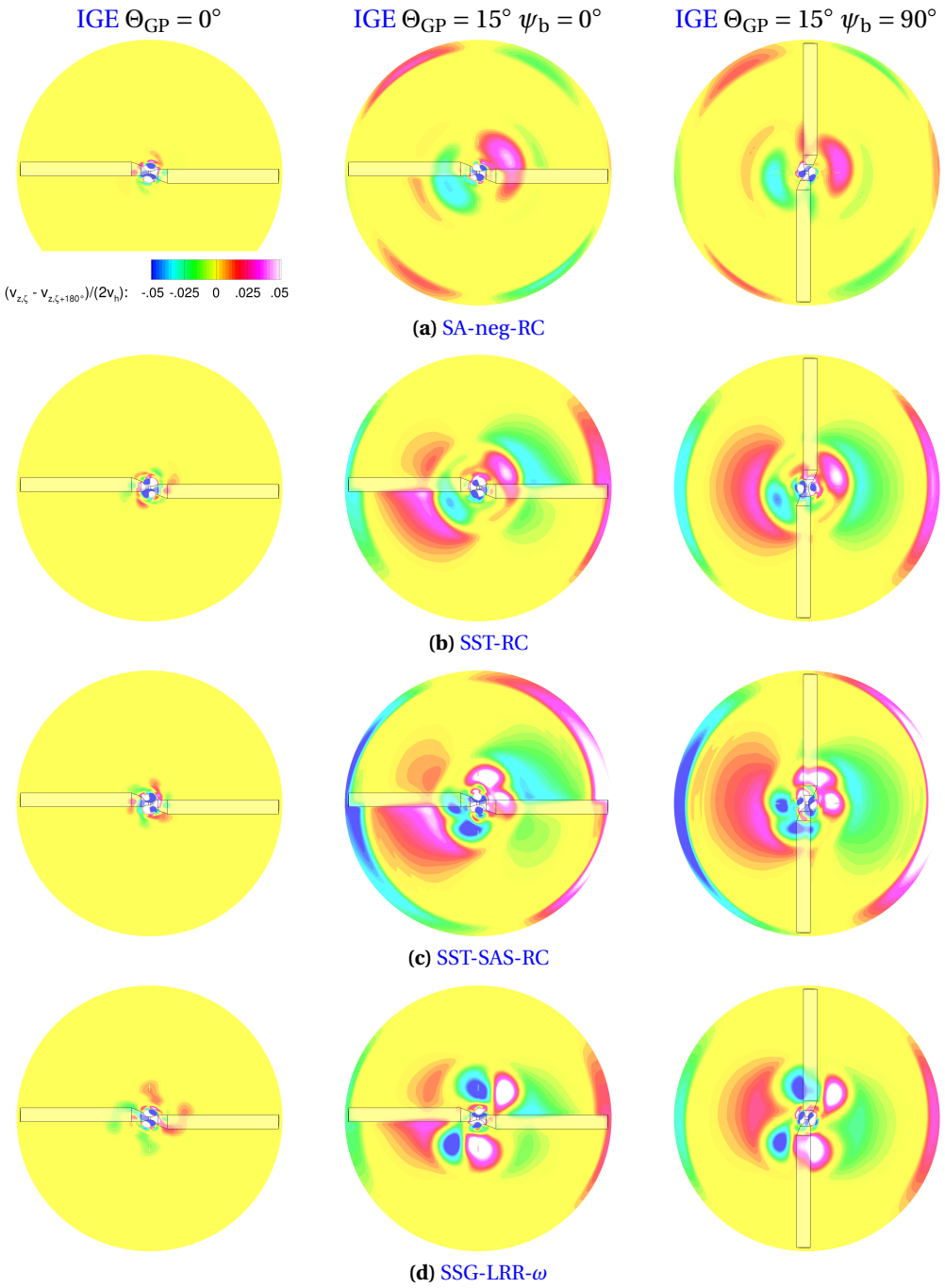

(a) SA-neg-RC

(b) SST-RC

(c) SST-SAS-RC

(d) SSG-LRR-ω

Figure 5.16.: Visualization of asymmetries in the axial velocity 0.25 c above the rotor hub (at $z/R = 1.027$) for the USNA rotor IGE. Values computed as pairwise differences in the point symmetry at equivalent radial location r/R and wake age ζ (with respect to the two blades) to the mean value, i.e., $\left(v_{z,\zeta} - v_{z,\zeta+180°}\right)/2$. Values normalized by theoretical hover induced velocity v_h. Rotor blade locations are indicated. Left edge of circular plane is uphill side, right edge is downhill side. Rotor plane shown from above.

5.4.4. Quantification of Inflow Velocities for Inclined Ground Plane

A quantification of the computed inflow velocities for hover IGE at $\Theta_{GP} = 15°$ was made using SSG-LRR-ω results. This turbulence model was chosen as it showed by far the best correlation with the available experimental data. For the subsequently shown quantification of inflow velocities, three additional revolutions were computed (26 revolutions in total). Out of these, the last two revolutions were used for time averaging and data extraction. Data was extracted at intervals of $\Delta\psi_b = 2°$.

Time-averaged axial velocity contours are shown above and below the rotor plane in Fig. 5.17. Close to the rotational axis an upward flow was observed at all vertical distances shown. The largest deviations from rotational symmetry in the inflow distribution were found to be located close to the center of the rotor disc, at azimuth angles in the range of $0° \leq \psi_b \leq 90°$, i.e., the top right quadrant in the image. Hence, the time-averaged inflow was most affected in a region starting when the blade was pointing towards the downhill side ($\psi_b = 0°$) as it was approaching the uphill side. This behavior was qualitatively identical for all tested turbulence models, where the largest deviations in inflow were aligned in the same quadrant; see Fig. 5.16.

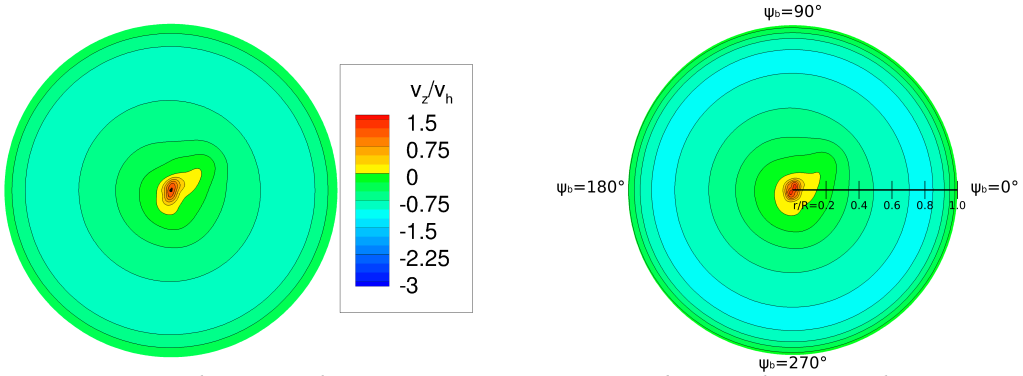

(a) 1.00 c above rotor plane.

(b) 0.50 c above rotor plane.

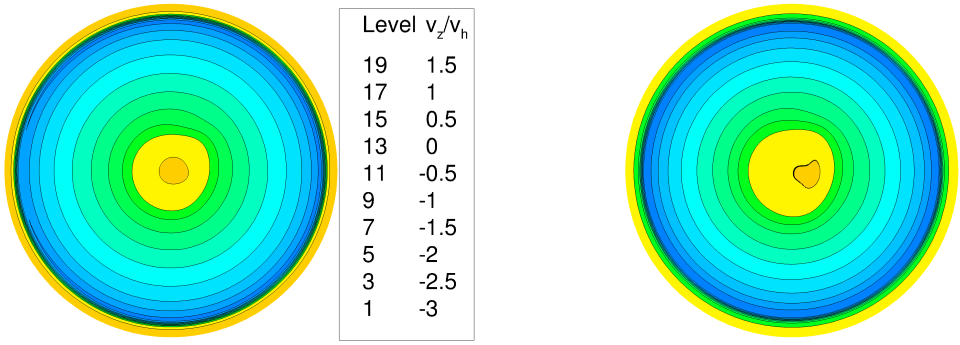

(c) 0.50 c below rotor plane.

(d) 1.00 c below rotor plane.

Figure 5.17.: Visualization of time-averaged axial velocity contours (v_z) normalized by theoretical hover induced velocity (v_h) for hover IGE at $\Theta_{GP} = 15°$. Contours superimposed by level curves of v_z/v_h. Rotor plane shown from above. Uphill side of ground plane is at $\psi_b = 180°$.

Instantaneous radial distributions of axial velocity above and below the rotor quarter chord line are shown in a blade fixed coordinate system in Fig. 5.18. Close to the rotor hub center, larger dif-

ferences were seen when the rotor blade was at an azimuth angle of $\psi_b = 90°$ (i.e., aligned with the ground plane axis of rotation, when the blade is approaching the uphill side). Here, larger inflow velocities were observed, compared to the other three blade azimuth angles shown. Further outboard, close to the rotor blade tip, all inflow distributions coincided, except for $\psi_b = 180°$. At this angle (i.e., when the rotor blade was pointing towards the uphill side) inflow velocities above the rotor plane were larger close to the blade tip. Slightly lower inflow velocities were observed further inboard, albeit the differences were marginal. In addition, discrepancies were observed in the 'S-shaped' velocity profile below the rotor plane. This was an indicator that the distance between the tip vortex and the rotor blade was altered at $\psi_b = 180°$, compared to the other three blade azimuth angles. This behavior further substantiates the findings in chapter 5.4.3, that variations in inflow distribution at the blade tips were mostly aligned with the rotor blades being perpendicular to the ground plane axis of rotation, i.e., the blades being at $\psi_b \approx 0°$ and $\psi_b \approx 180°$. In [54] a similar observation was made using a free-wake solver combined with a panel method to simulate a two-bladed rotor at $z/R = 1.5$ at $\Theta_{GP} = 25°$.

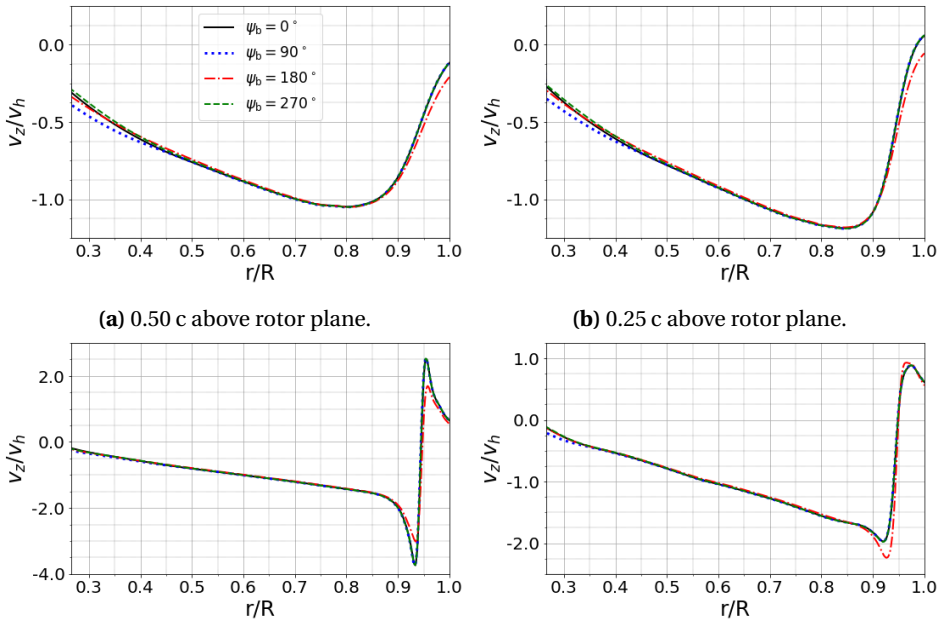

(a) 0.50 c above rotor plane.

(b) 0.25 c above rotor plane.

(c) 0.25 c below rotor plane.

(d) 0.50 c below rotor plane.

Figure 5.18.: Axial velocity (v_z) normalized by theoretical hover induced velocity (v_h) over rotor span for hover IGE at $\Theta_{GP} = 15°$. Data extracted at multiple distances above and below the rotor blade quater chord line for different rotor blade azimuth angles (ψ_b).

A different way of quantifying inflow variations over the rotor disk was used in Figs. 5.19 and 5.20. Here, the temporal evolution of the axial velocity was extracted at fixed radial locations over time with respect to different initial rotor blade azimuth angles (ψ_b). Radial distances up to $r/R = 0.450$ are shown in Fig. 5.19. Little variation was observed over the three consecutive blade passages included in the graph, an indicator that, within the accuracy of the simulations, trimmed solutions were achieved. In accordance with the previous findings, only data points extracted at $\psi_b = 45°$ and $\psi_b = 90°$ at $r/R = 0.265$ and $r/R = 0.350$ showed visible deviations in the inflow distribution. The axial velocity was lower for $\psi_b \approx 45°$ and larger for $\psi_b \approx 90°$ compared to the other angles.

At $r/R = 0.450$ the inflow was found to be quasi independent of the rotor blade azimuth angle. Further variations in the axial velocities were restricted to regions at high r/R, close to the blade tips; see Fig. 5.20. Inflow distributions were independent of the blade azimuth angles up to $r/R = 0.900$. Only at $r/R = 0.950$ a slightly increased axial velocity was observed above the uphill side of the inclined ground plane.

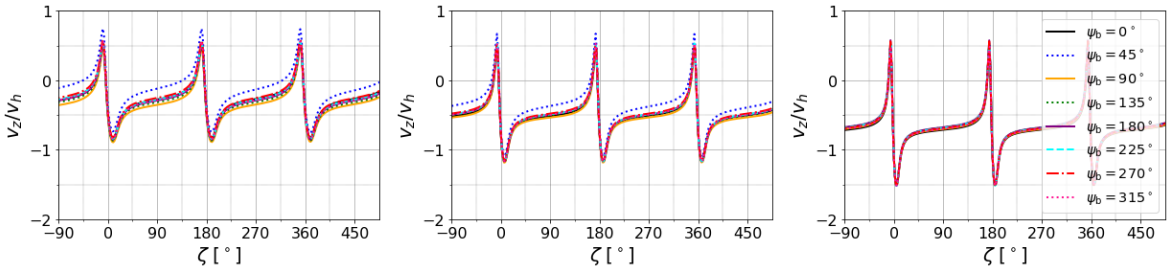

(a) $r/R = 0.265$. **(b)** $r/R = 0.350$. **(c)** $r/R = 0.450$.

Figure 5.19.: Temporal evolution of axial velocity (v_z) normalized by theoretical hover induced velocity (v_h) for multiple radial stations. Data shown as relative wake age ζ to eight different initial blade azimuth angles (ψ_b), i.e., at $\zeta = 0°$ data was probed above the rotor blade quarter chord line at the respective azimuth angle. Data extracted 0.25 c above the rotor plane.

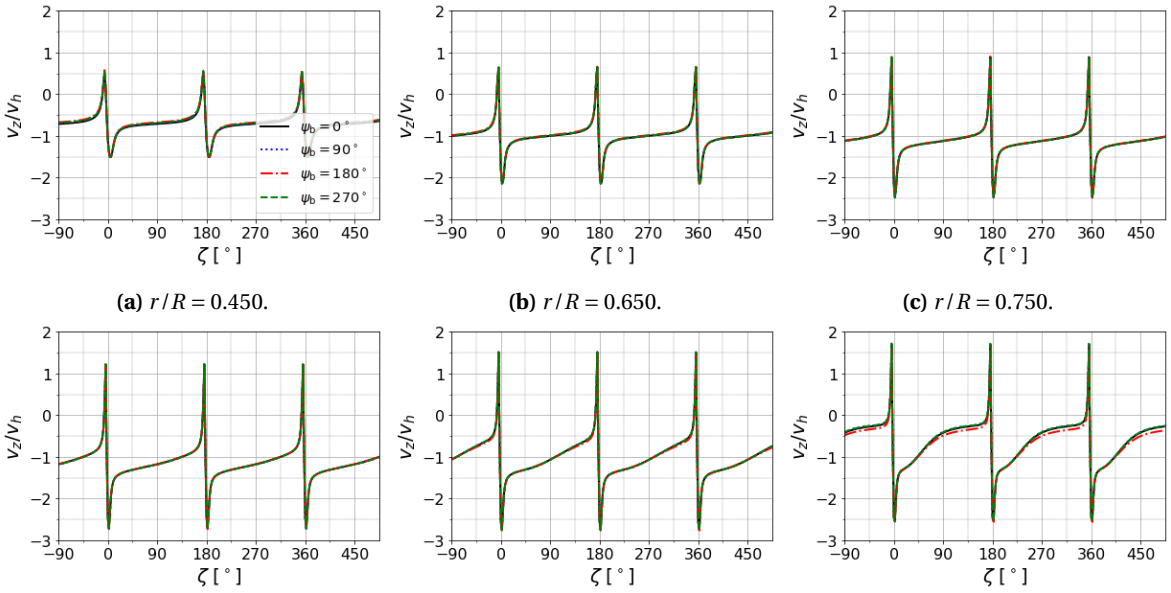

(a) $r/R = 0.450$. **(b)** $r/R = 0.650$. **(c)** $r/R = 0.750$.

(d) $r/R = 0.850$. **(e)** $r/R = 0.900$. **(f)** $r/R = 0.950$.

Figure 5.20.: Temporal evolution of axial velocity (v_z) normalized by theoretical hover induced velocity (v_h) for multiple radial stations. Data shown as relative wake age ζ to four different initial blade azimuth angles (ψ_b), i.e., at $\zeta = 0°$ data was probed above the rotor blade quarter chord line at the respective azimuth angle. Data extracted 0.25 c above the rotor plane.

A comparison of the resulting thrust variations over multiple rotor revolutions is shown in Fig. 5.21. Thrust fluctuations relative to the mean thrust over three consecutive revolutions were plotted per blade ($(F_{z,b} - \overline{F}_{z,b})/\overline{F}_{z,b}$) for hover IGE at the two different ground plane inclination angles (Θ_{GP}). For the parallel ground plane ($\Theta_{GP} = 0°$) a two-per-revolution characteristic was observed in the

thrust signal. For hover OGE a similar variation in thrust was observed (magnitude and frequency). The exact cause for this behavior could not be quantified. As these variations were within the desired trim target (see chapter 4.6), the results were considered valid for the study at hand. At $\Theta_{GP} = 15°$ the two-per-revolution fluctuations were superimposed by a one-per-revolution thrust variation. This was attributed to the influence of the inclined ground plane (forces are plotted per blade). Overall, the presence of the inclined ground plane not only changed the frequency content of the individual forces but also increased the maximum peak-to-peak variations in the thrust signal. Despite the overall mean thrust variation within the plotted revolutions, largest peak-to-peak fluctuations were observed when the blade was at azimuth angles in the range of $0° \leq \Theta_{GP} \leq 90°$ for each consecutive revolution. No frequency analysis of the thrust signals was made, as in the limited number of computed revolutions no N-per-revolution periodic thrust variation was observed.

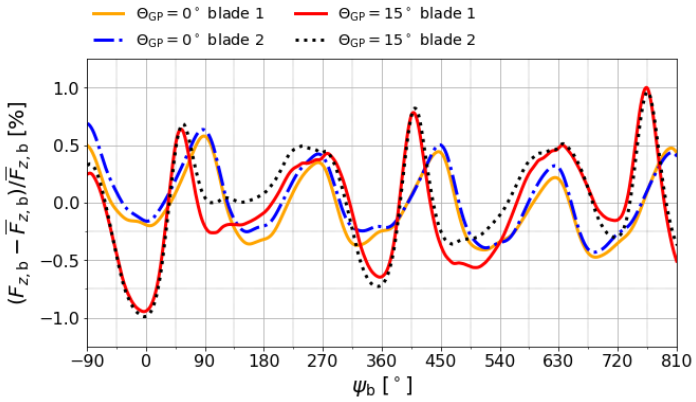

Figure 5.21.: Comparison of temporal variation in thrust per blade ($F_{z,b}$) between the parallel and inclined ground plane. Variations plotted as relative difference to mean thrust over three consecutive revolutions.

5.5. Effects of Turbulence Models on the Flow Field

5.5.1. Flow on Ground Plane

The used numerical method provided the complete flow field information at all points in space. In particular, for the USNA rotor test rig this allowed investigating the flow on the ground plane, for which no test instrumentation was installed during testing. In Fig. 5.22 the effects of hovering over inclined ground planes were visualized and compared to the parallel ground plane for the different tested turbulence models.

For $\Theta_{GP} = 0°$ the computed flow fields with the SA-neg-RC, SST-RC, and SST-SAS-RC turbulence model were well comparable. A distinct separation line formed on the ground separating the region of flow recirculation below the rotor (see also Fig. 5.1) from the wall jet that formed on the ground plane. For the RQEVM and LEA computations a second separation line formed right below

the rotor hub. Moreover, for the LEA turbulence model, the pressure distribution on the ground differed considerably from the other models used; see Fig. 5.22f. This was caused by the presence of a distinct, large circular vortex on the ground plane, a feature not seen in any of the other computations at this revolution number; see chapter 5.5.2 and Fig. 5.23f for further details. For all of the previously mentioned turbulence models a slight variation of the diameter of the separation line was observed. Due to the limited amount of revolutions computed in this study, no further details could be given on whether or not this was a characteristic of the used turbulence models or time dependent. A considerably different flow pattern was found for the SSG-LRR-ω model; see Fig. 5.22d. Here, the separation line deviated from the circular shape seen in the other models, though on average having a comparable diameter. This was caused by the presence of larger secondary vortical structures inside the recirculation region (see Fig. 5.23d) and the significantly improved ability to transport the tip vortices down to the ground plane; see chapters 5.2 and 5.3.

When the ground plane was inclined the flow changed considerably as the rotational symmetry of the flow was lost. On the uphill side, the reduced distance between the blade and the ground plane caused a significant increase in download on the ground. Magnitude and extension of this region of increased pressure were in close agreement between the turbulence models. Moreover, the circular shape of the separation line was broken up on the downhill side. This was a direct consequence of the larger separation distance between the rotor slipstream boundary and the ground plane, seen, for example, in the time averaged velocity contours (Fig. 5.1) and the extracted vortex trajectories (chapter 5.2). Most of the mass flux through the rotor was transported downhill with a dominant direction perpendicular to the axis of rotation of the ground plane. Also here, differences between the turbulence models were small.

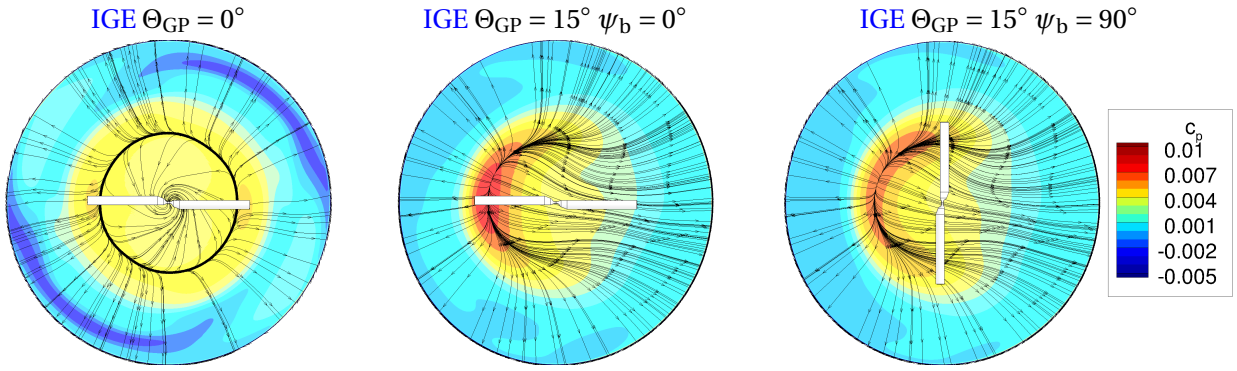

(a) SA-neg-RC

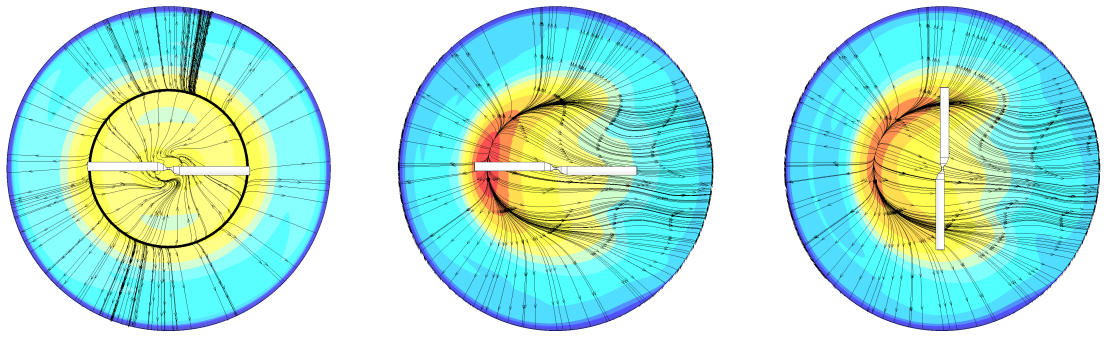

(b) SST-RC

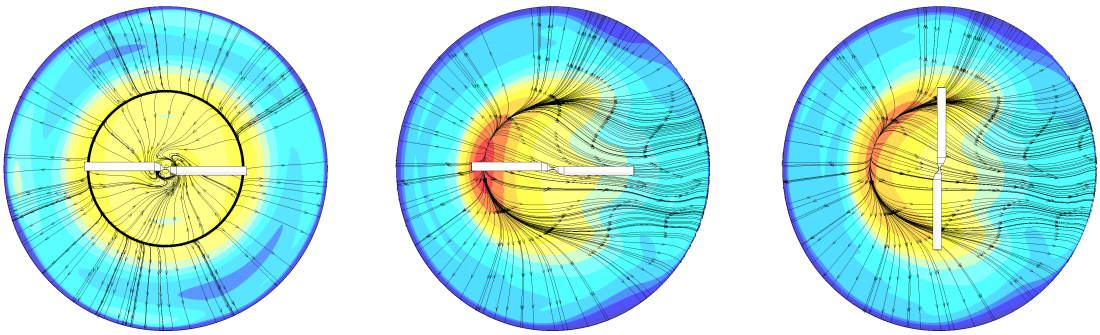

(c) SST-SAS-RC

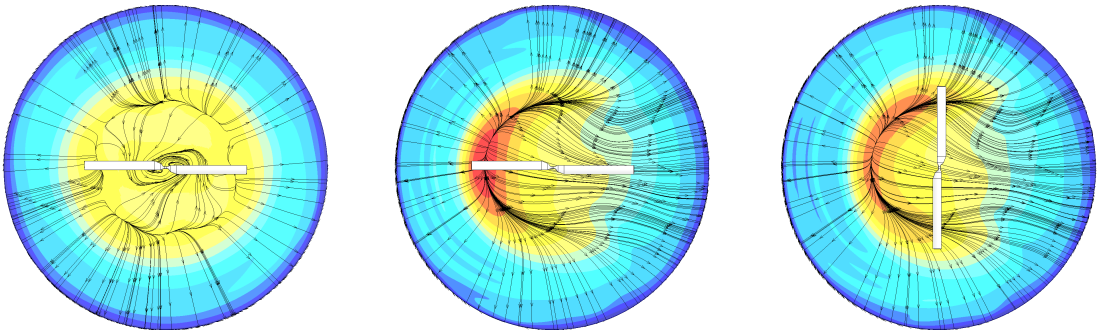

(d) SSG-LRR-ω

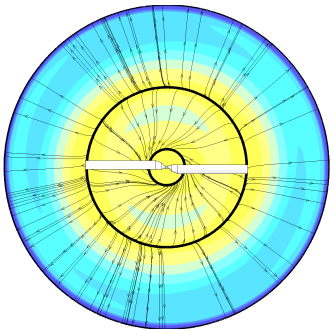

(e) RQEVM

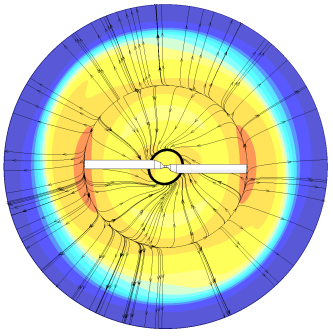

(f) LEA

Figure 5.22.: Comparison of computed flow field on ground plane for IGE simulations of the USNA rotor with different turbulence models. Data visualized as pressure coefficient (c_p) contours superimposed by stream traces on the frictionless ground plane. Left edge of circular ground plane is uphill side, right edge is downhill side. Note that no simulations were performed for the RQEVM and LEA turbulence models at $\Theta_{GP} = 15°$.

5.5.2. Vortex Structures

The previously described disability of some turbulence models to properly preserve the dominant flow features, i.e., the tip vortices, was not necessarily linked to an absence of helical vortex structures. Therefore, to gain a better understanding of the three-dimensional structure of the dominant flow characteristics, Q-criterion isosurfaces were extracted for the three hover flight cases; see Fig. 5.23.

As shown before, the RQEVM and LEA turbulence model computations gave the least accurate results of all tested turbulence models. This could also be seen when looking at the isosurfaces for hover OGE and IGE at $\Theta_{GP} = 0°$; see Figs. 5.23e and 5.23f. Vorticity levels dropped significantly within the first 0.5 revolutions, and the vortices suffered from significant core growth. This ultimately resulted in highly distorted vortical structures which merged with older vortex elements. In addition, for the LEA model, a dominant large vortex ring formed on the ground, while a secondary vortex ring lifted far of the ground. Neither of them was the starting vortex. Both features were not supported by experimental or other computational results.

More distinguishable tip vortex structures were found for the SST-RC and SST-SAS-RC model results. When using the SAS correction the ability of the simulation to preserve geometrically concentrated vortical structures over longer periods of time was improved. This was especially true for the inclined ground plane; see Figs. 5.23b and 5.23c. A further improvement was seen with the SA-neg-RC model. Only when leaving the refined region of the background grid (see blue parts of the grid in Fig. 4.9b), larger and quantitatively less vortical structures were observed; see Fig. 5.23a. Best vortex preservation was achieved with the SSG-LRR-ω model; see Fig. 5.23d. Especially at $\Theta_{GP} = 15°$ this model was the only one capable of preserving concentrated vortical structures down to the ground plane.

Furthermore, for the SSG-LRR-ω model distinct non-symmetrical secondary vortical structures were found inside the rotor slipstream for hover IGE. Similar structures were found for the two-equation models. However, these were more axisymmetric to the rotational axis. As the ground plane was computed as frictionless wall, no definite physical reasoning could be given for these differences and where these structures originated from.

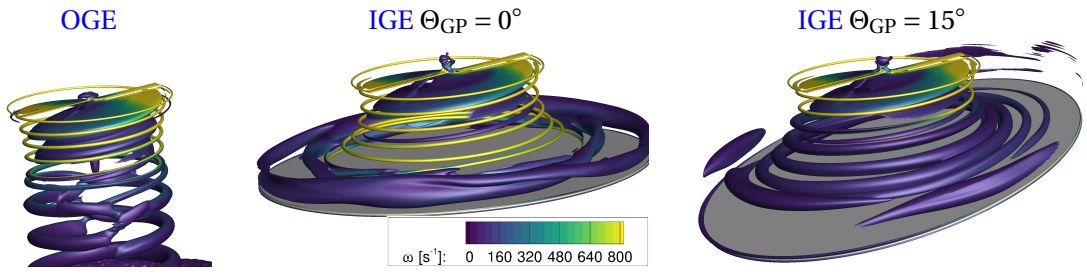

(a) SA-neg-RC

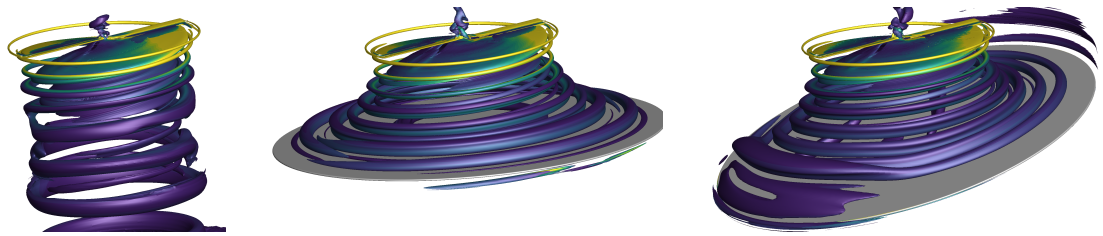

(b) SST-RC

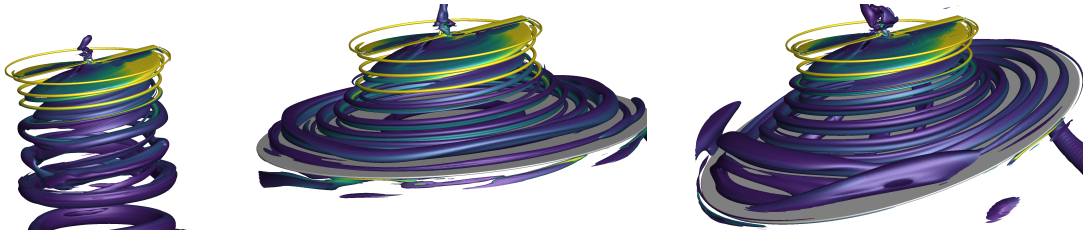

(c) SST-SAS-RC

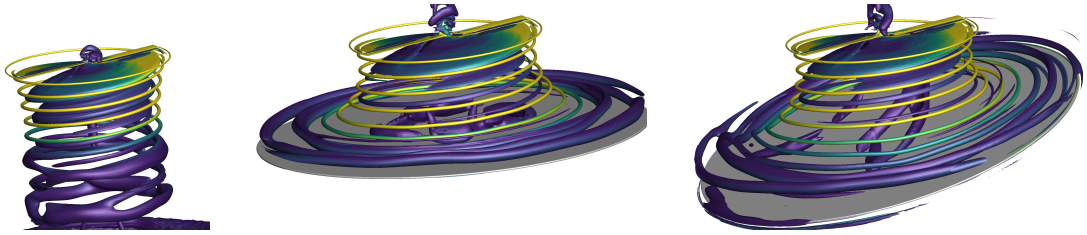

(d) SSG-LRR-ω

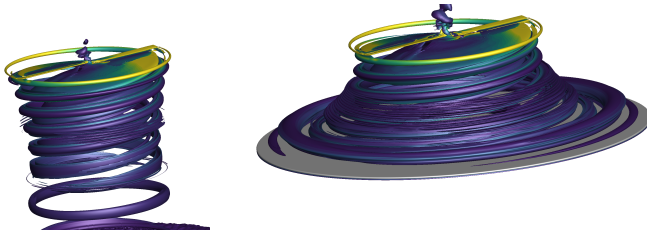

(e) RQEVM

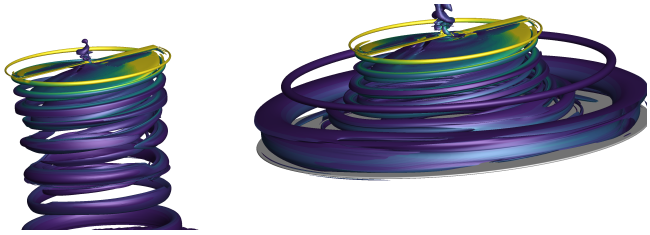

(f) LEA

Figure 5.23.: Comparison of computed vortical structures for the USNA rotor with different turbulence models at $\psi_b = 0°$ of the reference blade. Vortices visualized by Q-criterion isosurfaces ($Q = 750\ s^{-2}$) colored by total vorticity ω. Note that no simulations were performed for the RQEVM and LEA turbulence models at $\Theta_{GP} = 15°$.

5.5.3. Eddy Viscosity

Additional insights into the causes of the variations in vortex dissipation could be gained by comparing the levels of eddy viscosity (μ_t) computed by the individual turbulence models; see Fig. 5.24. Eddy viscosity contours were superimposed by total vorticity level curves and streamlines in a vertical plane through the rotor shaft axis. The vorticity contours depict the trailed vortex sheets and tip vortices. For the SA-neg-RC model an overall increased viscosity level was observed compared to the other simulations. In particular, the recirculation regions IGE caused high levels of viscosity close to the ground. These were most likely linked to the large scale curvature in the flow field, to which the model is receptive and the large distance from the next viscous surface[164]; see Fig. 5.24a and chapter 4.4. Similar, yet by far less pronounced effects were found for the SST-RC and SST-SAS-RC model results; see Figs. 5.24b and 5.24c. The usage of RC terms reduced the levels of eddy viscosity in the vortex cores significantly[84], and an additional reduction / improvement was achieved by using the SAS correction. For the RQEVM and LEA results, this was not observed (note that no RC terms were used). In contrast to the other turbulence models, high levels of eddy viscosity were already found close to the rotor hub plane, which diffused the tip vortices.

A somewhat different characteristic was observed for the SSG-LRR-ω model, for which the equivalent eddy viscosity was plotted ($\mu_{t,\text{equiv}} = \rho \cdot k/\omega$). Equivalent eddy viscosity was visible in the vortex cores and the magnitude built up over time, i.e., further downstream. Moreover, for hover IGE the recirculation regions below the rotor hub also caused increased levels of equivalent eddy viscosity. At $\Theta_{GP} = 15°$ increased levels of equivalent eddy viscosity were observed in the ground plane parallel flow on the downhill side, which were more pronounced compared to the SST models but significantly lower compared to the SA-neg-RC model.

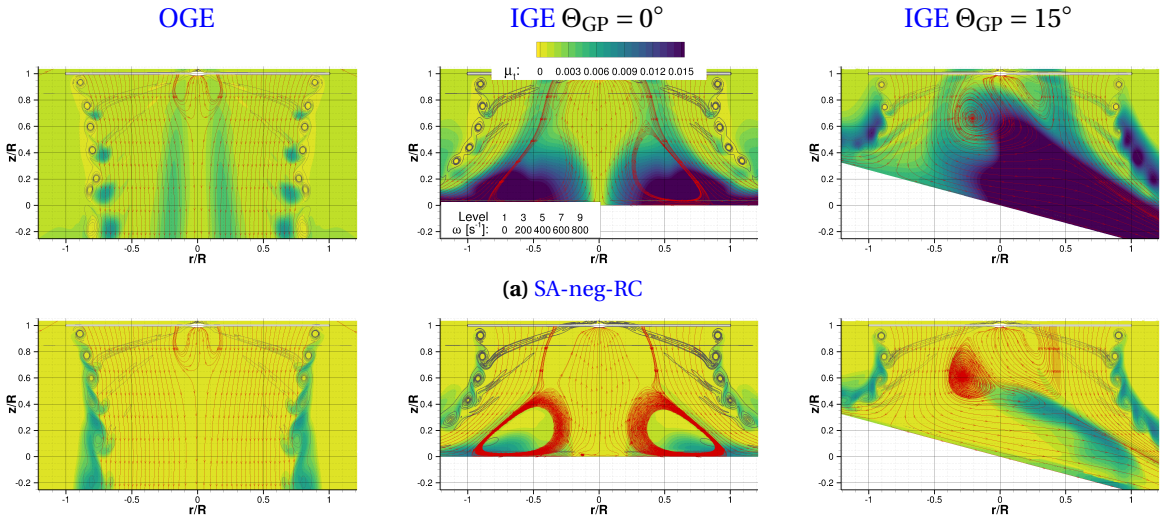

(a) SA-neg-RC

(b) SST-RC

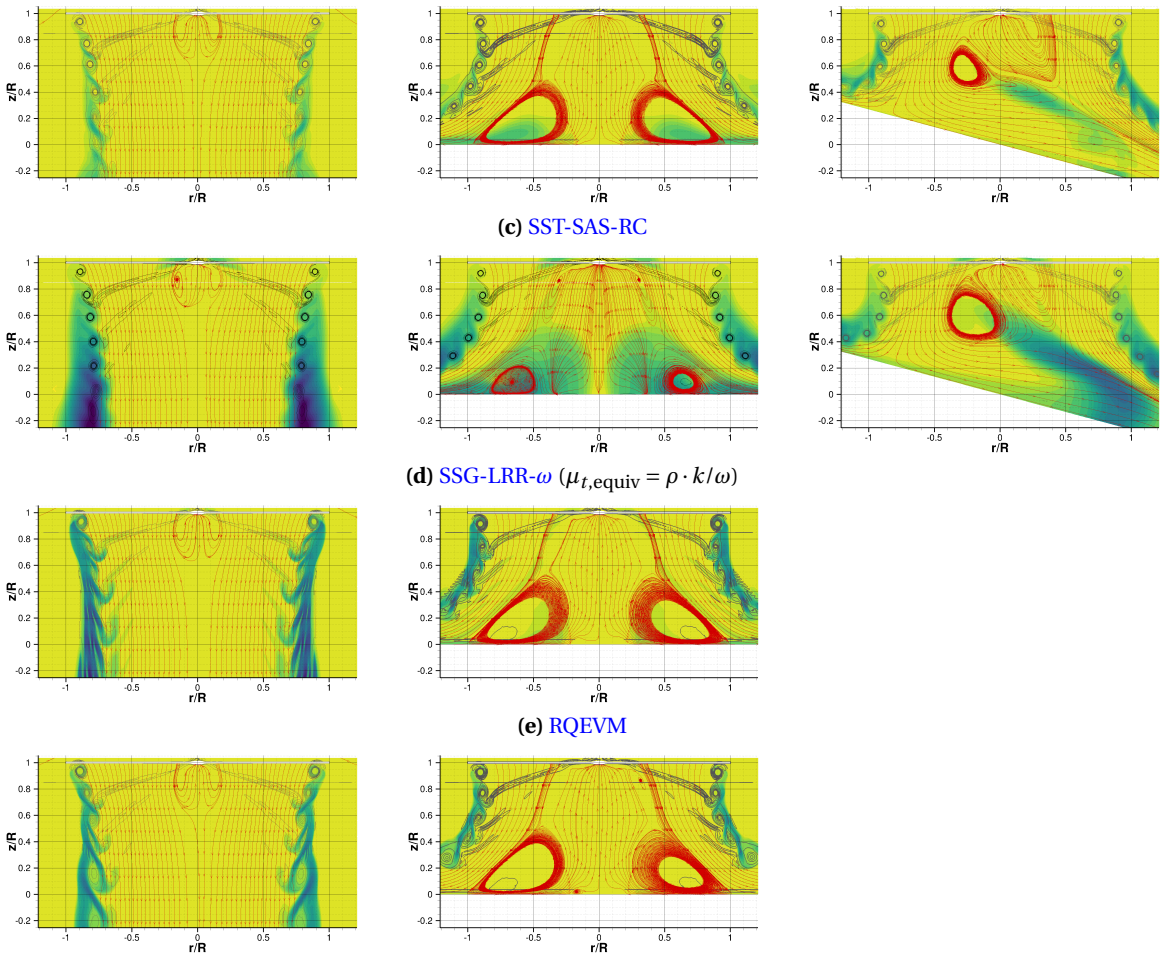

(c) SST-SAS-RC

(d) SSG-LRR-ω ($\mu_{t,\text{equiv}} = \rho \cdot k/\omega$)

(e) RQEVM

(f) LEA

Figure 5.24.: Comparison of eddy viscosity μ_t contours between turbulence models for the USNA rotor at $\psi_b = 0°$ of the reference blade. Contours superimposed by level curves of total vorticity ω (gray) and streamlines of the in plane velocity field (red). Plane of data extraction aligned with rotor shaft and rotor blade quarter chord axis.

5.5.4. Required Computing Time

Not only the accuracy of a simulation is crucial for the application but also the time required to compute the flow solution. For all turbulence models but SSG-LRR-ω the same numerical scheme (two-stage multigrid) and start sequence of the simulation was used. This means that the simulations were started with a comparatively coarse time step of $\Delta\psi_b = 45°$ and 250 inner iterations, which was successively reduced to $\Delta\psi_b = 1°$ and 25 inner iterations. Due to stability problems, this was not possible for the SSG-LRR-ω simulations. Here, no multigrid was used and a time step of $\Delta\psi_b = 1°$ and 100 inner iterations were fixed throughout the complete simulation. This increased the overall simulation time drastically for this turbulence model. However, it has to be noted that no particular efforts were made to reduce the time required to transport the starting vortex out of the region of interest due to the limited number of simulations that were run with this model. In Table 5.3 the wall clock time required per time step in the final revolution is given as an indicator

for differences in run time for the larger of the two grids, i.e., the IGE simulation. Using the SAS correction increased the wall clock time by ≈ 15%. Using turbulence models with RC increased the wall clock time considerably compared to the RQEVM and LEA model. A significant increase of wall clock time per time step was observed by the SSG-LRR-ω model. Compared to the SA-neg-RC model, the required time increased by ≈ 50% with the currently used settings.

Table 5.3.: Comparison of wall clock time required for one time step of the USNA simulations IGE between different turbulence models with a two-stage multigrid cycle and 25 inner iterations per time step (SSG-LRR-ω: single grid with 100 inner iterations). Simulation was run on 1920 processors distributed over 40 nodes on SuperMUC-NG at the Leibniz-Rechenzentrum Garching.

SA-neg-RC	SST-RC	SST-SAS-RC	SSG-LRR-ω	RQEVM	LEA
82 s	85 s	98 s	121 s	75 s	75 s

5.6. Summary and Conclusions – Rotors in Ground Effect

The combined numerical and experimental study revealed significant differences in the flow fields of hovering rotors when inclining the ground plane. This affected not only the instantaneous, but also the time-averaged flow fields to a great extent. When hovering over a parallel ground plane, the rotor wake was almost symmetric. This changed when the ground plane was inclined, where the rotor flow field was no longer symmetric to the rotational axis. Particularly on the uphill side the influence was evident, whereas on the downhill side the effects were less significant in terms of the vortex core locations and the time-averaged velocity contours. As a results, the stagnation point on the ground plane was shifted uphill and the downhill slipstream boundary was lifted significantly further off the ground compared to the parallel ground plane.

A distinct feature when inclining the ground plane ($\Theta_{GP} = 15°$) was a reduction in vortex wandering of the tip vortices over the complete span of wake ages investigated. Vortex centers were detected closer to their mean location, i.e., the standard deviation of the vortex center positions was reduced. No preferred direction of tip vortex wandering was dominant, especially at older wake ages. This was in contrast to the parallel ground plane and OGE. The effect was found for both the downhill and the uphill side.

The numerical simulations showed good agreement from a global, flow phenomenological perspective, i.e., time-averaged flow fields. OGE and for the parallel ground plane, the vortex trajectories were in good agreement with the experimental data. The correlation between simulation and experiment deteriorated slightly for the inclined ground plane, as the rotor wake contraction was overpredicted. It was hypothesized that because of numerical diffusion of the tip vortices the interaction with the inclined ground plane was underpredicted, and thus the asymmetry of the flow field was not fully captured. Overall, it could be concluded that all tested turbulence models,

along with the selected numerical settings and the spacial and temporal resolution, were able to compute the time-averaged quantities.

The various tested turbulence models differed significantly in their ability to preserve the tip vortices, and thus, the detailed structure of the flow field. In particular, the RQEVM and LEA turbulence models diffused the tip vortices significantly, so that they were no longer unambiguously detectable after one rotor revolution using the numerical settings chosen for this study. It was supposed that this was mainly caused by not including Rotation/Curvature Correction (RC) terms; see also the differences between the SST-SAS, SST-RC, and SST-SAS-RC model results for the UTA CCR rotor in chapter 6.1. The other turbulence models showed all major flow features. Best vortex preservation was achieved with the SSG-LRR-ω model, followed by the SA-neg-RC, and SST-SAS-RC models OGE and IGE at $\Theta_{GP} = 0°$. At $\Theta_{GP} = 15°$ the SSG-LRR-ω model was the only model that showed comparable performance to the other two tested hover flight conditions. Especially the SA-neg-RC model results were significantly deteriorated. With all models, except for SSG-LRR-ω, tip vortex swirl velocities were underestimated. However, all models overestimated the vortex core radii with the selected grid resolution.

When inclining the ground plane, experimental results showed that the inflow was mostly affected on the uphill side and at the inboard sections, whereas on the downhill side this influence was small. The numerical simulations showed good agreement with the time-averaged experimental data and the phase-averaged data on the downhill side for all cases. Differences were observed for the phase-averaged data on the uphill side. A possible cause for the discrepancies could be identified. It was hypothesized that a phase offset in the measurements caused the differences. However, further experimental data is required to prove this wrong or right.

The numerical simulations showed that inclining the ground plane caused asymmetries in the inflow close to the rotor hub and the blade tips. These areas with increased asymmetry remained fixed in space over time. This change in the inflow distribution was not observed OGE and for the parallel ground plane. A quantifiable influence on the rotor forces and moments caused by inclining the ground plane was not seen in the numerical results, even though a one-per-revolution characteristic was observed in the individual blade forces. As no N-per-revolution periodicity of the rotor forces was found within the computed rotor revolutions, further studies are required to precisely determine the ground plane influence on the rotor forces from a numerical perspective.

6. Rotor Aerodynamics Without Dynamic Actuation

Two different coaxial rotor concepts were investigated, namely a Coaxial-Counter Rotating (CCR) and a coaxial co-rotating (stacked) rotor design. For both, the geometries and operating conditions were based on rotor test rigs built and operated at UTA; see chapters 3.2.2 and 3.2.3. For all numerical simulations[1], grid resolutions and time step sizes were chosen according to the results of a sensitivity study; see chapter 4.5.2.6. Moreover, to be able to assess the accuracy of the numerical predictions, computational results were correlated to experimental data. Based on previous joint publications by the experimenters and the author, this was possible for two-bladed single rotors, which were derived from both coaxial rotor configurations[113, 102, 103], and, in parts, for the two-by-two-bladed CCR rotor[101, 114] and the stacked rotor[114]. For these rotors, PIV flow field measurements were conducted and analyzed at UTA, which allowed to asses the axial velocity distributions in the rotor plane (inflow) and the vortex dominated flow field below the rotor. For all remaining configurations, results were derived from numerical simulations only. The subsequently shown results are an extension of prior publications for the single rotors[113, 102, 103], including new computational grids for the CCR rotor test rig, and a more extensive data analysis for the stacked rotor test rig.

Details on the used grids are given in chapter 4.5.2, a description of the turbulence models in given in chapter 4.4, and the experimental configuration and flow field measurements are described in chapter 3.2. Throughout the following discussion, the origin of the coordinate system was located in the center of the upper rotor hub for the coaxial rotors and the rotor hub for the single rotors; see Figs. 3.9 and 3.10.

6.1. Coaxial Counter-Rotating Rotor Aerodynamics

6.1.1. Two-Bladed Single Rotor

Numerical simulations[2] for the two-bladed single rotor based on the CCR rotor setup (see chapter 3.2.2) were made at three different blade loadings (C_T/σ = 0.06, 0.08, 0.10) and correlated to

[1] For all simulations the the inverse fourth order dissipation coefficient was 64 and the second order dissipation coefficient was 0.5 for the employed matrix dissipation scheme. The reconstruction of gradients was computed with the Gauss divergence theorem.

[2] 11 rotor revolutions were computed using the SA-neg-RC turbulence model

experimental data recorded and analyzed at UTA. Experimental data was previously published and correlated to numerical results by the experimenters and the author of this thesis[113, 103]. The subsequently shown results are an extension of the previous work.

6.1.1.1. Rotor Flow Field

An indication of the quality of the numerical results could be gained by comparing numerical out-of-plane vorticity contours to experimental data. The contours indicated the locations of trailed vortex sheets, tip vortices, and gave a first estimate on vortex size and strength. In Fig. 6.1 numerical results were compared to experimental data[113] at multiple different blade azimuth angles (ψ_b) at a blade loading of $C_T/\sigma = 0.06$. Overall good correlation between the experiment and the numerical simulation was found. Especially close to the rotor blades and for young wake ages the numerical simulations showed excellent agreement with the experimental data (vortex locations, and size). At older wake ages, the experimental data included larger fluctuations of the tip vortex locations and vortex diffusion. The large amount of unsteadiness was not observed in the numerical simulations despite the relative fine temporal resolution of $\Delta\psi_b = 0.5°$. An example for the aforementioned phenomena at older wake ages can be seen in Fig. 6.1e. Here, the oldest vortex ($\zeta = 440°$) in the experimental data was already significantly diffused. On average the experimental tip vortex trajectories were well predicted by the numerical simulations; see chapter 6.1.1.2.

More global insights could be gained by comparing time-averaged axial velocity contours; see Fig. 6.2. The contours were superimposed by time-averaged in-plane velocity vectors. It was found that the continuous vortex wake contraction at early wake ages in the shown ROI was in good agreement between the experimental data and the numerical results. However, as less fluctuations were observed in the numerical simulations and fewer time steps were averaged compared to the experimental data, the region of highest axial velocity in the CFD simulations was smaller and showed a higher velocity magnitude. Moreover, slight discrepancies were observed between the locations of the blade tips; see region of highest positive (upward) axial velocity. As the blades were assumed to be infinitely rigid in the numerical simulations, deflections of the stiff (but not fully rigid) blades used in the experiment were not captured.

6.1.1.2. Tip Vortex Trajectories

Radial and axial tip vortex displacements (vortex trajectories) were extracted from numerical results and experimental data[103] for the three measured blade loadings. Vortex centers were identified using the algorithm described in Appendix C[3] and the results are shown in Fig. 6.3. The scatter in vortex core locations in the experimental data is displayed by shaded regions, indicating one standard deviation[103]. The characteristic kink in the axial vortex displacement caused by the first blade passage was well visible at all tested rotor thrusts. Good agreement between CFD and experiment was found for the axial vortex displacements over one rotor revolution, i.e., the maximum range that could be measured. The computed radial displacements showed good agreement

[3] Experiment (Exp.) threshold: $\Gamma_1 \geq 0.85$; CFD threshold[103]: $\Gamma_1 \geq 0.7$ and $\overline{\omega} \geq 450\ s^{-1}$

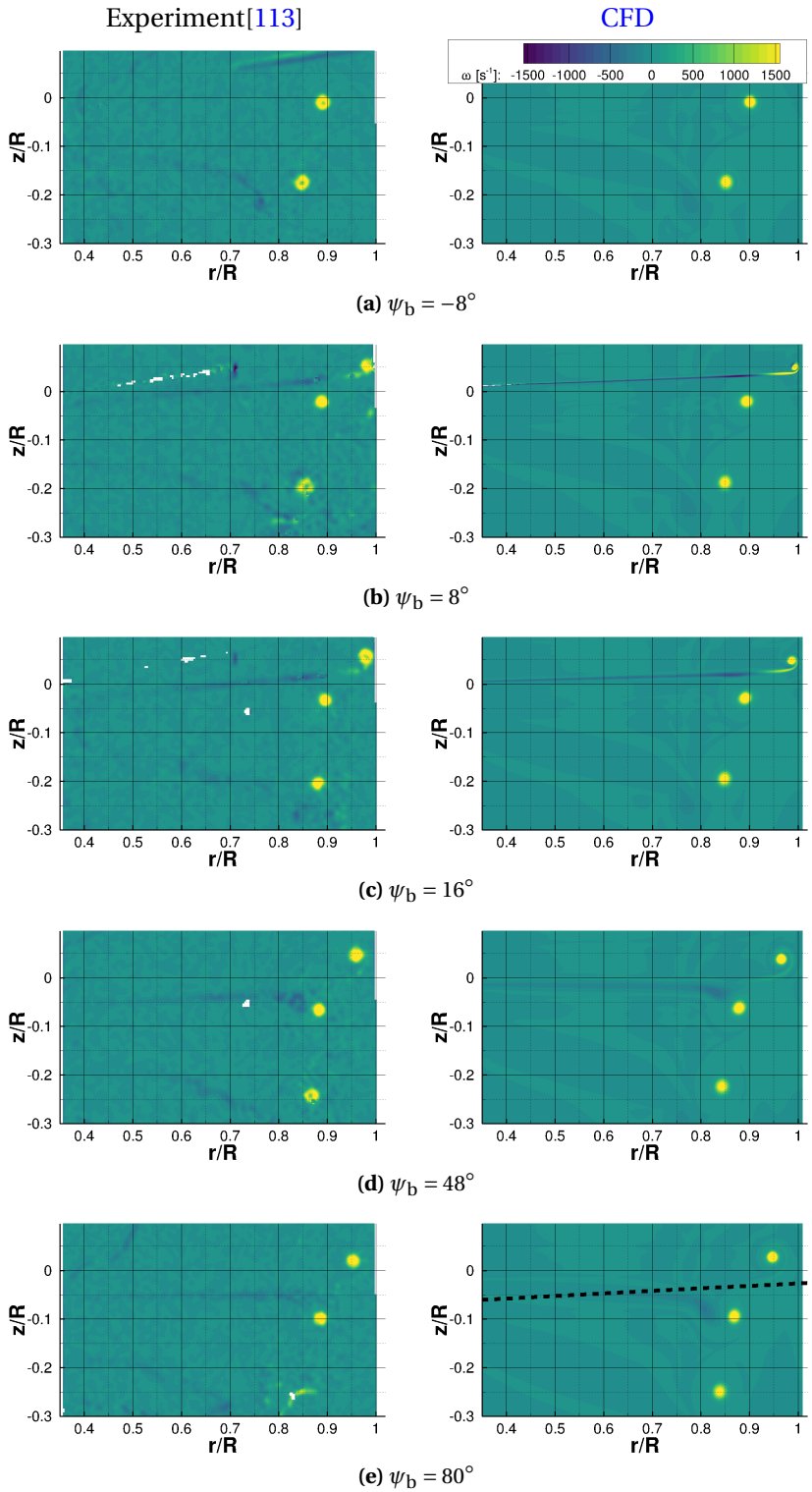

(a) $\psi_b = -8°$

(b) $\psi_b = 8°$

(c) $\psi_b = 16°$

(d) $\psi_b = 48°$

(e) $\psi_b = 80°$

Figure 6.1.: Comparison of instantaneous out-of-plane vorticity contours between experiment[113] and simulation for the two-bladed single rotor based on the UTA CCR rotor test rig at $C_T/\sigma = 0.06$. Contours shown at multiple rotor blade azimuth angles ψ_b. Dahsed line in (e) indicating distance $\Delta z/R = -1$ c below the rotor blade.

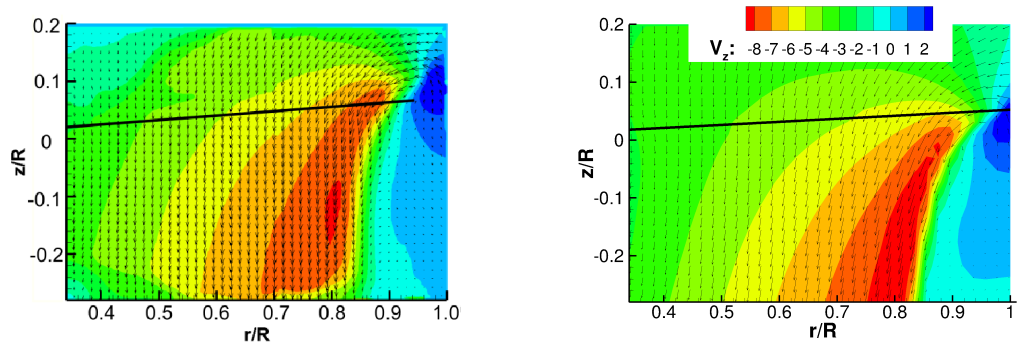

(a) Experiment[113]. **(b)** CFD.

Figure 6.2.: Comparison of time-averaged contours of axial velocity (v_z) between experiment[113] and simulation for the two-bladed single rotor based on the UTA CCR rotor test rig at $C_T/\sigma = 0.06$. Experimental data averaged over 200 rotor revolutions (9.000 flow field realizations). Numerical data averaged over one rotor revolution in increments of $\Delta\psi_b = 3°$ (i.e., 120 slices). Solid line indicating rotor blade intersection with measurement plane at rest ($\beta_p = 3°$).

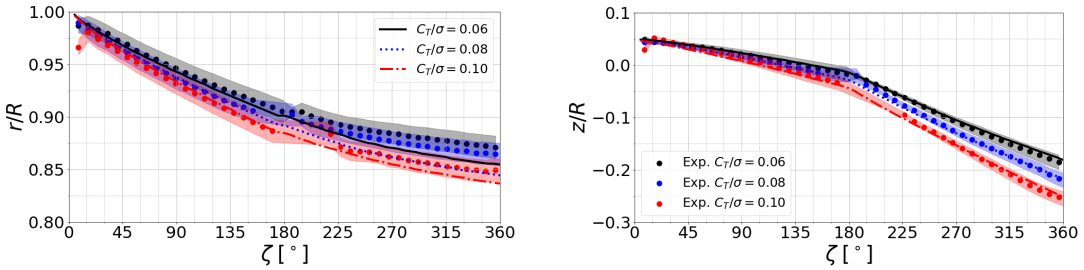

(a) r/R vs ζ. **(b)** z/R vs ζ.

Figure 6.3.: Comparison of measured[103] and computed radial (r/R) and axial (z/R) tip vortex displacements for the two-bladed single rotor based on the UTA CCR rotor test rig. Data shown for $C_T/\sigma = 0.06$, 0.08, and 0.10.

with the measurements until the first blade passage. For higher wake ages, the computed vortex contraction was slightly overpredicted. Note that the numerical results were processed at a fixed rotor location (i.e., based on one time step at $\psi_b = 0°$) and values were extracted at varying wake ages (ζ)[4]; see Fig. 3.8a. For the numerical results the flow solution did not show significant time-dependency up to the wake ages displayed and thus, one time step could be used to extract all required data. Note that vortex collocation was performed for the youngest tip vortices. Doing so allowed for a valid comparison between experiments and simulations as the blade deformations, which were not modeled, could be taken into account by shifting the experimental results by a constant offset value in z/R direction[102].

[4]This strategy was also used for the stacked rotor test rig and its applicability was assessed in more detail in chapter 6.2.2.

6.1.1.3. Tip Vortex Size and Strength

Vortex strength was quantified by investigating the tip vortex circulation Γ; see Fig. 6.4a. The circulation was computed by integrating the out-of-plane vorticity over a square region centered around the detected tip vortices. The integration region had a size of $48\,x\,48$ mm ($0.6\,x\,0.6$ c) and was chosen according to the experimental data processing used in [103]. Overall, the measurements showed a steady decrease over one rotor revolution. Only at the youngest wake ages, an increase was seen. However, at these young wake ages ($\zeta \leq 30°$) the measurements were impaired by laser light reflections from the passing blades and do not represent accurate measurement results. For the same reason, no data points could be extracted near the second blade passage ($\zeta = 180°$).[103] Overall it was found that the numerical results underpredicted the measured tip vortex circulation at all blade loadings. However, the trends were captured correctly.

In contrast to these findings better agreement was seen for the USNA rotor; see chapter 5.3. For this rotor, the square integration region had an edge length of 1 c, compared to 0.6 c for the UTA rotor. Hence, a possible cause of the discrepancy might stem from the extension of the integration region. If the vortex core radius was overpredicted and/or the swirl velocity was underpredicted, the square integration region might not cover the complete circulation entrained in the tip vortices[5]. However, no experimental data for the vortex core sizes and swirl velocities were available and consequently, no detailed comparison could be made. Only the numerical tip vortex core radii (r_c) and half peak-to-peak velocities (V_{hpp}) could be evaluated; see Figs. 6.4b and 6.4c. It was noted that the computed tip vortex core radii were only marginally affected when varying the blade loading, with a general trend of increasing vortex core sizes when increasing the blade loading. An overview study on experimental data concerning tip vortex core growth in the rotor near wake indicated that for increasing thrust the tip vortex core size was actually increasing, hence, indicating that the observed trends are plausible[167]. For V_{hpp} an increased blade loading led to increased swirl velocity magnitudes. However, based on the findings presented in chapter 5.3 for the USNA rotor test case, the shown results are most likely overestimating r_c and underestimating V_{hpp} if they could be compared to experimental data. Therefore, the shown data is indicating trends rather than giving absolute values.

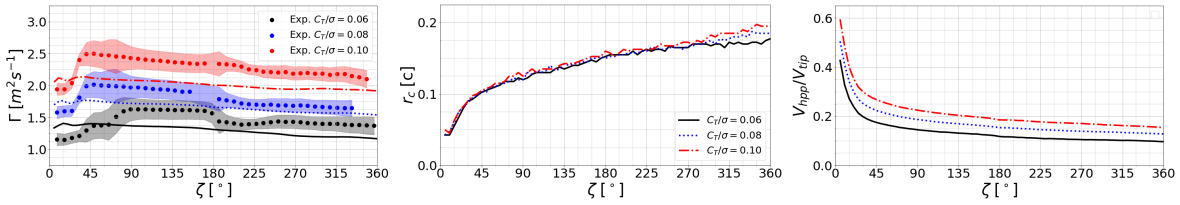

(a) Γ. **(b)** r_c. **(c)** V_{hpp}.

Figure 6.4.: Comparison of computed tip vortex circulation (Γ), core radius (r_c) as fraction of blade chord (c), and half peak-to-peak velocity (V_{hpp}) normalized by the blade tip velocity (V_{tip}) for the two-bladed single rotor based on the UTA CCR rotor test rig as a function of wake age (ζ). Results computed using the SA-neg-RC turbulence model at $C_T/\sigma = 0.06$, 0.08, and 0.10. Shaded region represents one standard deviation of the experimental tip vortex circulation values[103].

[5] Note that experimental studies by other researchers indicated that tip vortex circulation values grow for increasing sizes of the integration regions and do not necessarily converge to an absolute value of Γ[89, 97].

6.1.1.4. Rotor Inflow

Phase-averaged axial velocity profiles were extracted from the experimental data[103] at multiple different blade azimuth angles and compared to numerical results to assess the spacial inflow distribution; see Fig. 6.5. Data was extracted along a line parallel to the (deformed) rotor blades for both datasets. For the experimental data this line was defined by the mean coning angle at each blade loading. The scatter contained in the phase-resolved PIV data is shown by the shaded region which corresponds to one standard deviation.

Data was extracted at multiple rotor blade azimuth angles (ψ_b) one chord below the rotor blade ($\Delta z/c = -1$); see Fig. 6.1e. The influence of the blade tip vortex could be clearly seen at $\psi_b = 0°$ and $\psi_b = 8.1°$. It manifested as a 'S-shaped' profile in the axial velocity distribution; see Figs. 6.5a and 6.5b. As no vortex collocation was performed for the experimental data, these peaks do not represent the exact strength and size of the tip vortices, but rather the mean influence of the passing tip vortices at the spacial locations[103]. At these wake ages, the instantaneous computed results and phase-averaged measurements were in good agreement. At $r/R \approx 0.9$ both data sources contained the high gradient in the velocity profile, caused by the blade tip vortices passing through the line of data extraction. For $\psi_b = 0°$ excellent agreement was observed for $C_T/\sigma = 0.06$; see Fig. 6.5a. Larger differences were seen for higher blade loadings potentially caused by blade deformations (blade flapping), which was not modeled in the numerical simulations, and the higher wake contraction in the numerical simulations; see chapter 6.1.1.2. Moreover, for increasing ψ_b the correlations showed increasing deviations between the experimental and numerical data, likely caused by increased vortex dissipation in the simulations (reduced velocity peak in Fig. 6.5d). In addition, the tip vortices had already been convected further downstream at older wake ages. Therefore, the velocity distributions were more uniform along the complete span of the blade. Based on the comparison it could be concluded that all main flow field characteristics were computed correctly in terms of magnitude. Moreover, excellent agreement was found at radial locations close to the rotor blade axis. The corresponding sectional thrust distributions are shown in Fig. 6.6.

Besides extracting velocity distributions in radial direction at fixed blade azimuth angles, axial velocity variations were extracted over one complete rotor revolution at fixed coordinates in space; see Fig. 6.7. Data was probed below, at, and above the rotor blade ($\Delta z/c = -1.00,\ 0.00,\ 0.34$) at two radial locations ($r/R = 0.75$ and $r/R = 0.85$). The experimental results at $\Delta z/c = 0$ were interpolated from the values above and below the blade. Overall the phase-averaged experimental data consisted of 670 rotor revolutions, recorded at a capture rate of 44 images per revolution[103].

Two distinct locations were observed in the velocity distribution which were caused by blade passage ($\psi_b = 0°$ and $\psi_b = 180°$). The effect of blade bound circulation manifested as an increase in velocity magnitude immediately after the blade passage (downwash) and a decrease immediately before (upwash). Differences between the radial locations were small for $\Delta z/c = 0$ and $\Delta z/c = 0.34$. Furthermore, as expected, an increased blade loading resulted in an increased average axial velocity magnitude, while keeping the overall characteristic of the temporal evolution unchanged. Moreover, the effect of the blade tip vortices was significantly reduced when moving from $r/R = 0.85$ to $r/R = 0.75$, i.e., further away from the rotor slip stream boundary. At $r/R = 0.75$ a lower velocity fluctuation amplitude was observed; compare Figs. 6.7f and 6.7c.

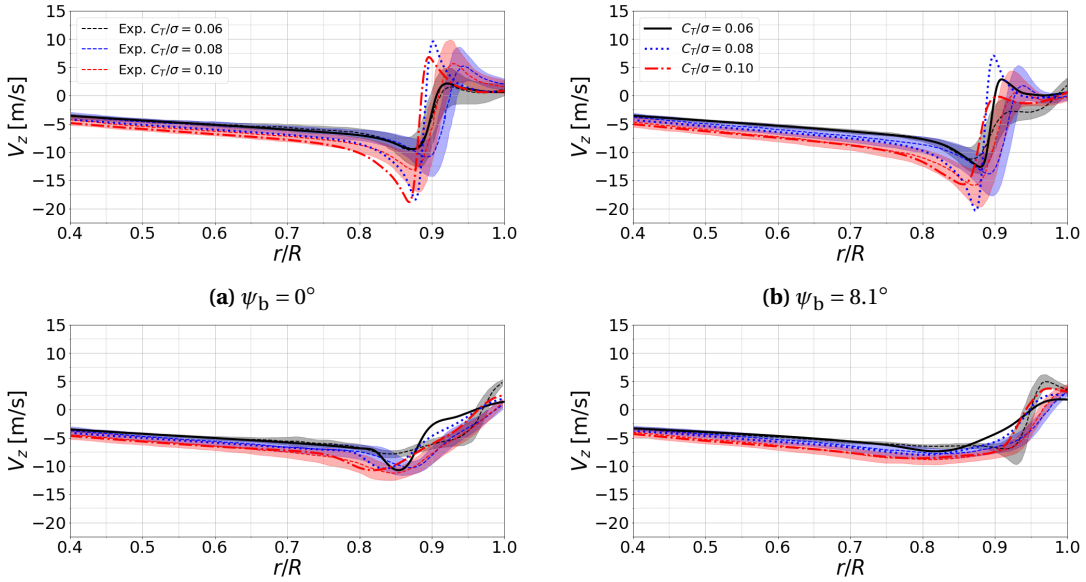

(a) $\psi_b = 0°$ **(b)** $\psi_b = 8.1°$

(c) $\psi_b = 48.6°$ **(d)** $\psi_b = 89.1°$

Figure 6.5.: Comparison of radial distributions of axial velocity between experiment[103] and CFD for the two-bladed single rotor based on the UTA CCR rotor test rig. Data was extracted one chord below the rotor blades ($\Delta z/c - 1$) at $C_T/\sigma = 0.06$, 0.08, and 0.10 at various rotor blade azimuth angles ψ_b. Shaded region represents one standard deviation of the experimental results.

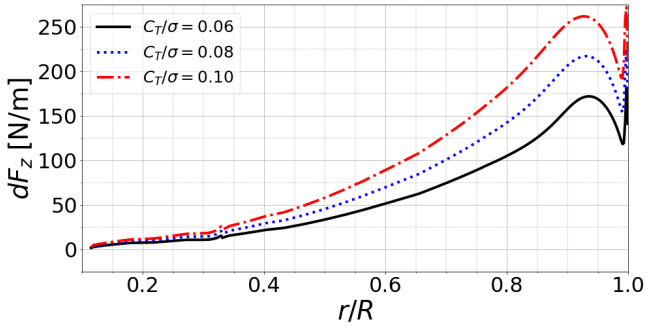

Figure 6.6.: Comparison of radial distribution of sectional thrust dF_z for the two-bladed single rotor based on the UTA CCR rotor test rig. Data was extracted at $C_T/\sigma = 0.06$, 0.08, and 0.10.[114]

The numerical data was extracted at intervals of $\Delta\psi_b = 1°$. It showed good agreement with the experimental data for all spacial locations. Due to the higher temporal resolution compared to the experimental data ($\Delta\psi_b = 8.2°$[103]), the effects of blade passage were more distinct in the numerical results. Excellent agreement between simulation and experiment was seen at $r/R = 0.75$ for all probing locations and at $r/R = 0.85$ for $\Delta z/c = -1.0$. It is noteworthy that the correlation at $r/R = 0.75$ and $\Delta z/c = 0$ was comparable to the other locations. Here, the experimental data was interpolated from above and below the probing location, while the numerical results could directly be extracted. This indicated that a simple interpolation to determine the axial velocity at the rotor blade gave good results for the single rotor[122]. Larger differences were observed at $r/R = 0.85$ for $\Delta z/c = 0.34$ and $\Delta z/c = 0$, while showing the same trends.

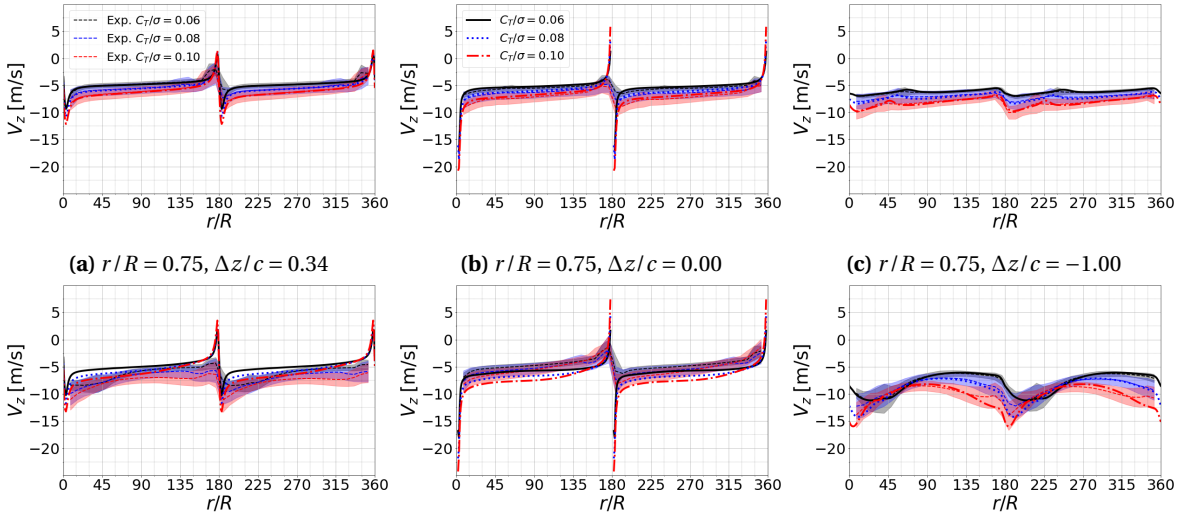

(a) $r/R = 0.75$, $\Delta z/c = 0.34$ **(b)** $r/R = 0.75$, $\Delta z/c = 0.00$ **(c)** $r/R = 0.75$, $\Delta z/c = -1.00$

(d) $r/R = 0.85$, $\Delta z/c = 0.34$ **(e)** $r/R = 0.85$, $\Delta z/c = 0.00$ **(f)** $r/R = 0.85$, $\Delta z/c = -1.00$

Figure 6.7.: Comparison of phase-averaged axial velocity (v_z) normalized by rotor blade tip speed (V_{tip}) between experiment[103] and simulation for the two-bladed single rotor based on the UTA CCR rotor test rig. Data shown over one revolution for $C_T/\sigma = 0.06$, 0.08, and 0.10 above, below, and in the rotor plane. Blade passage occurs at $\psi_b = 0°$ and 180°. Shaded region represents one standard deviation of the experimental results.

6.1.2. Two-by-Two-Bladed CCR Rotor

Experiments were performed at UTA for a two-by-two-bladed CCR rotor setup at a blade loading of $C_T/\sigma = 0.085$; see chapter 3.2.2. Experimental data was previously published in joint publication by the experimenters and the author of this thesis[101, 114]. This data set was subsequently correlated to simulation results, and used to investigate the effects of using different turbulence models. Moreover, the effects of varying blade loadings ($C_T/\sigma = 0.06$, 0.08, and 0.10) were assessed using the best performing turbulence model. For the latter, the blade loading levels were selected based on the previously described investigations for the single rotor; see chapter 6.1.1.

For all comparisons and correlations, the rotor was trimmed to the corresponding thrust and was torque balanced; see chapter 4.6. Grid resolution and time step sizes were chosen according to the temporal sensitivity study[6]; see chapter 4.5.2.6. Moreover, for CCR rotors the flow field is no longer a function of wake age only, but also of the plane of data extraction (azimuthal location in space). Therefore, two different vertical planes of data extraction were used in the subsequent discussions; see Fig 6.8. The planes were placed such that the flow field could be investigated during blade passage ($\xi = 0°$) and at a maximum distance to blade passage, where only one rotor blade crossed at a time ($\xi = 45°$).

[6] $C_T/\sigma = 0.085$ using different turbulence models: 9 revolutions were computed with $\Delta\psi_b = 0.25°$ and 50 inner iterations; $C_T/\sigma = 0.06$, 0.08, and 0.10: 12 revolutions were computed with $\Delta\psi_b = 0.25°$ and 25 inner iterations

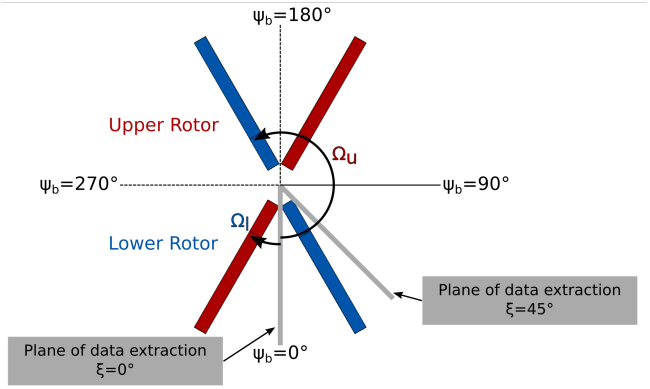

Figure 6.8.: Top view showing planes for data extraction for the UTA CCR rotor.

6.1.2.1. Flow Field

An experimental[101] time-averaged contour of axial velocity (v_z) superimposed by time-averaged in plane velocity vectors was compared to numerical results at $C_T/\sigma = 0.085$; see Fig. 6.9. The flow field shown in Fig. 6.9a comprised of three distinct regions[101]. The first region was located above $z/R = 0$, i.e., the region close to and above the upper rotor plane. Here, the velocity distribution was well comparable to that of an isolated single rotor; compare Fig. 6.2. The wake contraction inboard of $r/R = 0.95$ could be observed. An increase of velocity was observed between the rotor planes, along with a further contraction of the upper rotor slipstream boundary (region two). The amount of contraction caused fluid to be entrained from outside the upper rotor slipstream to enter the lower rotor plane close to the lower rotor blade tip. The region of highest velocity was located at $r/R \approx 0.75$. In region three, below the lower rotor plane, the lower rotor slipstream boundary could be observed at $r/R = 0.95 - 1.00$. The contraction of the lower rotor slipstream boundary was lower compared to the upper rotor. Due to the superposition of the induced velocity fields of the two rotor planes, the highest axial velocities were found to be below the lower rotor plane. The overall highest magnitude of the axial velocity was seen toward the outboard sections of the lower rotor blades ($r/R = 0.6 - 0.9$)[91, 121], an expected result for untwisted blades, where most thrust is produced at the outboard sections.

The numerical data showed comparable results and qualitatively all findings described before were computed correctly[114]; see Fig. 6.9b. From a quantitative perspective, it was found that the velocity magnitudes differed. A possible explanation for the differences are increased fluctuations in the experimental data. In the numerical simulations, the blade tip vortex trajectories showed negligible variations, while considerable fluctuations were observed in the experiment; see chapter 6.1.2.2. Time-averaging over long periods of time (520 rotor revolutions for the experimental data vs. 0.5 rotor revolutions for the numerical data) smeared out the region of highest velocities. As a consequence, the upper rotor slip stream boundary was clearly visible in the numerical simulations (even below the lower rotor blade), while it was not as clearly defined in the experimental velocity contour. Moreover, note that a recirculation region (upwash near the blade tip) formed below the lower rotor blade tip (similar to an isolated single rotor; see Fig. 6.2), which was not

visible for the upper rotor[7]. The findings were not altered by varying the turbulence model; see Fig. F.2.

A distinct difference was noted when comparing the results between the two different planes of data extraction[114]; compare Figs. 6.9b and 6.9c. At $\xi = 45°$ the upper rotor slipstream boundary contracted significantly less compared to $\xi = 0°$. The lower rotor slipstream boundary on the other hand only showed a little variation close to the blade tip (higher curvature at $\xi = 45°$). Hence, it could be concluded that the relative location of data extraction ($\xi = 0°$ vs. $\xi = 45°$) had a considerable influence for the time-averaged inflow of the lower rotor. The same flow field characteristics were visible for varying thrust levels and independent of the used turbulence model; see Figs. F.1 and F.2. A more detailed analysis is given in chapter 6.1.2.4.

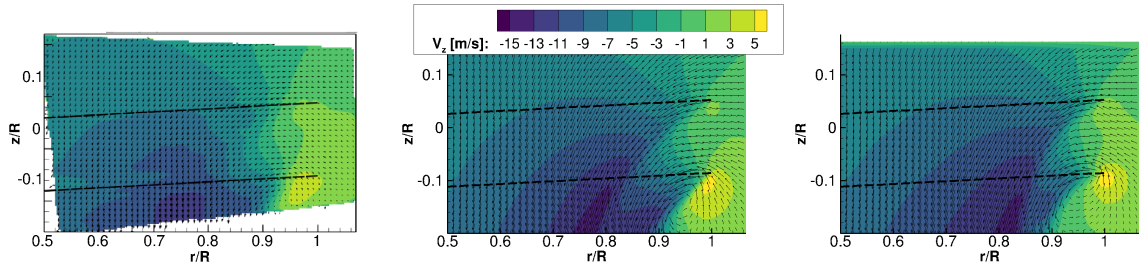

(a) Experiment[101]. Data extracted at $\xi = 0°$.

(b) CFD. Data extracted at $\xi = 0°$.

(c) CFD. Data extracted at $\xi = 45°$.

Figure 6.9.: Comparison of time-averaged axial velocity contours superimposed by in-plane velocity vectors between experiment[101] and simulation at $C_T/\sigma = 0.085$. Dashed lines indicate undeformed rotor blade axis. Experimental results recorded in increments of $\Delta\psi_b = 5.625°$ (data averaged over 520 rotor revolutions). Numerical results computed with the SA-neg-RC turbulence model and averaged over 0.5 rotor revolution in increments of $\Delta\psi_b = 3°$ (i.e., 60 slices averaged over $\Delta\psi_b = 180°$).

The effects of using different turbulence models on the computed flow fields were further analyzed at $C_T/\sigma = 0.085$ using instantaneous contours of total vorticity at two different index angles ($\phi = 0°$ and $-45°$); see Fig. 6.10. From a flow phenomenological perspective, all turbulence models showed similar results, i.e., the upper rotor tip vortices convected faster downward and inboard compared to the lower rotor tip vortices; see also chapter 6.1.2.2 or, e.g., [21]. Distinct vortex cores were seen below the lower rotor plane[144] at $\phi = 0°$ and significant interactions between the trailed vortex sheet and the upper rotor tip vortices were observed at $\phi = -45°$, irrespective of the used turbulence model. However, from a quantitative perspective, significant differences existed. The SST-SAS turbulence model diffused the tip vortices already significantly at a wake age of $\zeta = 180°$, i.e., during the first blade passage; see Fig. 6.10c at $\phi = 0°$. The SST-RC model showed only slight improvements over the SST-SAS model; see Fig. 6.10b. Best vortex conservation was achieved using the SA-neg-RC and SST-SAS-RC models; see Figs. 6.10a and 6.10d. These two models were the only ones which were able to preserve compact tip vortices down to the end of the refined grid region for improved vortex conservation; see red line Fig. 6.10a. However, the improved vortex preservation of the SST-SAS-RC model did not have a significant impact on the computed thrust and torque variations compared to the other two SST model variants; see chapter 6.1.2.5. A

[7] This flow phenomenon was previously described by other researchers. See, e.g., [88] where PIV measurements were made for a CCR rotor operated in a water tank

comparison of total vorticity contours for different blade loadings using the SA-neg-RC turbulence model is shown in Fig. F.3. Despite changing the absolute locations of the tip vortices and thus, the index angle where BVI occurred, the main flow features were identical.

The ability of the individual turbulence models to conserve compact tip vortices was further illustrated using Q-criterion isosurfaces colored by total vorticity; see Fig. 6.11. As described before, results computed with the SST-SAS model dissipated the tip vortices fastest. This could also be confirmed based on the corresponding isosurfaces; see Fig. 6.11c. The tip vortices showed significant core growth associated with reduced total vorticity levels. The overall higher vortex diffusion of the SST-RC and SST-SAS models also lead to less distinct, larger vortices below the lower rotor plane; see Figs. 6.11b and 6.11c. A further noticeable difference was observed between the SA-neg-RC and SST-SAS-RC models. In the flow field below the lower rotor, the SA-neg-RC model computed less vortical structures compared to the SST-SAS-RC model; compare Figs. 6.11a and 6.11d. This finding was similar to the observations made for the USNA rotor; see chapter 5.5.2. A comparison of Q-criterion isosurfaces for different blade loadings using the SA-neg-RC turbulence model is shown in Fig. F.4. Despite changing the absolute locations of the tip vortices and thus, the index angle where BVI occurs, the main flow features were identical.

Effects of using different turbulence models were also observed when comparing contours of eddy viscosity (μ_t); see Fig. 6.12. The contours were superimposed by level curves of total vorticity to indicate the locations of tip vortices and trailed vortex sheets. It was found that for the SA-neg-RC and SST-RC models, the average eddy viscosity levels were increased compared to the other two tested models. This was most pronounced close to the generic rotor hub assembly above the upper rotor plane and below the high-resolution grid region used to improve vortex conservation (red line in Fig. 6.12). Despite the increased values of eddy viscosity, the SA-neg-RC and SST-RC model showed superior vortex conservation over the SST-SAS model. Hence, it could be concluded that using RC correction terms in the turbulence model formulations was crucial for vortex preservation[84]. Furthermore, the positive effects of the SAS correction did not outweigh the drawbacks of not using RC corrections in the current application. However, combining the two approaches (i.e., using the SST-SAS-RC model) further improved the results.

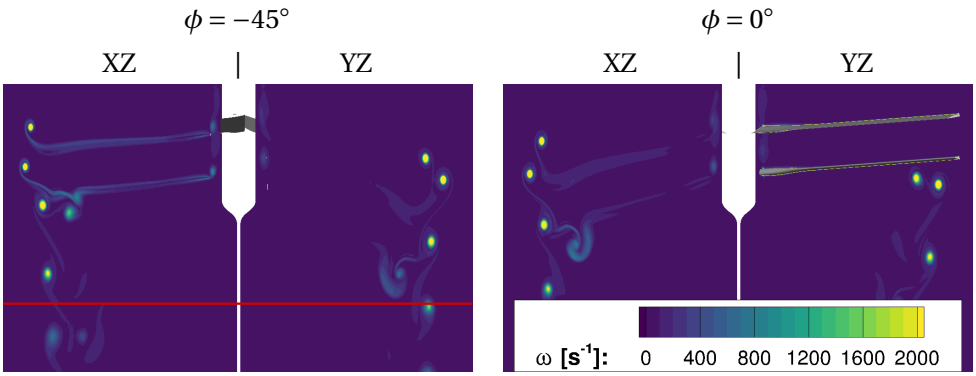

(a) SA-neg-RC

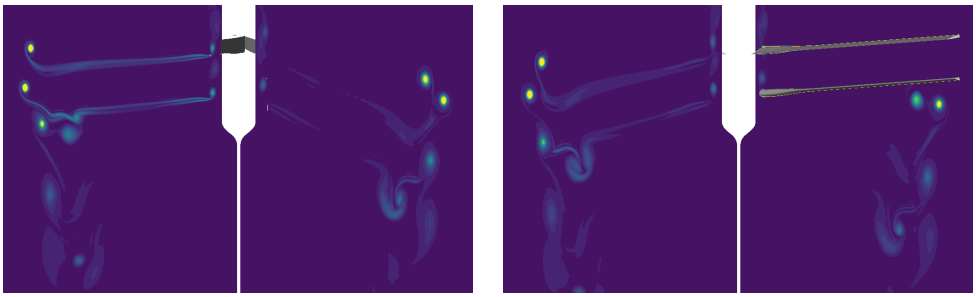

(b) SST-RC

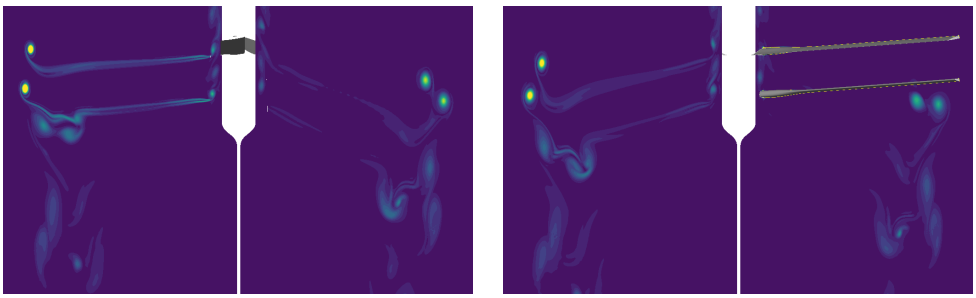

(c) SST-SAS

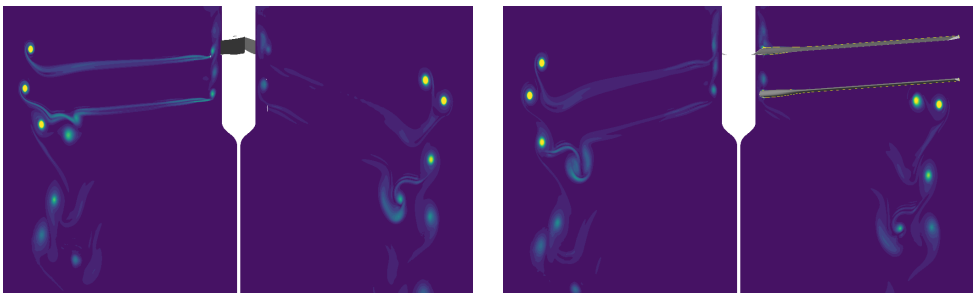

(d) SST-SAS-RC

Figure 6.10.: Comparison of total vorticity contours of the two-by-two-bladed CCR rotor ($C_T/\sigma = 0.085$) at multiple index angles ϕ using different turbulence models. Red line indicating end of high-resolution grid region for improved vortex preservation; see Fig. 4.22. Vorticity contours shown in two perpendicular vertical planes through the rotor shaft axis (XZ- and YZ-plane).

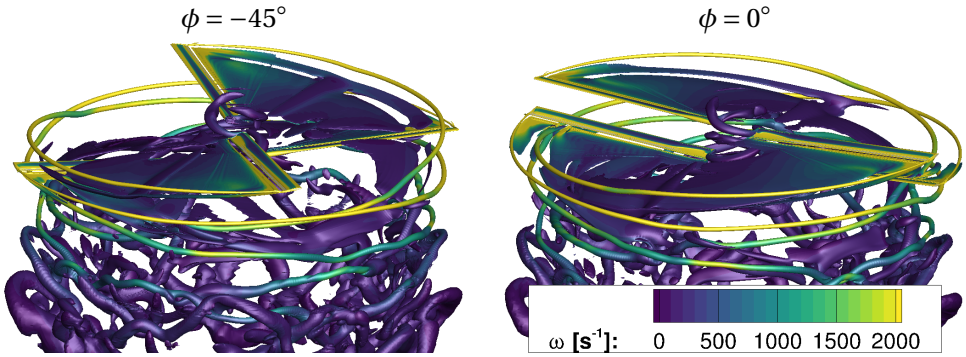

(a) SA-neg-RC

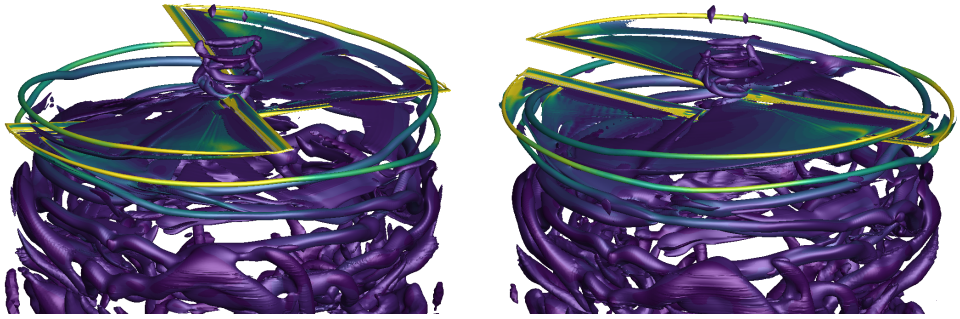

(b) SST-RC

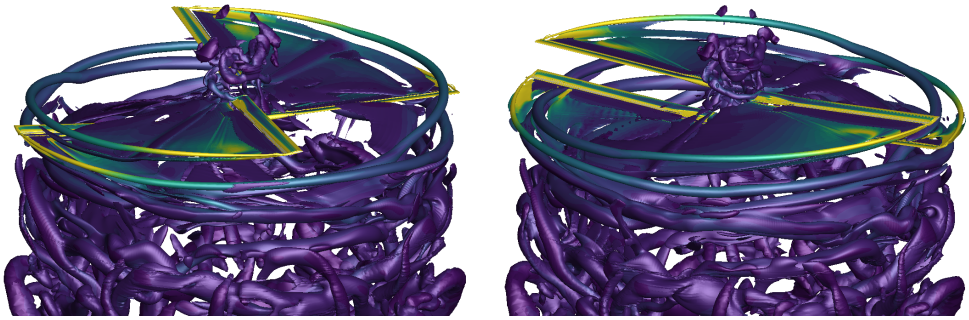

(c) SST-SAS

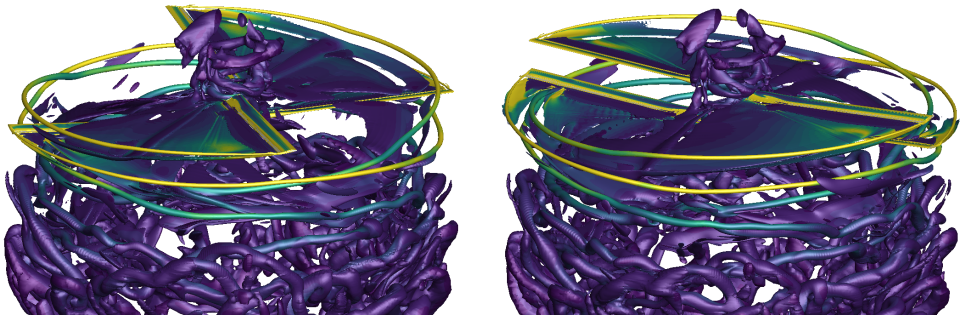

(d) SST-SAS-RC

Figure 6.11.: Comparison of computed vortical structures for the two-by-two-bladed CCR rotor (C_T/σ = 0.085) using different turbulence models and index angles ϕ. Vortices visualized by Q-criterion isosurfaces ($Q = 1500\ s^{-2}$) colored by total vorticity ω.

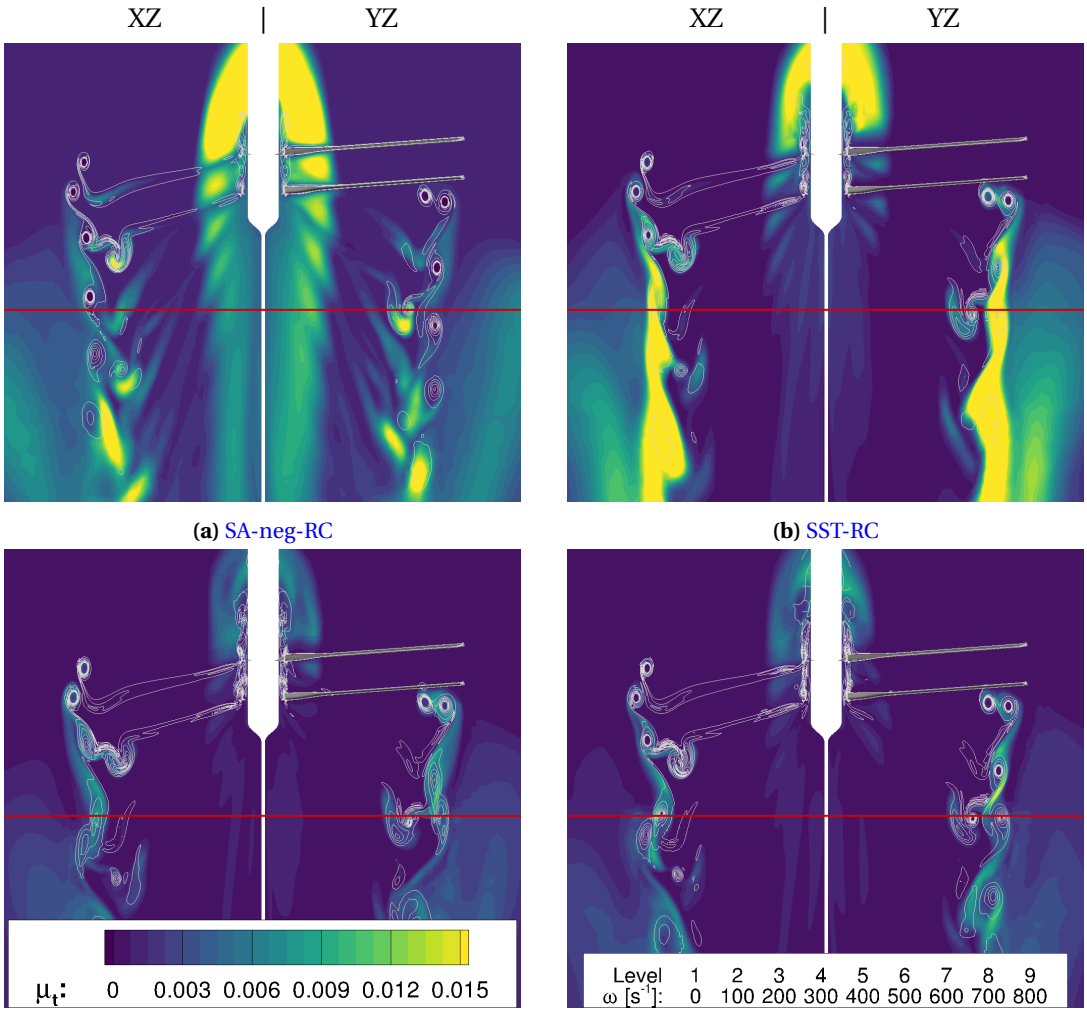

(a) SA-neg-RC **(b)** SST-RC

(c) SST-SAS **(d)** SST-SAS-RC

Figure 6.12.: Comparison of computed eddy viscosity μ_t contours for the two-by-two-bladed CCR rotor ($C_T/\sigma = 0.085$) using different turbulence models at $\phi = 0°$. Contours superimposed by level curves of total vorticity ω (gray). Red line indicating end of high-resolution grid region for improved vortex preservation; see Fig. 4.22. Eddy viscosity contours shown in two perpendicular vertical planes through the rotor shaft axis (XZ- and YZ-plane).

6.1.2.2. Tip Vortex Trajectories

A quantification of the findings from the time-averaged axial velocity contours (Fig. 6.9) and vorticity contours (Fig. 6.10) with respect to rotor wake contraction and vortex preservation was made by investigating blade tip vortex trajectories[114]. Measured and computed tip vortex trajectories were compared at $C_T/\sigma = 0.085$ in Fig. 6.13. Data was extracted using the algorithm described in chapter C[8]. As expected, the upper rotor tip vortex trajectory showed increased radial contraction and axial convection when compared to the lower rotor tip vortex[21]. The comparison between experimental data and simulation results showed that the upper rotor tip vortex trajectories matched well. Slight differences were observed for the lower rotor tip vortices. Here, the radial trajectory was well predicted, whereas a constant offset was observed for the axial displacement. An exact cause of this discrepancy could not be found. Note that no vortex collocation was made to account for blade deformations in the experiment in this comparison. Moreover, "due to reflection from the rotor blades, vortex core positions could not reliably be detected for low index angles, when the blades were close to the measurement plane. Furthermore, because of the limited camera field of view, the lower rotor tip vortices could only be detected for few phase angles before leaving the ROI"[101]. Besides, the tip vortex trajectories were only little affected by the choice of the turbulence model. Only the radial contraction of the lower rotor tip vortices showed slight differences when using the SST-SAS turbulence model after the first blade passage ($\zeta_l > 180°$); see Fig. 6.13a.

In addition, the effects of the location of data extraction on the tip vortex trajectories were investigated (i.e., data extraction at $\xi = 0°$ and $45°$ to determine the effects of the overall four-per-rev characteristic of the two-by-two-bladed CCR rotor[11]; see Fig. 6.8). The axial tip vortex displacements of the lower rotor showed a characteristic kink during the first blade passage ($\zeta_l = 180°$) for data extraction at $\xi = 0°$; see Fig. 6.14b. This behavior is well known from isolated rotors; see Figs. 5.7 and 6.3b. The upper rotor tip vortices, on the contrary, showed smoother, more gradual trajectories, which were less effected by blade passage. When data was extracted at $\xi = 45°$ neither of the two trajectories (upper and lower rotor) showed the characteristic kink; see Fig. 6.15b. Hence, it could be concluded that the upper rotor tip vortices experienced a constant influence from the superimposed flow fields of the upper and lower rotor, while this was only true for the lower rotor if data was extracted at $\xi = 45°$. Despite these differences, the axial tip vortex displacements of the lower rotor were well comparable between the two planes of data extraction. The axial convection barely showed any influences; see Fig. F.6b. Larger differences were observed for the upper rotor, especially as BVI occurred close to $\xi = 0°$. At $\xi = 45°$ the tip vortices could be tracked significantly longer as they were not diffused so quickly, i.e., no BVI event took place near the plane of data extraction; see also Fig. F.5b. Overall, a higher blade loading led to increased axial displacements of the tip vortices, as expected.

When comparing the radial contraction in the two planes, it was found that the upper rotor tip vortices contracted faster and further in plane $\xi = 0°$ compared to $\xi = 45°$; compare Figs. 6.14a and 6.15a and see Figs. F.5a and F.7. This was in line with the findings for the time-averaged contours of axial velocity in the two planes of data extraction; see Figs. 6.9, F.1, and F.2.

[8] Exp. threshold[101]: $\Gamma_{1,\min} \geq 0.8$; CFD threshold: $\Gamma_{1,\min} \geq 0.23$ and $\overline{\omega}_{\min} \geq 450\,s^{-1}$

The lower rotor tip vortices showed an increased radial contraction at $\xi = 45°$ compared to $\xi = 0°$; compare Figs. 6.14a and 6.15a and see Figs. F.6a and F.7. This caused the upper and lower rotor tip vortices to approach each other more at $\xi = 45°$; see Fig. F.7.

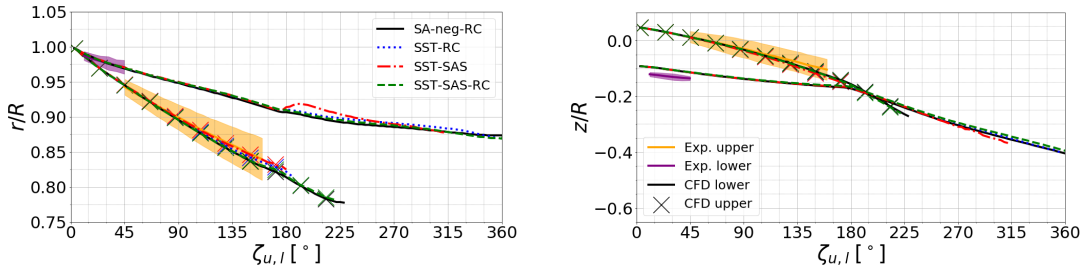

(a) r/R vs ζ **(b)** z/R vs ζ

Figure 6.13.: Comparison of measured[101] and computed radial (r/R) and axial (z/R) tip vortex displacements for the two-by-two-bladed CCR rotor using different turbulence models at $C_T/\sigma = 0.085$. Data extracted at $\xi = 0°$; see Fig. 6.8.

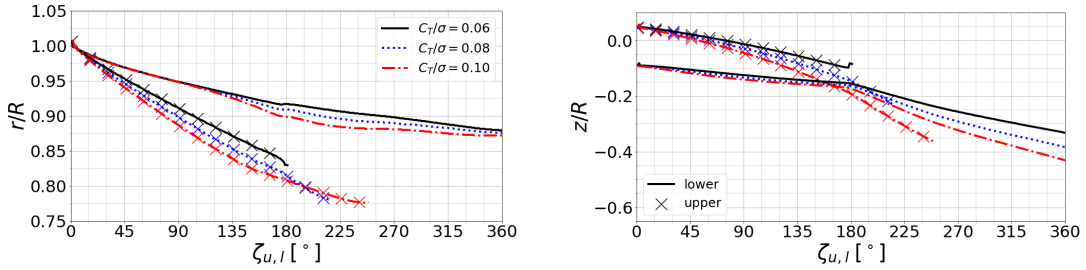

(a) r/R vs ζ **(b)** z/R vs ζ

Figure 6.14.: Comparison of computed radial (r/R) and axial (z/R) tip vortex displacements for the two-by-two-bladed CCR rotor at $C_T/\sigma = 0.06$, 0.08, and 0.10. Results computed using the SA-neg-RC turbulence model. Data extracted at $\xi = 0°$; see Fig. 6.8.

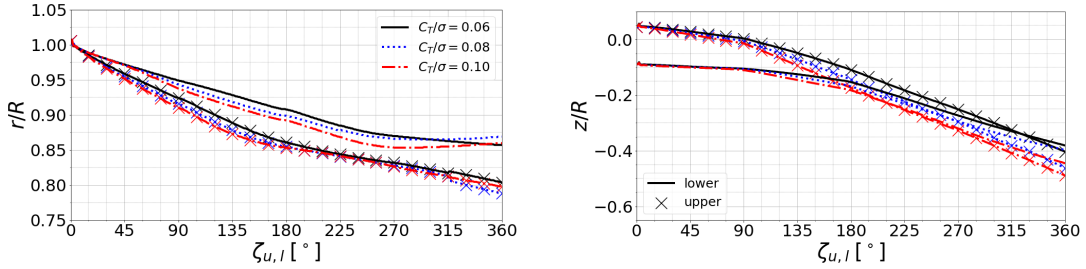

(a) r/R vs ζ **(b)** z/R vs ζ

Figure 6.15.: Comparison of computed radial (r/R) and axial (z/R) tip vortex displacements for the two-by-two-bladed CCR rotor at $C_T/\sigma = 0.06$, 0.08, and 0.10. Results computed using the SA-neg-RC turbulence model. Data extracted at $\xi = 45°$; see Fig. 6.8.

6.1.2.3. Tip Vortex Size and Strength

Besides the tip vortex trajectories, the tip vortex characteristics are of importance for a rotor flow field, especially in hover. Therefore, computed tip vortex circulation (Γ), core radius (r_c), and half peak-to-peak velocities (V_{hpp}) were investigated. Comparisons were made using different turbulence models ($C_T/\sigma = 0.085$) and blade loadings ($C_T/\sigma = 0.06$, 0.08, and 0.10). The circulation was computed by integrating the out-of-plane vorticity over a square region centered around the detected tip vortices. The integration region had a size of $48\,x\,48$ mm ($0.6\,x\,0.6$ c), identical to the single rotor data processing; see chapter 6.1.1.3. Values are shown up to wake ages ζ where a distinct inflection point could be found in the velocity profiles[9].

A comparison between the different turbulence models is shown in Fig. 6.16. In line with the previously described tip vortex evolution based on investigating the flow fields, the SST-SAS and SST-RC models showed the highest tip vortex growth rates associated with the lowest swirl velocity magnitudes. In particular, the SST-SAS model predicted excessive, almost identical vortex core growth for the upper and lower rotor tip vortices. The SA-neg-RC and SST-SAS-RC models showed well comparable trends and absolute values for r_c and V_{hpp} in the complete range of wake ages shown. When looking at the tip vortex circulation (Γ) all SST based models showed an increase at young wake ages compared to the SA-neg-RC model, before falling below the SA-neg-RC model value. A similar behavior was previously seen for the USNA test case, although, at higher wake ages; see chapter 5.3. Moreover, it should be kept in mind that all of the turbulence models overpredicted r_c and underpredicted V_{hpp} for the USNA test case, despite capturing the right trends.

A distinct difference between the upper and lower rotor tip vortices was observed irrespective of the turbulence model. The lower rotor showed increased Γ and V_{hpp}, as well as reduced r_c values compared to the upper rotor. In an experimental study published by the experimenter and the author on a one-by-one-bladed CCR rotor a similar behavior was observed for r_c and V_{hpp} up to the analyzed wakes of $\zeta_{u,l} = 180°$[101]. This change in V_{hpp} along with an increased growth of the upper rotor tip vortex core radii resulted in the reduced levels of Γ for the upper rotor. Both trends were observed despite the upper rotor producing more thrust to achieve torque balance, which is usually associated with larger V_{hpp} values. Note that the integration region to compute Γ was kept constant for the upper and lower rotor, i.e., it was not increased for increasing vortex core radii.

A comparison of tip vortex characteristics at multiple blade loadings is shown in Figs. 6.17 and 6.18 for two different planes of data extraction ($\xi = 0°$ and 45°; see Fig. 6.8). As excepted, increased thrust values raised Γ and V_{hpp}. The tip vortex core radius was only little affected at young wake ages[167], with the upper rotor tip vortex growing considerably after $\zeta_u = 180°$ at $\xi = 45°$. A direct comparison of the upper and lower rotor tip vortex characteristics in the two planes of data extraction is in addition shown in Figs. F.8 and F.9. Vortices originating at these two locations were created when the rotor blades were at comparable thrust levels; see chapter 6.1.2.5. The temporal evolution of all quantities was well comparable in the planes of data exaction for the lower rotor; see Fig. F.9. Differences increased with increasing blade loading. Moreover, the vortex core growth was increased at $\xi = 0°$. Trends were similar for the upper rotor with a stronger dependency on blade loading; see Fig. F.8.

[9] See [106] for an experimental study into low-dimensional characteristics of CCR rotor tip vortices in hover.

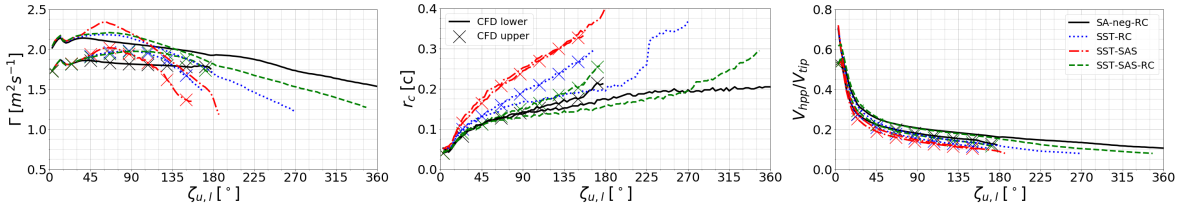

(a) Γ. **(b)** r_c. **(c)** V_{hpp}.

Figure 6.16.: Comparison of computed tip vortex circulation (Γ), core radii (r_c) as fraction of blade chord (c), and half peak-to-peak velocities (V_{hpp}) normalized by the blade tip velocity (V_{tip}) for the two-by-two-bladed CCR rotor at $C_T/\sigma = 0.085$ using different turbulence models. Data extracted at $\xi = 0°$; see Fig. 6.8.

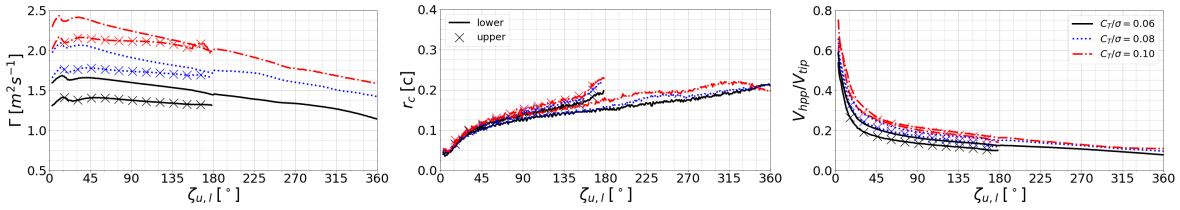

(a) Γ. **(b)** r_c. **(c)** V_{hpp}.

Figure 6.17.: Comparison of computed tip vortex circulation (Γ), core radii (r_c) as fraction of blade chord (c), and half peak-to-peak velocities (V_{hpp}) normalized by the blade tip velocity (V_{tip}) for the two-by-two-bladed CCR rotor at $C_T/\sigma = 0.06$, 0.08, and 0.10. Results computed using the SA-neg-RC turbulence model. Data extracted at $\xi = 0°$; see Fig. 6.8.

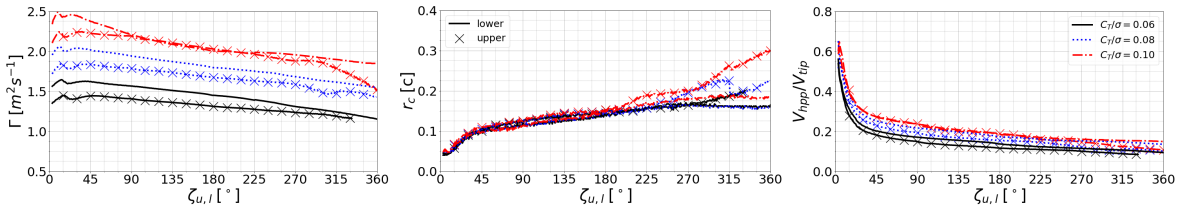

(a) Γ. **(b)** r_c. **(c)** V_{hpp}.

Figure 6.18.: Comparison of computed tip vortex circulation (Γ), core radii (r_c) as fraction of blade chord (c), and half peak-to-peak velocities (V_{hpp}) normalized by the blade tip velocity (V_{tip}) for the two-by-two-bladed CCR rotor at $C_T/\sigma = 0.06$, 0.08, and 0.10. Results computed using the SA-neg-RC turbulence model. Data extracted at $\xi = 45°$; see Fig. 6.8.

6.1.2.4. Rotor Inflow

Axial velocity distributions parallel the rotor blades were extracted at multiple different locations above, between, below, and in the rotor planes. To facilitate a comparison of flow features with the single rotor experimental and computational data, locations were selected with respect to the two rotor planes as defined in [103]; see chapter 6.1.1.4. In addition, a further line for data extraction was defined between the two rotor planes ($\Delta z/c = -0.875$). An illustration of these locations with respect to the coaxial rotor setup is shown in Fig. 6.19.

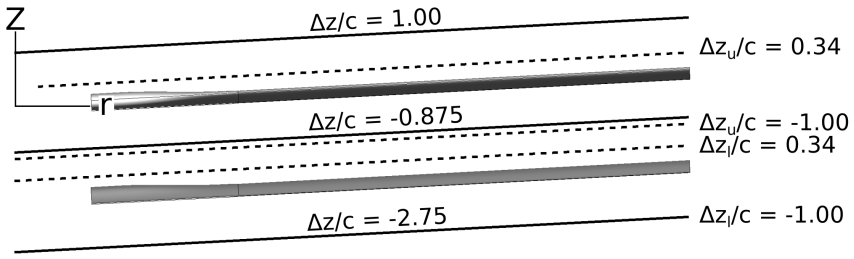

Figure 6.19.: Visualization of lines of data extraction.

Time-averaged velocity contours were plotted in chapter 6.1.2.1 in two different vertical planes; see Fig. 6.8. It was found that the flow field showed a strong dependency on the location of data extraction. A different way to visualize this dependency was used in Fig. 6.20 where time-averaged axial velocity data were extracted in conical slices defined by the rotor blade axis. The time-averaged axial velocity distribution showed a clear four-per-revolution signature (i.e., four blade crossings per revolution) when data was extracted between the upper and lower rotor blades ($\Delta z/c = -0.875$) and below the lower rotor blade ($\Delta z/c = -2.75$); see Fig. 6.19. This characteristic was less dominant above the upper rotor plane, albeit still visible. The axial velocity distributions were highly biased towards the tip, as expected for untwisted rotors.

Time-averaged axial velocity distributions were further quantified by extracting data parallel to the blade axis in the two different vertical planes and at three different axial offsets[10]; see Fig. 6.21. It was found that the time-averaged axial velocity above the upper rotor blade was practically independent of the location of data extraction, with the velocity magnitude increasing as the blade loading was increased. A similar trend was observed between the rotor planes. Only close to the blade tip (at $r/R \approx 0.85$) slight differences were observed between the two planes of data extraction. Higher velocity magnitudes were seen at $\xi = 0°$, i.e., when the plane of data extraction was located at the location of blade crossing. Below the lower rotor plane, distinct differences could be observed for $r/R > 0.65$. At this location the differences in vortex trajectories between the two planes of data extraction (see chapter 6.1.2.2) were significant enough to cause major differences in the time-averaged velocity profiles. At $\xi = 45°$ an altered, time-averaged wake contraction was observed, in line with the axial velocity contours shown in Figs. 6.9c, F.1, and F.2. For $r/R < 0.65$ the velocity profiles were basically identical, i.e., not influenced by the observed differences in the tip vortex trajectories. Note that the selection of the two planes of data extraction had a significant influence on the inflow distribution, and other choices of ξ lead to different velocity profiles. Both locations were selected based on the distance to blade passage and not based on, e.g., maximum and minimum average axial velocity or velocity variations; see Fig. 6.20.

[10] see also [91, 121] for similar comparisons

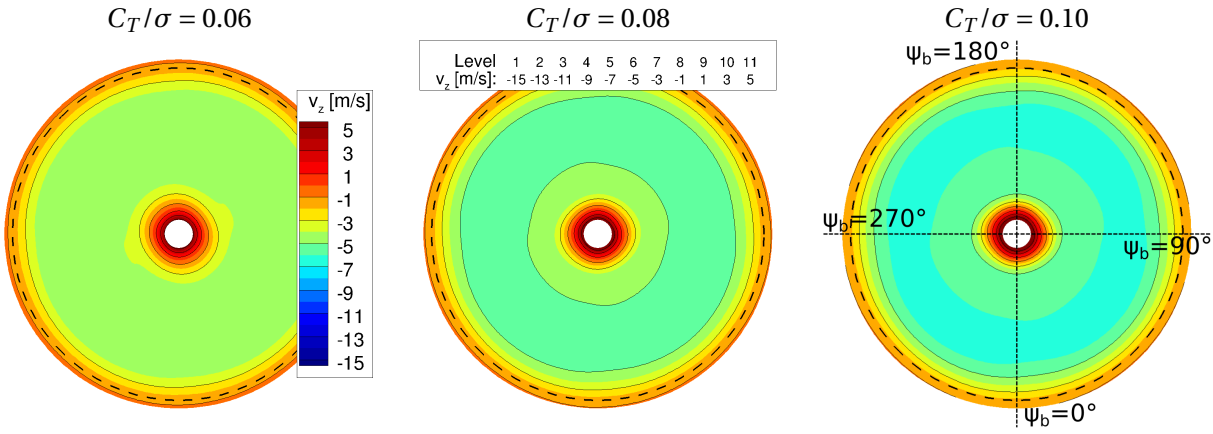

(a) $\Delta z/c = 1.0$.

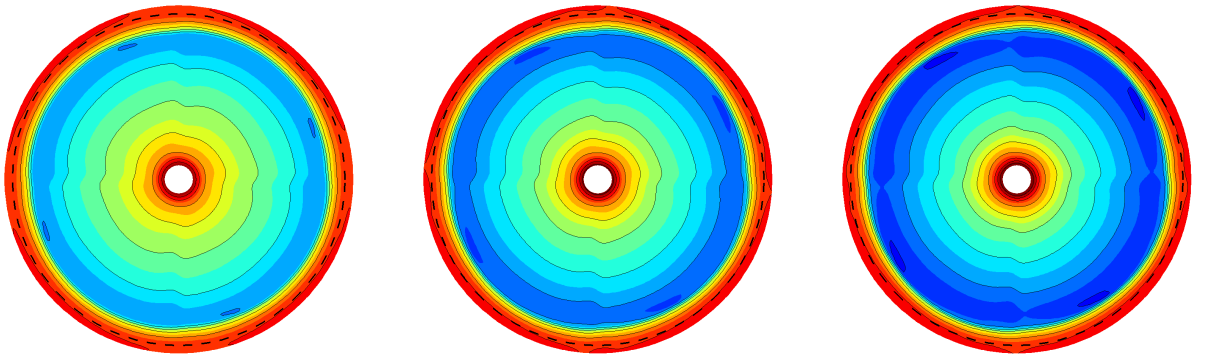

(b) $\Delta z/c = -0.875$.

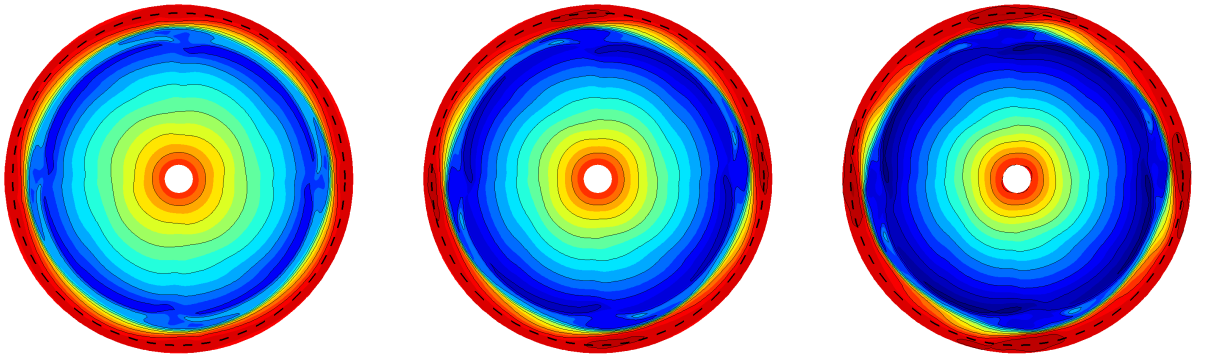

(c) $\Delta z/c = -2.75$.

Figure 6.20.: Comparison of contours of time-averaged axial velocity distributions in slices defined by the rotor blade axis for the two-by-two-bladed CCR rotor at $C_T/\sigma = 0.06$, 0.08, and 0.10 using the SA-neg-RC turbulence model. Data extracted at three different locations with respect to the upper and lower rotor plane rotor blades respectively; $\Delta z/c = 1.0$ (1 chord above upper rotor blades), $\Delta z/c = -0.875$ (centered between the rotor planes), and $\Delta z/c = -2.75$ (1 chord below the lower rotor blades); see Fig. 6.19. Dashed line indicating rotor diameter.

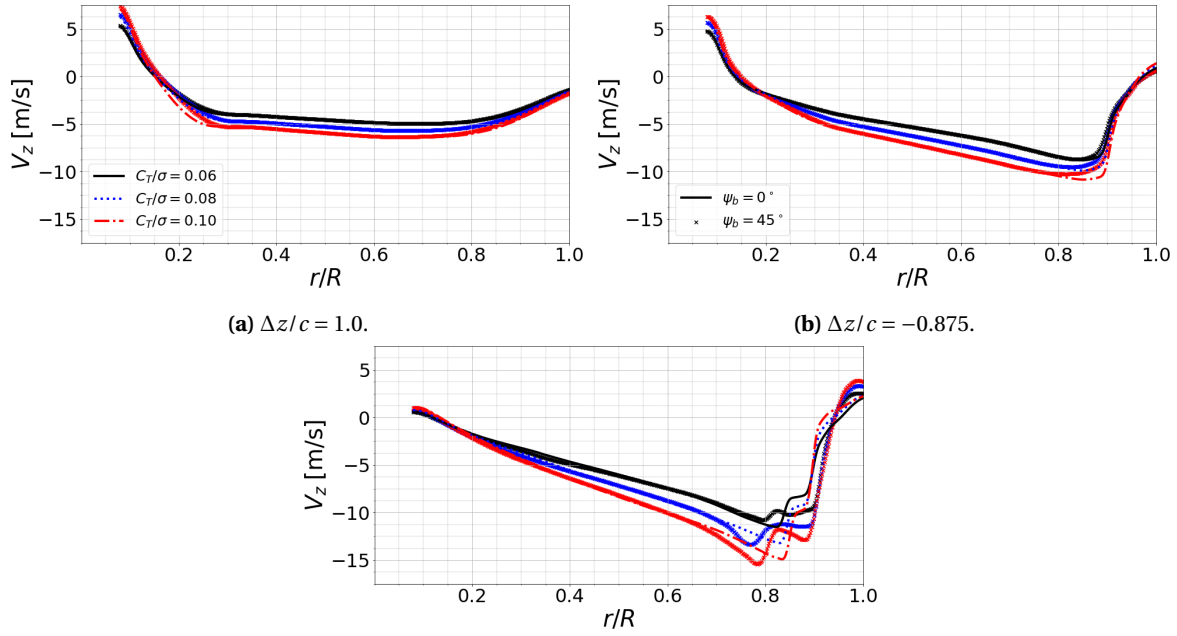

(a) $\Delta z/c = 1.0$.

(b) $\Delta z/c = -0.875$.

(c) $\Delta z/c = -2.75$.

Figure 6.21.: Comparison of time-averaged computed radial distributions of axial velocity for the two-by-two-bladed CCR rotor at $C_T/\sigma = 0.06$, 0.08, and 0.10 using the SA-neg-RC turbulence model. Data extracted at two different azimuthal locations (in plane of blade crossing ($\xi = 0°$) and offset by 45° ($\xi = 45°$); see Fig. 6.8) and three different locations with respect to the upper and lower rotor plane rotor blades respectively; $\Delta z/c = 1.0$ (1 chord above upper rotor blades), $\Delta z/c = -0.875$ (centered between the rotor planes), and $\Delta z/c = -2.75$ (1 chord below the lower rotor blades); see Fig. 6.19.

The time-averaged axial velocity distributions showed that a higher temporal dependency of the inflow in the lower rotor is to be expected. This could be confirmed by comparing the temporal evolution axial velocity at $r/R = 0.75$ for the upper and lower rotor at $C_T/\sigma = 0.085$; see Fig. 6.22. Here, experimental data[101] were correlated to numerical results computed with the SA-neg-RC turbulence model (the other tested turbulence models showed almost identical results). The experimental data was interpolated from quantities extracted at $\Delta z/R = 0.06$ above and below rotor planes and averaged over 520 rotor revolutions. The equivalent procedure was done for the averaged CFD quantities. In addition, numerical data was also extracted directly in the plane of the upper and lower rotor ($\Delta z_{u|l}/c = 0$).

The numerical results resembled the general characteristic of the experimental data well. However, an overall increased axial velocity magnitude was computed. Due to differences in the upper rotor thrust sharing between experiment (48.87%) and simulation (53.95%) slight differences were expected but could not be quantified[114]. The data directly extracted in the plane of the rotor blades showed larger gradients during blade passage compared ot the experimental data, whereas the averaged numerical results were in good agreement with the measurements. Overall, a comparison between the averaged and directly extracted numerical data showed only minor differences for the upper rotor. The difference was mainly caused by the upper rotor vortex sheet passing the lower point of data extraction for the interpolated values at $\psi_b \approx 30°$ and 210°. Dif-

ferences were more significant for the lower rotor plane. Here, differences in the time required to convect the trailed vortex sheets of the upper and lower rotor blades to the points of data extraction were responsible for the deviations. When directly extracting data at $\Delta z/c = 0$ only the upper rotor vortex sheet caused velocity fluctuations between blade passages. Hence, interpolating quantities from above and below the rotor blades lead to phase offsets with respect to the directly extracted quantities and additional oscillations in the velocity curve. As the upper rotor experiences less interactions in hover (no BVI and interactions with trailed vortex sheets) the effect of interpolating flow quantities were less distinct here[11]. Interpolated axial velocity values in the lower rotor plane are thus highly dependent on the thrust levels (convection velocity), distances of the points of data extraction to the rotor blades (time required to transport flow phenomena), and radial location (increased inflow velocities close to blade tips for untwisted blades and distance to tip vortices).

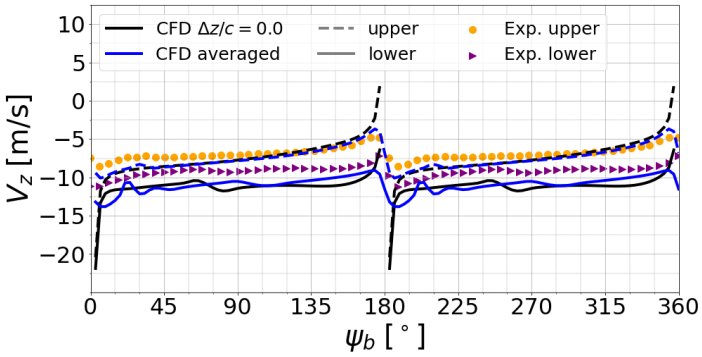

Figure 6.22.: Comparison of axial velocity (v_z) between experiment[101] and CFD for the two-by-two-bladed CCR rotor using the SA-neg-RC turbulence model[114]. Data is shown over one revolution at $C_T/\sigma = 0.085$ in the rotor plane at $r/R = 0.75$. Blade passage occurred at $\psi_b = 0°$ and 180°. Data extracted every $\Delta\psi_{b,\text{exp}} = 5.625°$, $\Delta\psi_{b,\text{sim}} = 3°$, respectively, at $\xi = 0°$; see Fig. 6.8.

Further insights into the temporal variation of axial velocity in the rotor planes were gained by analyzing numerical data computed with the SA-neg-RC turbulence model. Computations were made at different blade loadings and data was extracted at multiple vertical distances ($\Delta z_{u|l}/c$); see Fig. 6.19. Moreover, data were extracted at two different radial locations; see Figs. 6.23 and 6.24.

At first data were extracted in the plane of blade passage ($\psi_b = 0°$); see Fig. 6.23. The upper rotor inflow velocity distribution closely resembled the single rotor case; see Fig. 6.7. Note that despite the rotors being trimmed to the same blade loading, the overall thrust level was different in the rotor plane (two-bladed single rotor vs. trimmed two-by-two-bladed CCR rotor with larger thrust sharing in upper rotor; see Table 6.1). For the lower rotor at $r/R = 0.75$, secondary peaks were visible at axial distances of $\Delta z_l/c = 0.34$ and $\Delta z_l/c = 0.0$ at $\psi_b \approx 60°$ which were caused by the upper rotor trailed vortex sheets; see Figs. 6.23a and 6.23b. Their exact temporal occurrence was dependent on the thrust level. For higher thrust levels, the trailed vortex sheets convected downward faster and therefore, a lower temporal offset ($\Delta\psi_b$) was observed. This was further confirmed as the the secondary peak occurred at higher ψ_b values, i.e., later, when lowering the point of data

[11] Following a similar reasoning, interpolating velocity components from above and below for single rotors is often done; see e.g., [122, 113, 102, 103]

extraction from $\Delta z/c = 0.34$ to $\Delta z/c = 0.0$ and therefore, increasing the distance to the upper rotor blades. Below the upper rotor plane ($\Delta z/c = -1.0$), this secondary peak was also seen; see Fig. 6.23c. Below the lower rotor plane, the upper rotor tip vortex passed the point of data extraction at $C_T/\sigma = 0.08$, and 0.10 at a temporal offset from the vortex sheet (two distinct fluctuations in of the axial velocity with temporal offset); see Fig. 6.23c. At $C_T/\sigma = 0.06$, when BVI occurred close to the plane of data extraction, the vortex sheet passed the point of data extraction along with the upper rotor tip vortex after the BVI event. Hence, no large velocity fluctuation caused by the upper rotor tip vortex was observed at $C_T/\sigma = 0.06$ in the range of $0° \leq \psi_b \leq 45°$, as the tip vortex was highly diffused here; see Fig. F.3.

When extracting data further outboard at $r/R = 0.85$ the lower rotor inflow distribution changed considerably, while for the upper rotor the differences manifested mainly as an increase in overall inflow velocity and velocity gradients; see Fig. 6.23. The large amplitude fluctuations in the lower rotor inflow at $\Delta z/c = 0.34$ and $\Delta z/c = 0.0$ were caused by the upper rotor tip vortices. At $\Delta z/c = 0.34$ the upper rotor tip vortices passed the probing location at $r/R > 0.85$, while at $\Delta z/c = 0.0$ they passed at $r/R < 0.85$ for $C_T/\sigma = 0.08$, and 0.10 and almost directly at $r/R \approx 0.85$ for $C_T/\sigma = 0.06$. Hence, the upper rotor tip vortex caused increased downwash at $\Delta z/c = 0.34$ and upwash $\Delta z/c = 0.0$. Below the rotor plane, the inflow variations were comparable to $r/R = 0.75$. Individual plots for the upper and lower rotor inflow components at both radial locations are appended in Figs. F.10 and F.11.

By changing the vertical plane of data extraction from $\xi = 0°$ to $\xi = 45°$, the temporal variations of the axial velocity got significantly more complex; compare Figs 6.23 and 6.24. Here, the upper rotor passed the plane of data extraction at $\psi_b = 45°$ and $\psi_b = 225°$, while the lower rotor blade passes at $\psi_b = 135°$ and $\psi_b = 315°$. Therefore, a distinct four-per-rev characteristic was visible at all radial and axial locations caused by the four individual blade passages (at $\xi = 0°$ upper and lower rotor blades passed at the same time). This was even visible at $\Delta z/c = 0.34$ above the upper rotor ($\psi_b = 135°$ and $315°$); see Figs. 6.24a and 6.24d.

At $r/R = 0.75$ and $\Delta z/c = 0.34$ an additional peak before the lower blade passage ($\psi_b = 225°$ and $315°$) was visible in the lower rotor velocity curves for the higher two blade loadings. This peak was caused by the upper rotor trailed vortex sheet. As previously described, these fluctuations in the axial velocity were thrust and location dependent. As a consequence, at $\Delta z/c = 0.0$ this peak was only observed for $C_T/\sigma = 0.10$; see Fig. 6.24b.

At $r/R = 0.85$ and $\Delta z/c = 0.34$ the upper rotor plane inflow variations were comparable to $r/R = 0.75$ with an increased velocity magnitude. For the lower rotor plane, the large fluctuations before the upper rotor blade passage were caused by the upper rotor tip vortices; see Fig. 6.24d. If the thrust level was further increased BVI would occur at this location and consequently, the secondary peak would coincide with the velocity fluctuations caused by blade passage. When looking at the lower rotor plane at $\Delta z/c = 0.0$ the peaks before blade passage were significantly increased, due to a decreased distance between the tip vortices and the point of data extraction; see Fig. 6.24e.

At $r/R = 0.85$ and $\Delta z/c = -1.0$ the upper rotor plane inflow distribution showed the characteristic peaks of upper and lower rotor blade passage in addition to the peaks caused by the passage of

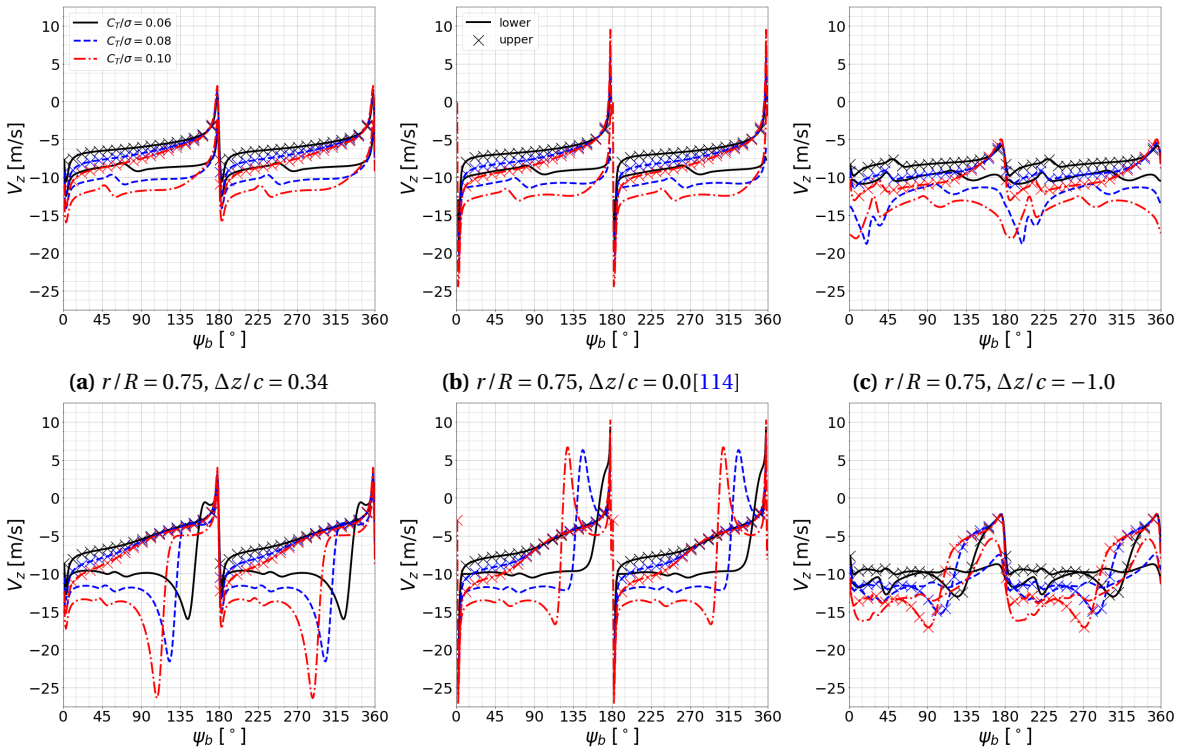

(a) $r/R = 0.75$, $\Delta z/c = 0.34$ **(b)** $r/R = 0.75$, $\Delta z/c = 0.0$[114] **(c)** $r/R = 0.75$, $\Delta z/c = -1.0$

(d) $r/R = 0.85$, $\Delta z/c = 0.34$ **(e)** $r/R = 0.85$, $\Delta z/c = 0.0$[114] **(f)** $r/R = 0.85$, $\Delta z/c = -1.0$

Figure 6.23.: Comparison of computed axial velocity (v_z) for the two-by-two-bladed CCR rotor at multiple radial locations r/R. Data shown over one revolution for $C_T/\sigma = 0.06$, 0.08, and 0.10 above, below, and in the rotor plane. Results computed using the SA-neg-RC turbulence model. Blade passage occurred at $\psi_b = 0°$ and 180°. Data extracted every $\Delta\psi_b = 1°$ at $\xi = 0°$; see Fig. 6.8. Axial offsets ($\Delta z/c$) are given with respect to the upper and lower rotor blades.

the upper rotor vortex sheet; see Fig. 6.24f. Moreover, the inflow distribution was superimposed by the swirl velocity of the upper rotor tip vortices. Depending on the blade loading the vortex passage occurred before the upper rotor blade passage ($C_T/\sigma = 0.06$), or slightly after the lower rotor blade passage ($C_T/\sigma = 0.10$). Hence, a strong dependency on the blade loading was visible with significantly altered velocity distributions (magnitudes and phasing of peaks).

This dependency was even more severe for the lower rotor plane. For $C_T/\sigma = 0.06$ at $\psi_b = 0°$ the lower rotor vortex sheet was passing the point of data extraction while interacting with the lower rotor tip vortex. The vortex itself passed to the right of the point of data extraction. Here, however, the reduction in axial velocity magnitude (spike towards positive axial velocities) was caused by the upper rotor tip vortex passing left of the point of data extraction. Due to a change in miss distance and phasing, this strong gradient was not observed for $C_T/\sigma = 0.10$, i.e., at this blade loading the axial velocity distribution showed a completely different behavior due to the chosen location for data extraction; compare also Figs. 6.23f and 6.24f. Hence, especially for the lower rotor towards the tip of the blades and when extracting data at $\xi = 45°$, care must be taken when interpolating the axial velocity in the rotor plane. Individual plots for the upper and lower rotor axial velocity at $\xi = 45°$ for both radial locations are shown in Figs. F.12 and F.13.

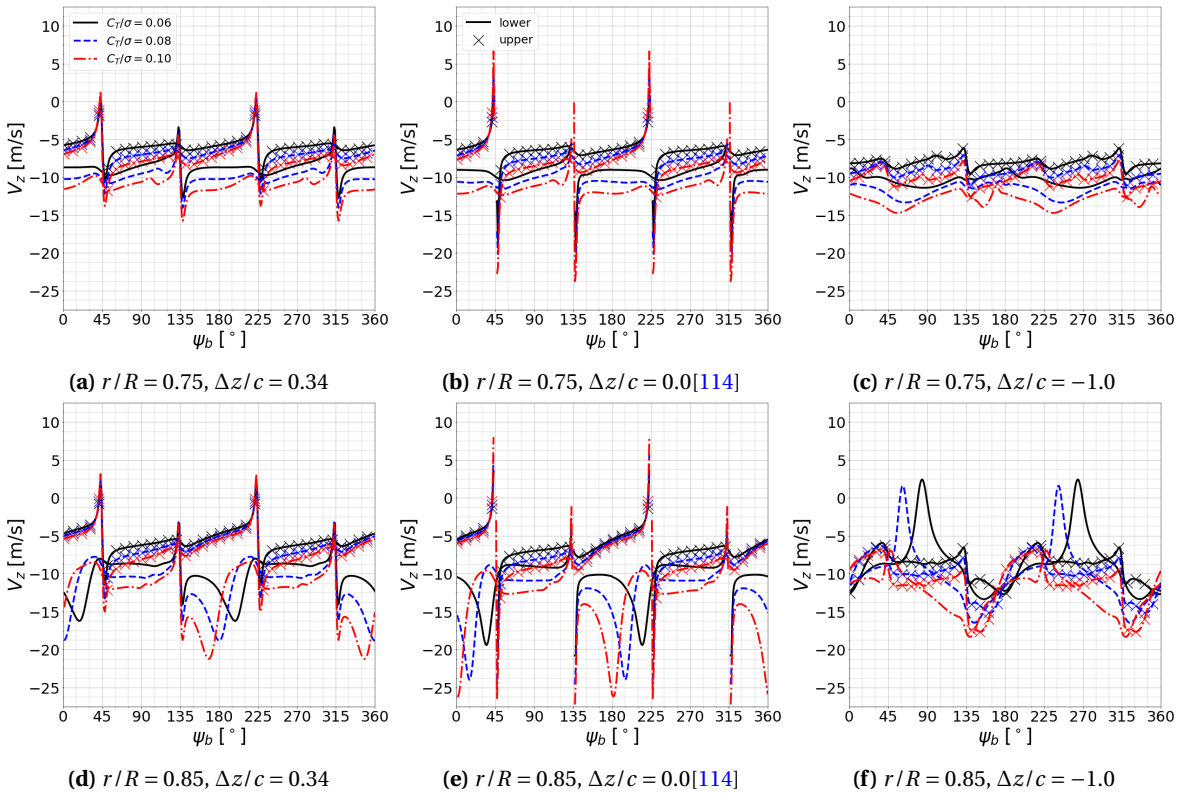

(a) $r/R = 0.75$, $\Delta z/c = 0.34$ **(b)** $r/R = 0.75$, $\Delta z/c = 0.0$[114] **(c)** $r/R = 0.75$, $\Delta z/c = -1.0$

(d) $r/R = 0.85$, $\Delta z/c = 0.34$ **(e)** $r/R = 0.85$, $\Delta z/c = 0.0$[114] **(f)** $r/R = 0.85$, $\Delta z/c = -1.0$

Figure 6.24.: Comparison of computed axial velocity (v_z) for the two-by-two-bladed CCR rotor at multiple radial locations r/R. Data shown over one revolution for $C_T/\sigma = 0.06$, 0.08, and 0.10 above, below, and in the rotor plane. Results computed using the SA-neg-RC turbulence model. Blade passage occurred at $\psi_b = 45°$ and 225° for the upper blade, and at $\psi_b = 135°$ and 315° for the lower blade. Data extracted every $\Delta\psi_b = 1°$ at $\xi = 45°$; see Fig. 6.8. Axial offsets ($\Delta z/c$) are given with respect to the upper and lower rotor blades.

The radial variation of axial velocity was further assessed in the two vertical planes of data extraction. Data was extracted at three axial distances: one chord above the upper rotor plane ($\Delta z/c = 1.0$), between the two rotor planes ($\Delta z/c = -0.875$), and one chord below the lower rotor plane ($\Delta z/c = -2.75$); see Fig. 6.19. As the two rotor blades pass the plane of data extraction $\xi = 45°$ at different times, data was extracted during the upper rotor blade passage ($\psi_{b,u} = 45°$) and during the lower rotor blade passage ($\psi_{b,l} = 135°$); see Fig. 6.25.

At $\Delta z/c = 1.0$, i.e., above the upper rotor blade, the inflow distribution was not affected by the plane of data extraction when the upper rotor blade was crossing the plane of data extraction ($\phi = 0°$ and $\psi_{b,u} = 45°$). Slight variations were only observed during the passage of the lower rotor blade ($\psi_{b,l} = 135°$). Similarly, at $\Delta z/c = -0.875$ the shape and magnitude of the inflow distribution was well comparable for $\phi = 0°$ and $\psi_{b,u} = 45°$ with only slight deviations at the outboard sections of the blade ($r/R > 0.6$). To the contrary, when only the lower rotor blade was in the plane of data extraction ($\psi_{b,l} = 135°$), a large variation of the axial velocity was observed close to the blade tip. This was caused by the upper rotor blade tip vortex, and hence, the strength of this peak showed a strong dependence on the blade loading. Blade stations at $r/R > 0.8$ were most affected. Below

the lower rotor plane ($\Delta z/c = -2.75$), the inflow variations showed a different behavior, depending both on the blade loading and the plane of data extraction. Depending on the axial convection velocity (i.e., blade loading) either one peak (mostly caused by lower rotor tip vortex), or two peaks (caused by both, upper and lower rotor tip vortices) in the inflow velocity were observed. This gave a second perspective on the different characteristics of the inflow time histories at $r/R = 0.75$ compared to $r/R = 0.85$ in the two planes of data extraction described before; see Figs. 6.23 and 6.24.

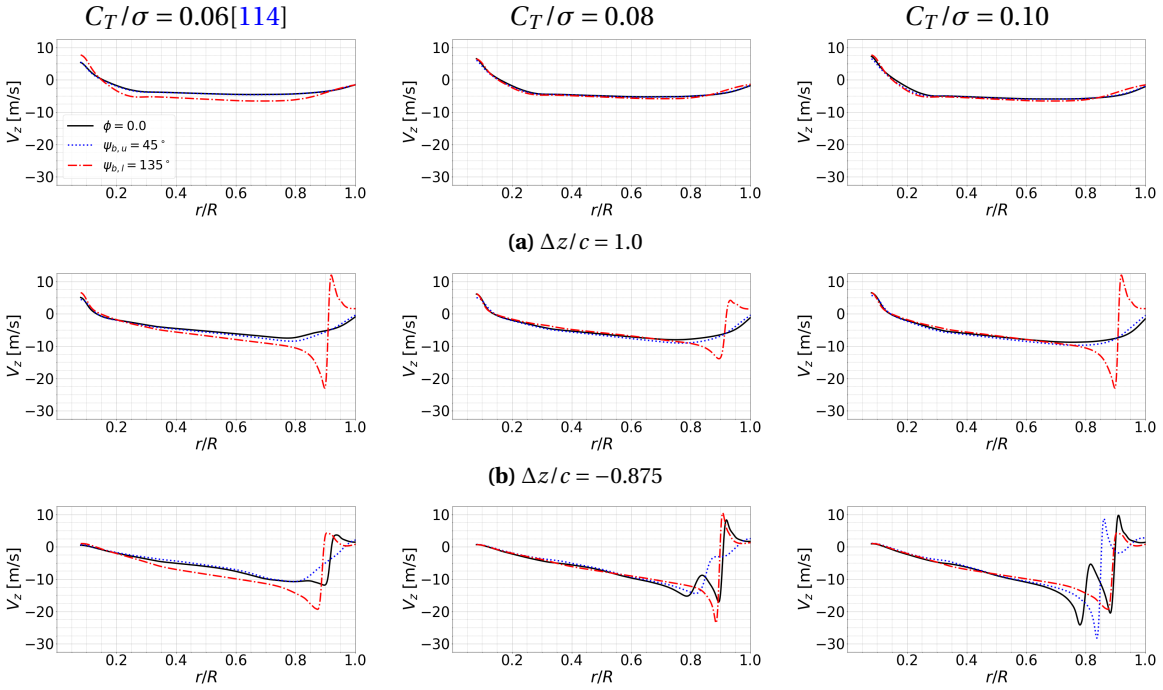

(a) $\Delta z/c = 1.0$

(b) $\Delta z/c = -0.875$

(c) $\Delta z/c = -2.75$

Figure 6.25.: Comparison of computed radial distributions of axial velocity for the two-by-two-bladed CCR rotor at $C_T/\sigma = 0.06$, 0.08, and 0.10 using the SA-neg-RC turbulence model. Data extracted at two different azimuthal locations; in plane of blade crossing ($\xi = 0°$) at $\phi = 0°$ (i.e., during upper and lower rotor blade crossing), and at $\xi = 45°$; see Fig. 6.8. For the latter, the upper rotor blade crossed the plane of data extraction at $\psi_{b,u} = 45°$ and the lower rotor blade at $\psi_{b,l} = 135°$, respectively.

6.1.2.5. Forces and Moments

The influences of using different turbulence models on the thrust and torque fluctuations are illustrated in Figs. 6.26 and 6.27. It could be seen that the upper rotor thrust did not show a significant dependence on the used turbulence model. Only the SST-SAS model results were somewhat different and showed marginally higher variations between successive blade passages. The lower rotor thrust showed a comparable behavior, with slightly higher variations between successive blade passages for all SST model variants compared to the SA-neg-RC model result. As the data were almost identical between the second and third blade passage ($\psi_b > 90°$) the results were considered practically independent of the used turbulence model. Higher differences were seen for the

torque coefficient. Overall, the computation using the SA-neg-RC model showed higher torque values compared to the SST type models ($\Delta C_Q \approx 2.9\%$)[114]. For the lower rotor, the SST-SAS model result slightly deviated from the other two model variants.

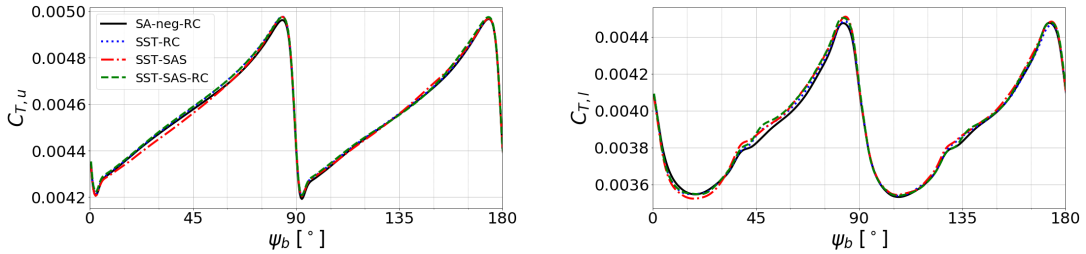

(a) $C_{T,u}$ **(b)** $C_{T,l}$

Figure 6.26.: Comparison of computed thrust (C_T) coefficients for the two-by-two-bladed CCR rotor at $C_T/\sigma = 0.085$ using different turbulence models.

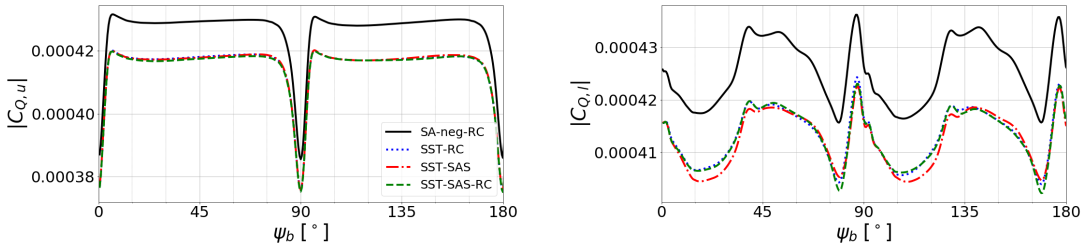

(a) $C_{Q,u}$ **(b)** $C_{Q,l}$

Figure 6.27.: Comparison of computed torque (C_Q) coefficients for the two-by-two-bladed CCR rotor at $C_T/\sigma = 0.085$ using different turbulence models.

When varying the blade loading, the overall rotor thrust and torque characteristic was not altered. Higher blade loadings, as expected, resulted in higher thrust and torque values. Moreover, prior to blade passage the thrust was increasing, whereas after blade passage it was decreasing, an effect also visible when looking at the relative sectional force variations in the upper and lower rotor planes[73, 148]; see Fig. F.15.[12].

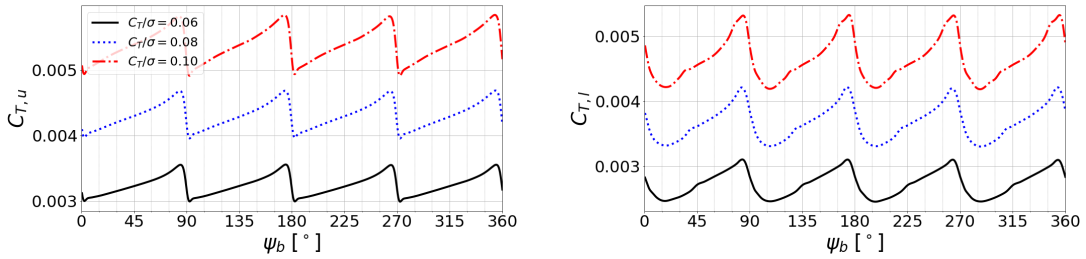

(a) $C_{T,u}$ **(b)** $C_{T,l}$

Figure 6.28.: Comparison of computed thrust (C_T) coefficients for the two-by-two-bladed CCR rotor at $C_T/\sigma = 0.06$, 0.08, and 0.10 using the SA-neg-RC turbulence model.

[12] See, e.g., [73] for the effects of blade passage on thrust and torque for CCR rotors at $C_T = 0$, or [136] for the effects of airfoil passage at zero lift.

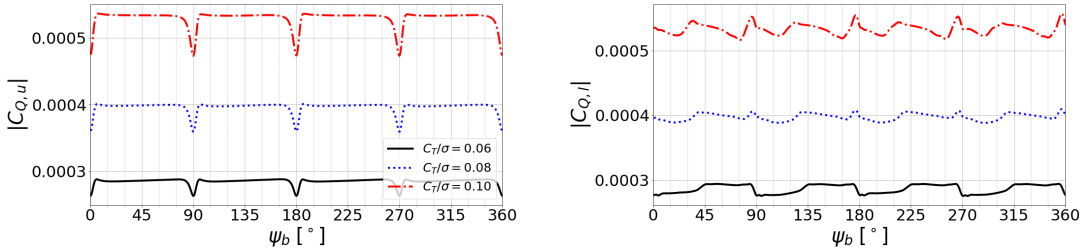

(a) $C_{Q,u}$ **(b)** $C_{Q,l}$

Figure 6.29.: Comparison of computed torque (C_Q) coefficients for the two-by-two-bladed CCR rotor at $C_T/\sigma = 0.06$, 0.08, and 0.10 using the SA-neg-RC turbulence model.

Sectional force distributions (dF_z) are shown in Fig. 6.30 for the two planes of data extraction. For these locations, the upper rotor showed little variation; see Fig. 6.30a. This was in line with the extracted axial velocity distributions above and below the upper blade quarter chord discussed in chapter 6.1.2.4; see Fig. 6.25. The general shape of the thrust distribution was similar to that obtained with the two-bladed single rotor; see Fig. 6.6.

Velocity variations were larger for the lower rotor (Fig. 6.25) and hence, the lower rotor thrust variation was more influenced by changing the azimuthal location of data extraction; see Fig. 6.30b. Moreover, the thrust distributions for the lower rotor were more biased towards the tip, a direct consequence of the additional downwash caused by the upper rotor at inboard sections[73]; see also Fig. F.14. Note that identical untwisted blades were used in the upper and lower rotor plane. In addition, the BVI event for $C_T/\sigma = 0.06$ at $\phi = 0°$ showed a strong influence on the lower rotor blade thrust distribution. As a result, the upper rotor thrust was comparable at these two blade azimuth angles, whereas the lower rotor thrust was slightly lower at $\phi = 45°$.[114] The complete sectional thrust distribution in the rotor plane is shown in Fig. F.14. See, e.g., [73, 148] for further remarks.

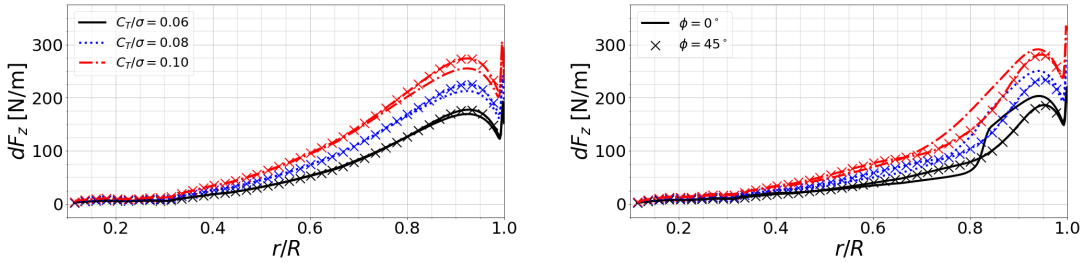

(a) $dF_{z,u}$ **(b)** $dF_{z,l}$

Figure 6.30.: Comparison of computed radial distribution of sectional force (dF_z) for the two-by-two-bladed CCR rotor at $C_T/\sigma = 0.06$, 0.08, and 0.10 using the SA-neg-RC turbulence model[114].

The effects on the radial distribution of sectional torque ($|dM_z|$) are shown in Fig. 6.31. At the two selected index angles (ϕ) the torque magnitude of the upper rotor differed; see Fig. 6.29. This resulted in reduced $|dM_z|$ levels during blade passage ($\phi = 0°$). An inverse correlation with blade loading was observed, i.e., the reduction of $|dM_z|$ at $\phi = 0°$ compared to $\phi = 45°$ increased with increasing C_T/σ; see Fig. 6.31a. For the lower rotor a less clear trend was seen; see Fig. 6.31b. Here,

more torque variation was seen close to the blade tips at $\phi = 45°$ compared to $\phi = 0°$, in line with the axial velocity variations above and below the quarter chord lines shown in Fig. 6.25.

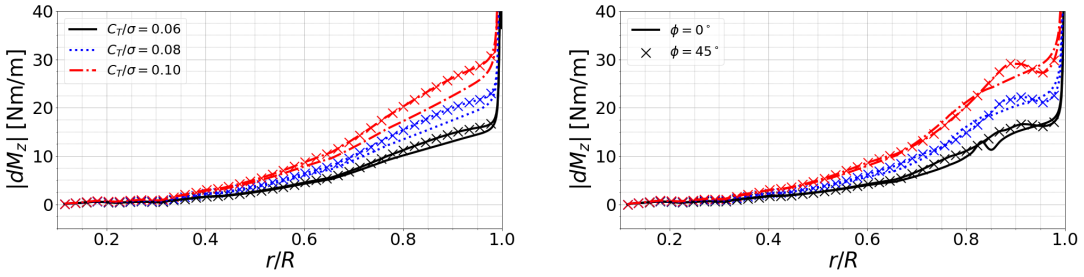

(a) $dM_{z,u}$ **(b)** $dM_{z,l}$

Figure 6.31.: Comparison of computed radial distribution of sectional torque (dM_z) for the two-by-two-bladed CCR rotor at $C_T/\sigma = 0.06$, 0.08, and 0.10 using the SA-neg-RC turbulence model.

An overview of the averaged thrust and torque values of the CCR rotor is given in Table 6.1. Furthermore, the corresponding single rotor quantities are added. It has to be noted, that a direct comparison is not possible, as the thrust potential between the two rotors is different, i.e., despite using the same rotor blade geometry, the total number of rotor blades differed and therefore, the solidity [5, 123, 150].

Table 6.1.: Comparison of collective pitch angle (Θ_0), thrust (C_T), torque (C_Q), and power (C_P) coefficients for the UTA CCR rotor test rig in single rotor and CCR configuration at different blade loadings. Data averaged over one rotor revolution. Results computed with the SA-neg-RC turbulence model.

	$C_T/\sigma = 0.06$		$C_T/\sigma = 0.08$		$C_T/\sigma = 0.10$	
	single	CCR	single	CCR	single	CCR
Θ_u	5.7°	6.88°	7.4°	8.84°	9.1°	10.78°
Θ_l	-	7.27°	-	9.14°	-	10.987°
$C_{T,u}$	0.00300	0.00324	0.00398	0.00430	0.00499	0.00538
$C_{T,l}$	-	0.00273	-	0.00367	-	0.00464
C_T/σ	0.0598	0.0596	0.0794	0.0795	0.0995	0.1000
$C_{Q,u}$	$2.3476 \cdot 10^{-4}$	$2.8503 \cdot 10^{-4}$	$3.1716 \cdot 10^{-4}$	$3.9611 \cdot 10^{-4}$	$4.1630 \cdot 10^{-4}$	$5.2909 \cdot 10^{-4}$
$C_{Q,l}$	-	$2.8621 \cdot 10^{-4}$	-	$3.9736 \cdot 10^{-4}$	-	$5.3303 \cdot 10^{-4}$
C_P/σ	$4.6834 \cdot 10^{-3}$	$5.6978 \cdot 10^{-3}$	$6.3270 \cdot 10^{-3}$	$7.9146 \cdot 10^{-3}$	$8.3048 \cdot 10^{-3}$	$1.0594 \cdot 10^{-2}$

6.1.3. Summary and Comparison of the Rotors

Time-averaged flow fields were used to give general insights into the flow topology of the single and CCR rotor concept. A comparable, continuous wake contraction was seen near the upper rotor plane of the CCR rotor and the single rotor. Differences were seen near the blade tips. Here, the single rotor and the lower rotor of the CCR configuration showed an upwash region, whereas

the upper rotor did not. Overall, the flow field near the lower rotor plane was more complex due to interactions with the upper rotor downwash at inboard regions. At outboard regions, the contraction of the upper rotor wake caused fluid to be entrained into the lower rotor from outside the upper rotor slipstream boundary. A comparison between the experimental and numerical data showed higher velocity magnitudes in the simulations along with more defined slipstream boundaries, with generally good agreement between experimental and numerical results. Furthermore, the choice of the measurement plane was found to cause variations in the time-averaged axial velocity distributions close to the lower rotor, and the upper and lower rotor slipstream boundary locations. The N_b-per-revolution blade crossings of the CCR rotor caused variations in the tip vortex trajectories, resulting in local changes of the slipstream radius. In other words, corresponding to four blade crossings per revolution, a cross-section of the rotor wake in a plane parallel to the rotor disk will not be purely circular, but will have four lobes. Conversely, the flow field of the single rotor can be considered time independent for an observer rotating with the rotor hub.

Experimental and numerical tip vortex trajectories were correlated for the single and CCR rotor. Overall, good agreement was observed over the complete range of wake ages measured in the experiments. Only a constant axial offset was seen for the lower rotor tip vortices of the CCR rotor and the radial contraction for the single rotor was slightly increased after the first blade passage in the simulations. The numerical analysis revealed that the general shape of the trajectories showed little dependence on the employed turbulence model or rotor thrust. The latter mostly affected the convection and contraction rate. As for the time-averaged velocity contours, changing the azimuthal plane of data evaluation revealed an azimuthal dependency of the CCR rotor vortex trajectories. This dependency could be linked to the changed interactions of the upper and lower rotor wakes caused by changes of the relative distance of the measurement plane to the locations of blade crossings. Moreover, the typical kink in the axial tip vortex displacement, caused by blade passage, was only seen for the single rotor and the lower rotor tip vortex in the plane of data extraction $\xi = 0°$, i.e, when the tip vortex was created during blade passage, whereas the lower rotor at $\xi = 45°$ and the upper rotor the tip vortices followed a comparatively smooth trajectory.

In addition, tip vortex size and strength were investigated. Despite the significantly increased complexity of the CCR rotor flow field (inter-rotor and intra-rotor vortex interactions, loading and inflow velocity variations, blade passage), no direct link between circulation (Γ), vortex core radius (r_c) and half peak-to-peak velocities (V_{hpp}) and the altered tip vortex roll-up process could be drawn. While absolute quantities differed from the single rotor data, the general characteristics were identical, i.e., a continuous increase in vortex core size along with a continuous decrease in circulation and half peak-to-peak velocities. However, a strong influence was seen when changing turbulence models. The SST-RC and SST-SAS turbulence models showed a significantly increased tip vortex core growth and peak velocity reduction. Significantly better and comparable vortex conservation was achieved using the SST-SAS-RC and SA-neg-RC model. The influence on rotor trim, thrust, torque, and velocity distributions near the rotor planes was found to be small.

Temporal variations in the axial velocity distributions were correlated to experimental data at fixed locations in space. For both rotors, blade passage caused an upwash before and a downwash after crossing the point of data extraction. Excellent agreement between simulation and experiment was observed for the single rotor. For the CCR rotor an overall increased velocity magnitude was computed, possibly caused by differences in the upper and lower rotor thrust sharing between

experiment and simulation. However, the exact cause could not be identified. The comparison revealed that averaging velocity data from above and below the single rotor and CCR upper rotor plane showed comparable results to extracting data directly in the plane of the rotor blades. Only the large velocity gradients during blade passage were reduced and smoothed by this approach. However, for the lower rotor plane larger differences were seen in between blade passage, caused by the finite time required for the upper and lower rotor blade vortex sheets and tip vortices to be convected to the points of data extraction. Changing the blade loading (and therefore, the average inflow velocity) lead to different phasing relations between vortex sheet and tip vortex passage with regard to the effects caused by blade passage. Moreover, changing the plane of data extraction from $\xi = 0°$ to $\xi = 45°$ was found to change the velocity signal significantly for the CCR rotor. As the upper and lower rotor blade were now passing the points of data extraction at different times, a clear N_b-per-revolution velocity variation caused by blade passage was seen in the upper and lower rotor plane.

Furthermore, variations in the axial velocity distributions along the blade span were linked to the rotor blade sectional force distributions. While the upper rotor blade showed little variation for the two investigated planes of data extraction ($\xi = 0°$ and $45°$), the upper rotor wake contraction along with the modified tip vortex trajectories caused notable differences in the flow field seen by the lower rotor blade, and therefore, also in its thrust distribution. The thrust distributions of the lower rotor blades were more biased towards the tip, i.e., outside the upper rotor wake, and showed greater variations in magnitude and shape.

In summary, it could be shown that a strong influence of the plane of data extraction existed for the CCR rotor. It was shown that for a comprehensive description of the CCR rotor flow field, data needs to be evaluated at multiple planes of data extraction with varying offsets to the plane of blade passage. In particular, this had a significant influence on the results when investigating velocity distributions near the rotor planes. Moreover, correlations with experimental data showed that the numerical model was capable of accurately predicting the complex flow fields of CCR rotors and single rotors.

6.2. Stacked Rotor Aerodynamics

Stacked (coaxial co-rotating) rotor aerodynamics were analyzed based on the UTA stacked rotor test rig described in chapter 3.2.3. In addition, two single rotor designs, namely a two-bladed and a four-bladed rotor, were derived from this configuration. The two-bladed rotor simulations were trimmed to $C_{T,2b}/\sigma = 0.08$ and 0.10 to allow for a correlation with experimental data[102]. The upper rotor of the stacked rotor concept at $\phi = 0°$ was trimmed to the same thrust values. The resulting upper rotor collective pitch angles (Θ_0) were also set for the lower rotor, all blades of the other stacked rotor configurations ($\phi = -22.5°$ and $+22.5°$), and the four-bladed single rotor; see chapter 4.6. At the time of writing the thesis no flow field measurements were available for the four-bladed and stacked rotors[13]. Therefore, only numerical results using the SA-neg-RC turbu-

[13] A first correlation study was made by the experimenters and the author prior to submission of the final thesis but could only partially be used in the present work[114]

lence model were used to investigate the flow field characteristics.

In the following sections the blade loading will be defined based on the trimmed two-bladed single rotor ($C_{T,2b}$). The corresponding thrust levels for the other configurations are given in Tables 6.2 and 6.3; see chapter 6.2.4. Moreover, the flow fields of all rotor configurations based on the stacked rotor test rig were, to a great extend, independent of the blade azimuth angle ψ_b, i.e., in a reference frame fixed at the rotating rotor hub the flow field was quasi stationary; see chapter 6.2.2 for a detailed discussion of this assumption. Therefore, all rotor concepts were analyzed simultaneously without further subdividing the subsequent chapters with respect to the different configurations. A total of 14 rotor revolutions were computed for the single rotors, and 13 for the stacked rotors.

6.2.1. Flow Field

A qualitative understanding of the flow fields of the different configurations could be gained by comparing time-averaged contours of axial velocity. In Fig. 6.32 these were superimposed by time-averaged in-plane velocity vectors at $C_{T,2b}/\sigma = 0.08$. Both single rotor configurations showed the characteristic wake contraction at early wake ages; see Figs. 6.32a and 6.32b. Note that both rotors were operated at comparable collective pitch angles. Therefore, the velocity magnitude was greater for the four-bladed rotor due to the higher disk loading.

The time-averaged flow fields showed an increased complexity for the stacked rotor configurations, with a strong dependency of the flow fields on the index angle ϕ; see Fig. 6.32. For all index angles two distinct slip stream boundaries formed, originating from the upper and lower rotor. At $\phi = -22.5°$ the lower rotor blades were intersecting the upper rotor tip vortices, i.e., the stacked rotor was operating continuously in a BVI condition; see also Fig. 6.33a. This was also visible in the time-averaged axial velocity contours. In comparison to all other configurations, the slipstream boundaries were less distinct below the lower rotor plane, and the regions of highest axial velocities were wider along with lower velocity magnitudes, despite an overall higher blade loading; see Fig. 6.32c and Table 6.2. At $\phi = +22.5°$ both rotor slipstream boundaries merged below the lower rotor plane, resulting in higher time-averaged axial velocity magnitude below the lower rotor plane at $r/R \approx 0.8$; see Fig. 6.32e. At this index angle the upper and lower rotor tip vortices were also merging; see Fig. 6.33c and chapter 6.2.2. When the rotor was operated at $\phi = 0°$ both slipstream boundaries remained clearly separated.

The general observations were also correct at $C_{T,2b}/\sigma = 0.10$ in the shown ROI; see Fig. G.1. At the higher blade loading the overall axial velocity magnitudes were increased, as expected. The largest qualitative difference was observed at $\phi = 0°$, where the lower rotor slipstream boundary showed an increased contraction at the higher blade loading, i.e., an increased tendency to merge with or cross the upper rotor slipstream boundary; compare Figs. 6.32d and G.1d. The tip vortex trajectories, supporting this statement, were further analyzed in chapter 6.2.2.

The observed flow field characteristics were qualitatively comparable to those of the CCR rotor when comparing time-averaged contours in the two different planes of data extraction; see chapter 6.1.2.1. For the CCR rotor at $\xi = 0°$ the upper and lower rotor slipstream boundaries remained

separated, while at $\xi = 45°$ they were getting closer; see Figs. 6.9 and F.1. As for the CCR rotor, a recirculation region close to the blade tips only formed for the lower rotor of the stacked rotor configurations. In addition, fluid was entrained from outside the upper rotor slipstream boundary into the lower rotor near the lower rotor blade tips.

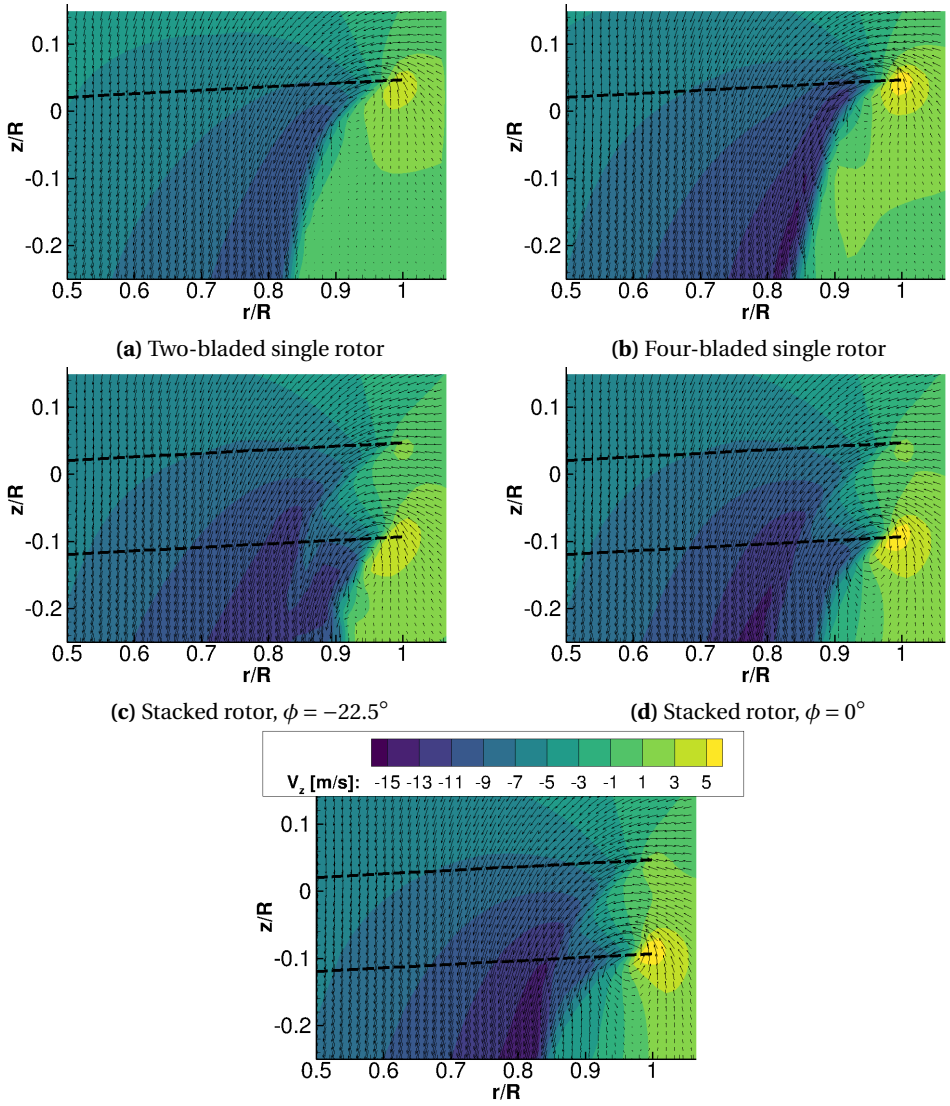

(a) Two-bladed single rotor

(b) Four-bladed single rotor

(c) Stacked rotor, $\phi = -22.5°$

(d) Stacked rotor, $\phi = 0°$

(e) Stacked rotor, $\phi = +22.5°$

Figure 6.32.: Comparison of time-averaged contours of axial velocity (v_z) for the UTA stacked rotor test rig[114]. The blade loading of the two-bladed single rotor is $C_{T,2b}/\sigma = 0.08$. Corresponding blade loadings for the other configurations are given in Table 6.2 based on the trim strategy defined in chapter 4.6. Data was averaged in increments of $\Delta\psi_b = 1°$ between the rotational periodicity boundary conditions (90 slices for the four-bladed configuration; 180 slices for all other configurations).

More detailed insights into the structure of the stacked rotor flow fields were possible by comparing total vorticity contours and Q-criterion isosurfaces; see Fig. 6.33. As previously discussed for the contours of time-averaged axial velocity, the variation in index angle changed the flow fields

considerably. At $\phi = -22.5°$ the lower rotor blades intersected the upper rotor tip vortices. As a result, the upper rotor tip vortex was split into two discrete vortical structures after BVI, out of which only one was clearly visible at a wake age of $\zeta = 112.5°$ after the interaction with the lower rotor blade; see XZ-plane in Fig. 6.33a. In comparison to the other two index angles, this vortical structure was weaker and smaller. Moreover, the flow field at $\phi = -22.5°$ showed significantly increased vortex-vortex interactions and vortex wandering below the lower rotor plane compared to $\phi = 0°$ and $+22.5°$. In addition, the tip vortices were closer to the radial extensions of the refined grid regions for improved tip vortex conservation at young wake ages and outside of this region for older wake ages (i.e., far below the lower rotor); see blue region in Fig. 4.22.

At $\phi = 0°$ the tip vortices of the upper and lower rotor remained separated down to the end of the refined region for improved tip vortex conservation; see red line in Fig. 6.33b. At $\phi = +22.5°$ the lower rotor tip vortex was pairing with the upper rotor tip vortex, after rotating around it. As a consequence less vortical structures were observed far below the lower rotor plane compared to the other two index angles; see Fig. 6.33c. Both types of vortex interactions (BVI and vortex pairing) increased the width of the vortex tubes seen in the Q-criterion isosurfaces and reduced the total vorticity levels.

At $C_{T,2b}/\sigma = 0.10$ the results were comparable; see Fig. G.2. Due to the increased axial velocity caused by the higher rotor thrust, the mutual interactions of the upper and lower rotor tip vortices were altered. As a consequence the upper rotor tip vortex passed below the lower rotor blade during the BVI event at $\phi = -22.5°$, increased vortex interaction was observed at $\phi = 0°$ and vortex paring was not observed within the refined grid region for improved vortex conservation at $\phi = +22.5°$, but only strong interactions were seen.

For the single rotors, the flow fields were qualitatively comparable to the two-bladed single rotor based on the UTA CCR rotor test rig and are not discussed further; see chapter 6.1.1. A detailed comparison of vortex trajectories is given in chapter 6.2.2.

6.2.2. Tip Vortex Trajectories

Vortex trajectories were extracted and analyzed to further illustrate similarities and differences between the different rotor configurations. As for the two-bladed single rotor based on the CCR rotor test rig, results were processed at a fixed rotor locations (i.e., based on one time step at $\psi_b = 0°$) and values were extracted at varying wake ages (ζ); see Fig. 3.8a. Due to the chosen trim strategy, all rotors were operated at different blade loadings (C_T/σ); see Tables 6.2 and 6.3. Therefore, the subsequent evaluation of vortex trajectories is a trend statement and quantitative differences must be interpreted with care. Vortex center detection was made using the algorithm described in chapter C[14]. A similar study was made in [11] using a free vortex wake solver with rigid blades. In contrast to the current study, the upper and lower rotor plane were trimmed to identical torque values, similar to CCR rotors.

[14] CFD threshold: $\Gamma_{1,min} \geq 0.15$ for the stacked rotors / $\Gamma_{1,min} \geq 0.7$ for the single rotors and $\overline{\omega}_{min} \geq 450\,s^{-1}$

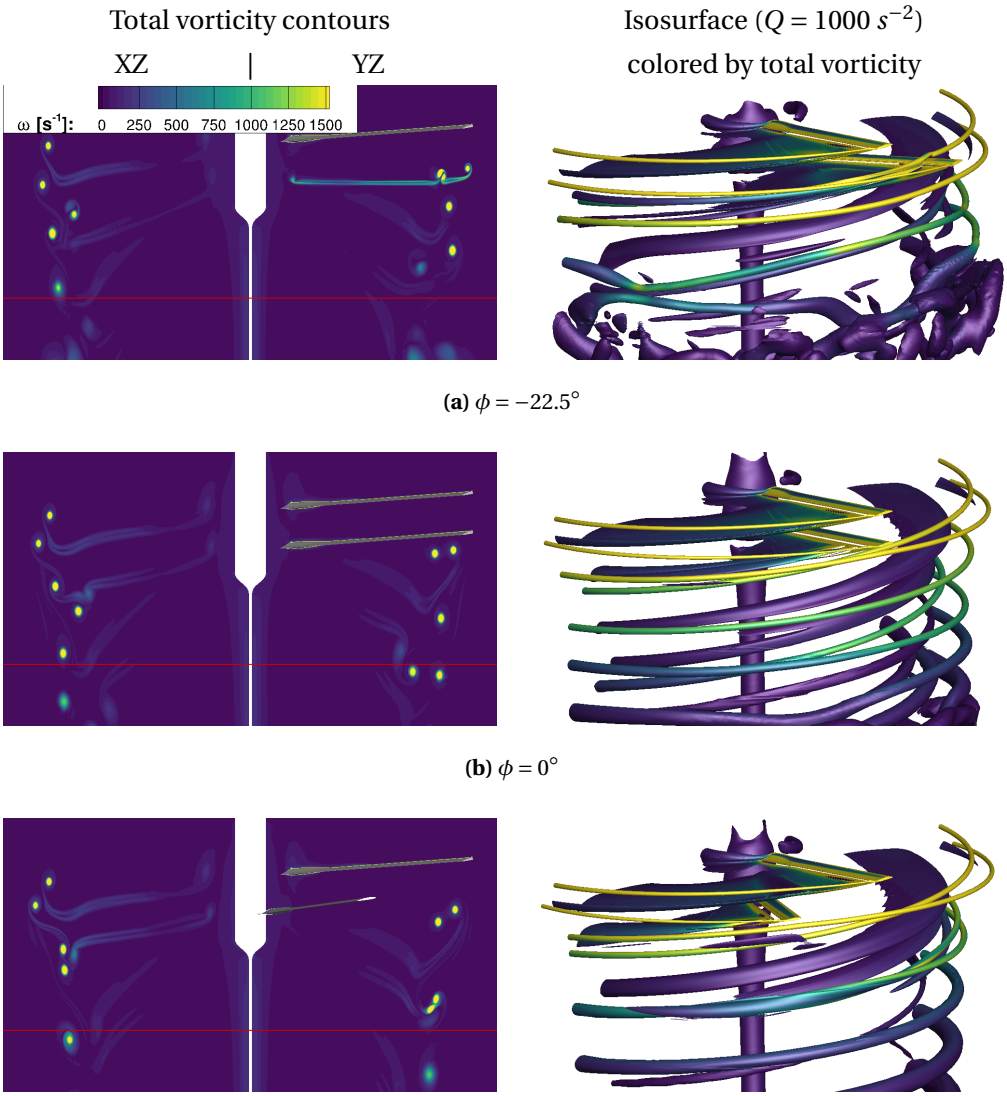

(a) $\phi = -22.5°$

(b) $\phi = 0°$

(c) $\phi = +22.5°$

Figure 6.33.: Comparison of total vorticity (ω) contours and vortical structures (Q-criterion isosurfaces) of the UTA stacked rotor at $C_{T,2b}/\sigma = 0.08$ for different index angles ϕ. Corresponding blade loadings for the other configurations are given in Table 6.2 based on the trim strategy defined in chapter 4.6. Red line indicating end of high-resolution grid region for improved vortex preservation; see Fig. 4.22. Vorticity contours shown in two perpendicular vertical planes through the rotor shaft axis (XZ- and YZ-plane).

At $C_{T,2b}/\sigma = 0.08$ the single rotor configurations showed the well known behavior, i.e., a steady contraction at early wake ages and the characteristic king in the evolution of z/R caused by blade passage ($\zeta_u = 180°$ for the two-bladed rotor; $\zeta_u = 90°$ for the four-bladed rotor[15]); see Fig. 6.34b. Note that the radial contraction of the four-bladed rotor was increased while the axial displacements were in good agreement with the two-bladed rotor up to the first blade passage, despite the

[15] See [105] for an experimental study into dynamical characteristics of tip vortices from a four-bladed rotor in hover.

difference in blade loadings; see Fig. 6.34. At $C_{T,2b}/\sigma = 0.10$, due to the increased average inflow velocity, the axial convection and radial contraction of the tip vortices was increased compared to $C_{T,2b}/\sigma = 0.08$; compare Figs. 6.34 and G.4.

For the stacked rotor configurations the vortices of the upper rotor did not show the characteristic kink in the vortex trajectories caused by blade passage for single rotor configurations; see Fig. 6.34b. This was in line with the findings for the CCR rotor; see chapter 6.1.2.2. At $\phi = -22.5°$ the BVI event manifested as a kink in the r/R trajectory, while only a slight excursion was visible in z/R. Note that after BVI the vortex was split into two separate structures with high vorticity and swirl levels. In the graphs the vortical structure which had higher vorticity, along with $\Gamma_1 \geq \Gamma_{1,\min}$ was plotted.

At $\phi = 0°$ the vortex trajectories showed a great deviation from the four-bladed configuration, even though the rotor was operated at comparable blade loading. Both, the axial convection and radial contraction were significantly increased. During blade passage ($\zeta_u = 180°$) only a gradual increase in the axial convection rate was observed compared to the four bladed rotor. Note that this was mostly caused by passing below the lower rotor which was operated at significantly lower thrust per blade compared to the upper rotor and the four-bladed rotor; see Fig. 6.33b and Table 6.2. At $\phi = +22.5°$ both quantities, the radial contraction and axial convection, showed almost identical behavior compared to $\phi = 0°$ up to $\zeta_u \approx 135°$. At higher wake ages the radial contraction reduced significantly, along with a reduction of the axial convection speed; see Fig. 6.34. For this index angle, this wake age was not directly linked with upper or lower rotor blade passage, but primarily caused by intra-rotor vortex interactions; see Fig. 6.33c.

For the lower rotor vortex trajectory at $\phi = -22.5°$ the BVI event caused fluctuations in r/R and z/R. These oscillations increased at older wake ages. At $\phi = 0°$ blade passage manifested as the characteristic kink in the axial displacement at $\zeta_l = 180°$. The effect of blade passage was less distinct (i.e., no kink) at $\phi = +22.5°$ but linked with increased radial contraction and axial convection afterwards; see Fig. 6.34b. Note that due to vortex paring at $\phi = +22.5°$ the lower rotor tip vortex trajectories ended at $\zeta_l \approx 330°$. The lower rotor tip vortex rotated around the upper rotor tip vortex prior to merging. The involved tip vortex deformations smeared the vortex center and thus it could not uniquely be detected in between $\zeta_l \approx 330°$ and the final merging of the vortices; see Fig. 6.33c.

A direct comparison between the upper and lower rotor tip vortices is given in Fig. 6.35. Here, axial displacement is plotted against radial contraction up to a maximum wake age of $\zeta = 540°$. Data was extracted at four points in time ($\psi_b = 0°$, 90°, 180°, and 270°) to illustrate the temporal dependency of the tip vortex trajectories within one rotor revolution. For $\phi = 0°$ and +22.5° all four curves lied on top of each other. Only far below the lower rotor small differences were visible. Hence, for these index angles the assumption that extracting data at a fixed instance of time and varying wake age was justified. As indicated by the contours of time averaged vorticity the upper and lower rotor tip vortex trajectories remained clearly separated at $\phi = 0°$; see Figs. 6.32d and 6.35b. Moreover, at $\phi = +22.5°$ the lower rotor tip vortex was spinning around the upper rotor tip vortex prior to merging; see Fig. 6.35c.

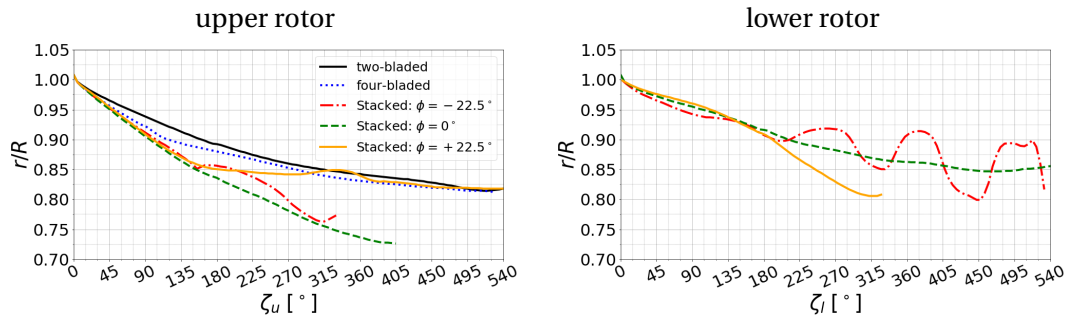

(a) r/R vs. $\zeta_{u,l}$

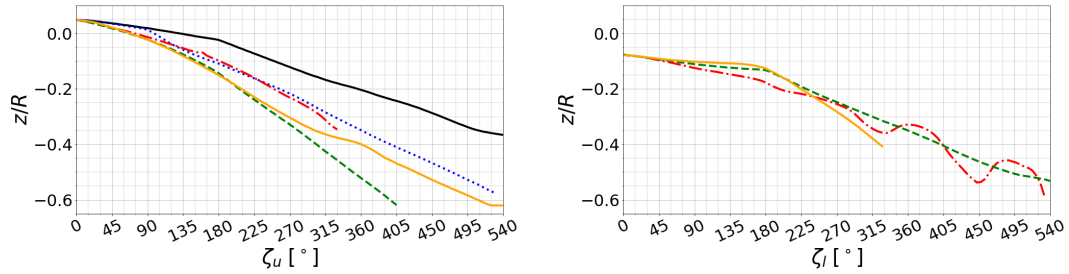

(b) z/R vs. $\zeta_{u,l}$

Figure 6.34.: Comparison of computed axial (z/R) and radial (r/R) tip vortex displacements for the UTA stacked rotor test rig at $C_{T,2b}/\sigma = 0.08$. Corresponding blade loadings for the other configurations are given in Table 6.2 based on the trim strategy defined in chapter 4.6.

In contrast, the flow field showed high unsteadiness at $\phi = -22.5°$; see Fig. 6.35a. Quasi stationary behavior could only be observed up to a short distance below the lower rotor ($z/R > -0.15$). Hence, for this rotor configuration, a detailed investigation of the temporal evolution of the tip vortex trajectories would require averaging multiple rotor revolutions, which goes beyond the scope of the current thesis. Therefore, a quantification or further description of the vortex behavior below this axial level is not made here.

The corresponding data for $C_{T,2b}/\sigma = 0.10$ is shown in Fig. 6.36. At $\phi = -22.5°$ the previously described unsteadiness caused by BVI could also be seen. The ambiguity of the vortex center definition after BVI caused the different characteristics of the upper rotor tip vortex trajectory; see Fig. 6.36a. In contrast to the lower blade loading the vortex trajectories were intertwined at $\phi = 0°$ and did not show clearly separated, almost parallel paths; compare Figs. 6.35b and 6.36b. Due to the phase relationship no vortex merging or pairing took place. The same was true for $\phi = +22.5°$. The upper rotor tip vortex trajectory intersected the lower tip vortex trajectory multiple times; see Fig 6.36c. These observations provided a further support for the observed differences in the time-averaged contours of axial velocity; compare Figs. 6.32 and G.1.

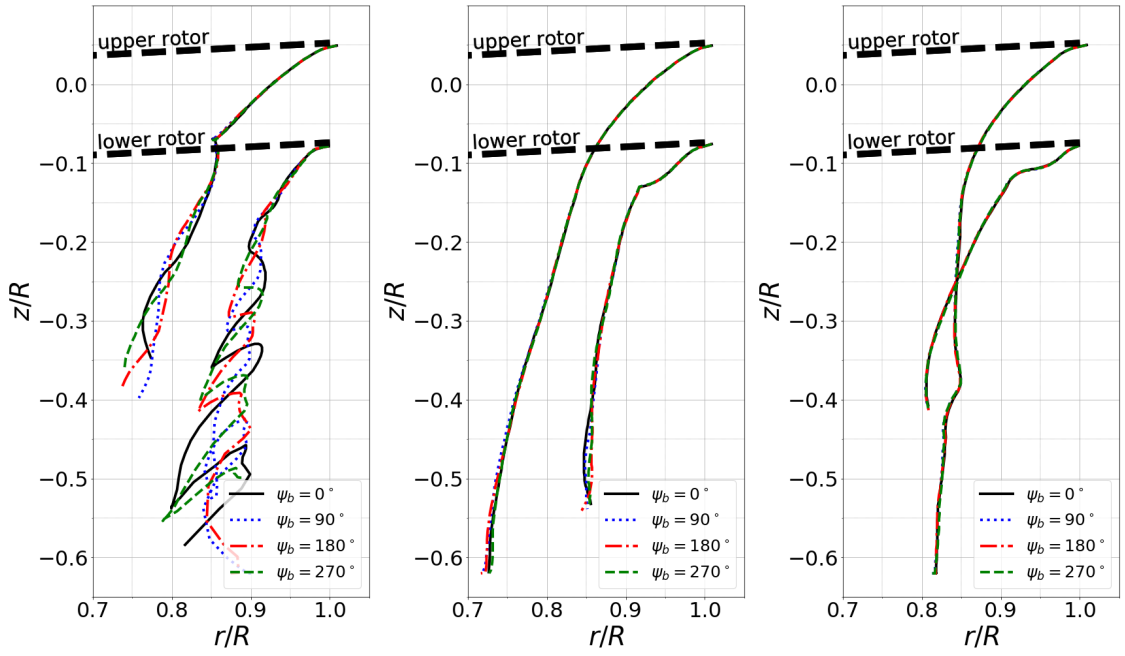

(a) $\phi = -22.5°$. **(b)** $\phi = 0°$. **(c)** $\phi = +22.5°$.

Figure 6.35.: Comparison of computed axial (z/R) and radial (r/R) tip vortex displacements for the UTA stacked rotor test rig at $C_{T,2b}/\sigma = 0.08$. Corresponding blade loadings for the other configurations are given in Table 6.2 based on the trim strategy defined in chapter 4.6.

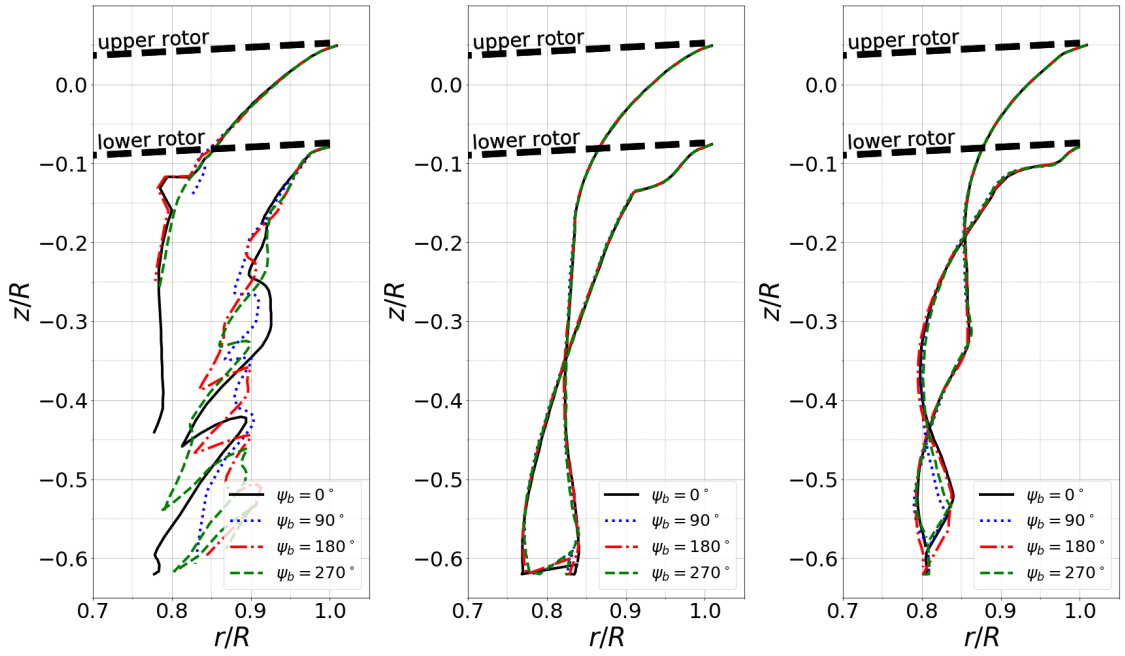

(a) $\phi = -22.5°$. **(b)** $\phi = 0°$. **(c)** $\phi = +22.5°$.

Figure 6.36.: Comparison of computed axial (z/R) and radial (r/R) tip vortex displacements for the UTA stacked rotor test rig at $C_{T,2b}/\sigma = 0.10$. Corresponding blade loadings for the other configurations are given in Table 6.2 based on the trim strategy defined in chapter 4.6.

6.2.3. Rotor Inflow

6.2.3.1. Two-Bladed Single Rotor

For the two-bladed single rotor experimental phase- and time-resolved velocity distributions were published by the experimenter and the author of this thesis in a previous study[102]. These data were correlated to the numerical simulation results to assess the accuracy of the computations. A comparison of the radial distribution of axial velocity at $\Delta z/c = -1$ below the lower rotor blade at various index angles is shown in Fig. 6.37. From the experimental and numerical results data were extracted along a line parallel to the deformed rotor blade in the experiments, i.e., "along a line defined by the mean coning angle of the loaded rotor"[102]. The mean coning angle was defined based on the experimental data, with the tip displacement being estimated to 27.18 mm[102]. The correlation revealed that the axial velocity distributions were in good agreement at the inboard sections of the blade. Increased differences were observed closer to the blade tip where the influence of the tip vortices was dominating. The effect of the tip vortices passing through the plane of data extraction was clearly visible by the 'S-shaped' profile. In the numerical simulations the vortex passage was located further outboard, i.e., the wake contraction showed slight differences between simulation and experiment. It has to be noted that a infinitely rigid rotor blade was assumed in the simulations and hence, differences were to be expected due to the chosen line of data extraction.

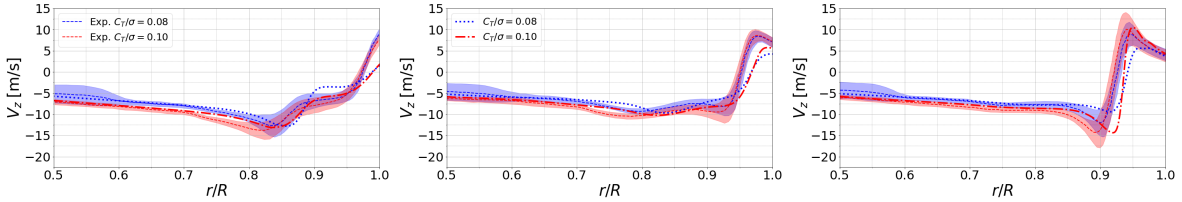

(a) $\psi_b = 8.8°$ **(b)** $\psi_b = 43.9°$ **(c)** $\psi_b = 87.8°$

Figure 6.37.: Comparison of radial distribution of axial velocity (v_z) between experiment[102] and CFD for the two-bladed single rotor based on the UTA stacked rotor test rig. Data was extracted at $\Delta z/c = -1$ below the line defined by the mean coning angle of the loaded rotor in the experiment at $C_{T,2b}/\sigma = 0.08$, and 0.10. Data plotted at various rotor blade azimuth angles ψ_b. Shaded region represents one standard deviation.

The variation of axial velocity at a fixed point in space over one rotor revolution is shown in Fig. 6.38. Two characteristic extremes caused by blade passage occurred at $\psi_b = 0°$ and 180°. At both radial stations the computed velocity distributions were in good agreement with the experimental data for $\Delta z/c = 0.34$. The computational results were located within the experimental scatter. At $r/R = 0.75$ and $\Delta z/c = -1.0$ the simulations showed reduced velocity magnitudes. The effects of blade passage and vortex sheet passage were well captured. Only a small phase delay was observed, which was most likely a direct consequence of the reduced axial velocity magnitudes; see Fig. 6.38b. At $r/R = 0.85$ and $\Delta z/c = -1.0$ the experimental velocity distributions differed significantly from all other velocity distributions shown previously in this thesis; compare Figs. 6.38 and 6.7. The numerical data showed the same behavior previously described. The exact cause of the behavior could not be determined[102].

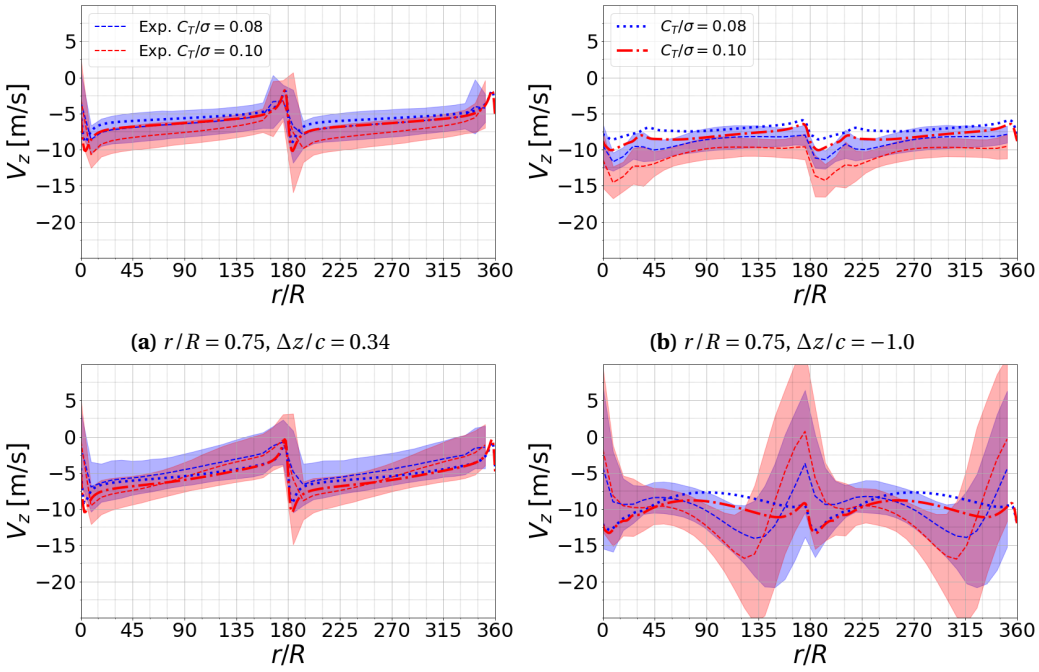

(a) $r/R = 0.75$, $\Delta z/c = 0.34$

(b) $r/R = 0.75$, $\Delta z/c = -1.0$

(c) $r/R = 0.85$, $\Delta z/c = 0.34$

(d) $r/R = 0.85$, $\Delta z/c = -1.0$

Figure 6.38.: Comparison of axial velocity (v_z) between experiment[102] and CFD for the two-bladed single rotor based on the UTA CCR rotor test rig at multiple radial locations r/R. Data shown over one revolution for $C_{T,2b}/\sigma = 0.08$, and 0.10 above and below the rotor plane. Blade passage occurred at $\psi_b = 0°$ and 180°. Shaded region represent one standard deviation.

6.2.3.2. Stacked Rotor

A comparison of the radial distributions of axial velocity above and below the upper and lower rotor blade quarter chord line is shown in Figs. 6.39 and 6.40. In addition, the velocity distributions of the two-bladed and four-bladed single rotors were plotted. An illustration of the lines of data extraction is shown in Fig. 6.19.

When comparing the axial velocity distributions $\Delta z/c = 1.0$ above the upper rotor blade, it was found that the overall shape of the velocity profile was well comparable between all rotors; see Fig. 6.39a. Overall, rotor thrust was the main driver of the inflow velocity magnitudes of the single rotors, i.e., higher rotor thrust lead to higher axial velocity magnitudes; see Tables 6.2 and 6.3. When comparing the four-bladed rotor with the stacked rotor at $\phi = -22.5°$ it was found that the axial velocity magnitude of the four-bladed rotor was higher. Moreover, the stacked rotor at $\phi = -22.5°$ showed an overall flatter velocity profile with a lower gradient towards the blade tip. The velocity distribution of the other two stacked rotor configurations were well comparable in shape and magnitude, in line with their similar blade loadings.

In between the upper and lower rotor plane ($\Delta z/c = -0.875$) a strong dependency on the location of the upper rotor tip vortices was observed; see Fig. 6.39b. For both single rotor configurations, the upper rotor tip vortices were close to the line of data extraction for both blade loadings (see the

'S-shaped' profile). For all stacked rotor configurations, the upper rotor tip vortices were already convected further downwards below the lower rotor plane; see Fig. G.3. Hence, the influence of the tip vortices was not dominating. The highest blade loading ($\phi = -22.5$) lead to the highest velocity magnitudes, along with the lowest upper rotor thrust. For the other two stacked rotor configurations, the index angle changed the inflow velocity profiles, despite comparable overall rotor thrust levels. At $\phi = 0°$ the axial velocity magnitude was lower inboard of $r/R < 0.875$ and higher outboard compared to $\phi = +22.5°$.

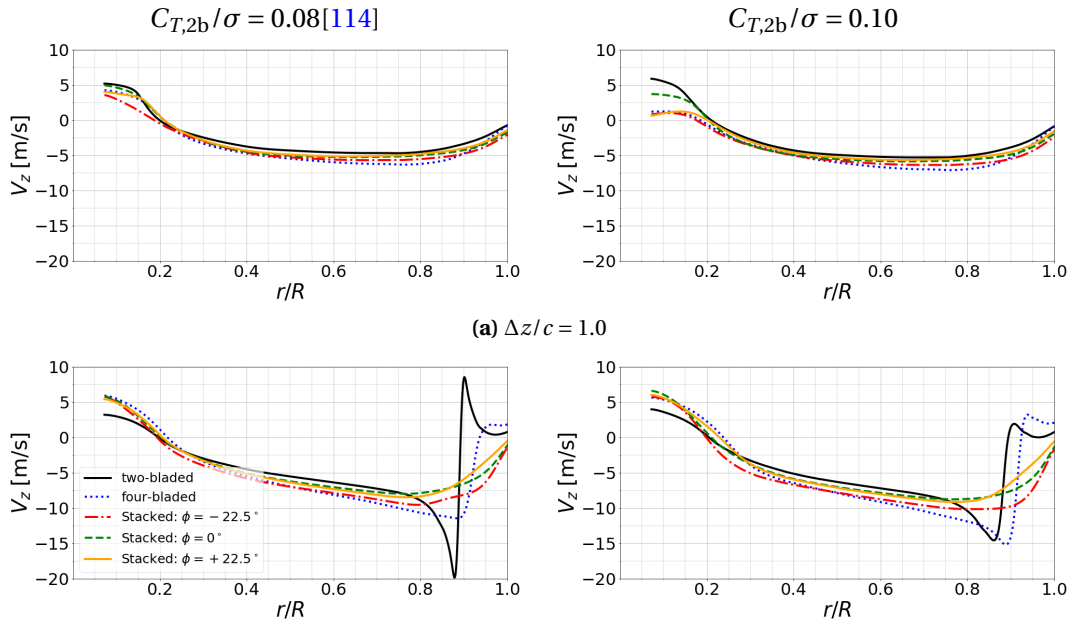

(a) $\Delta z/c = 1.0$

(b) $\Delta z/c = -0.875$

Figure 6.39.: Comparison of computed radial distributions of axial velocity (v_z) for the upper rotor of the stacked rotor test rig at $C_{T,2b}/\sigma = 0.08$ and 0.10. Data was extracted at two different axial distances above and below the upper rotor blade quarter chord axes; see Fig. 6.8.

The same analysis was made for the lower rotor; see Fig. 6.40. Note that data was extracted above and below the rotor blade quarter chord axes, i.e., taking the index angles into account. Therefore, data shown for the lower blade at $\Delta z/c = -0.875$ for $\phi = -22.5°$ and $\phi = +22.5°$ differed from the data shown for the upper blade, whereas for $\phi = 0°$ data was identical; compare Figs. 6.39 and 6.40. The axial velocity distribution for $\phi = -22.5°$ showed the lowest magnitude, despite the overall highest thrust for this configuration. Moreover, at $\phi = +22.5°$ the velocity magnitude was greatest towards the tip. At $\phi = 0°$ the axial velocity distribution showed mostly values between the other two cases. Hence, an increased downwash was seen at $\phi = +22.5°$, i.e., when the lower rotor blade was trailing the upper rotor blade and vice versa for $\phi = -22.5°$[56].

One chord below the lower rotor ($\Delta z/c = -2.75$) the axial velocity distribution was mostly affected by the relative location of the upper and lower rotor tip vortices. At $\phi = -22.5°$, i.e., when BVI occurred, only one strong, compact tip vortex was intersecting the line of data extraction, resulting in only one 'S-shaped' velocity profile; see Fig. 6.40b. At $\phi = 0°$ and $C_{T,2b}/\sigma = 0.08$ the upper and lower rotor tip vortices were passing below the lower rotor at comparable distances, hence leading to two positive and negative velocity peaks in the radial velocity distribution. At $C_{T,2b}/\sigma =$

0.10 the upper rotor tip vortex was convected further downwards compared to $C_{T,2b}/\sigma = 0.08$, hence, reducing the influences from the upper rotor tip vortex and therefore, reducing velocity peaks at $r/R \approx 0.85$. Overall it was found that an increase of thrust affected the miss-distances of the upper rotor tip vortices to the lower rotor blades more than those of the lower rotor tip vortices; see Fig. G.3. At $\phi = +22.5°$ the upper rotor tip vortices had a reduced effect on the axial velocity distribution as a result of higher miss-distances. At $C_{T,2b}/\sigma = 0.08$ a small fluctuation in the velocity distribution was visible at $r/R \approx 0.85$, whereas at $C_{T,2b}/\sigma = 0.10$ the influence was barely visible; see Fig. 6.40b.

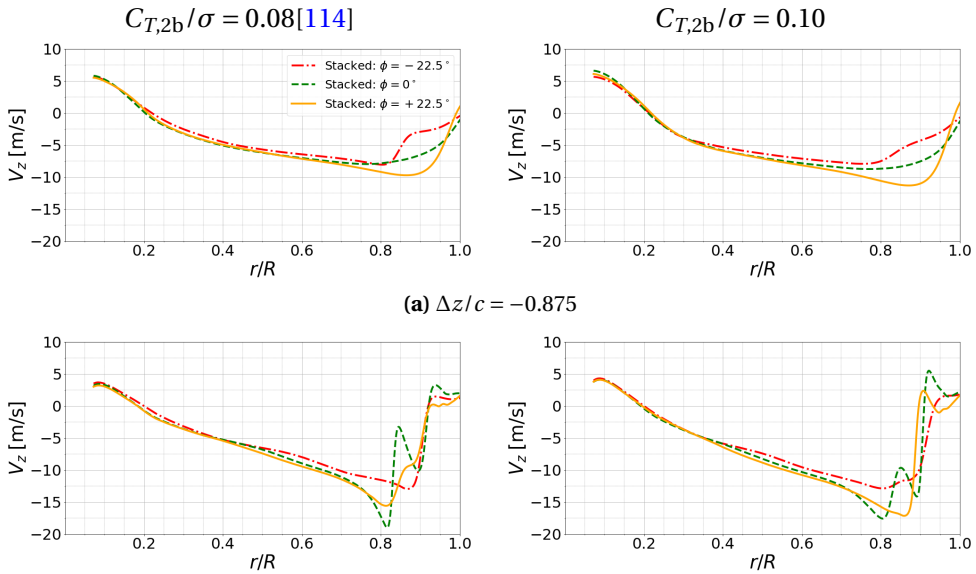

(a) $\Delta z/c = -0.875$

(b) $\Delta z/c = -2.75$

Figure 6.40.: Comparison of computed radial distributions of axial velocity (v_z) for the lower rotor of the stacked rotor test rig at $C_{T,2b}/\sigma = 0.08$ and 0.10. Data was extracted at two different axial distances above and below the lower rotor blade quarter chord axes; see Fig. 6.8.

The temporal evolution of axial velocity at $C_{T,2b}/\sigma = 0.08$ is shown in Figs. 6.41 and 6.42 for the upper and lower rotor, respectively. Data were extracted at two radial locations ($r/R = 0.75$ and 0.85) and three different axial offsets from the rotor blades ($\Delta z/c = 0.34$, 0.0, and -1.0); see Fig. 6.19. The upper rotor showed the characteristic features previously discussed for single rotors. Blade passage manifested as a sudden change in velocity magnitude above and in the plane of the rotor blades. Before blade passage the axial velocity magnitude was reduced, after blade passage it was increased; see Fig. 6.41. Blade passage of the lower rotor blade could be seen as a decrease in velocity magnitude after the upper rotor blade crossing for $\phi = +22.5°$ and an increase in velocity magnitude before the upper rotor blade crossing for $\phi = -22.5°$. Moreover, the four-bladed rotor axial velocity variation was in good agreement with the stacked rotor at $\phi = 0°$ for almost a quarter of a revolution after blade passage of the stacked rotor upper blade. Below the upper rotor blade, the axial velocity time history got more complex, clearly showing the tailing vortex sheet passages and both blade passages for the stacked rotor configurations at $\phi \neq 0°$. Furthermore, at $r/R = 0.85$ the variations in velocity magnitude were increased compared to $r/R = 0.75$ showing the increased influences of the upper rotor tip vortices on the velocity distributions; compare Figs. 6.41c and 6.41f.

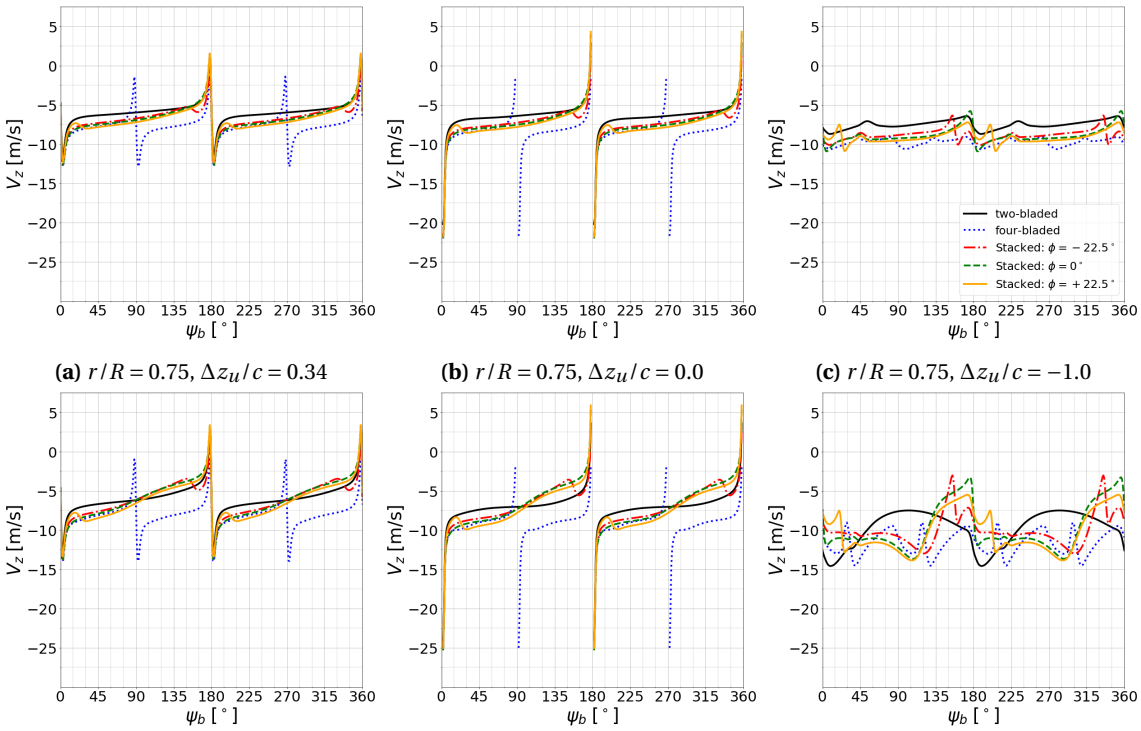

(a) $r/R = 0.75$, $\Delta z_u/c = 0.34$ **(b)** $r/R = 0.75$, $\Delta z_u/c = 0.0$ **(c)** $r/R = 0.75$, $\Delta z_u/c = -1.0$

(d) $r/R = 0.85$, $\Delta z_u/c = 0.34$ **(e)** $r/R = 0.85$, $\Delta z_u/c = 0.0$ **(f)** $r/R = 0.85$, $\Delta z_u/c = -1.0$

Figure 6.41.: Comparison of computed phase-averaged axial velocity (v_z) for the stacked rotor with different index angles ϕ. Data shown over one revolution for $C_{T,2b}/\sigma = 0.08$ above, below, and in the upper rotor plane. Blade passage occurred at $\psi_b = 0°$ and 180°.

Data extracted above, below and at the lower rotor blades showed a different characteristic compared to the upper rotor; see Fig. 6.42. At $r/R = 0.75$ velocity fluctuations were reduced between blade passages compared to the upper rotor, whereas the average velocity magnitude was increased. Above and in the plane of the lower rotor blade the passage of the upper rotor vortex sheet was visible at $\psi_b \approx 60°$ for $\Delta z_l/c = 0.34$ and at $\psi_b \approx 75°$ for $\Delta z_l/c = 0.0$. At $\Delta z_l/c = -1.0$ the vortex sheets trailing from the upper and lower rotor were seen with the respective offsets in ψ_b caused by the varying index angles ϕ.

At $r/R = 0.85$ the velocity distributions showed larger fluctuations. This was caused by the reduced distance of the point of data extraction to upper and lower rotor tip vortices. Above and at the lower rotor blades the basic findings discussed for the probing location at $r/R = 0.75$ were still valid. Below the lower rotor blades large reductions in axial velocity magnitude were seen; see Fig. 6.42f. This was caused by the the upper rotor tip vortices passing to the left of the probing point. The phase relationship was determined by the convection and contraction velocities of the tip vortices along with the different index angles.

At $C_{T,2b}/\sigma = 0.10$ the general findings were also valid. Data is shown for the upper and lower rotor in Figs. G.5 and G.6, respectively. A notable difference was observed for the lower rotor at $r/R = 0.85$ and $z_l/c = -1.0$. Here, the strong influence from the passing tip vortices was only seen for $\phi = 0°$.

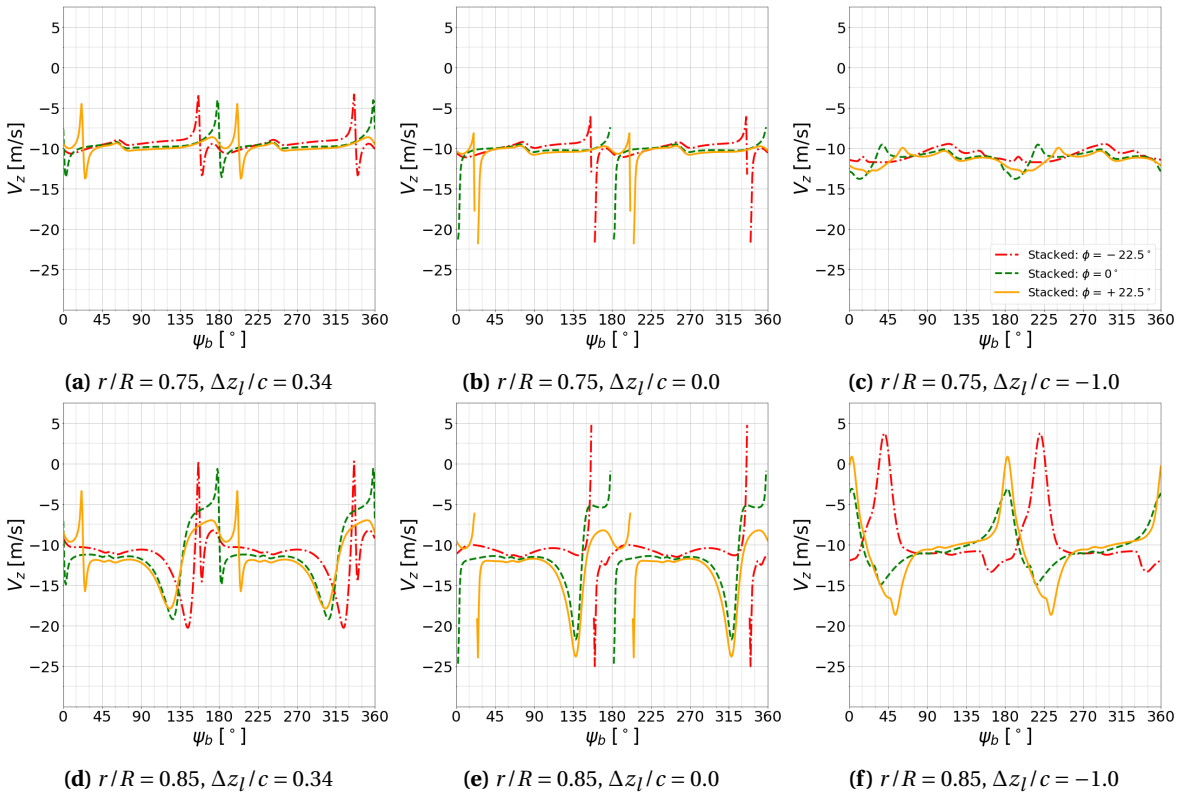

(a) $r/R = 0.75$, $\Delta z_l/c = 0.34$ **(b)** $r/R = 0.75$, $\Delta z_l/c = 0.0$ **(c)** $r/R = 0.75$, $\Delta z_l/c = -1.0$

(d) $r/R = 0.85$, $\Delta z_l/c = 0.34$ **(e)** $r/R = 0.85$, $\Delta z_l/c = 0.0$ **(f)** $r/R = 0.85$, $\Delta z_l/c = -1.0$

Figure 6.42.: Comparison of computed phase-averaged axial velocity (v_z) normalized by rotor blade tip speed (V_{tip}) for the stacked rotor with different index angles ϕ. Data shown over one revolution for $C_{T,2b}/\sigma = 0.08$ above, below, and in the lower rotor plane. Blade passage occurred at $\psi_b = 0°$ and 180°.

6.2.4. Forces and Moments

A summary of computed rotor thrust and torque values is given in Table 6.2 for $C_{T,2b}/\sigma = 0.08$[16] and Table 6.3 for $C_{T,2b}/\sigma = 0.10$. The four-bladed rotor and all stacked rotors were operated at identical pitch angles at both blade loadings. Consequently, the effects on C_T and C_Q caused by varying the index angle and stacking the rotor could be investigated. For a more detailed analysis of performance variations caused by varying the inter-rotor spacing and index angles the reader is referred to the cited publications in the literature review; see, e.g., [11, 58, 57]. Previous research showed that the overall power required and thrust produced is highly dependent on the index angle, inter-rotor spacing, and overall thrust level. It was shown in [57] that small index angle variations ($-5° < \phi < 5°$) at small inter-rotor spacings ($\Delta z_r = 0.73$) can lead to changes in FM of ≈ 0.06. Moreover, at $\Delta z_r = 0.73$ the rotor was most efficient at $\phi = 16.875°$, whereas at $\Delta z_r = 1.75$ highest efficiency was achieved at $\phi = -11.25°$. Hence, as the focus of the current study was to investigate the rotor flow fields, the following results only give a brief insight into the complex dependency of performance on the geometric rotor details at each thrust level.

[16] The final blade loading of the two-bladed rotor at $C_{T,2b}/\sigma = 0.08$ was -1.125% lower than the target blade loading and therefore, the deviation was higher than the trim target of $\pm 1\%$; see chapter 4.6.

It was found that at both thrust levels $C_{T,u}$ was increasing with increasing index angle, whereas $C_{T,l}$ was decreasing. Moreover, when the lower rotor was leading, the blade loading was highest[17]. The four-bladed rotor reached thrust levels which were slightly below ($C_{T,2b}/\sigma = 0.08$) or equal ($C_{T,2b}/\sigma = 0.10$) to the stacked rotor at $\phi = +22.5$. Note that the four-bladed single rotor required more power, hence showed inferior hover efficiency.

When comparing the hover efficiency of the three stacked rotor variants highest efficiency was achieved at $\phi = -22.5°$, followed by $\phi = 0°$ and $\phi = +22.5°$. It should be pointed out that the rotor at $\phi = -22.5°$ was operated continuously in a BVI condition, a complex highly three-dimensional flow phenomenon. In real life large fluctuations in the vortex locations, and hence, the BVI interaction are to be expected. This, the used trim strategy (identical Θ_0 for all blades), in addition to using the SA-neg-RC turbulence model (see chapters 4.4.2 and 6.1.2.5) requires cautiousness when interpreting the results. In [11] it was stated that stacked rotor performance was highly affected by the axial convection of the tip vortices and that higher miss-distances between the vortices and the blades lead to improved hover performance. In the current analysis the opposite was true for the lower rotor, i.e., direct interaction lead to highest overall efficiency; see Fig. G.3.

Table 6.2.: Comparison of thrust (C_T) and torque (C_Q) coefficients for the UTA stacked rotor test rig. $C_{T,2b}/\sigma = 0.08$ for the two-bladed single rotor. The used trim strategy is defined in chapter 4.6. Data was averaged over last rotor revolution.

	two-bladed	four-bladed	$\phi = -22.5°$	$\phi = 0°$	$\phi = +22.5°$
Θ_0	7.241°	8.00°			
$C_{T,u}$	0.00363	0.00624	0.00337	0.00363	0.00390
$C_{T,l}$	-	-	0.00310	0.00253	0.00238
C_T/σ	0.0791	0.0679	0.0703	0.0671	0.0684
$C_{Q,u}$	$2.8414 \cdot 10^{-4}$	$6.1803 \cdot 10^{-4}$	$3.2188 \cdot 10^{-4}$	$3.1502 \cdot 10^{-4}$	$3.2894 \cdot 10^{-4}$
$C_{Q,l}$	-	-	$2.8727 \cdot 10^{-4}$	$2.7534 \cdot 10^{-4}$	$2.8275 \cdot 10^{-4}$
C_P/σ	$6.1816 \cdot 10^{-3}$	$6.7227 \cdot 10^{-3}$	$6.6262 \cdot 10^{-3}$	$6.4219 \cdot 10^{-3}$	$6.6538 \cdot 10^{-3}$
C_T/C_P	12.80	10.10	10.61	10.45	10.28

A comparison of the experimental[114] and numerical thrust sharing and overall rotor thrust for the stacked rotors is shown in Fig. 6.43. The experimental trends were accurately captured by the numerical simulations. With increasing index angle, the upper rotor thrust was increased while the lower rotor thrust was reduced. Slight differences were seen in the absolute magnitudes. Highest total thrust was produced at $\phi = -22.5°$. The collective pitch angles of the trimmed stacked rotors were $\Theta_{0,\text{Exp.}} = 8.5°$ in the experiment and $\Theta_{0,\text{CFD}} = 8.00°$ in the simulation. The two-bladed single rotor pitch angles were $\Theta_{0,\text{Exp.}} = 8°$ and $\Theta_{0,\text{CFD}} = 7.24°$, respectively.[114]

The variations in the velocity distribution (see chapter 6.2.3.2 Figs. 6.39 and 6.40) manifested in changes in the sectional force distributions; see Fig. 6.44. At $\phi = -22.5°$ the increased overall inflow

[17] In [11], when the lower rotor blade was leading the upper rotor blade at small values of ϕ the same dependency was found for a stacked rotor configuration based on the UTA CCR rotor test rig. Note that the rotors were trimmed to identical torque in the upper and lower rotor plane in addition to overall rotor thrust, i.e., a different trim target was used compared to this study

Table 6.3.: Comparison of thrust (C_T) and torque (C_Q) coefficients for the UTA stacked rotor test rig. $C_{T,2b}/\sigma = 0.10$ for the two-bladed single rotor. The used trim strategy is defined in chapter 4.6. Data was averaged over last rotor revolution.

	two-bladed	four-bladed	$\phi = -22.5°$	$\phi = 0°$	$\phi = +22.5°$
Θ_0	8.94°	9.72°			
$C_{T,u}$	0.00457	0.00788	0.00418	0.00452	0.00481
$C_{T,l}$	-	-	0.00398	0.00322	0.00307
C_T/σ	0.0993	0.0858	0.0888	0.0842	0.0858
$C_{Q,u}$	$3.7596 \cdot 10^{-4}$	$8.1825 \cdot 10^{-4}$	$4.2280 \cdot 10^{-4}$	$4.2167 \cdot 10^{-4}$	$4.2610 \cdot 10^{-4}$
$C_{Q,l}$	-	-	$3.7481 \cdot 10^{-4}$	$3.6893 \cdot 10^{-4}$	$3.7877 \cdot 10^{-4}$
C_P/σ	$8.1793 \cdot 10^{-3}$	$8.9008 \cdot 10^{-3}$	$8.6762 \cdot 10^{-3}$	$8.5020 \cdot 10^{-3}$	$8.7553 \cdot 10^{-3}$
C_T/C_P	12.14	9.64	10.23	9.90	9.80

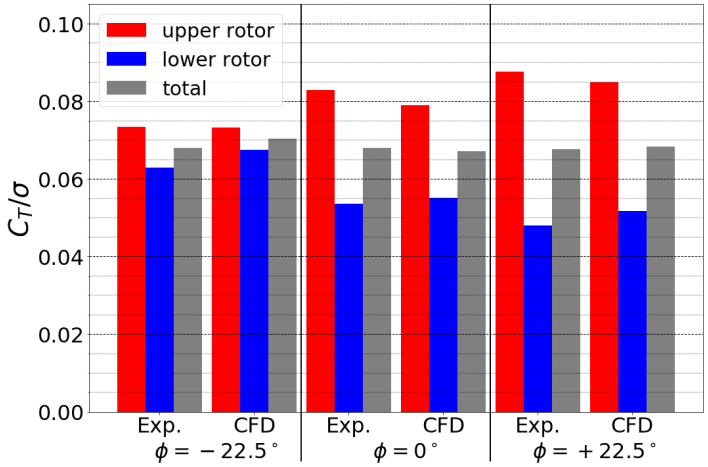

Figure 6.43.: Comparison of measured and computed thrust sharing for the two-by-two-bladed stacked rotor at different index angles[114]. Numerical data averaged over the last rotor revolution.

for the upper rotor blade lead to a reduction dF_z over the complete rotor radius; see Fig. 6.44a. At $\phi = +22.5°$ highest thrust was achieved, associated with the lowest axial velocity magnitude. In line with the velocity distributions, the single rotor configurations showed a higher loading bias towards the tips with reduced levels further inboard compared to the stacked rotor. Note that due to the chosen trim strategy the thrust was not trimmed to identical values (Θ_0 was identical for all blades of the four-bladed and stacked rotor configuration; see Fig. 6.43) and therefore, the particular numerical values were a result of the chosen trim strategy and not only a fundamental characteristic for stacked rotors at the particular index angles.

For the lower rotor, similar links between the axial velocities above and below the rotor blade and the thrust distribution could be made; see Figs. 6.40 and 6.44b. Furthermore, similarities could be seen when qualitatively comparing the sectional force distribution between the CCR and stacked rotor; compare Figs. 6.30 and 6.44b. The lower rotor distribution showed a bias towards the blade tips, i.e., towards the region which was least influenced by/outside of the upper

rotor downwash. Furthermore, the baggy shape of the distribution for the stacked rotor BVI case ($\phi = -22.5°$) showed strong similarities to the corresponding distribution for the CCR rotor during BVI ($C_T/\sigma = 0.06$ at $\phi = 0°$); compare Figs. 6.30b and 6.44b.

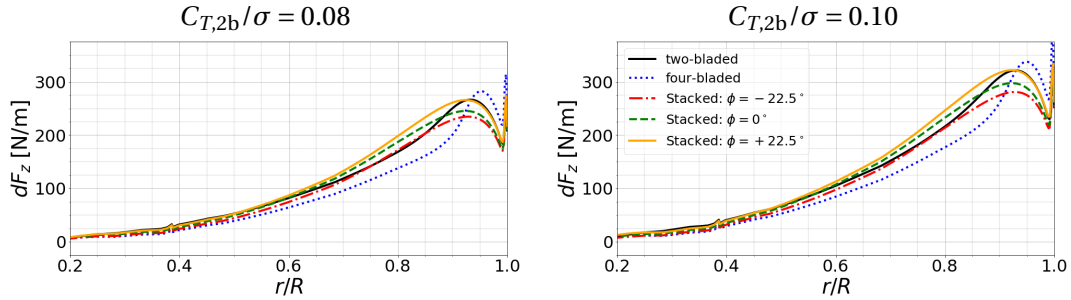

(a) Upper rotor.

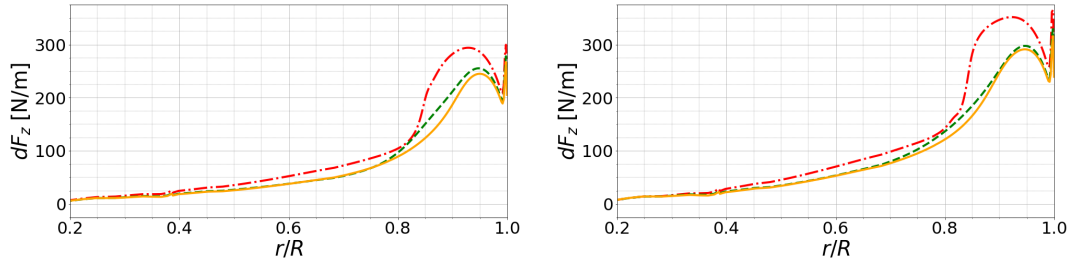

(b) Lower rotor.

Figure 6.44.: Comparison of computed radial distribution of sectional force (dF_z) for the stacked rotor operated at $C_{T,2b}/\sigma = 0.08$[114] and 0.10.

Radial distributions of sectional torque (dM_z) are shown in Fg. 6.45. In accordance with the small variations in the radial distributions of axial velocity and sectional force, the stacked upper rotor blades showed little variations; see Fig. 6.45a. More variation was seen for the lower rotor blades; see Fig. 6.45b. In particular, the BVI events for $\phi = -22.5°$ lead to noticeable oscillations. Despite the different radial distributions the absolute torque was well comparable for the lower rotors ($\Delta C_{Q,l} < 2.7\%$ when compared to $C_{Q,l}$ at $\phi = 0°$); see Tables 6.2 and 6.3.

6.2.5. Summary and Comparison of the Rotors

Time-averaged flow fields were investigated to gain general insights into the flow topology of the single and stacked rotors at multiple index angles (ϕ) and blade loadings. A comparable, continuous wake contraction was seen near the upper rotor plane of the stacked rotor and the single rotor. Differences were seen near the blade tips. Here, the single rotor and the lower rotor showed an upwash region, whereas the upper rotor did not. Overall, the flow field near the lower rotor plane was more complex due to interactions with the upper rotor downwash at inboard sections. At outboard sections, the contraction of the upper rotor wake caused fluid to be entrained into the lower rotor from outside the upper rotor slipstream boundary. Varying the index angles for the stacked rotor was found to cause large variations in the time-averaged axial velocity distributions close to the lower rotor and the upper and lower rotor slipstream boundary locations.

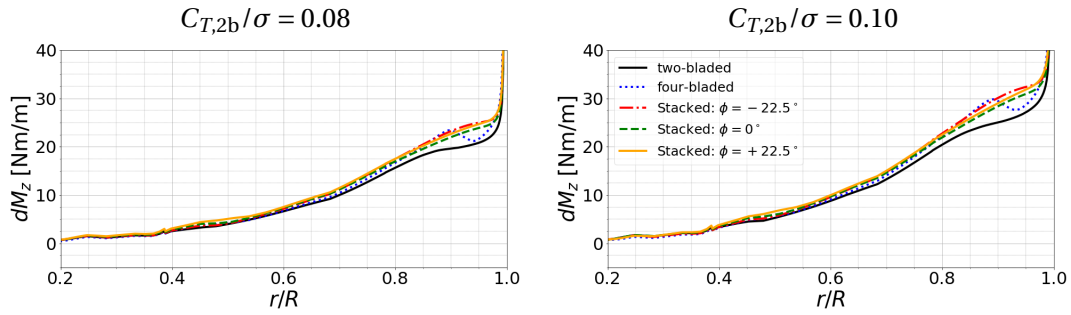

(a) Upper rotor.

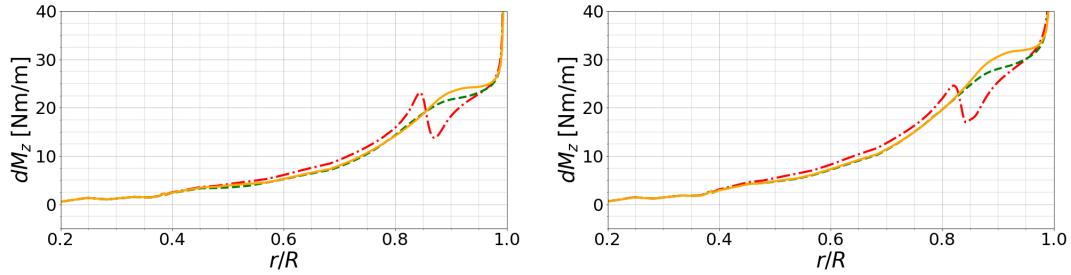

(b) Lower rotor.

Figure 6.45.: Comparison of computed radial distribution of sectional torque (dM_z) for the stacked rotor operated at $C_{T,2b}/\sigma = 0.08$ and 0.10.

These variations could be explained by variations in the tip vortex trajectories. While the two-bladed and four-bladed single rotor showed the well-known continuous contraction and axial convection of the tip vortices, the behavior was more elaborate for the stacked rotor configurations. Vortex trajectories were significantly influenced by index angle and blade loading variations. At $C_{T,2b}/\sigma = 0.08$, when the upper rotor blade was leading by $\phi = +22.5°$, the upper and lower rotor vortex trajectories (and therefore, also the slipstream boundaries) intersected and ultimately, the lower rotor tip vortex merged with the upper rotor tip vortex. In contrast, they remained equally spaced at $\phi = 0°$. The numerical simulations showed a quasi time-independence for these two operating conditions (index angles), whereas at $\phi = -22.5°$ BVI occurred, which caused the tip vortex trajectories to become highly unsteady. At $C_{T,2b}/\sigma = 0.10$ no tip vortex merging was observed at $\phi = +22.5°$ and the trajectories intersected multiple times. At $\phi = 0°$ the tip vortex trajectories were no longer equally spaced but showed intersections.

Moreover, variations in the axial velocity distributions were correlated to experimental data at fixed locations in space for the two-bladed single rotor. Radial distributions of axial velocity showed well comparable behavior between experiment and simulation. For fixed radial locations and varying blade azimuth angles an upwash was caused before and a downwash after blade passage. Good agreement between simulation and experiment was observed, proving the overall simulation approach suitable.

Furthermore, axial velocity distributions above and below the blade quarter chord axis were compared between the different rotor configurations. Above the upper rotor plane, the velocity distributions showed little dependence on blade loading, number of blades and index angle. Differences were more pronounced below the upper rotor plane. For the single rotor configurations a

strong influence caused by the tip vortex of the preceding blade was seen. This influence was not observed for the stacked rotor configurations. Here, the tip vortex passed the upper rotor blades close to or below the lower rotor plane, i.e., with an increased axial distance compared to the single rotors. Moreover, the axial velocity magnitude was largest for $\phi = -22.5°$, which resulted in the lowest thrust compared to the other two index angles at identical collective pitch angles. Close to the lower rotor plane, the radial distribution of axial velocity was significantly influenced by the upper rotor downwash and the upper and lower rotor tip vortices. The first resulted in overall increased velocity magnitudes in the lower rotor plane, the latter in more complex velocity variations near the blade tips. Again, the velocity distributions could be linked to the thrust of the rotor plane. The higher overall velocity magnitude lead to reduced thrust at identical collective pitch angles in the lower rotor plane for all index angles, when compared to the upper rotor plane. The highest overall velocity magnitude at $\phi = +22.5°$ showed the lowest thrust. Furthermore, a comparison of the thrust sharing between experiment and simulation showed that the experimental trends were well captured by the simulations. Overall, increasing the index angles increased the upper rotor thrust, while decreasing the lower rotor thrust. Moreover, a bias of the lower rotor blade sectional thrust towards the blade tips, i.e., outside of the upper rotor slipstream boundary, was observed.

6.3. Summary and Conclusions – Coaxial Rotors

URANS simulations were performed to investigate the flow fields of a CCR and a co-rotating/stacked rotor. The focus was on the exploration of fundamental similarities and differences between the CCR and stacked rotor flow fields, in addition to the effects of adding a second rotor plane when compared to a single rotor configuration. Furthermore, experimental data, provided by and analyzed together with the project partners at the University of Texas at Austin (UTA), were correlated to the numerical results to support the experimental campaign and assess the accuracy of the numerical simulations.

CCR rotor simulations were performed using four different turbulence models to investigate their influence on the simulation results. Besides a one-equation model (SA-neg-RC), three different variations of two-equation models based on the SST model were tested. It was found that all models computed comparable trim results along with similar axial velocity distributions close to the rotor planes. Differences were seen in their ability to conserve tip vortices. As a result of this study the numerically robust SA-neg-RC model, which also showed best tip vortex conservation, was used for all other rotor configurations. Comparisons with available experimental data of the coaxial and single rotor configurations showed that good agreement between experiment and simulation could be achieved with this model. Hence, the chosen turbulence model, along with the used numerical schemes and the temporal and spacial discretization was found to be well suited for the computation of (coaxial) rotors in hover.

Summaries of the results for the coaxial and single rotors are provided in chapters 6.1.3 for the CCR and 6.2.5 for the stacked rotor test rig. Hence, the subsequent conclusions focus on commonalities and differences between the two coaxial rotor configurations.

Time-averaged axial velocity contours were investigated for both rotor configurations. It was found that near the upper rotor plane the flow field was similar to that of a single rotor, i.e., showing a continuous wake contraction. Differences were seen near the blade tips for both rotor configurations. Here, the single rotor and the lower rotor showed an upwash region, whereas the upper rotor did not. Higher complexity was seen for the lower rotor. The contraction of the upper rotor wake caused fluid to be entrained into the lower rotor from outside the upper rotor slipstream boundary. For the CCR rotor a dependency on the chosen plane of data extraction was seen. Increased upper rotor slipstream contraction was observed at $\xi = 0°$ compared to $\xi = 45°$ (see Fig. 6.8), whereas the lower rotor showed opposite trends. The blade loading was found to have a small influence on the time-averaged flow fields. The stacked rotor flow fields (slipstream boundaries) showed a strong sensitivity to index angle variations and were more sensitive to changes in blade loading. In contrast to the CCR rotor, the slipstream boundaries not only approached each other more but also intersected or merged, depending on the specific combination of blade loading and index angle.

According changes were seen in the tip vortex trajectories. The CCR rotor tip vortex trajectories kept their separate paths independent of the plane of data extraction or rotor thrust. The latter mostly influenced the radial contraction and axial convection velocities but did not alter the general characteristics. By changing the azimuthal plane of data evaluation, the azimuthal dependency of the CCR rotor slipstream boundaries could be related to changes of the upper-lower rotor wake interactions, which were influenced by the relative distance of the measurement plane to blade crossings. The stacked rotor trajectories showed a strong sensitivity to variations of the index angle and blade loading. Both factors not only changed the radial contraction and axial convection velocities, but also caused significant changes in the wake interactions. As a results, variations in the flow fields ranged from BVI, over quasi parallel upper and lower rotor tip vortex trajectories (i.e., a similar behavior to that seen for the CCR rotor), to vortex merging, and crossings of the vortex trajectories.

The influence of the upper rotor wake on the lower rotor manifested in changes in the radial force distributions. For both configurations the lower rotor thrust was highly biased towards the blade tips. Note that identical, untwisted and untapered rotor blades were used for both configurations and in both rotor planes, i.e., the rotor blade geometry was not 'optimized' to improve the loading distribution[82]. Overall, the lower rotor thrust distribution showed larger variations compared to the upper rotor in the two planes of data extraction for the CCR rotor and for the stacked rotor configurations.

It was found that the changes in the (upper) rotor tip vortex trajectories caused by adding a second rotor plane for coaxial rotors, and therefore, changes of the miss-distance of the tip vortices to the rotor blades, had the greatest influence on coaxial rotor flow fields. In particular, the increased axial convection of the upper rotor tip vortices had a great impact on the upper and lower rotor axial velocity distributions. This resulted in changes in the rotor blade sectional thrust and torque distributions, which ultimately influenced overall rotor performance.

7. Rotor Aerodynamics with Dynamic Actuation

Dynamic pitch and RPM inputs were investigated using the UTA rotor configurations in hover. Collective pitch inputs with varying amplitude and duration were commanded for the CCR rotor test rig and RPM inputs were commanded for the stacked rotor test rig. Two additional rotor revolutions were computed after completing the pitch and RPM inputs to assess the transient behavior of the rotor aerodynamics after the control inputs. The operating conditions and numerical settings were identical to those described in chapter 6. A detailed overview of the test rigs is given in chapter 3.2 and the baseline operating conditions (i.e., before pitch and RPM inputs) are summarized in Table 3.2 for the CCR rotor test rig and in Table 3.3 for the stacked rotor test rig. The SA-neg-RC turbulence model was used for all simulations. Time step sizes and grid resolutions were chosen according to the findings of the grid and temporal sensitivity study; see chapter 4.5.2.6. An assessment of the accuracy of the numerical simulations was made by correlation with experimental data, wherever possible. This could in parts be done for each of the two-bladed single rotors, which were derived from both coaxial rotor configurations, based on previous publications by the experimenters and the author[113, 102, 103]. Blade, control system, or drive train elasticities/dynamics were not considered in the simulations, so that only the aerodynamic influences caused by the control inputs could be investigated.

7.1. Dynamic Pitch Actuation

An experiment using a two-bladed single rotor was performed at UTA in which the collective pitch was increased ($\Delta\Theta_0 = 1°$) at a ramp rate of approximately $\Delta\Theta_0 = 0.25°$ per revolution[113, 103]; see Fig. 7.1. This experiment was the basis for evaluating the simulation accuracy. It was decided to approximate the experimental pitch input in the simulations by a '1 − Cosine' function, i.e., a smooth, continuous function:

$$\Theta_0 = \Theta_{0,\text{ref}} + \frac{\Delta\Theta_0}{2} - \frac{\Delta\Theta_0}{2}\cos(\frac{2\pi\Omega}{2N}t) \tag{7.1}$$

where $\Theta_{0,\text{ref}}$ is the pitch angle before pitch input, Ω is the rotational frequency of the rotor, and N is the input duration given in number of revolutions. This allowed computing the averaged response of the rotor measured in the experiment. Additional simulations were made using a higher pitch input amplitude ($\Delta\Theta_0 = 2°$) and shorter input durations ($\Delta\psi_b = 180°$ and $\Delta\psi_b = 360°$) for the single rotor; see Fig. 7.4a. For the CCR rotor an input duration of $\Delta\psi_b = 360°$ combined with input amplitudes of $\Delta\Theta_0 = 1°$ and $\Delta\Theta_0 = 2°$ was commanded.

7.1.1. Forces and Moments

7.1.1.1. Two-Bladed Single Rotor

The measured and simulated thrust response of the two-bladed single rotor at $C_T/\sigma = 0.06$ caused by a pitch input of $\Delta\Theta_0 = 1°$ over $\Delta\psi_b = 1440°$ (Fig. 7.1) is shown in Fig. 7.2. The experimental data showed oscillations in thrust that my by be attributed to a slightly varying rotor rotational speed (Fig. 7.3) or blade flapping[113]. Both effects were not included in the numerical simulations. A slight overshoot in thrust was observed in the computed rotor response. However, a potential overshoot in the measured thrust was obscured by the fluctuations in the experimental data.

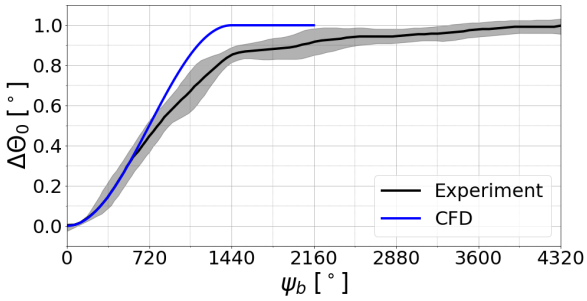

Figure 7.1.: Comparison of experimental[103] collective pitch angle variation with the curve fit used for the numerical simulations at a pitch input magnitude of $\Delta\Theta_0 = 1°$ commanded over four rotor revolutions ($\Delta\psi_b = 1440°$). Shaded region indicates one standard deviation.

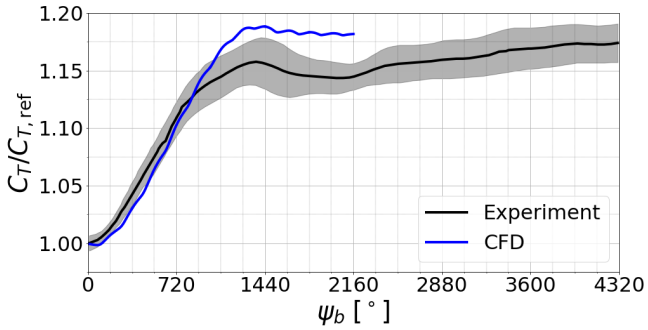

Figure 7.2.: Comparison measured[103] and computed rotor thrust variation normalized by thrust prior to pitch input ($C_T/C_{T,\mathrm{ref}}$) for a pitch amplitude of $\Delta\Theta_0 = 1°$ over $\Delta\psi_b = 1440°$. Rotor trimmed to $C_T/\sigma = 0.06$ before pitch input.

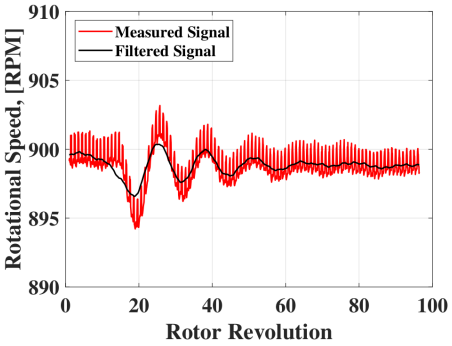

Figure 7.3.: Experimental rotor speed variation due to change in blade pitch of $\Delta\Theta_0 = 1°$ over four rotor revolutions ($\Delta\psi_b = 1440°$)[103].

As the rotor did not show a significant thrust overshoot at $C_T/\sigma = 0.06$ for a pitch input of $\Delta\Theta_0 = 1°$ over $\Delta\psi_b = 1440°$, the numerical model was used to extend the test matrix to higher input amplitudes and shorter input durations; see Fig. 7.4a. The rotor thrust and torque response caused by a pitch input of $\Delta\Theta_0 = 1°$ over $\Delta\psi_b = 180°$ and $\Delta\psi_b = 360°$, as well as $\Delta\Theta_0 = 2°$ over $\Delta\psi_b = 360°$ were investigated at $C_T/\sigma = 0.06$ and 0.08; see Figs. 7.4b and 7.4c.

The change in pitch amplitude, as well as in input duration increased the thrust overshoot significantly; see Fig. 7.4b. At a rate of $\Delta\psi_b = 180°$ the maximum thrust occurred right after the maximum pitch angle was reached. For the slower rates ($\Delta\psi_b = 360°$ and $1440°$) the maximum thrust was observed before the maximum pitch angle was reached. The qualitative temporal characteristic of the relative thrust increase was independent of the blade loading before the pitch input. From a quantitative perspective, the relative thrust increase and overshoot was reduced when increasing the blade loading. As the pitch angle amplitude was identical in both cases, and therefore, the relative pitch angle increase was lower at higher blade loadings, this was an expected result.

The effects of the different commanded pitch angle inputs on rotor torque are shown in Fig. 7.4c. Neither of the commanded inputs lead to large overshoots in torque and the rotor response smoothly followed the pitch angle changes. Note that blade deformation and inertial effects were not included in the simulations and the shown characteristic was caused by aerodynamic effects only. The torque response may change significantly depending on the dynamic response of the rotor system; see chapter 7.2.1. Equivalent to the rotor thrust response, the relative increase in rotor torque was reduced when increasing blade loading before the pitch input.

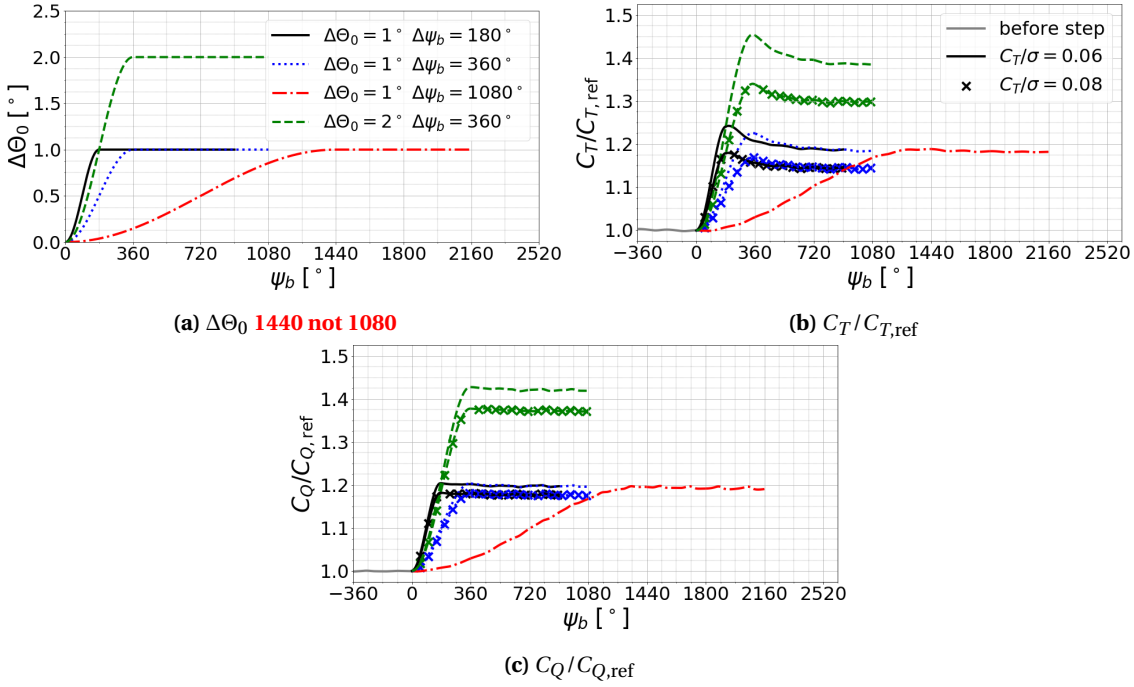

(a) $\Delta\Theta_0$ **1440 not 1080** **(b)** $C_T/C_{T,\mathrm{ref}}$

(c) $C_Q/C_{Q,\mathrm{ref}}$

Figure 7.4.: Pitch input ($\Delta\Theta_0$) and relative rotor thrust ($C_T/C_{T,\mathrm{ref}}$) and torque ($C_Q/C_{Q,\mathrm{ref}}$) variations of the two-bladed single rotor based on the UTA CCR rotor test rig. Rotor trimmed to $C_T/\sigma = 0.06$ and 0.08 before pitch inputs. Thrust and torque were normalized by mean values prior to pitch input.

Changes in the radial distribution of sectional thrust (dF_z) during and after the pitch inputs ($\Delta\Theta_0 = 1°$ and $\Delta\Theta_0 = 2°$ over $\Delta\psi_b = 360°$) at a baseline blade loading of $C_T/\sigma = 0.06$ are shown in Fig. 7.5. The absolute increase of sectional thrust (ΔdF_z) was largest close to the blade tips and only small changes were seen near the blade root; see Fig. 7.5a. This was in line with the radial distribution of axial force at varying blade loadings shown in chapter 6.1.1.4; see Fig. 6.6. However, the tem-

poral evolution was affected by the radial location of the blade sections. Close to the end of the input ($\psi_b = 360°$) a thrust overshoot was observed at inboard sections, which was subsequently reduced after reaching the maximum pitch angle. This could more clearly be seen when looking at the relative sectional thrust variation ($dF_z/\overline{dF_z}$); see Fig. 7.5b. As infinitely rigid, untwisted rotor blades were modeled in the simulations the pitch angle increase and magnitude were identical for all blade sections. Hence, it was assumed that the thrust overshoot at inboard sections was the result of a slower build up of inflow at the inboard sections compared to the blade tips. This effect contributed to the observed thrust overshoot of the rotor; see Fig. 7.4b. The effect was more pronounced at increased pitch input amplitudes, and was also visible at an increased baseline blade loading of $C_T/\sigma = 0.08$; see Fig. H.1. The radial variations in inflow during pitch inputs were previously qualitatively described in [19]. It was stated that flow visualization results "indicate that the induced-velocity flow builds up first at the rotor tips and then proceeds inboard"[19], a conclusion supporting the observed effect.

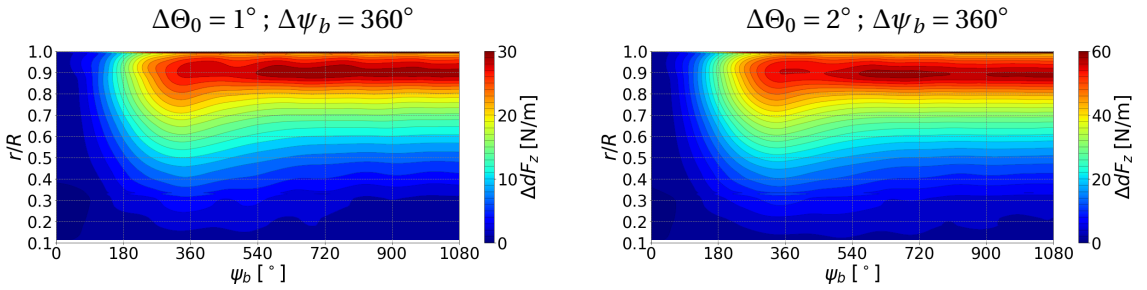

(a) ΔdF_z

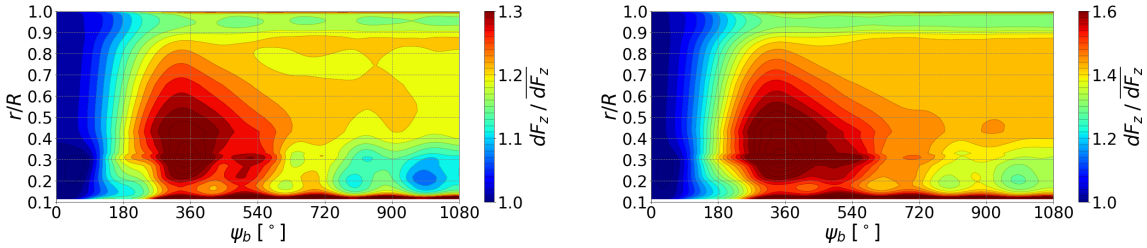

(b) $dF_z/\overline{dF_z}$

Figure 7.5.: Comparison of computed sectional thrust increase ($\Delta dF_z = dF_z - \overline{dF_z}$) and relative variation ($dF_z/\overline{dF_z}$) during and after collective pitch step inputs for the two-bladed single rotor based on the UTA CCR rotor test rig. Relative data scaled by the sectional thrust before pitch input ($\overline{dF_z}$). Rotor trimmed to $C_T/\sigma = 0.06$ before pitch input. Pitch angle variations are shown in Fig. 7.4a.

7.1.1.2. Two-by-Two-Bladed CCR Rotor

Two different pitch angle amplitudes ($\Delta\Theta_0 = 1°$ and $\Delta\Theta_0 = 2°$) were commanded for the CCR rotor over one rotor revolution ($\Delta\psi_b = 360°$). The pitch input was initialized during blade passage, i.e., at an index angle of $\phi = 0°$. The upper and lower rotor thrust and torque responses at a baseline blade loadings of $C_T/\sigma = 0.06$ and $C_T/\sigma = 0.08$ are shown in Fig. 7.6. Data was normalized with the corresponding average value before the pitch inputs at the respective blade azimuth angle ψ_b.

Similarly to the two-bladed single rotor described in the previous chapter a thrust overshoot occurred in both rotor planes before the maximum pitch angle was reached. The overall thrust increase and overshoot was higher for the lower rotor and was reduced with increasing baseline blade loading; see Figs. 7.6a and 7.6c. Permanent relative thrust fluctuations after the pitch inputs were observed, which were caused by increased thrust fluctuations at the increased blade loadings after the input. This phenomenon was previously described when investigating the CCR rotor at baseline operating conditions; compare Fig. 6.28 and Figs. 7.6a and 7.6c. Note that data at $C_T/\sigma = 0.08$ is shown up to the maximum wake age computed before the residual of the turbulence model transport variable $\rho\tilde{\nu}$ diverged.

Changes in rotor torque are shown in Figs. 7.6b and 7.6d. As for the thrust variations, the increased inter-rotor interactions at increased blade loadings lead to permanent relative torque fluctuations after the pitch input; see Fig. 6.29. Due to the chosen trim strategy, i.e., using the same collective pitch angle input in both rotor planes, the CCR rotor was no longer torque balanced after the inputs; see chapter 4.6. The differences in torque at $C_T/\sigma = 0.06$; (0.08) were $\left|\frac{|Q_l|}{|Q_u|} - 1\right| = 0.0133$; (0.0130) for a pitch input of $\Delta\Theta_0 = 1°$ and $\left|\frac{|Q_l|}{|Q_u|} - 1\right| = 0.0218$; (0.0225) for $\Delta\Theta_0 = 2°$.

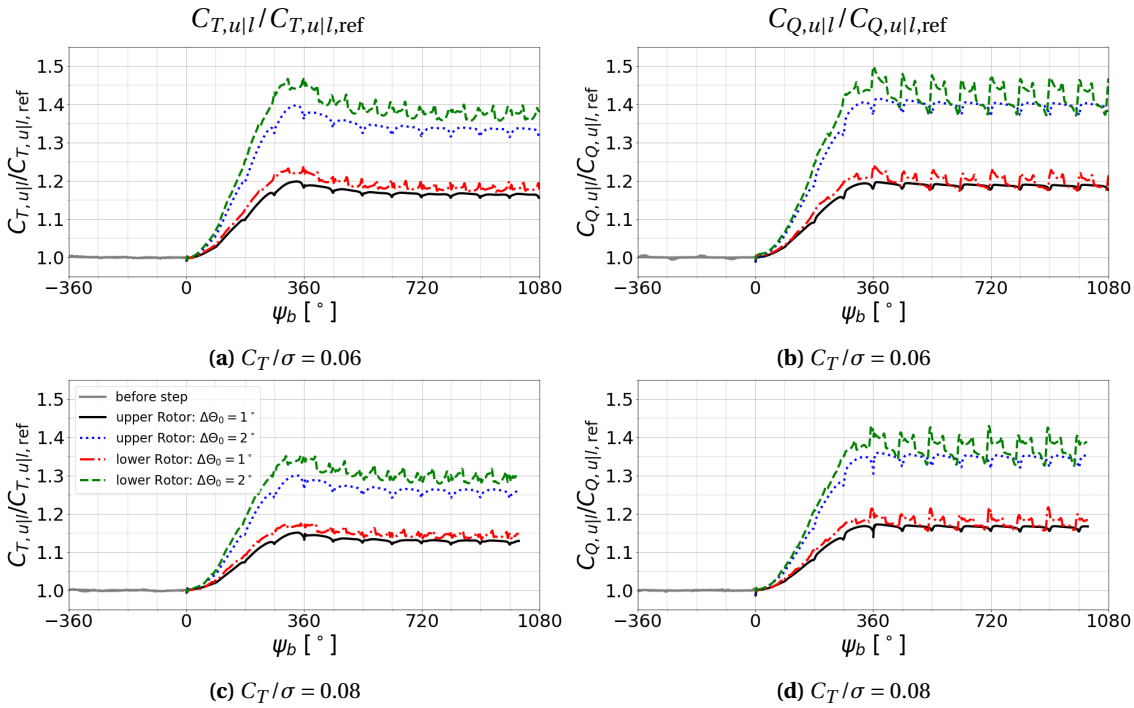

(a) $C_T/\sigma = 0.06$ **(b)** $C_T/\sigma = 0.06$

(c) $C_T/\sigma = 0.08$ **(d)** $C_T/\sigma = 0.08$

Figure 7.6.: Computed relative rotor thrust ($C_{T,u|l}/C_{T,u|l,\mathrm{ref}}$), and torque ($C_{Q,u|l}/C_{Q,u|l,\mathrm{ref}}$) variations before, during and after collective pitch step inputs for the CCR rotor. Rotor trimmed to $C_T/\sigma = 0.06$ and 0.08 before pitch input. Thrust and torque normalized by mean values prior to pitch input. Pitch angle variations are shown in Fig. 7.4a.

Changes in the radial distribution of sectional thrust (dF_z) during and after the pitch inputs for a baseline blade loading of $C_T/\sigma = 0.06$ are shown for the upper and lower rotor in Figs. 7.7 and 7.8, respectively. Data was normalized with the corresponding value before the pitch inputs at the respective blade azimuth angle ψ_b.

For the upper rotor the same characteristics previously described for the two-bladed single rotor were observed; see chapter 7.1.1.1. Close to the end of the pitch input ($\psi_b = 360°$), a thrust overshoot was observed at inboard blade sections and the overall increase in sectional thrust was highest near the blade tips; see Fig. 7.7. The increased inter-rotor interactions at increased blade loading resulted in the four-per-revolution thrust variations seen in the plots; see also Figs. F.14 and F.15 for sectional thrust and relative sectional thrust variations at the baseline blade loading.

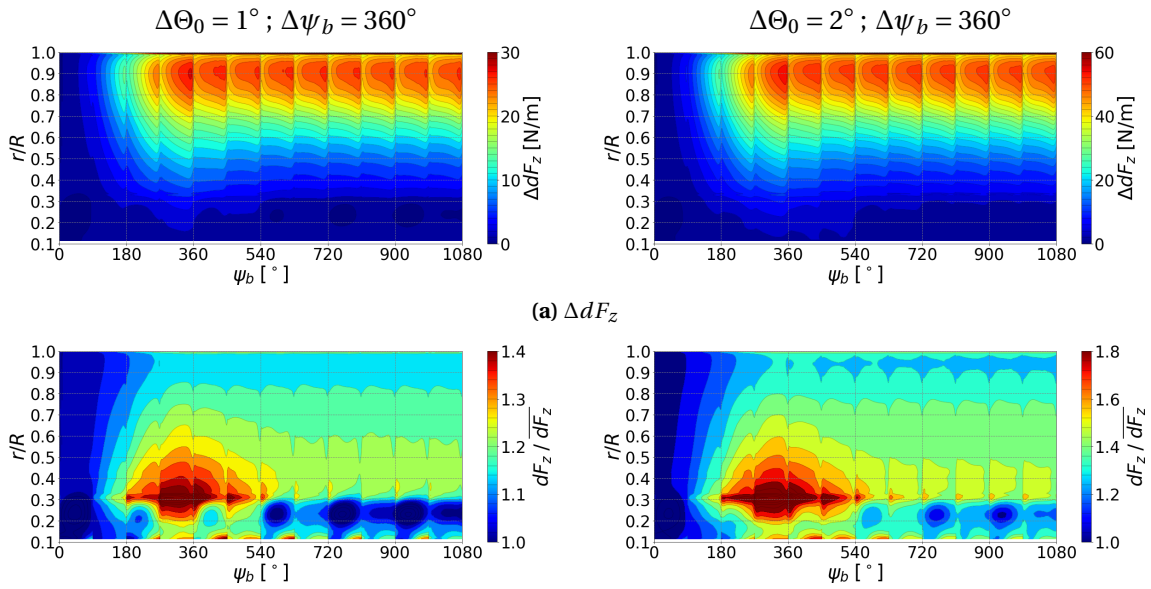

(a) ΔdF_z

(b) $dF_z/\overline{dF_z}$

Figure 7.7.: Comparison of computed sectional thrust increase ($\Delta dF_z = dF_z - \overline{dF_z}$) and relative variation ($\Delta dF_z/\overline{dF_z}$) during and after collective pitch step inputs for the upper rotor of the CCR rotor. Relative data scaled by the sectional thrust before pitch input ($\overline{dF_z}$). Rotor trimmed to $C_T/\sigma = 0.06$ before pitch input. Pitch angle variations are shown in Fig. 7.4a.

The lower rotor showed the same general characteristics; see Fig. 7.8. However, the effects were more complex and affected larger regions of the rotor blades. Interactions with the upper rotor downwash resulted in sectional thrust overshoots during and after the pitch input. It was assumed that the time required to convect the higher downwash to the lower rotor plane was the main driver for the observed behavior. As a result, the rotor thrust overshoot was higher for the lower rotor compared to the upper rotor; see Fig. 7.6a. Moreover, the increased convection velocities of the upper rotor trailed vortex sheets and tip vortices, caused by increasing the blade pitch angle, resulted in phase differences of the aerodynamics interactions for the lower rotor blades after the pitch input; see also Figs. 6.23 and 6.24. As a result, variations in ΔdF_z at inboard locations were not aligned with vertical lines in the plots. Compared to before the pitch input (i.e., the data used for normalization), the aerodynamic interactions occurred at different azimuth angles after the pitch input; see Figs. 7.8b and F.15. At an increased blade loading of $C_T/\sigma = 0.08$ equivalent effects could be seen; see Figs. H.2 and H.3.

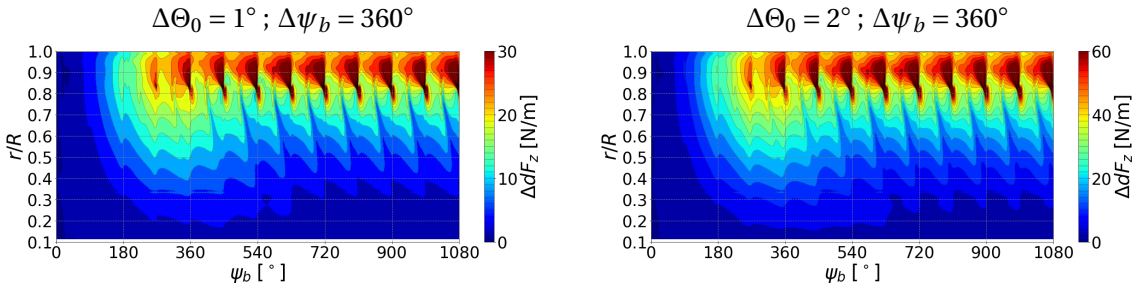

(a) ΔdF_z

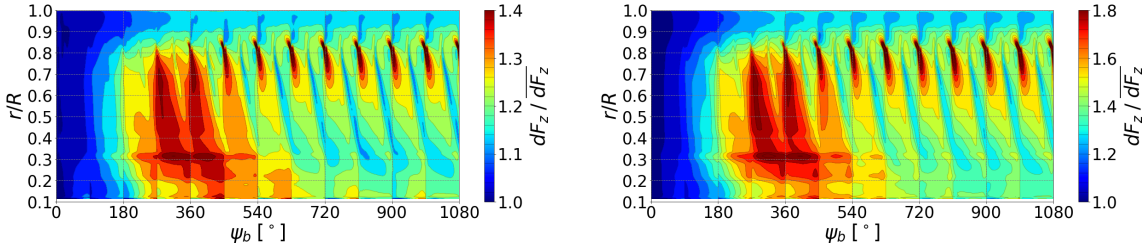

(b) $dF_z/\overline{dF_z}$

Figure 7.8.: Comparison of computed sectional thrust increase ($\Delta dF_z = dF_z - \overline{dF_z}$) and relative variation ($\Delta dF_z/\overline{dF_z}$) during and after collective pitch step inputs for the lower rotor of the CCR rotor. Relative data scaled by the sectional thrust before pitch input ($\overline{dF_z}$). Rotor trimmed to $C_T/\sigma = 0.06$ before pitch input. Pitch angle variations are shown in Fig. 7.4a.

7.1.2. Rotor Inflow

The temporal evolution of axial velocity in the plane of data extraction $\xi = 0°$ (see Fig. 6.8) caused by increasing the blade pitch angle by $\Delta\Theta_0 = 1°$ over $\Delta\psi_b = 1440°$ at $C_T/\sigma = 0.06$ and 0.08 is shown in Fig. 7.9. Qualitatively, the mean axial velocity was gradually increasing and was superimposed by the previously described axial velocity curves before the pitch inputs; see Fig. 6.7. The observed smooth transition to steady state after the pitch input was an indicator that the wake developed at a similar rate as the blade pitch angle increased. However, these gradual effects caused the variations in the relative sectional thrust increase described before; see chapter 7.1.1.

Moreover, a comparison with experimental data[103] was possible at two radial locations ($r/R = 0.75$ and 0.85); see Figs. 7.9c and 7.9d. The findings derived from the numerical results could be confirmed. Overall, an increased velocity magnitude was computed, but trends were identical.

Increasing the pitch amplitude and rates gave qualitatively identical results; see Figs. H.4 and H.5. Differences between the two inputs durations $\Delta\psi_b = 180°$ and $\Delta\psi_b = 360°$ for $\Delta\Theta_0 = 1°$ were small and limited to an azimuth angle range of $180° \lessapprox \psi_b \lessapprox 360°$. Velocity distributions for $\Delta\Theta_0 = 1°$ and $\Delta\Theta_0 = 2°$ at an input duration of $\Delta\psi_b = 360°$ were quasi identical in the same ψ_b range and only started to notably differ in velocity magnitude at higher blade azimuth angles.

Equivalent results were achieved for the CCR rotor and therefore, are not discussed in more detail here. Data for the upper and lower rotor plane at $C_T/\sigma = 0.06$ is shown in Figs. H.6 and H.7. Results at $C_T/\sigma = 0.08$ are shown in Figs. H.8 and H.9.

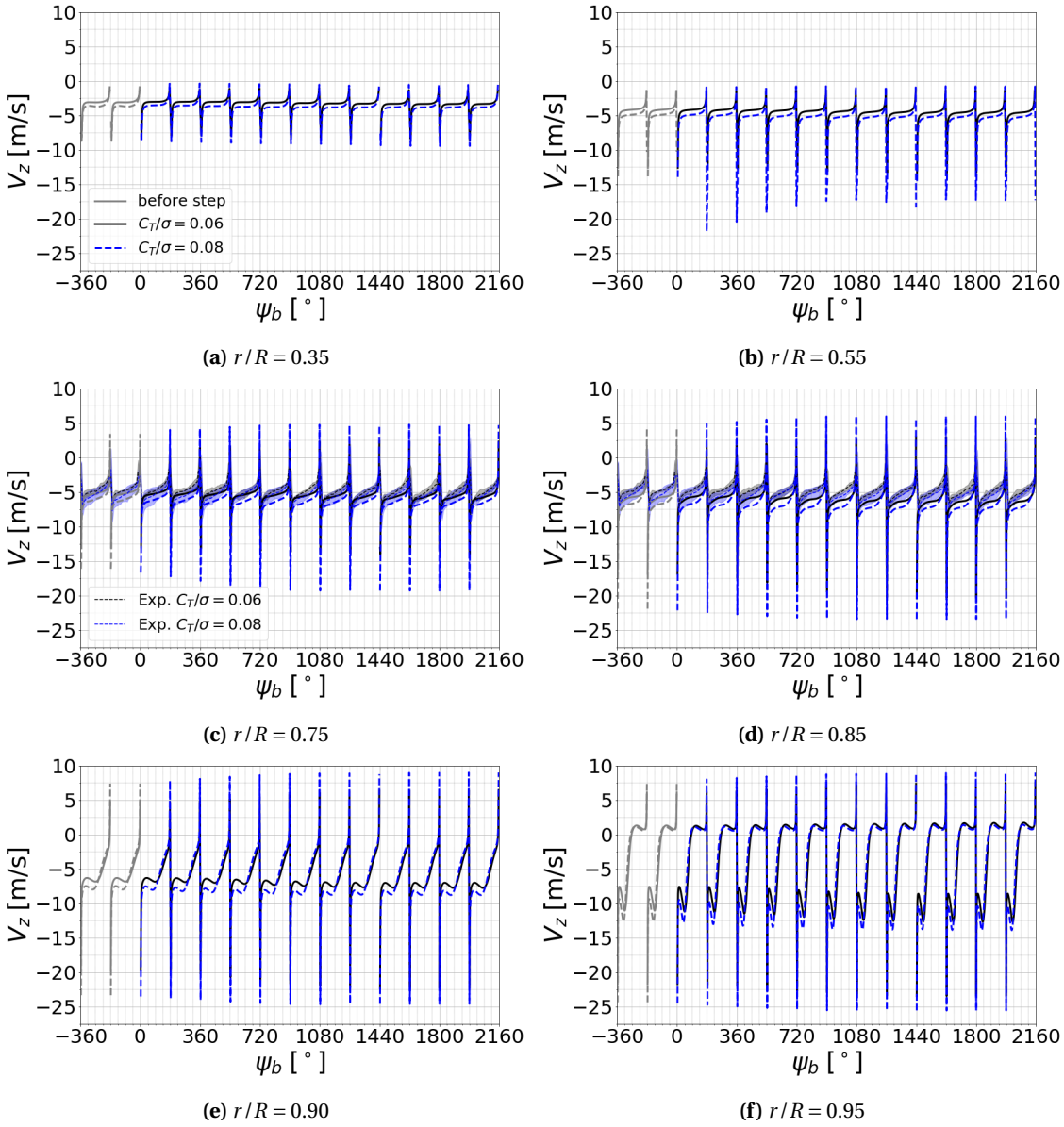

(a) $r/R = 0.35$ **(b)** $r/R = 0.55$

(c) $r/R = 0.75$ **(d)** $r/R = 0.85$

(e) $r/R = 0.90$ **(f)** $r/R = 0.95$

Figure 7.9.: Comparison of experimental[103] ($r/R = 0.75$ and $r/R = 0.85$) and computed variations of axial velocity (v_z) before, during and after collective pitch step inputs ($\Delta\Theta_0 = 1°$, $\Delta\psi_b = 1440°$) for the two-bladed single rotor based on the UTA CCR rotor test rig. Data was extracted in plane $\xi = 0°$; see Fig. 6.8. Rotor was trimmed to $C_T/\sigma = 0.06$ and $C_T/\sigma = 0.08$ before pitch input. Pitch angle variations are shown in Fig. 7.4a. Experimental data averaged from $\Delta z/c = 0.34$ above and $\Delta z/c = -1$ below the rotor blade. Numerical data extracted at $\Delta z/c = 0$.

7.2. Dynamic Rotational Speed Actuation

Simulations were made using rotational speed variations of $\Delta\Omega = 20\%$ (180 RPM) and two different input durations ($\Delta\psi_b$) and blade loadings ($C_{T,2b}/\sigma = 0.08$ and 0.10). In the two-bladed single rotor experiment performed at UTA the rotational speed was increased by $\Delta\Omega = 18\%$ over three revolutions ($\Delta\psi_b = 1080°$)[102]; see Fig. 7.10a. It was decided to approximate the experimental RPM input in the numerical simulations by a '1 − Cosine' function, i.e., a smooth, continuous function which allowed computing the averaged response of the rotor measured in the experiment. Moreover, a reduced input duration ($\Delta\psi_b = 360°$) was commanded for the single rotor; see Fig. 7.4a. Furthermore, the two input durations ($\Delta\psi_b = 360°$ and $\Delta\psi_b = 1080°$) combined with the same input amplitude of $\Delta\Omega = 20\%$ were commanded for the stacked rotor at the three index angles previously used in chapter 6.2 and the four-bladed single rotor at both blade loadings. Note that the absolute time step size (Δt) during the RPM input was identical to the value before the RPM command and that it was set to $\Delta\psi_b = 0.5°$ after reaching constant rotational speed again.

7.2.1. Forces and Moments

A comparison of the experimental thrust response[102] with the numerical simulations results for the two-bladed single rotor is shown in Fig. 7.11a. The computed thrust magnitude and rate of change agreed well with the experimental results. Note that the higher RPM amplitude in the numerical simulations (20% compared to 18% in the experiment) resulted in an increased final steady-state value in the simulations. Moreover, a slight thrust overshoot was observed in the simulations, which was not seen in the averaged experimental data.

In addition to the rotor thrust response, the temporal evolution of the rotor torque was investigated. The relative increase in torque was computed correctly after the rotor rotational speed reached its steady-state value ($\psi_b > 1080°$); see Fig. 7.11b. The assessment of the numerical data showed that the torque overshoot during the RPM input was mostly caused by inertial forces, which were not included in the numerical model. The aerodynamic torque (Q_{aer}) only contributed a fraction to the total torque (Q_{tot}); compare Figs. 7.11b and 7.11c. Adding the approximate inertial torque (Q_i) during the RPM ramp (Fig. 7.11d) to the computed aerodynamic torque was key to getting good agreement between the numerical and experimental data; see Fig. 7.11b. The inertial torque was calculated by multiplying the angular acceleration by the rotor moment of inertia ($I = 0.3328\,\text{kg}\,\text{m}^2$).[102] Note that the inertial torque was normalized with the mean torque at each blade loading before the RPM input. Hence, the different magnitude in normalized form should not be confused with different absolute values of the inertial torque.

Computed thrust and torque responses of the different rotors (two-bladed and four-bladed single rotor; stacked rotor at different index angels) for a rotational speed increase of $\Delta\Omega = 20\%$ over one rotor revolution are shown in Figs. 7.12 and 7.13. The decreased input duration resulted in notable thrust overshoots for all rotor configurations, as well as in both rotor planes; see Fig. 7.12. The overall thrust overshoot was higher for the lower rotor plane, while the absolute thrust increase after the RPM input was larger for the upper rotor at both computed blade loadings. Data

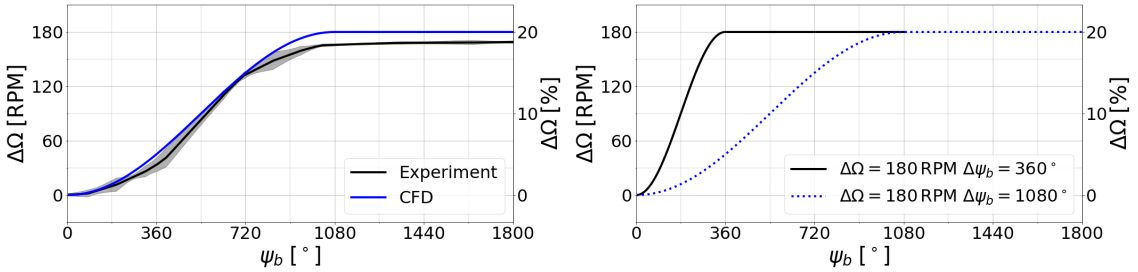

(a) Experimental data for the single rotor, averaged over eight tests[102], and curve fit in numerical simulation. Shaded region indicating one standard deviation.

(b) Rotor rotational speed inputs used in the numerical simulations.

Figure 7.10.: Rotor speed inputs for the UTA stacked rotor test rig.

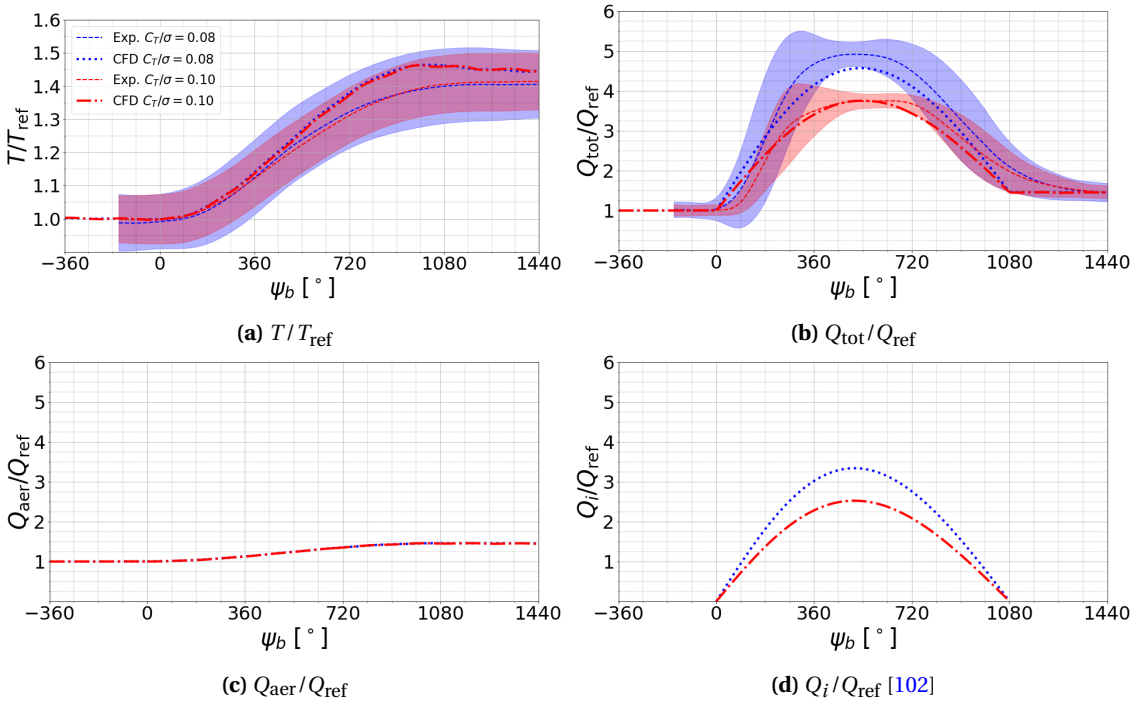

(a) T/T_{ref}

(b) $Q_{\mathrm{tot}}/Q_{\mathrm{ref}}$

(c) $Q_{\mathrm{aer}}/Q_{\mathrm{ref}}$

(d) Q_i/Q_{ref} [102]

Figure 7.11.: Comparison of experimental[102] and computed rotor thrust ($C_{T,u|l}/C_{T,u|l,\mathrm{ref}}$), and torque ($C_{Q,u|l}/C_{Q,u|l,\mathrm{ref}}$) variations of the single rotor based on the UTA stacked rotor test rig. Rotor trimmed to $C_{T,2b}/\sigma = 0.08$ and 0.10 before RPM input. Thrust and torque normalized by mean values prior to pitch input. RPM variations shown in Fig. 7.10a. Aerodynamic ($C_{Q,\mathrm{aer}}$) and inertial ($C_{Q,i}$) rotor torque variations shown in addition to the total torque ($C_{Q,\mathrm{tot}}$).

for the four-bladed rotor and the stacked rotors were well comparable, whereas the two-bladed rotor showed an overall reduced thrust increase at steady-state after the RPM input. The corresponding data for an input duration of $\Delta\psi_b = 1080°$ is shown in Fig. I.1. The difference between the two input durations was that a thrust overshoot was not clearly visible when increasing the rotor rotational frequency over three revolutions.

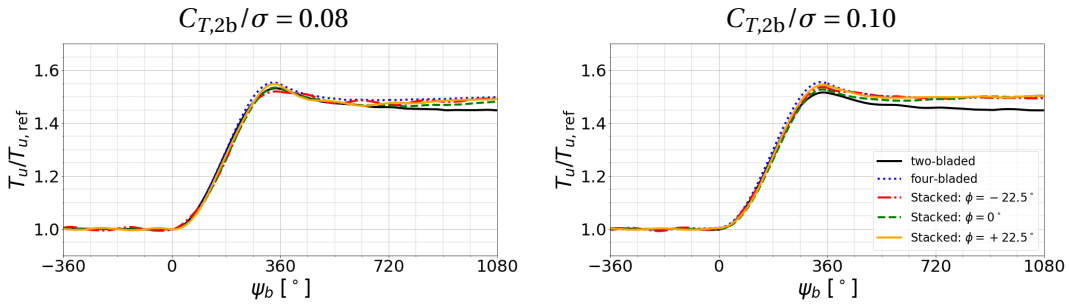

(a) Upper rotor

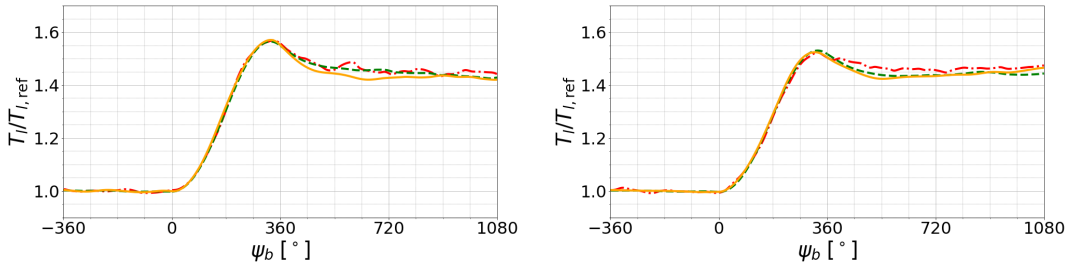

(b) Lower rotor

Figure 7.12.: Rotor thrust ($T_{u|l}/T_{u|l,\mathrm{ref}}$) variations of rotors based on the UTA stacked rotor test rig for $\Delta\Omega$ = 20% over $\Delta\psi_b = 360°$. Rotor trimmed to $C_{T,2b}/\sigma = 0.08$ and 0.10 before pitch input. Thrust was normalized by mean values prior to RPM input. The RPM commands shown in Fig. 7.10b.

Similarly, aerodynamic rotor torque changes were investigated; see Fig. 7.13. For the upper rotor no torque overshoots were computed and the relative increase was well comparable for all rotor types and configurations; see Fig. 7.13a. To the contrary, a torque overshoot was observed for the lower rotor at both blade loadings and all index angles; see Fig. 7.13. The magnitude was in good agreement for all index angles at both blade loadings. As for the thrust response no torque overshoot was observed at $\Delta\psi_b = 1080°$; see Fig. I.2.

Changes in the radial distribution of sectional thrust (dF_z) during and after the RPM inputs for the two-bladed single rotor based on the UTA stacked rotor test rig are shown in Fig. 7.14. Data was normalized with the corresponding value before the RPM inputs. The corresponding rotor thrust response is shown in Figs. 7.12a and I.1a. Similarly to the dynamic collective pitch input results (Fig. 7.5) a local thrust overshoot was observed at inboard sections of the rotor blade for the lower input duration of $\Delta\psi_b = 360°$; see Fig. 7.14. This was an indicator that, equivalently to the collective pitch inputs previously described in chapter 7.1, dynamic RPM changes caused the induced-velocity to built up first near the rotor blade tips and then to proceeded inboard. No significant overshoot in thrust was observed at an input duration of $\Delta\psi_b = 1080°$, which was in accordance with the findings from the overall rotor thrust response; compare Figs. 7.14 and I.1a. At increased blade loading equivalent findings could be made; see Fig. I.3. Note that an increased oscillating sectional thrust (at an overall low mean level) was seen near the blade root at this blade loading; see Fig. I.3b. A similar oscillation was seen in the rotor thrust and torque response; see Figs. I.1a and I.2a. This phenomenon was not seen for the four-bladed rotor; see Figs. I.4 and I.5. It was supposed that the increased thrust and therefore, changes in the axial velocity distribution of the four-bladed rotor stabilized the inboard wake region and prevented the

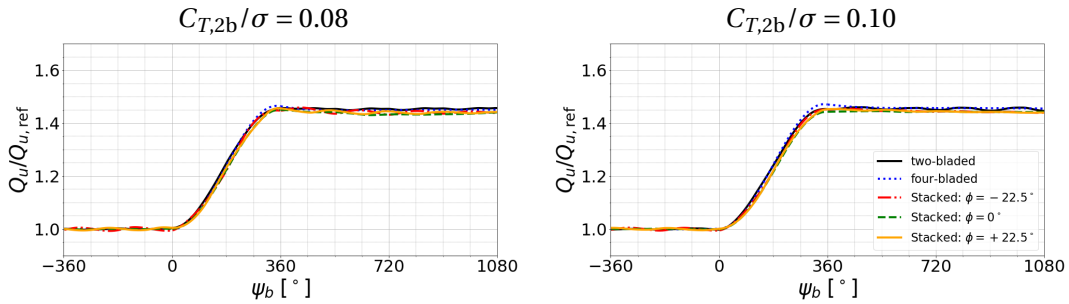

(a) Upper rotor

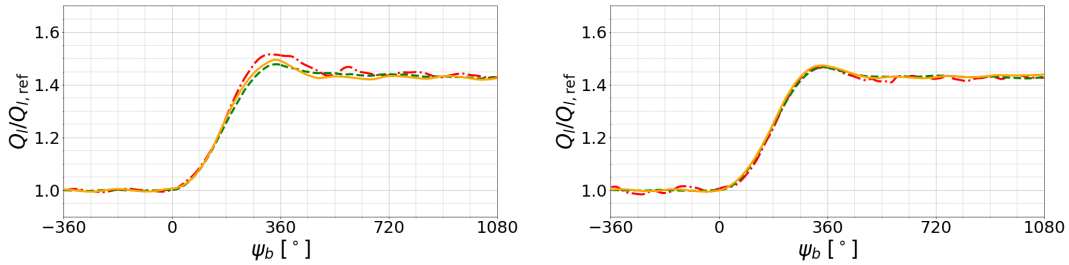

(b) Lower rotor

Figure 7.13.: Aerodynamic rotor torque ($Q_{u|l}/Q_{u|l,\mathrm{ref}}$) variations of rotors based on the UTA stacked rotor test rig for $\Delta\Omega = 20\%$ over $\Delta\psi_b = 360°$. Rotor trimmed to $C_T/\sigma = 0.08$ and 0.10 before pitch input. Torque was normalized by mean values prior to the RPM input. The RPM commands shown in Fig. 7.10b.

observed oscillations. However, this shall strictly be treated as a hypothesis at this point, especially as a similar oscillations in sectional thrust were observed for the stacked rotor configurations; see Figs. 7.15, 7.16, I.6, and I.7. Moreover, within the computed two rotor revolutions after the RPM input the local thrust distribution differed for the two input durations, despite the rotors being operated at the same RPM after the input. It was supposed that the chosen trim target before the RPM command was not strict enough and as a consequence no fully stationary rotor state was used as restart solution prior to the RPM command, or that more rotor revolutions were required to reach steady-state after the RPM command.

Changes of the stacked rotor upper rotor blade sectional thrust distribution for an input duration of $\Delta\psi_b = 360°$ are shown in Fig. 7.15 for a baseline blade loading of $C_{T,2b} = 0.08$. As for the single-rotors, data was normalized with the corresponding value before the RPM inputs. The corresponding rotor thrust response is shown in Fig. 7.12a. The magnitude of the sectional thrust increment (ΔF_z) increased with increasing index angle (ϕ). Equivalently, the rotor thrust was increasing with increasing index angle at nominal RPM; see Fig. 6.43. The relative thrust increase ($dF_z/\overline{dF_z}$) was comparable for all index angles. An overshoot in the relative thrust increase at inboard sections of the rotor blade close to the end of the RPM input was also observed here. When comparing the two-bladed single rotor to the upper rotor of the stacked rotor at $\phi = 0°$, i.e., when both rotors were operated at identical thrust before the RPM input, it was found that the absolute thrust increase near the blade tips was reduced for the stacked rotor and that the shape of the region of maximum relative thrust increase was altered; compare Figs. 7.14 and 7.15b. For the stacked rotor the thrust increase was more evenly distributed along the rotor blade, leading to an overall higher

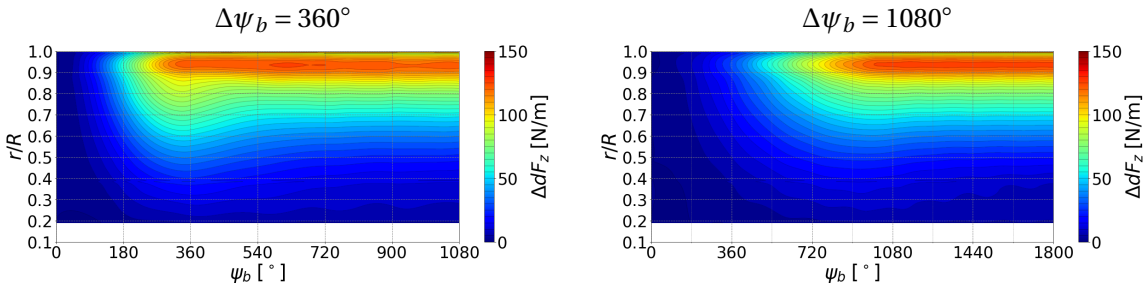

(a) ΔdF_z

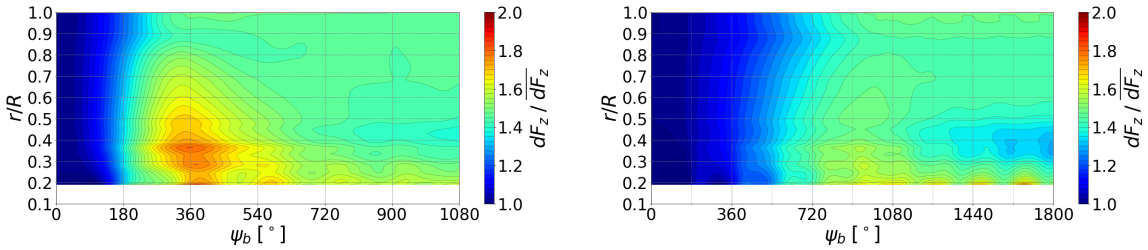

(b) $dF_z/\overline{dF_z}$

Figure 7.14.: Comparison of computed sectional thrust increase ($\Delta dF_z = dF_z - \overline{dF_z}$) and relative variation ($\Delta dF_z/\overline{dF_z}$) during and after RPM inputs for the two-bladed single rotor based on the UTA stacked rotor test rig. Relative data scaled by the sectional thrust before RPM input ($\overline{dF_z}$). Rotor trimmed to $C_{T,2b}/\sigma = 0.08$ before RPM input. RPM variations are shown in Fig. 7.10b.

thrust increase at steady-state after the RPM input; see Fig. 7.12a. It was supposed that this was caused by the influence of the lower rotor for the stacked rotor configuration. Equivalent data for $C_{T,2b} = 0.10$ is shown in Fig. I.6.

The same data evaluation was performed for the lower rotor plane; see Fig. 7.16. For all index angles the highest sectional thrust increase (ΔdFz) was observed near the blade tips, outside the upper rotor slipstream boundary. As for the dynamic collective pitch inputs commanded for the CCR rotor the region of thrust overshoot was spanning a larger portion of the rotor blade compared to the upper rotor plane; compare Figs. 7.8 and 7.16. It was assumed that the time required for the increased upper rotor downwash velocity to reach the lower rotor blade was responsible for the observed increased region of thrust overshoot for the lower rotor blade. Note also the changed interaction of the upper rotor tip vortex and the lower rotor blade at $\phi = -22.5°$ which delayed the thrust increase near the blade tip; see Fig. 7.16a and G.3a. In addition, only little variation was seen after the inputs near the blade root, in line with the sectional thrust distributions at baseline operating conditions, which showed little sensitivity to an overall increased blade loading at $r/R < 0.4$; see Fig. 6.44. Corresponding data at $C_{T,2b} = 0.10$ is shown in Fig. I.7.

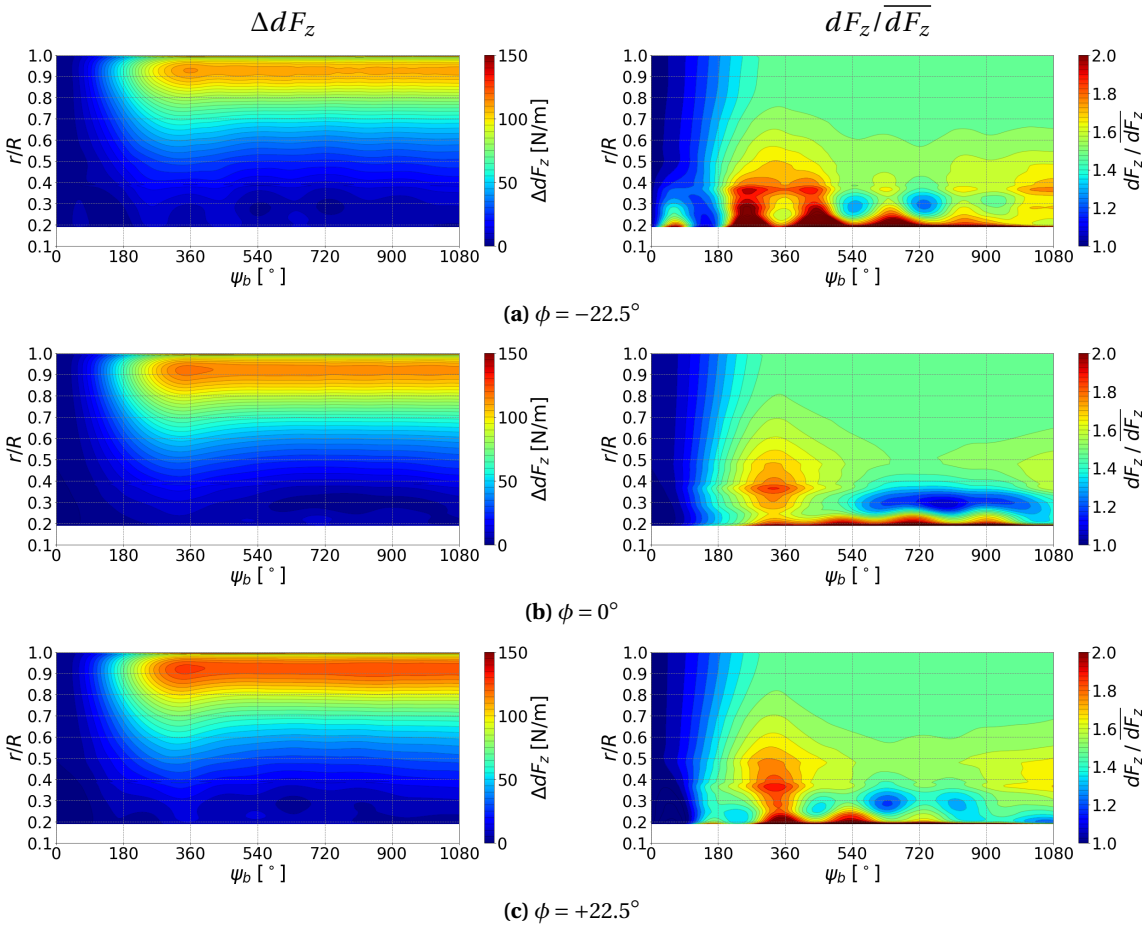

(a) $\phi = -22.5°$

(b) $\phi = 0°$

(c) $\phi = +22.5°$

Figure 7.15.: Comparison of computed upper rotor sectional thrust increase ($\Delta dF_z = dF_z - \overline{dF_z}$) and relative variation ($\Delta dF_z/\overline{dF_z}$) during and after RPM inputs ($\Delta\Omega = 20\%$) for the stacked rotor Rotor trimmed to $C_{T,2b}/\sigma = 0.08$ before RPM input. Relative data scaled by the sectional thrust before RPM input ($\overline{dF_z}$). Rotor rotational frequency was increased by $\Delta\Omega = 20\%$ over $\Delta\psi_b = 360°$.

7.2.2. Rotor Inflow

The temporal evolution of axial velocity in the plane of data extraction $\xi = 0°$ (see Fig. 6.8) caused by increasing the rotor rotational speed by $\Delta\Omega = 20\%$ over $\Delta\psi_b = 360°$ at $C_{T,2b}/\sigma = 0.08$ for the stacked rotor is shown in Figs. 7.17 and 7.18 for the upper and lower rotor, respectively. Qualitatively, the mean axial velocity was gradually increasing and was superimposed by the previously described axial velocity curves before the pitch inputs; see Figs. 6.41 and 6.42. The observed smooth transition to steady state after the RPM input was an indicator that the wake developed at a similar rate as the rotor rotational speed increased. As for the dynamic collective pitch inputs discussed in chapter 7.1, these gradual effects caused the variations in the relative sectional thrust increase described before; see chapter 7.2.1. Note that the time step size (Δt) during the RPM input was identical to before the RPM input, despite the increasing rotor rotational speed. This caused slight variations in the extracted velocity fluctuations during blade passage, as data was extracted at $\Delta\psi_b \approx 1°$. This, in addition to using non-integer index angles ($\phi = -22.5°$ and $+22.5°$)

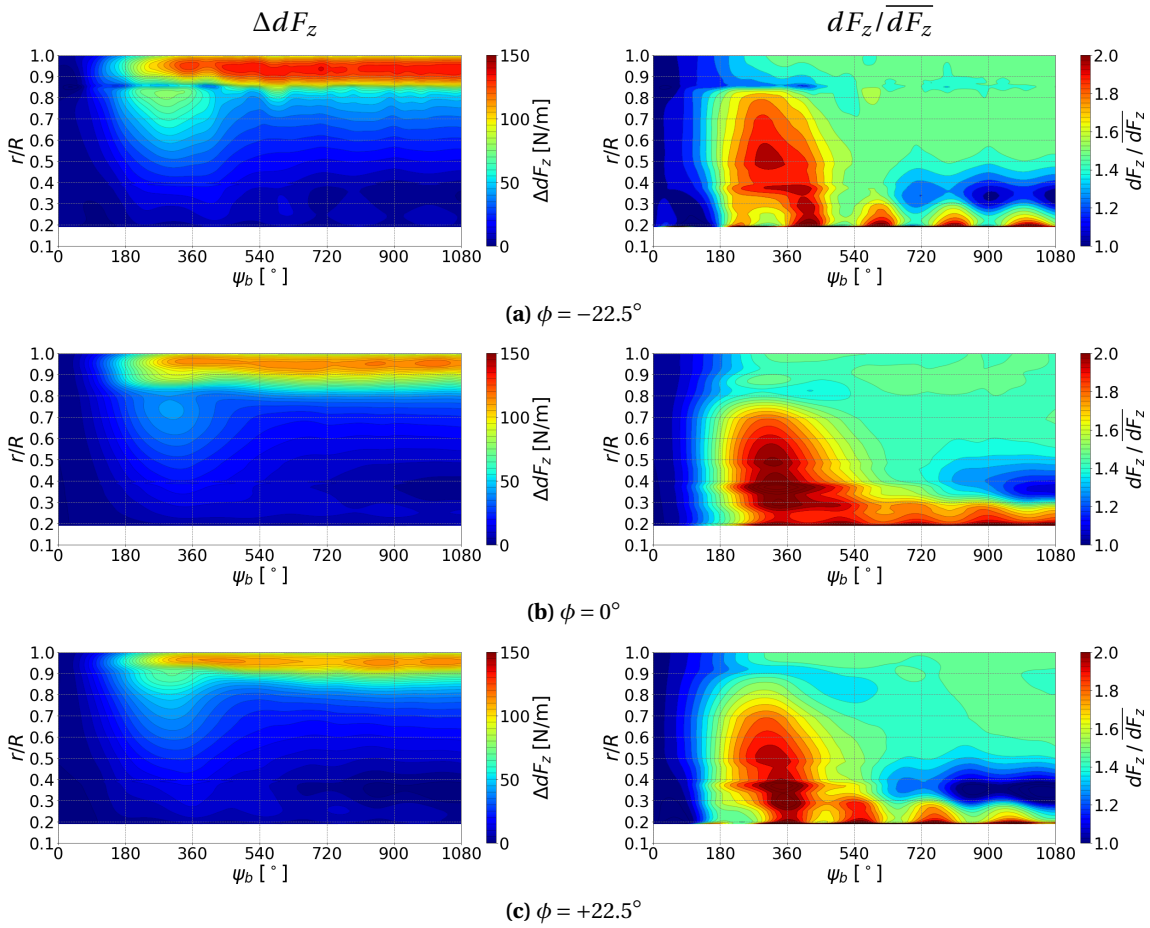

(a) $\phi = -22.5°$

(b) $\phi = 0°$

(c) $\phi = +22.5°$

Figure 7.16.: Comparison of computed lower rotor sectional thrust increase ($\Delta dF_z = dF_z - \overline{dF_z}$) and relative variation ($\Delta dF_z/\overline{dF_z}$) during and after RPM inputs ($\Delta\Omega = 20\%$) for the stacked rotor. Rotor trimmed to $C_{T,2b}/\sigma = 0.08$ before RPM input. Relative data scaled by the sectional thrust before RPM input ($\overline{dF_z}$). Rotor rotational frequency was increased by $\Delta\Omega = 20\%$ over $\Delta\psi_b = 360°$.

prevented a direct comparison of velocity magnitudes between rotors with different index angles right during blade passage, i.e., every $\Delta\psi_b = 180°$. However, the general information value is not reduced. Data at $C_{T,2b} = 0.10$ is shown in Figs. I.9 and I.10. Experimental data for the two-bladed single rotor with a RPM increase over $\Delta\psi_b = 1080°$ was previously published by the experimenter and the author[102] and numerical data are shown in Fig. I.8. As results were comparable to those obtained from pitch step inputs discussed in chapter 7.1.2 no further discussion of the details was made.

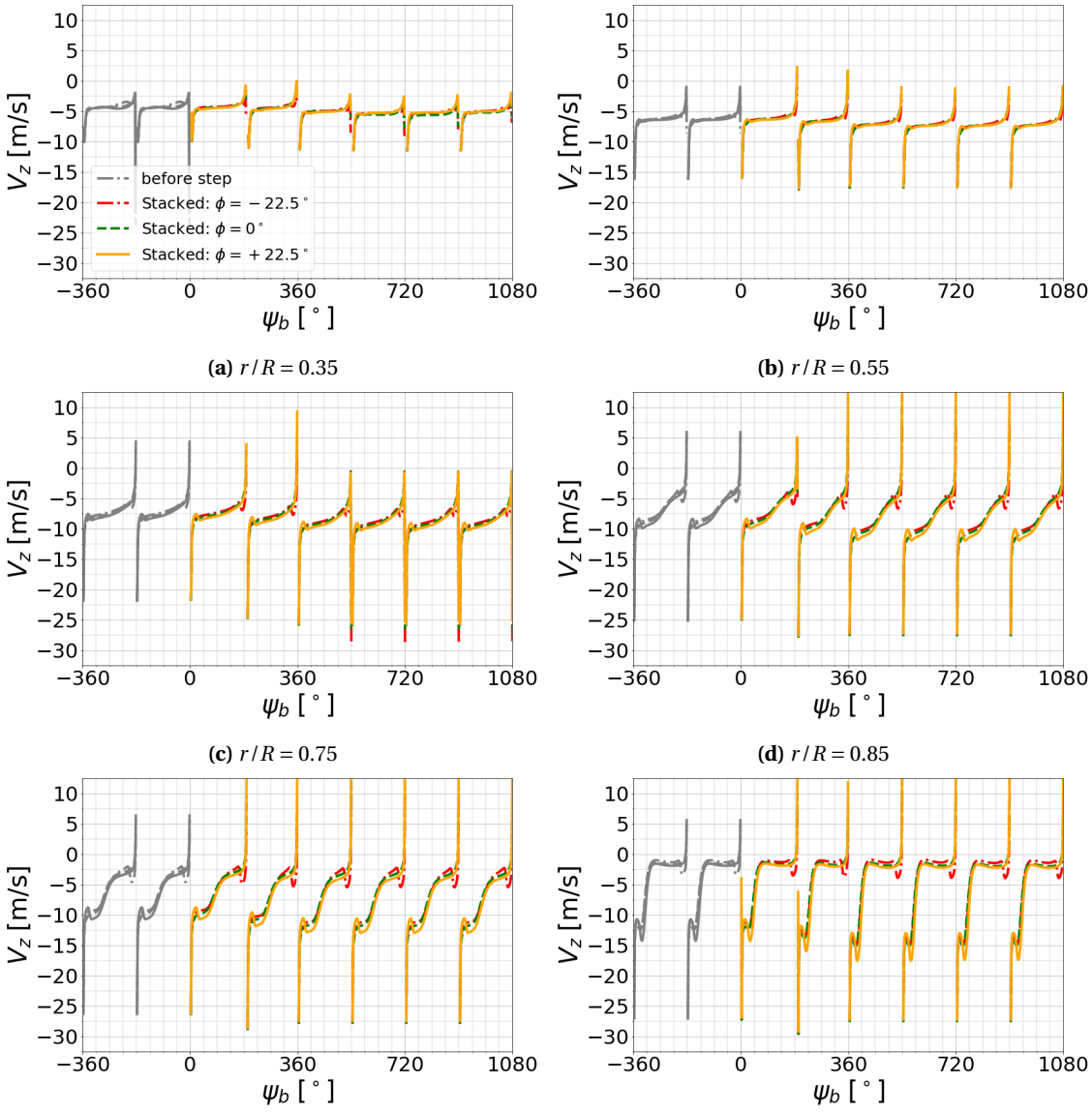

(a) $r/R = 0.35$ **(b)** $r/R = 0.55$

(c) $r/R = 0.75$ **(d)** $r/R = 0.85$

(e) $r/R = 0.90$ **(f)** $r/R = 0.95$

Figure 7.17.: Axial velocity (v_z) variations before, during and after RPM inputs in the upper rotor plane ($\Delta z/c = 0$) of the UTA stacked rotor at $C_T/\sigma = 0.08$ before the input. Data shown for three index angles ($\phi = -22.5, 0°$, and $22.5°$) and ΔRPM = 20% over $\Delta\psi_b = 360°$.

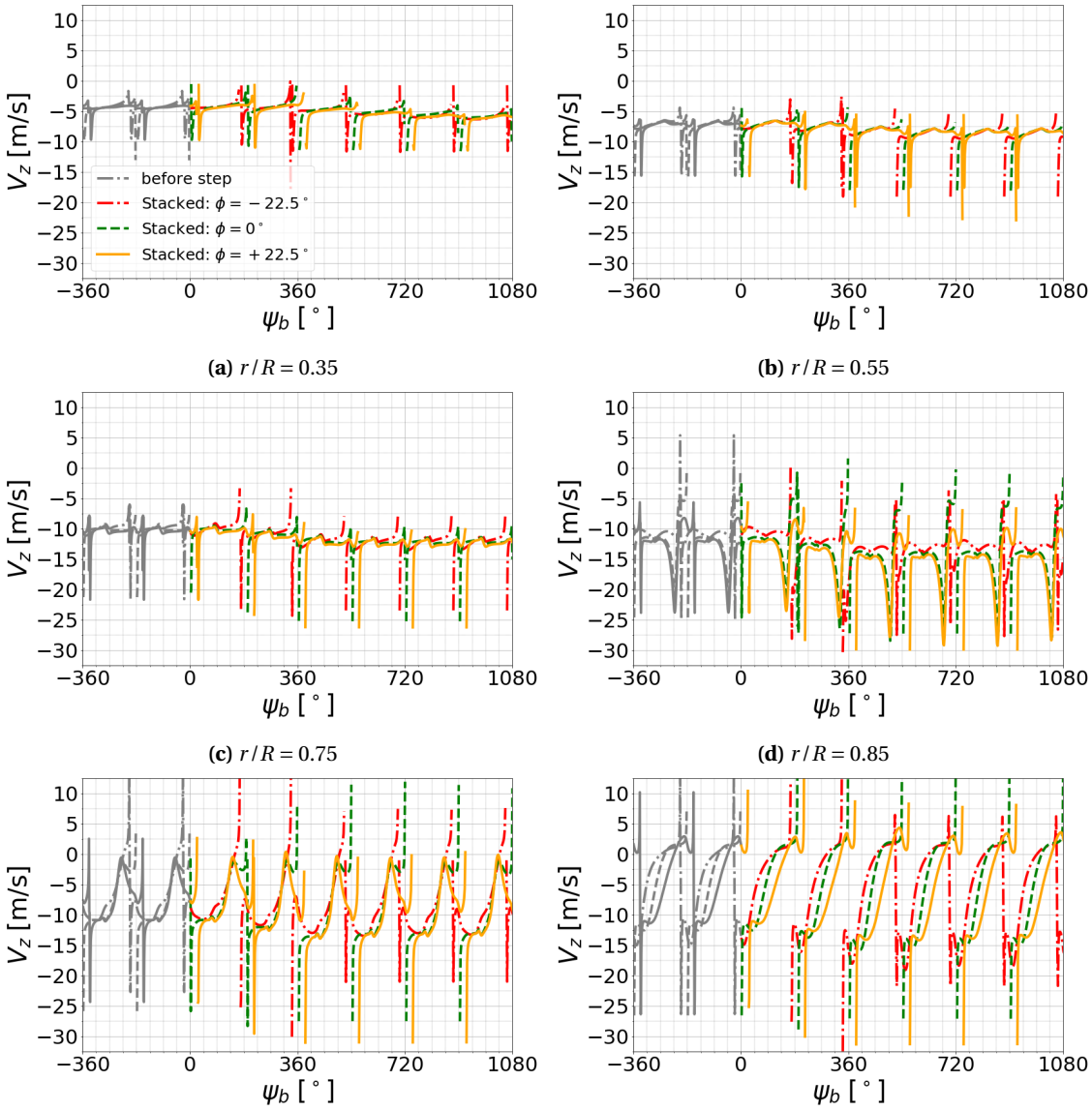

(a) $r/R = 0.35$ **(b)** $r/R = 0.55$

(c) $r/R = 0.75$ **(d)** $r/R = 0.85$

(e) $r/R = 0.90$ **(f)** $r/R = 0.95$

Figure 7.18.: Axial velocity (v_z) variations before, during and after RPM inputs in the lower rotor plane ($\Delta z/c = 0$) of the UTA stacked rotor at $C_T/\sigma = 0.08$ before the input. Data shown for three index angles ($\phi = -22.5, 0°$, and $22.5°$) and ΔRPM = 20% over $\Delta\psi_b = 360°$.

7.3. Summary and Conclusions – Dynamic Actuation

The transient characteristics of single, CCR, and stacked rotor configurations were investigated by means of URANS simulations to study the aerodynamic response to dynamic collective pitch ($\Delta\Theta_0$) and RPM (ΔRPM) inputs. $\Delta\Theta_0$ inputs were commanded for a two-by-two-bladed CCR rotor and the corresponding two-bladed single rotor. ΔRPM inputs were commanded for a stacked rotor at varying index angles and the corresponding two-bladed and four-bladed single rotors. Inputs were defined using '1 − Cosine' functions with varying input durations and amplitudes. The objectives were to investigate the temporal evolution of inflow, rotor forces and moments, and sectional thrust. Where possible, experimental results provided by UTA were correlated to the numerical results to assess the accuracy of the numerical simulations.

For both types of inputs a gradual transition from the reference thrust value before the input to the steady-state value after the input was observed for the two-bladed single rotors using the input durations commanded in the experiments ($\Delta\psi_b = 1440°$ for $\Delta\Theta_0 = 1°$, and $\Delta\psi_b = 1080°$ for ΔRPM = 20%). In both cases only marginal thrust overshoots were observed, indicating that the self-induced rotor inflow could build up at comparable rates along with the commanded collective pitch/rotor speed input. Good agreement was seen between experiment and simulation. Only at higher inputs rates ($\Delta\psi_b = 180°$ and $\Delta\psi_b = 360°$) significant thrust overshoots were observed. For both types of inputs the aerodynamic rotor torque followed the commanded inputs smoothly, i.e., the aerodynamic rotor torque reached the steady-state value after the inputs without overshoots. Note, that the inertial torque exceeded the aerodynamic torque by far when changing the rotor RPM and was the main driver for the torque overshoot observed in the experimental data[102].

A similar behavior was observed for the two-by-two-bladed CCR and stacked rotors. In the CCR rotor configuration the lower rotor showed a higher relative thrust increase and overshoot compared to the upper rotor for the commanded dynamic collective pitch inputs ($\Delta\psi_b = 360°$). The rotor torque signal did not show overshoots. In contrast, the upper rotor of the stacked rotor test rig showed a higher thrust increase after the RPM input, whereas the lower rotor showed the higher thrust overshoot for the same input duration. Moreover, a slight aerodynamic torque overshoot was computed for the lower rotor, a feature not seen for the CCR rotor. Furthermore, the relative thrust increase during and after the RPM command of the corresponding four-bladed single rotor was comparable to the upper rotor of the stacked rotor configurations. For the corresponding two-bladed rotor a reduced thrust increase was computed after the RPM input, but with comparable thrust overshoots during the input.

A more detailed insight into the temporal evolution of the rotor thrust was possible by investigating the temporal evolution of sectional thrust (dF_z) along the rotor blade span during and after the input commands. For the tested inputs which showed a significant thrust overshoot, a comparable behavior was seen for all rotor configurations and rotor planes. The absolute sectional thrust increase was highest close to the blade tips. However, the relative sectional thrust increase was highest at inboard sections of the rotor blades close to the end of the input duration. This force overshoot was significantly higher compared to blade sections close to the blade tips and the integral thrust overshoot of the complete rotor. For the lower rotor blades of the coaxial rotor configurations the region of thrust overshoot extended significantly further towards the tips

compared to the single and upper rotors. It was assumed that the rotor inflow built up first near the blade tips and afterwards progressed inboard, a feature previously concluded from flow field visualizations[19]. Hence, inboard sections see a time-delay in the buildup of inflow which results in an increased sectional thrust overshoot.

Furthermore, the temporal evolution of axial velocity in a fixed plane in space was investigated. It was found that the axial velocity continuously increased to the steady-state values after the inputs. Neither of the investigated inputs resulted in any oscillations or sudden changes in the axial velocity distributions. It was concluded that the axial velocity at fixed locations in space could build up at similar rates as the commanded inputs. Based on flow visualization experiments a qualitative similarity in the transient behavior between rapid increases of RPM from rest and rapid changes of collective pitch angles was also previously described[144].

Overall, a good correlation between the numerical and experimental results could be achieved. This was true for the rotor thrust and torque responses as well as the axial velocity distributions in the PIV measurement plane. The simulation method, i.e., URANS simulations using the SA-neg-RC turbulence model, along with the chosen temporal and spacial discretization was considered capable of simulating the relevant flow physics and was deemed suitable for the performed investigations.

8. Summary, Conclusions and Outlook

8.1. Summary

In the presented work the flow fields of model scale hovering rotors were investigated in flight conditions (non-parallel ground effect) and configurations (CCR and stacked rotors) that received comparatively little attention in the past. Moreover, the transient aerodynamic response of (coaxial) rotors in hover to dynamic collective pitch and rotor rotational speed step inputs were assessed. The research was conducted as a joint numerical and experimental study in cooperation with project partners at USNA[112] and UTA[101, 113, 102, 103, 114] who were performing rotor experiments. The numerical results were correlated to the measurement data that were provided by the partners to assess the accuracy of the chosen modeling approach and its general applicability for the research undertaking. In addition, the joint analysis provided a solid data base for an in-depth investigation of the aerodynamic characteristics of the tested rotors and the numerical simulation models allowed to expand the test matrix to data points that could not yet be measured experimentally.

Hovering rotors over non-parallel (inclined) ground planes can be regarded as a first step towards a better understanding of the complex aerodynamics that occur when rotorcraft are landing on moving ship decks. The simulations were based on a rotor test rig that was operated at USNA and is described in chapter 3.1. Computations for hover OGE, IGE over parallel ground planes, and IGE over a 15° inclined ground plane at a rotor height of 1 R above ground were made; see chapter 5. The numerical results were correlated to experimental data provided by USNA. Data were analyzed based on time-averaged and instantaneous flow field data, tip vortex trajectories, wandering, size and strength, as well as axial velocity distributions near the rotor plane. The numerical simulation results were used to extend the investigations using the computed three-dimensional flow fields and to assess the flow structures on the ground plane; aspects that could not be measured with the current experimental setup. Besides, the sensitivity of computed flow solutions to multiple turbulence models was assessed. A detailed summary is given in chapter 5.6.

A two-by-two-bladed CCR rotor, as well as a two-by-two-bladed stacked rotor were investigated to gain insights into the aerodynamic interactions of the rotor planes and to assess fundamental differences and similarities between them. In addition, the effects of adding a second rotor plane were investigated by comparing the results to those of single-rotor simulations. The simulations were based on two rotor test rigs that were operated at UTA. Details are given in chapter 3.2. The effects of using different turbulence models were assessed based on the CCR rotor design and by correlation to experimental data. With the used grid and numerical settings the SA-neg-RC turbulence model was performing best (vortex preservation and comparison to experimental data) and

was therefore used for all other simulations. The rotor configurations were assessed and compared to each other based on time-averaged and instantaneous flow field data, tip vortex trajectories, size and strength, as well as axial velocity distributions near the rotor plane. Computed sectional force distributions were linked to axial velocity distributions near the rotor blades. A summary of the results for the CCR rotor test rig is given in chapter 6.1.3 and for the stacked rotor test rig in chapter 6.2.5. A comparison of the different coaxial rotor configurations is given in chapter 6.3.

The effects of commanded collective pitch and rotor rotational speed step inputs were assessed based on the UTA (coaxial) rotor test rigs. Numerical results were correlated to two-bladed single rotor experimental data provided by UTA, and the numerical setup was used to extend the test matrix by investigating shorter input durations and higher pitch input amplitudes that could not be measured so far. The transient aerodynamic response of the rotors was assessed based on the rotor thrust and torque response, as well as the temporal evolution of blade sectional thrust and axial velocity distributions at fixed points in space. A summary of the results is given in chapter 7.3.

8.2. Conclusions

Detailed conclusions for the individual rotor configurations and operating conditions are given in chapter 5.6 for hover over non-parallel ground planes, in chapter 6.3 for the coaxial rotors, and in chapter 7.3 for the effects of control inputs. General conclusion valid for all investigated cases are presented hereafter.

Based on the available experimental data provided by the project partners at USNA and UTA, it was found that the chosen numerical method, i.e., a finite volume CFD method to solve the URANS equations in combination with turbulence models based on the eddy-viscosity hypothesis of Boussinesq or a RSM for turbulence closure was well suited to provide answers to the research objectives stated in chapters 2.1.1, 2.2.3, and 2.3.1. The performed studies showed that using RC terms was required for proper vortex conservation for the eddy-viscosity based turbulence models. Out of the tested turbulence models the one-equation SA-neg-RC model and the two-equation SST-SAS-RC showed best performance for IGE and coaxial rotor simulations, i.e, best vortex preservation in terms of vortex core size, circulation and swirl velocity. For the IGE simulations the tested RSM (SSG-LRR-ω) outperformed all other turbulence models with regard to vortex preservation, coming at the expense of significantly increased computational cost. However, after trimming the rotors the effects on pitch angles, the velocity distributions close to the rotor blades and vortex trajectories were small.

In addition, the used overset/chimera grid generation strategy proved to be a flexible and accurate way to answer the stated research questions for all tested rotor configurations and operating conditions; see chapter 4.5. In particular, the usage of transfer grids to connect the cuboid blade grids to the background grids helped to reduce the overall point count while locally increasing the grid resolution during blade and vortex passages, as well as in the path of the tip vortices.

In summary, it can be stated that well-performing numerical models were created for various different rotor configurations which showed good agreement with instantaneous and time-averaged velocity distributions and vortex trajectories. As a result of the close cooperation with the experimenters at USNA and UTA and the detailed correlation of experimental and numerical data a complete picture of the underlying flow physics could be gained for the investigated flight conditions and configurations. Furthermore, the models were used to expand the experimental test matrices by assessing operating conditions, as well as regions of the flow field or quantities that could not yet be measured experimentally.

8.3. Outlook

Research is a never ending journey. Therefore, the presented results and findings shall serve as a basis for further research activities. Most of the experimental data provided by the research partners at USNA and UTA has not yet been extensively used to validate numerical methods. Therefore, it is highly encouraged that other researchers make use of the data and findings from the joint publications[112, 101, 113, 102, 103, 114] and this thesis to validate their numerical methods or flow solvers, to substantiate the findings and to allow for a comparison of numerical techniques.

The conducted investigations in this thesis provided new insights into the underlying flow physics of the different rotor configurations and operating conditions. These shall serve as a stimulus to conduct new experimental and numerical studies in order to assess the accuracy of the presented numerical predictions. For hovering rotors over inclined ground planes it would be desirable to be able to correlate flow patterns on the ground plane, as well as time-averaged and instantaneous axial velocity distributions at additional rotor blade azimuth angles to other datasets. For both coaxial rotor configurations PIV measurements in a larger ROI below the lower rotor plane and further simulations are required to validate the findings concerning the tip vortex trajectories and interactions caused by variations of blade loading, index angle, and plane of data extraction. Moreover, further studies at the reduced collective pitch and RPM input durations and increased input amplitudes assessed in this thesis are desirable. In particular, the observed thrust overshoot near the blade root at the end of the input has, to the author's knowledge, never been shown experimentally or numerically before.

Furthermore, the numerical and experimental results should be used to validate existing or to develop new inflow models. The different rotor configurations and operating conditions, along with the complete three-dimensional flow field information from the numerical simulations, could be used to develop new or validate existing approaches and potentially refine models if deemed necessary. In particular, it would be desirable to establish a direct link between computed/measured velocity distributions near the blades, inflow, and blade sectional force distributions in order to design new experiments which could provide the velocity information at the required locations.

A. List of Publications by the Author Relating to the Dissertation

Platzer, S., Hajek, M., Rauleder, J., Mortimer, P., Sirohi, J.: "Investigation of the Flow Fields of Coaxial Stacked and Counter-Rotating Rotors using PIV Measurements and URANS Simulations," Vertical Flight Society 77th Annual Forum, Virtual Conference, 2021. [114]

Mortimer, P., Sirohi, J., **Platzer, S.**, Rauleder, J.: "Single Rotor Inflow and Wake Characterization in Hover with Dynamic Pitch Excitation," Vertical Flight Society 76th Annual Forum, Virtual Conference, 2020. [103]

Mortimer, P., Johnson, C., Sirohi, J., **Platzer, S.**, Rauleder, J.: "Experimental and Numerical Investigation of a Variable-Speed Rotor for Thrust Control," AIAA Aviation 2020 Forum, June, Virtual Conference, 2020. [102]

Platzer, S., Rauleder, J., Hajek, M., Mortimer, P., Jain, P., Sirohi, J.: "Experiments and Computations Towards an Improved Understanding and Modeling of the Dynamic Inflow of Rotors in Hover," Aeromechanics for Advanced Vertical Flight Technical Meeting, San Jose, USA, 2020. [113]

Mortimer, P., Sirohi, J., **Platzer, S.**, Rauleder, J.: Coaxial Rotor Wake Measurements in Hover Using Phase-Resolved and Time-Resolved PIV, Vertical Flight Society 75th Annual Forum, Philadelphia, Pennsylvania, USA, 2019. [101]

Platzer, S., Milluzzo, J., Rauleder, J.: Investigation on Hovering Rotors over Inclined Ground Planes – a Computational and Experimental Study, 44th European Rotorcraft Forum, Delft, The Netherlands, 2018. [112]

Platzer, S., Rauleder, J., Hajek, M., Milluzzo, J.: Experimental and Computational Investigation on Rotor Blades with Spanwise Blowing, 42nd European Rotorcraft Forum, Lille, France, 2016. [111]

Platzer, S., Rauleder, J., and Hajek, M.: Investigation of Centrifugal Pumping Rotor Blades in Hover Using CFD, 34th AIAA Applied Aerodynamics Conference, Washington D.C., USA, June 2016.[110]

B. Acknowledgment of Computing Resources and Funding

Computing Resources

The author gratefully acknowledges the Leibniz Supercomputing Centre for funding this project by providing computing time and support on its Linux-Cluster.

The author gratefully acknowledge the Gauss Centre for Supercomputing e.V. (www.gauss-centre.eu) for funding this project by providing computing time on the GCS Supercomputer SuperMUC-NG at Leibniz Supercomputing Centre (www.lrz.de).

Funding

This research was supported by the U.S. Army, Navy, and NASA Vertical Lift Research Center of Excellence (VLRCOE) program, and partly sponsored by the U.S. Army under grant number W911NF-17-0579.

C. Vortex Center Detection Algorithm

In order to automatically process the experimental and numerical data sets, a vortex center identification algorithm first proposed by Michard et al.[96] and described in Graftieaux et al.[41] was adapted. In the algorithm, a dimensionless scalar variable Γ_1 is computed at each point P in a two-dimensional slice of the flow field (PIV image plane, or slice of CFD volume). As the PIV data were sampled at discrete spatial locations in a Cartesian grid and the numerical results were extracted by interpolation to a Cartesian grid, an approximate version of the algorithm could be applied[41]. The algorithm equates Γ_1 for a fixed point P in a two-dimensional dataset to:

$$\Gamma_1(P) = \frac{1}{N}\sum_S \frac{(\mathbf{P}\times\mathbf{U})\cdot\mathbf{z}}{||\mathbf{P}||\cdot||\mathbf{U}||} = \frac{1}{N}\sum_S \sin(\Theta_M) \tag{C.1}$$

S is a two-dimensional area surrounding P, M lies in S, and $\mathbf{z}$ is the unit vector normal to the measurement plane. Θ_M is the angle between the velocity vector $\mathbf{U}$ and the radius vector $\mathbf{P}$[41]. The number of points in S is given by N. In the present thesis, S was defined as a square region centered in P. If the vortex was axisymmetric, the center is located where $\Gamma_1 = 1$. In [41] a threshold value of $\Gamma_1 \geq 0.9$ was suggested for a different application to account for any deviations from the perfectly symmetric shape of a vortex. In the present study, only the rotor tip vortices were of interest. Therefore, an additional minimum threshold for the average vorticity $\overline{\omega}$ in S was defined to exclude any small-scale vortical structures.

The dimensions of S were adjusted for the individual setups investigated, primarily to account for differences in the geometric dimensions of the rotor test rigs. Moreover, the lower bound of Γ_1 was chosen differently from [41] and adapted for each setup. This was required to account for the asymmetry of the swirl velocity profile due to the rotor downwash and slipstream boundary. Furthermore, as thrust values varied significantly between the different rotor configurations, the lower bound of the average vorticity was also altered. Vortex centers were determined based on the maximum of these values and fused if multiple possible vortex centers were to close together., i.e., within the same vortex. The threshold values are given in the respective results sections.

The algorithm proved to be simple, fast, relatively robust and easy to implement, and was used successfully used in previous studies by the author[112, 101, 103]. However, vortex pairing, burst, and wandering prevented the automatic detection of wake age for some PIV data sets. Therefore, data was checked manually after the automatic detection to assure correct labeling of the vortices. If no unambiguous assignment of wake age was possible, the respective vortices were manually excluded from further statistical analysis.

D. Grid and Temporal Convergence Study

D.1. NACA 0012 Airfoil Grid Convergence

Table D.1.: Overview of mesh spacings (Δs) node counts (N) for the airfoil grids used in the grid convergence study for the NACA 0012 airfoil. Definition of spacings for the airfoil grids (G) and the chimera airfoil grid (C) are shown in Fig. 4.3.

NACA 0012 - single grid												
	Δs1 [%c]	Δs2 [%c]	Δs3 [%c]	Δs4 [%c]	Δs5 [%c]	N1	N2	N3	N4	N5	Δs_{bl} [%c]	g_{bl}
G1	0.025	0.05	0.5	0.05	0.025	34	258	251	27	14	0.0018	1.05
G2	0.025	0.05	0.5	0.05	0.025	34	258	251	27	14	0.0018	1.1
G3	0.025	0.05	0.5	0.05	0.025	34	258	251	27	14	0.0018	1.2
G4	0.025	0.05	0.5	0.05	0.025	34	258	251	27	14	0.0009	1.05
G5	0.025	0.05	0.5	0.05	0.025	34	258	251	27	14	0.0009	1.1
G6	0.025	0.05	0.5	0.05	0.025	34	258	251	27	14	0.0009	1.2
G7	0.05	0.06	0.75	0.06	0.0337	24	111	109	19	12	0.0018	1.05
G8	0.05	0.06	0.75	0.06	0.0337	24	111	109	19	12	0.0018	1.1
G9	0.05	0.06	0.75	0.06	0.0337	24	111	109	19	12	0.0018	1.2
G10	0.05	0.06	0.75	0.06	0.0337	24	111	109	19	12	0.0009	1.05
G11	0.05	0.06	0.75	0.06	0.0337	24	111	109	19	12	0.0009	1.1
G12	0.05	0.06	0.75	0.06	0.0337	24	111	109	19	12	0.0009	1.2
G13	0.1	0.1	3	0.1143	0.0337	13	47	47	13	11	0.0018	1.075
G14	0.1	0.1	3	0.1143	0.0337	13	47	47	13	11	0.0018	1.1
G15	0.1	0.1	3	0.1143	0.0337	13	47	47	13	11	0.0018	1.2
G16	0.1	0.1	3	0.1143	0.0337	13	47	47	13	11	0.0009	1.075
G17	0.1	0.1	3	0.1143	0.0337	13	47	47	13	11	0.0009	1.1
G18	0.1	0.1	3	0.1143	0.0337	13	47	47	13	11	0.0009	1.2
NACA 0012 - chimera airfoil grid												
C1	0.1	0.1	3	0.1143	0.0337	13	47	47	13	11	0.0018	1.175

D.2. VR-12 Airfoil Grid Convergence

Table D.2.: Overview of mesh spacings (Δs) node counts (N) for the airfoil grids used in the grid convergence study for the VR 12 airfoil. Definition of spacings for the airfoil grids (G) and the chimera airfoil grid (C) are shown in Fig. 4.16.

VR-12 - single grid												
	Δs1 [%c]	Δs2 [%c]	Δs3 [%c]	Δs4 [%c]	Δs5 [%c]	N1	N2	N3	N4	N5	Δs_{bl} [%c]	g_{bl}
G1	0.025	0.125	0.5	0.125	0.025	239	139	167	86	10	0.00088	1.05
G2	0.025	0.125	0.5	0.125	0.025	239	139	167	86	10	0.00088	1.1
G3	0.025	0.125	0.5	0.125	0.025	239	139	167	86	10	0.00088	1.2
G4	0.025	0.125	0.5	0.125	0.025	239	139	167	86	10	0.00044	1.05
G5	0.025	0.125	0.5	0.125	0.025	239	139	167	86	10	0.00044	1.1
G6	0.025	0.125	0.5	0.125	0.025	239	139	167	86	10	0.00044	1.2
G7	0.05	0.15	0.75	0.15	0.025	121	71	85	44	10	0.00088	1.05
G8	0.05	0.15	0.75	0.15	0.025	121	71	85	44	10	0.00088	1.1
G9	0.05	0.15	0.75	0.15	0.025	121	71	85	44	10	0.00088	1.2
G10	0.05	0.15	0.75	0.15	0.025	121	71	85	44	10	0.00044	1.05
G11	0.05	0.15	0.75	0.15	0.025	121	71	85	44	10	0.00044	1.1
G12	0.05	0.15	0.75	0.15	0.025	121	71	85	44	10	0.00044	1.2
G13	0.1	0.5	1.5	0.5	0.0494	61	36	43	23	6	0.00088	1.05
G14	0.1	0.5	1.5	0.5	0.0494	61	36	43	23	6	0.00088	1.1
G15	0.1	0.5	1.5	0.5	0.0494	61	36	43	23	6	0.00088	1.2
G16	0.1	0.5	1.5	0.5	0.0494	61	36	43	23	6	0.00044	1.05
G17	0.1	0.5	1.5	0.5	0.0494	61	36	43	23	6	0.00044	1.1
G18	0.1	0.5	1.5	0.5	0.0494	61	36	43	23	6	0.00044	1.2
VR-12 - chimera airfoil grid												
C1	0.1	0.5	1.5	0.5	0.0494	61	36	43	23	6	0.00069	1.15
C2	0.075	0.5	2	0.25	0.025	66	30	38	27	8	0.00069	1.15
C3	0.075	0.375	1.875	0.1875	0.025	63	31	40	27	8	0.00069	1.15

Table D.3.: Overview of mesh spacings (Δs) node counts (N) for the transfer grids (T) used in the grid convergence study for the VR 12 airfoil. Definition of spacings is shown in Fig. 4.17a.

VR-12 - chimera airfoil grid								
	Δs6 [%c]	Δs7 [%c]	Δs8 [%c]	Δs9 [%c]	N6	N7	N8	N9
C1	1.491	2.229	2.229	0.620	46	63	58	80
C2	1.491	2.229	2.229	0.620	46	63	58	80
C3	0.898	2.764	2.764	0.535	58	51	58	80
C4	0.898	2.764	2.764	0.554	58	51	59	84

Table D.4.: Overview of mesh spacings (Δs) node counts (N) for the transfer grids (T) used in the grid convergence study for the VR 12 airfoil. Definition of spacings is shown in Fig. 4.17b.

VR-12 - chimera transfer grid							
	Δs10 [%c]	Δs11 [%c]	Δs12 [%c]	Δs13 [%c]	N10	N11	N12
T1	1.491	2.229	2.229	0.620	46	63	58
T2	1.491	2.229	6.535	0.620	46	31	58
T3	1.110	2.764	5.950	0.516	51	31	58

E. Rotor Aerodynamics in Non-Parallel Ground Effect

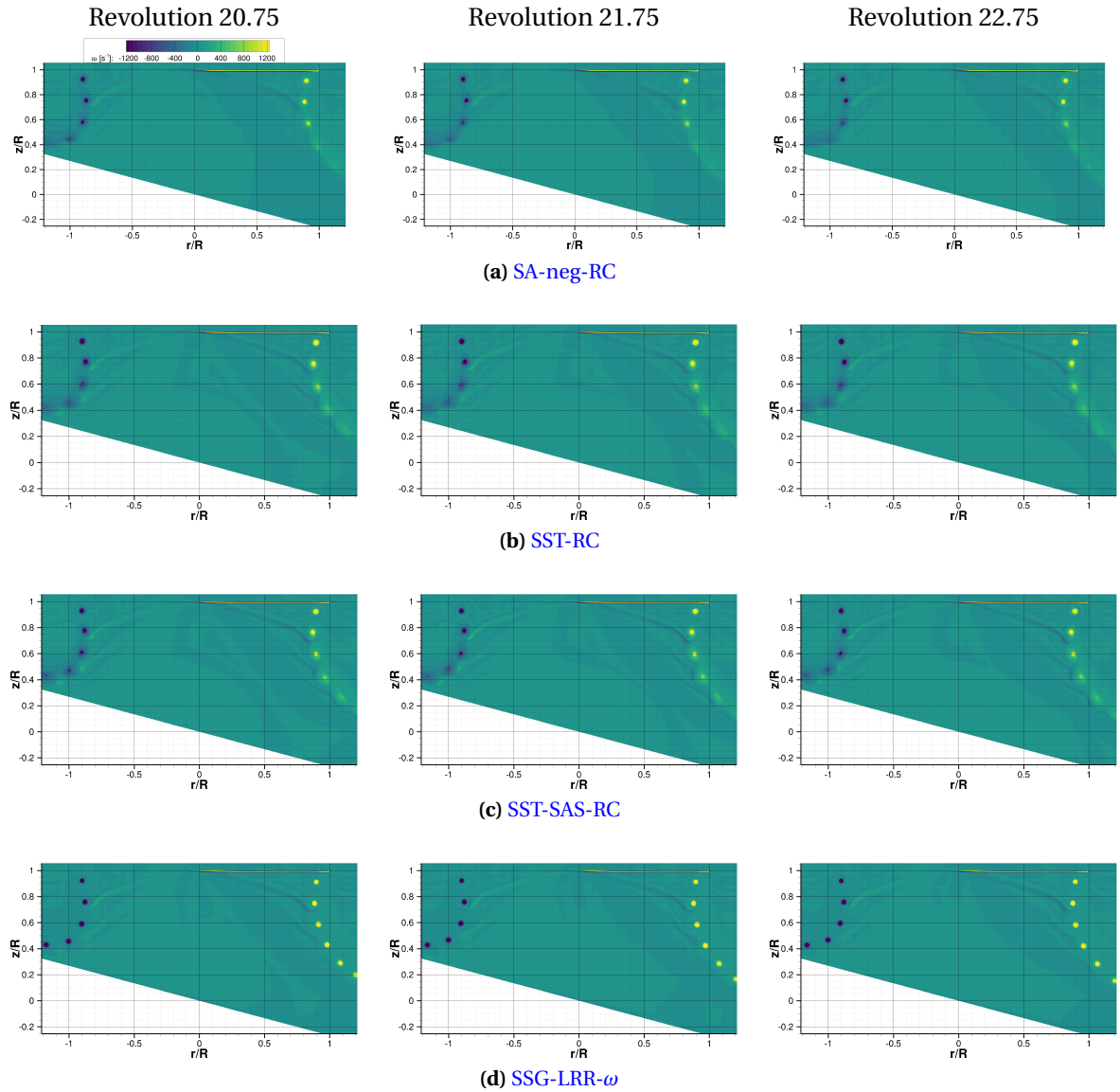

(a) SA-neg-RC

(b) SST-RC

(c) SST-SAS-RC

(d) SSG-LRR-ω

Figure E.1.: Temporal evolution of the flow field of the USNA rotor IGE at $\Theta_{GP} = 15°$. Out-of-plane vorticity contours shown for second through fourth revolution after tilting the ground plane at $\psi_b = 0°$ of the reference blade. Data extracted in PIV plane; see Fig. 3.5.

F. Coaxial Counter-Rotating Rotor Aerodynamics

F.1. Flow Field

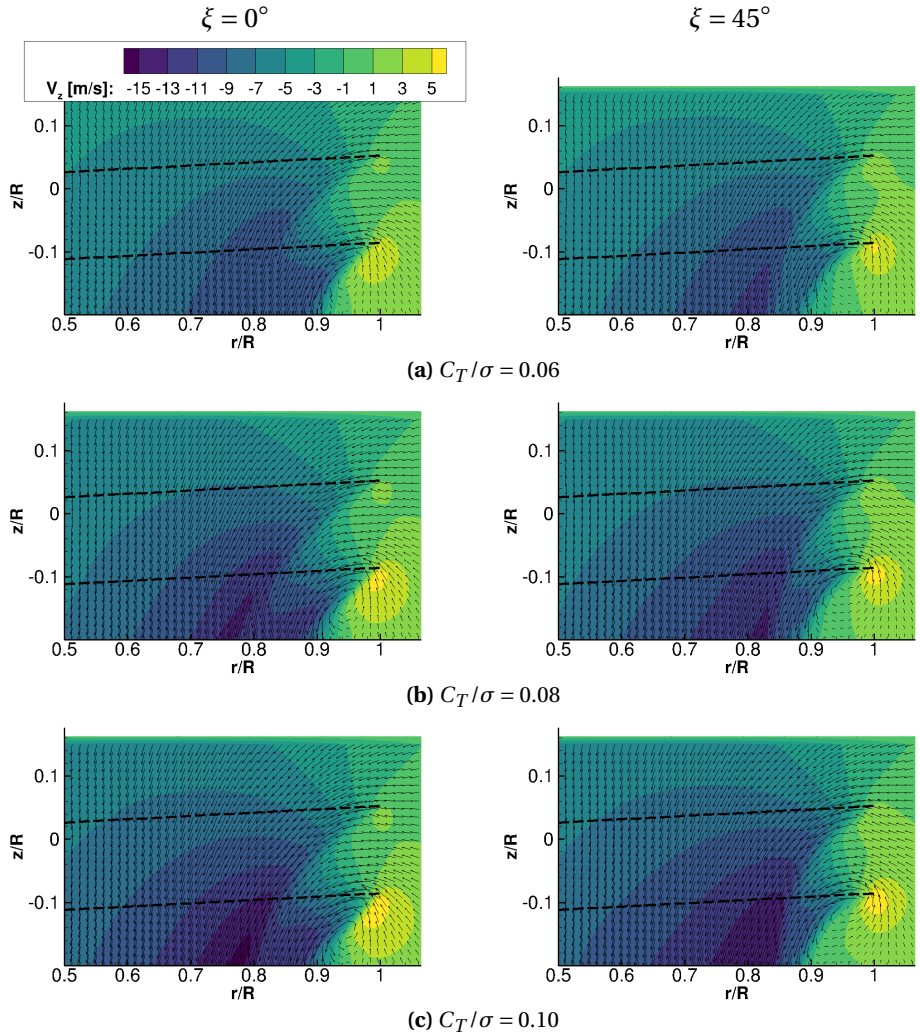

(a) $C_T/\sigma = 0.06$

(b) $C_T/\sigma = 0.08$

(c) $C_T/\sigma = 0.10$

Figure F.1.: Comparison of time-averaged axial velocity contours superimposed by in-plane velocity vectors at different blade loadings. Results computed with the SA-neg-RC turbulence model. Dashed lines indicate undeformed rotor blade axis. Results averaged over 0.5 rotor revolution in increments of $\Delta\psi_b = 1°$ (i.e., 180 slices averaged over $\Delta\psi_b = 180°$).

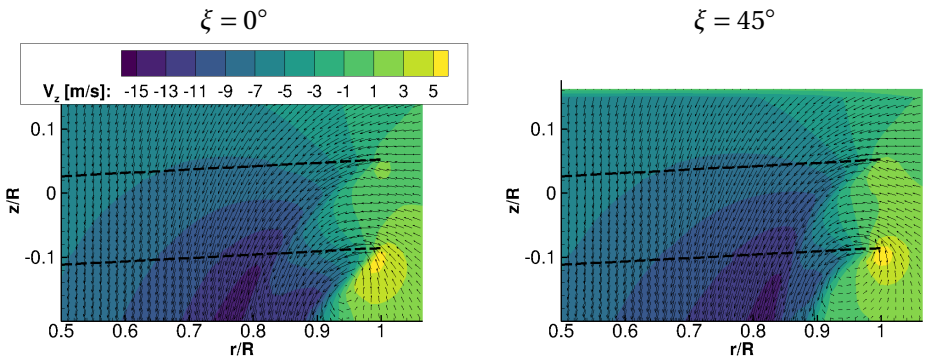

(a) SA-neg-RC

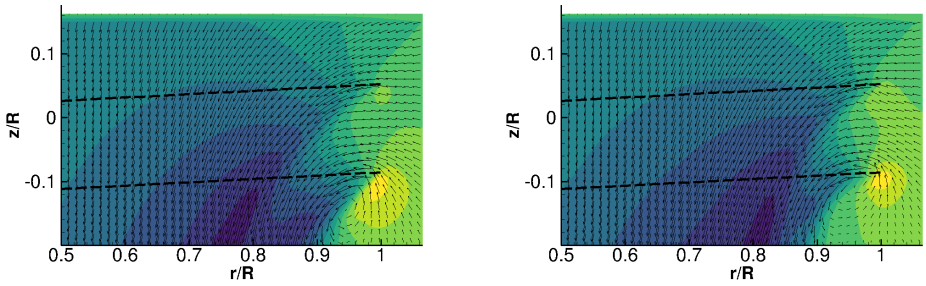

(b) SST-RC

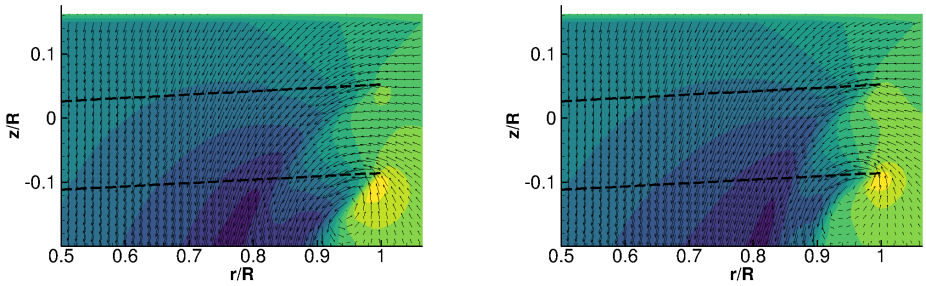

(c) SST-SAS

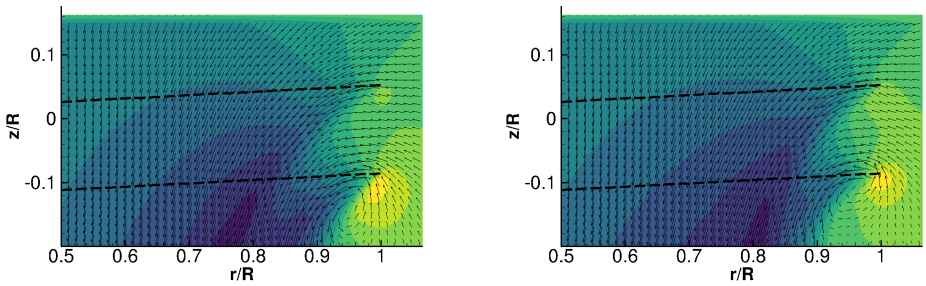

(d) SST-SAS-RC

Figure F.2.: Comparison of time-averaged axial velocity between different turbulence at $C_T/\sigma = 0.085$. Dashed lines indicate undeformed rotor blade axis. Results averaged over 0.5 rotor revolution in increments of $\Delta\psi_b = 3°$ (i.e., 60 slices averaged over $\Delta\psi_b = 180°$).

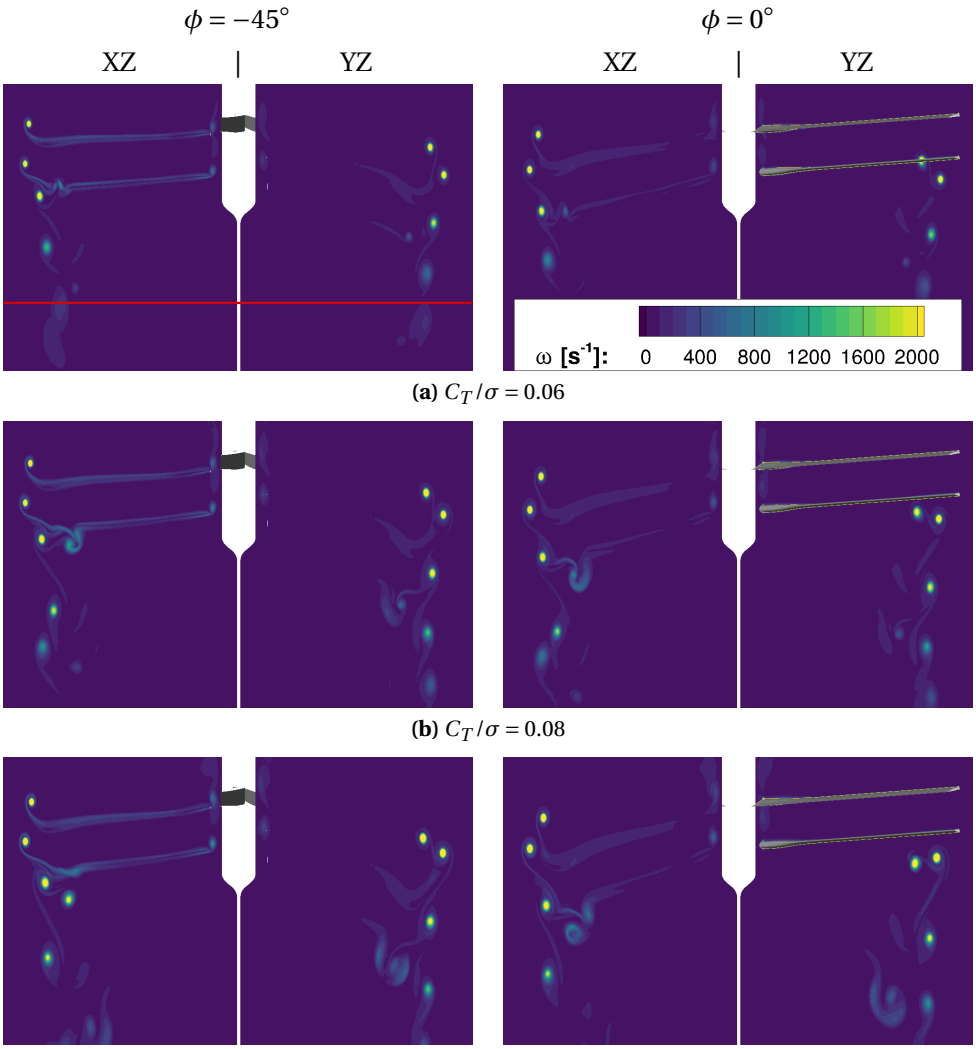

(a) $C_T/\sigma = 0.06$

(b) $C_T/\sigma = 0.08$

(c) $C_T/\sigma = 0.10$

Figure F.3.: Comparison of total vorticity contours of the two-by-two-bladed CCR rotor at different blade loadings and multiple index angles ϕ. Results computed with the SA-neg-RC turbulence model. Red line indicating end of high-resolution grid region for improved vortex preservation; see Fig. 4.22. Vorticity contours shown in two perpendicular vertical planes through the rotor shaft axis (XZ- and YZ-plane).

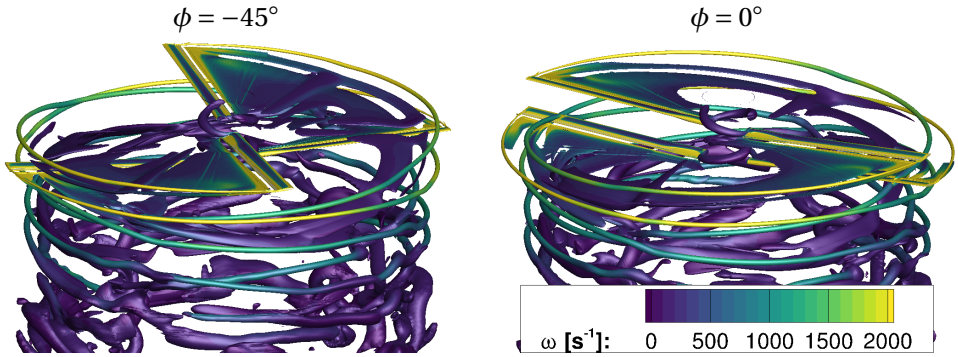

(a) $C_T/\sigma = 0.06$

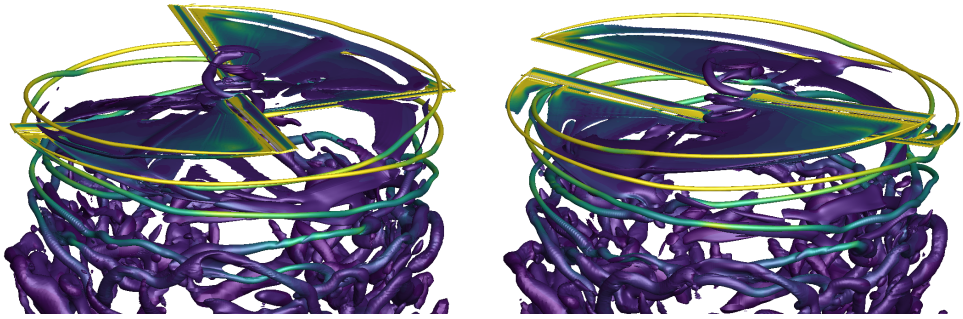

(b) $C_T/\sigma = 0.08$

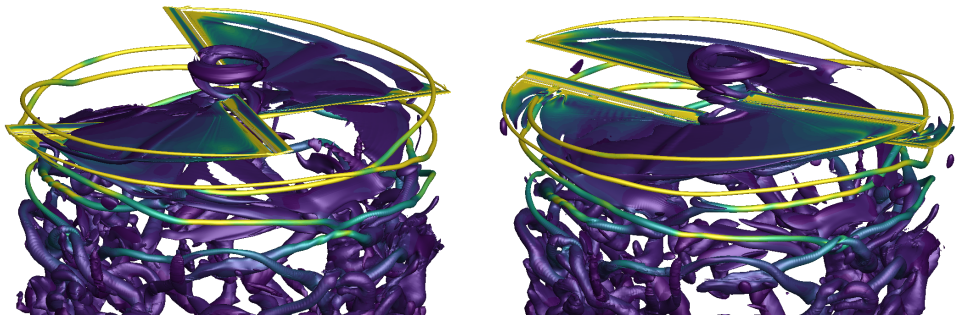

(c) $C_T/\sigma = 0.10$

Figure F.4.: Comparison of computed vortical structures for the two-by-two-bladed CCR rotor for different blade loadings and index angles ϕ. Results computed with the SA-neg-RC turbulence model. Vortices visualized by Q-criterion isosurfaces ($Q = 1500\ s^{-2}$) colored by total vorticity ω.

F.2. Tip Vortex Trajectories

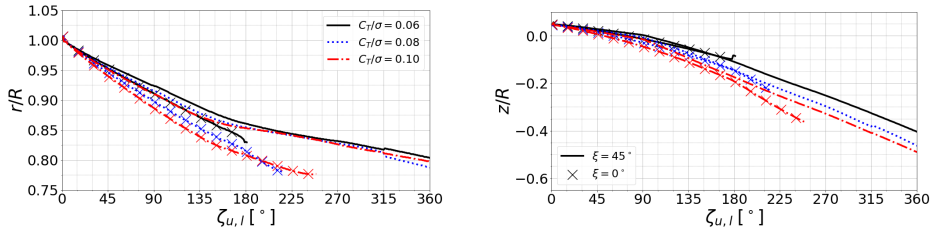

(a) r/R vs ζ **(b)** z/R vs ζ

Figure F.5.: Comparison of computed radial (r/R) and axial (z/R) tip vortex displacements for the upper rotor of the two-by-two-bladed CCR rotor at C_T/σ = 0.06, 0.08, and 0.10. Results computed using the SA-neg-RC turbulence model. Data extracted at $\xi = 0°$ and $\xi = 45°$; see Fig. 6.8.

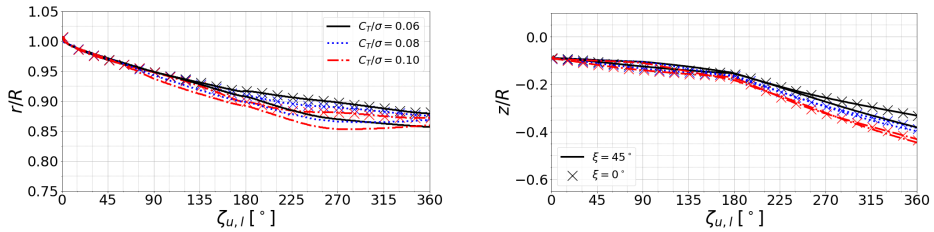

(a) r/R vs ζ **(b)** z/R vs ζ

Figure F.6.: Comparison of computed radial (r/R) and axial (z/R) tip vortex displacements for the lower rotor of the two-by-two-bladed CCR rotor at C_T/σ = 0.06, 0.08, and 0.10. Results computed using the SA-neg-RC turbulence model. Data extracted at $\xi = 0°$ and $\xi = 45°$; see Fig. 6.8.

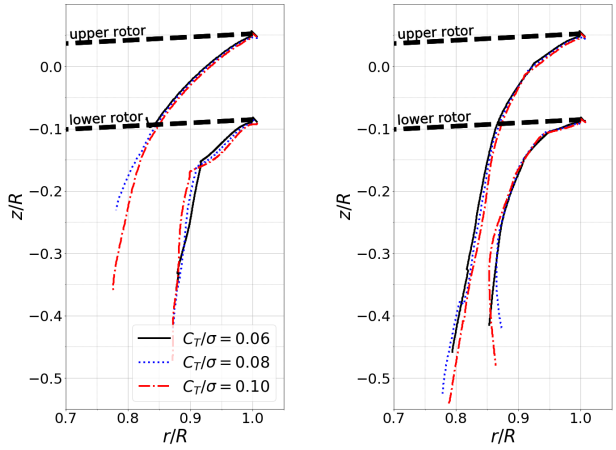

(a) $\xi = 0°$ **(b)** $\xi = 45°$

Figure F.7.: Comparison of computed tip vortex trajectories (z/R vs r/R) for the two-by-two-bladed CCR rotor at $C_T/\sigma = 0.06$, 0.08, and 0.10 up to wake ages of $\zeta_{u,l} = 390°$ [114]. Results computed using the SA-neg-RC turbulence model. Data extracted at $\xi = 0°$ and $\xi = 45°$; see Fig. 6.8.

F.3. Tip Vortex Size and Strength

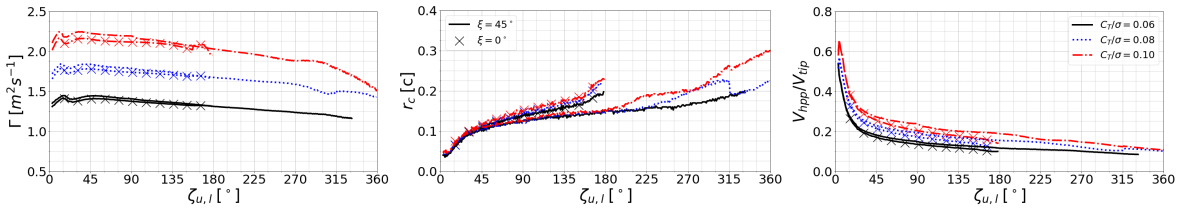

(a) Γ. **(b)** r_c. **(c)** V_{hpp}.

Figure F.8.: Comparison of computed tip vortex circulation (Γ), core radii (r_c) as fraction of blade chord (c), and half peak-to-peak velocities (V_{hpp}) normalized by the blade tip velocity (V_{tip}) of the upper rotor of the two-by-two-bladed CCR rotor at C_T/σ = 0.06, 0.08, and 0.10. Results computed using the SA-neg-RC turbulence model. Data extracted at $\xi = 0°$ and 45°; see Fig. 6.8.

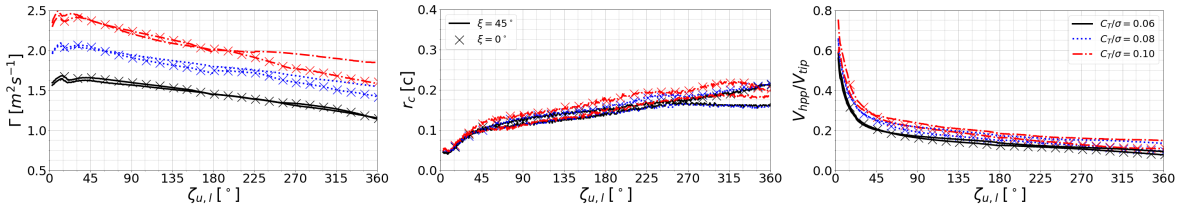

(a) Γ. **(b)** r_c. **(c)** V_{hpp}.

Figure F.9.: Comparison of computed tip vortex circulation (Γ), core radii (r_c) as fraction of blade chord (c), and half peak-to-peak velocities (V_{hpp}) normalized by the blade tip velocity (V_{tip}) of the lower rotor of the two-by-two-bladed CCR rotor at C_T/σ = 0.06, 0.08, and 0.10. Results computed using the SA-neg-RC turbulence model. Data extracted at $\xi = 0°$ and 45°; see Fig. 6.8.

F.4. Rotor Inflow

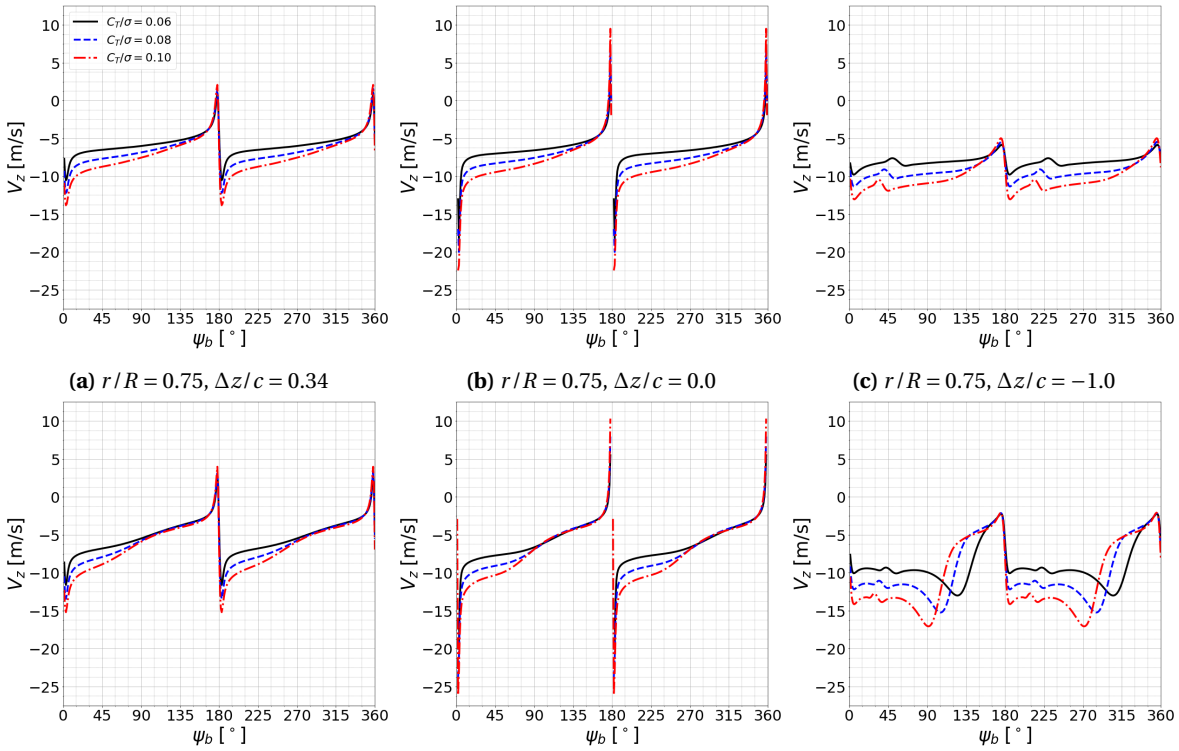

(a) $r/R = 0.75$, $\Delta z/c = 0.34$ **(b)** $r/R = 0.75$, $\Delta z/c = 0.0$ **(c)** $r/R = 0.75$, $\Delta z/c = -1.0$

(d) $r/R = 0.85$, $\Delta z/c = 0.34$ **(e)** $r/R = 0.85$, $\Delta z/c = 0.0$ **(f)** $r/R = 0.85$, $\Delta z/c = -1.0$

Figure F.10.: Comparison of computed axial velocity (v_z) for the two-by-two-bladed CCR rotor. Data shown for the upper rotor over one revolution for C_T/σ = 0.06, 0.08, and 0.10 above, below, and in the rotor plane. Results computed using the SA-neg-RC turbulence model. Blade passage occurred at $\psi_b = 0°$ and 180°. Data extracted every $\Delta\psi_b = 1°$ at $\xi = 0°$; see Fig. 6.8.

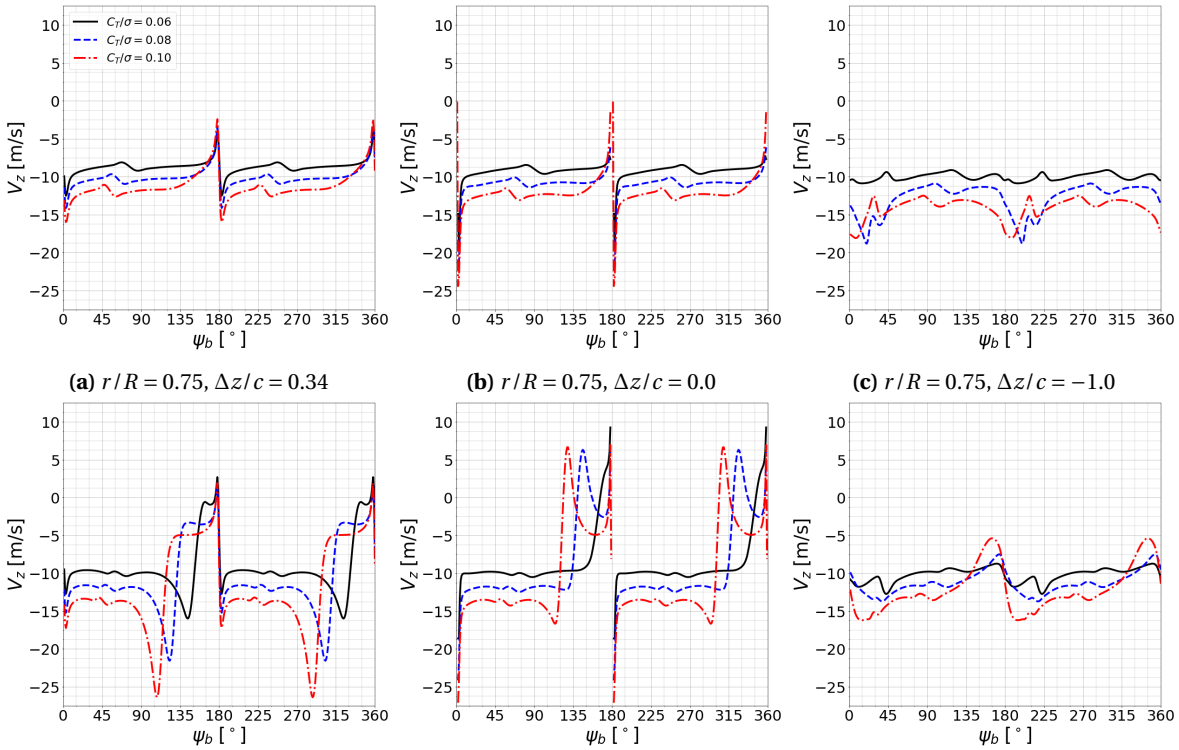

(a) $r/R = 0.75$, $\Delta z/c = 0.34$ **(b)** $r/R = 0.75$, $\Delta z/c = 0.0$ **(c)** $r/R = 0.75$, $\Delta z/c = -1.0$

(d) $r/R = 0.85$, $\Delta z/c = 0.34$ **(e)** $r/R = 0.85$, $\Delta z/c = 0.0$ **(f)** $r/R = 0.85$, $\Delta z/c = -1.0$

Figure F.11.: Comparison of computed axial velocity (v_z) for the two-by-two-bladed CCR rotor. Data shown for the lower rotor over one revolution for C_T/σ = 0.06, 0.08, and 0.10 above, below, and in the rotor plane. Results computed using the SA-neg-RC turbulence model. Blade passage occurred at $\psi_b = 0°$ and 180°. Data extracted every $\Delta\psi_b = 1°$ at $\xi = 0°$; see Fig. 6.8.

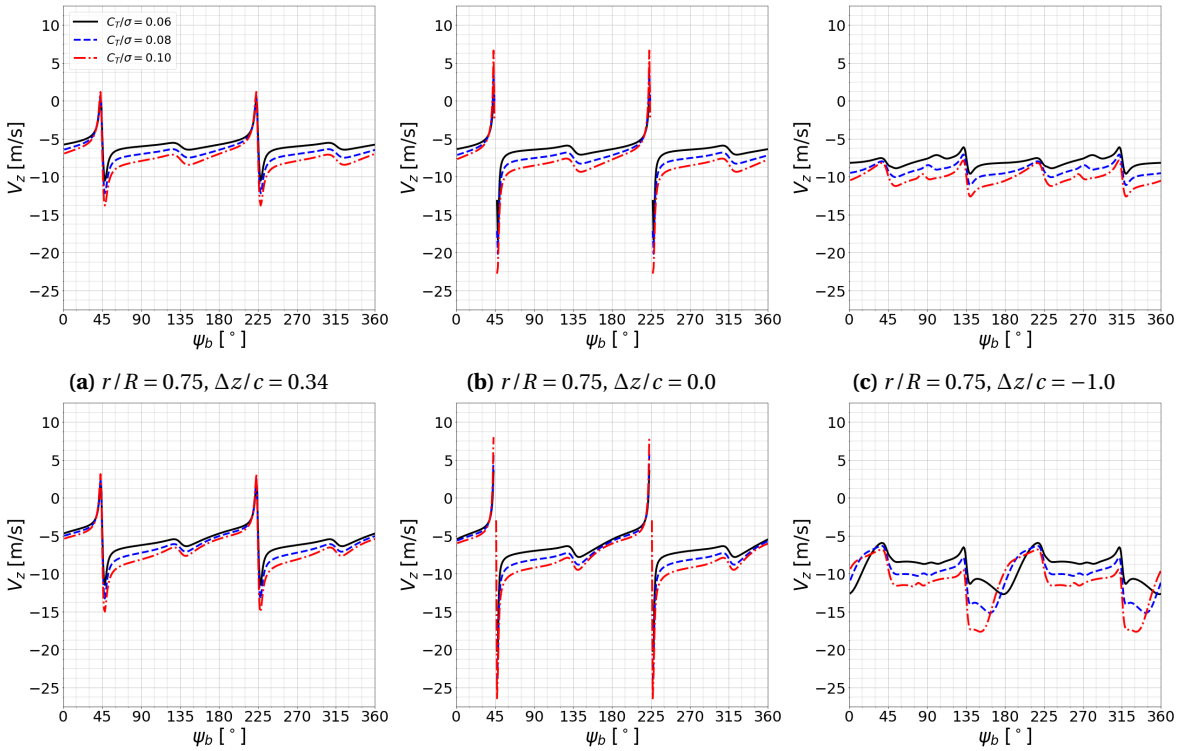

(a) $r/R = 0.75$, $\Delta z/c = 0.34$ **(b)** $r/R = 0.75$, $\Delta z/c = 0.0$ **(c)** $r/R = 0.75$, $\Delta z/c = -1.0$

(d) $r/R = 0.85$, $\Delta z/c = 0.34$ **(e)** $r/R = 0.85$, $\Delta z/c = 0.0$ **(f)** $r/R = 0.85$, $\Delta z/c = -1.0$

Figure F.12.: Comparison of computed axial velocity (v_z) for the two-by-two-bladed CCR rotor. Data shown for the upper rotor over one revolution for $C_T/\sigma = 0.06$, 0.08, and 0.10 above, below, and in the rotor plane. Results computed using the SA-neg-RC turbulence model. Blade passage occurred at $\psi_b = 45°$ and 225° for the upper blade, and at $\psi_b = 135°$ and 315° for the lower blade. Data extracted every $\Delta\psi_b = 1°$ at $\xi = 45°$; see Fig. 6.8.

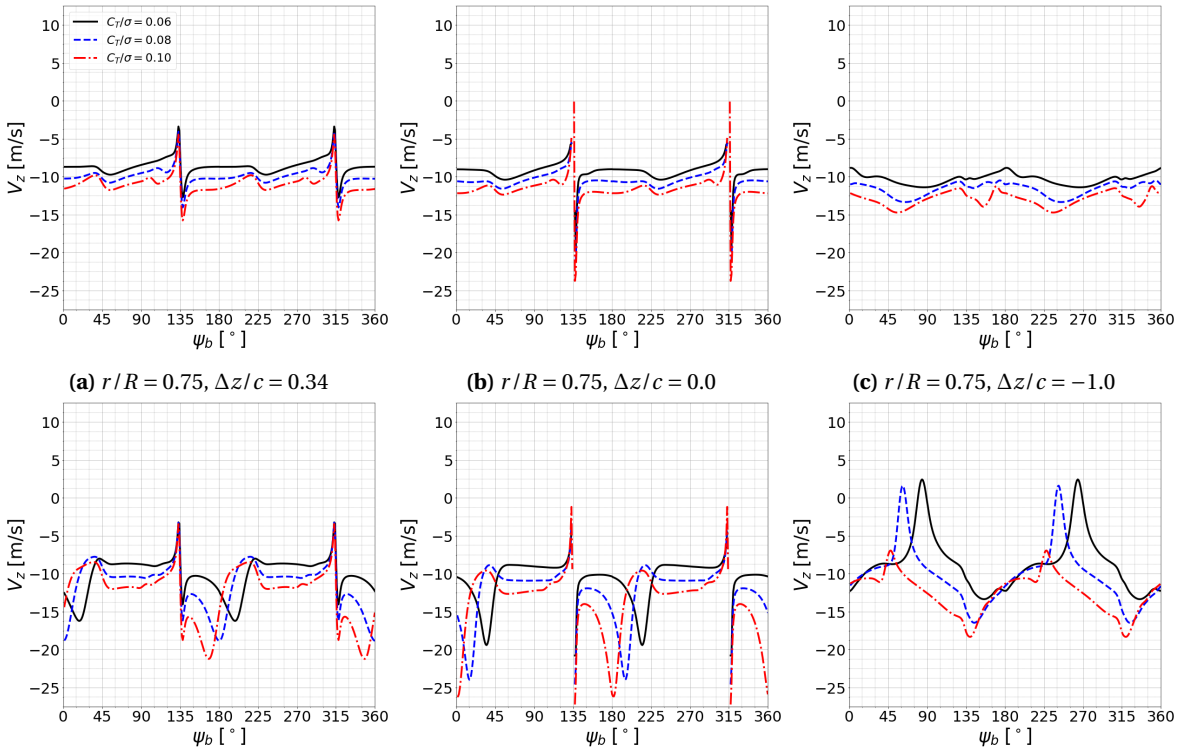

(a) $r/R = 0.75$, $\Delta z/c = 0.34$ **(b)** $r/R = 0.75$, $\Delta z/c = 0.0$ **(c)** $r/R = 0.75$, $\Delta z/c = -1.0$

(d) $r/R = 0.85$, $\Delta z/c = 0.34$ **(e)** $r/R = 0.85$, $\Delta z/c = 0.0$ **(f)** $r/R = 0.85$, $\Delta z/c = -1.0$

Figure F.13.: Comparison of computed axial velocity (v_z) for the two-by-two-bladed CCR rotor. Data shown for the lower rotor over one revolution for C_T/σ = 0.06, 0.08, and 0.10 above, below, and in the rotor plane. Results computed using the SA-neg-RC turbulence model. Blade passage occurred at $\psi_b = 45°$ and 225° for the upper blade, and at $\psi_b = 135°$ and 315° for the lower blade. Data extracted every $\Delta\psi_b = 1°$ at $\xi = 45°$; see Fig. 6.8.

F.5. Forces and Moments

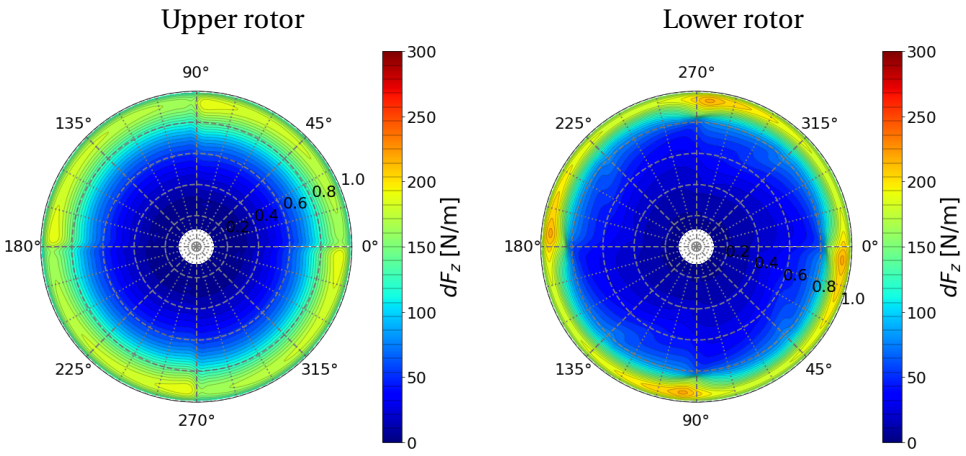

(a) $C_T/\sigma = 0.06$

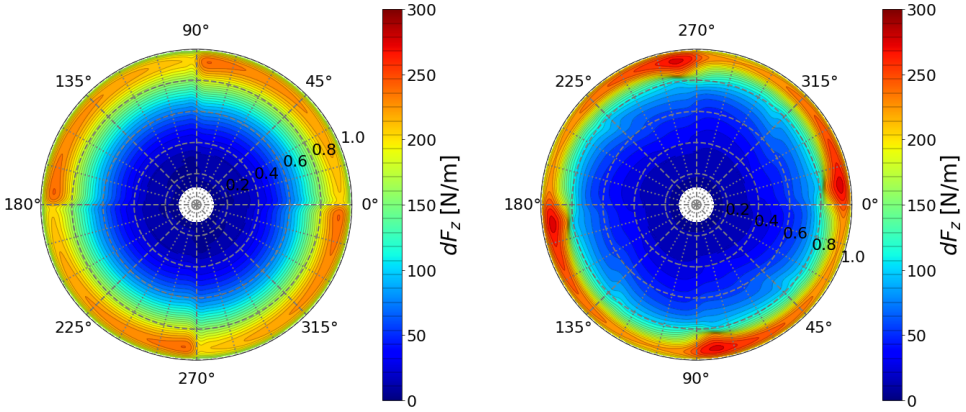

(b) $C_T/\sigma = 0.08$

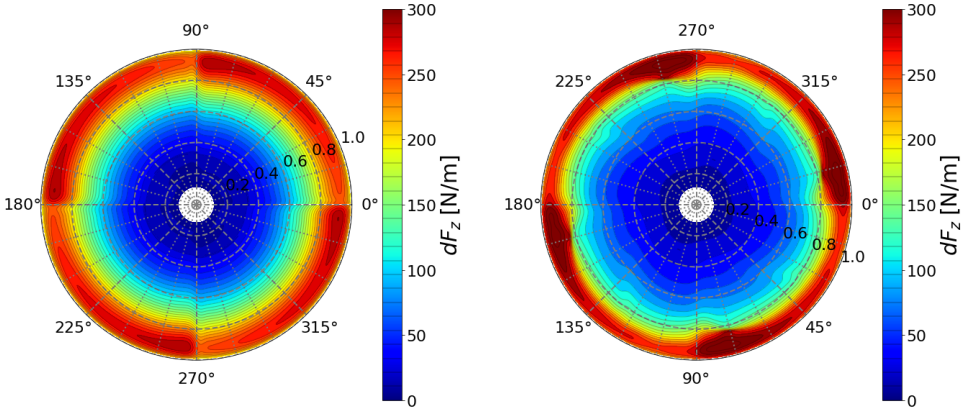

(c) $C_T/\sigma = 0.10$

Figure F.14.: Comparison of computed sectional thrust distributions (dF_z) of the upper and lower rotor plane for the two-by-two-bladed CCR rotor for different blade loadings. Results computed with the SA-neg-RC turbulence model.

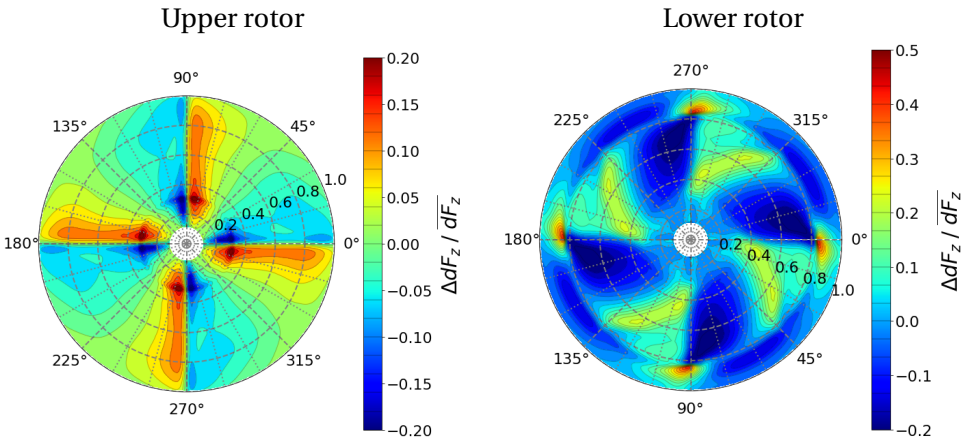

(a) $C_T/\sigma = 0.06$

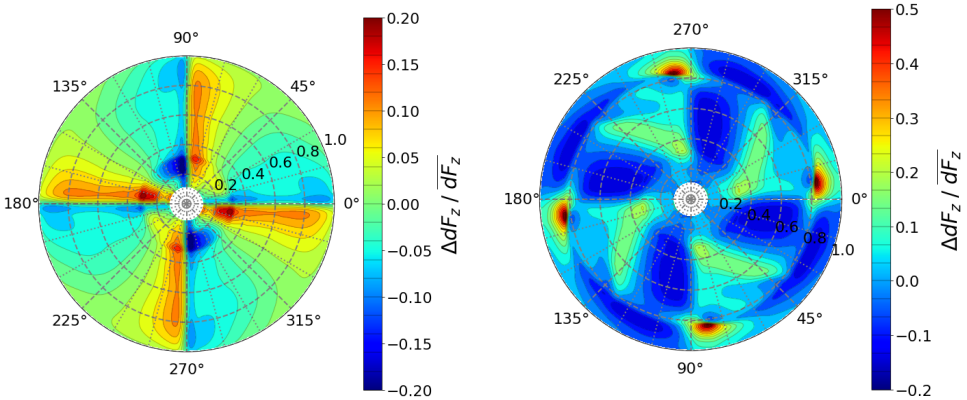

(b) $C_T/\sigma = 0.08$

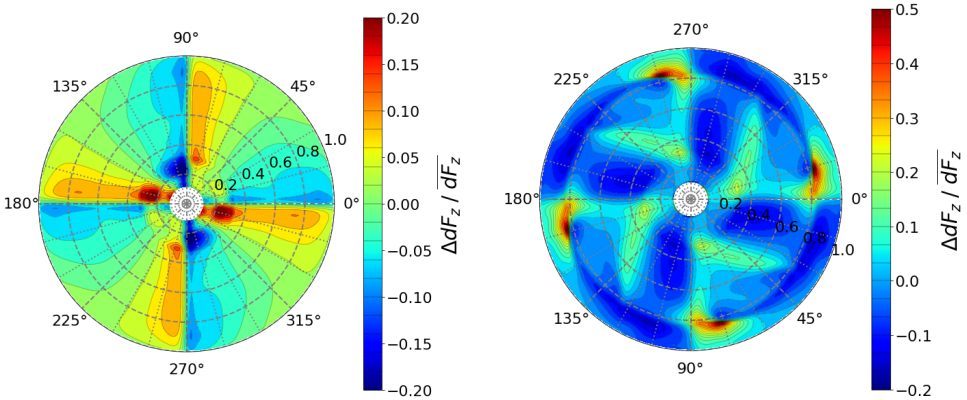

(c) $C_T/\sigma = 0.10$

Figure F.15.: Comparison of computed relative sectional thrust distribution variations ($\Delta dF_z = dF_z - \overline{dF_z}$) scaled by the average sectional thrust over one rotor revolution ($\overline{dF_z}$) of the upper and lower rotor plane for the two-by-two-bladed CCR rotor for different blade loadings. Results computed with the SA-neg-RC turbulence model.

G. Coaxial Co-Rotating Rotor Aerodynamics

G.1. Flow Field

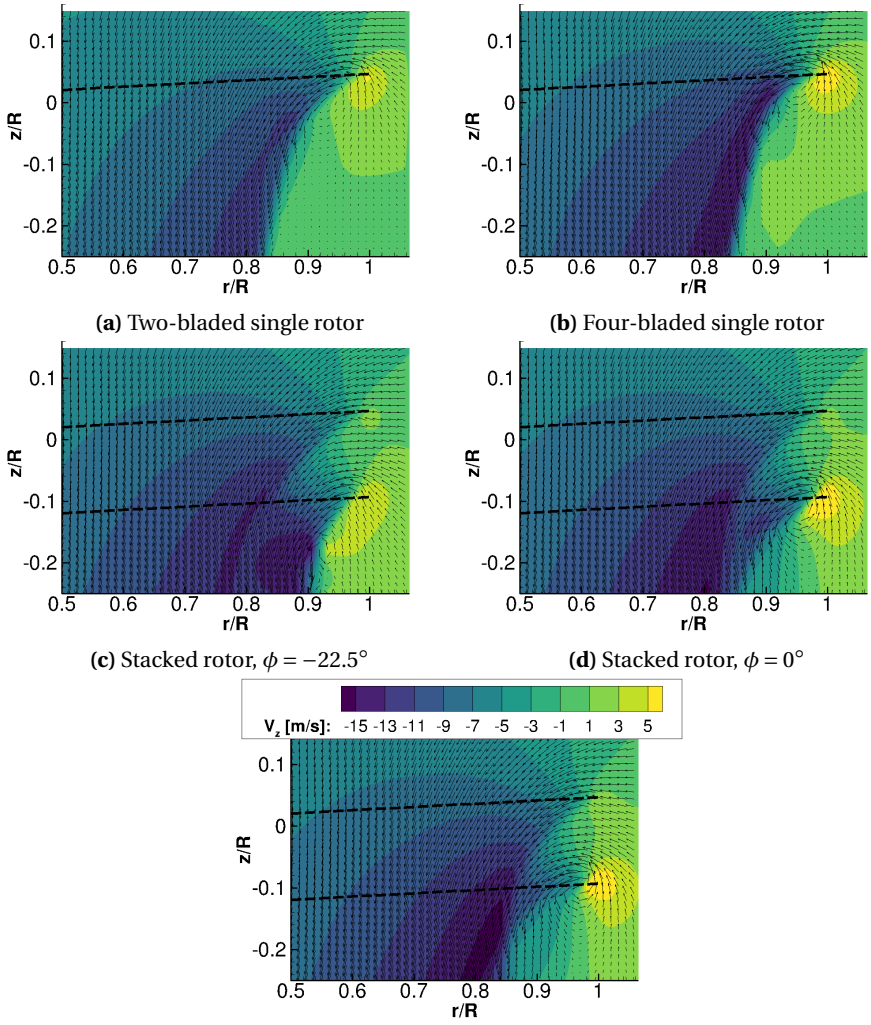

(a) Two-bladed single rotor

(b) Four-bladed single rotor

(c) Stacked rotor, $\phi = -22.5°$

(d) Stacked rotor, $\phi = 0°$

(e) Stacked rotor, $\phi = +22.5°$

Figure G.1.: Comparison of time-averaged contours of axial velocity (v_z) for the UTA stacked rotor test rig. The blade loading of the two-bladed single rotor is $C_{T,2b}/\sigma = 0.10$. Corresponding blade loadings for the other configurations are given in Table 6.2 based on the trim strategy defined in chapter 4.6. Data was averaged in increments of $\Delta\psi_b = 1°$ between the rotational periodicity boundary conditions (90 slices for the four-bladed configuration; 180 slices for all other configurations).

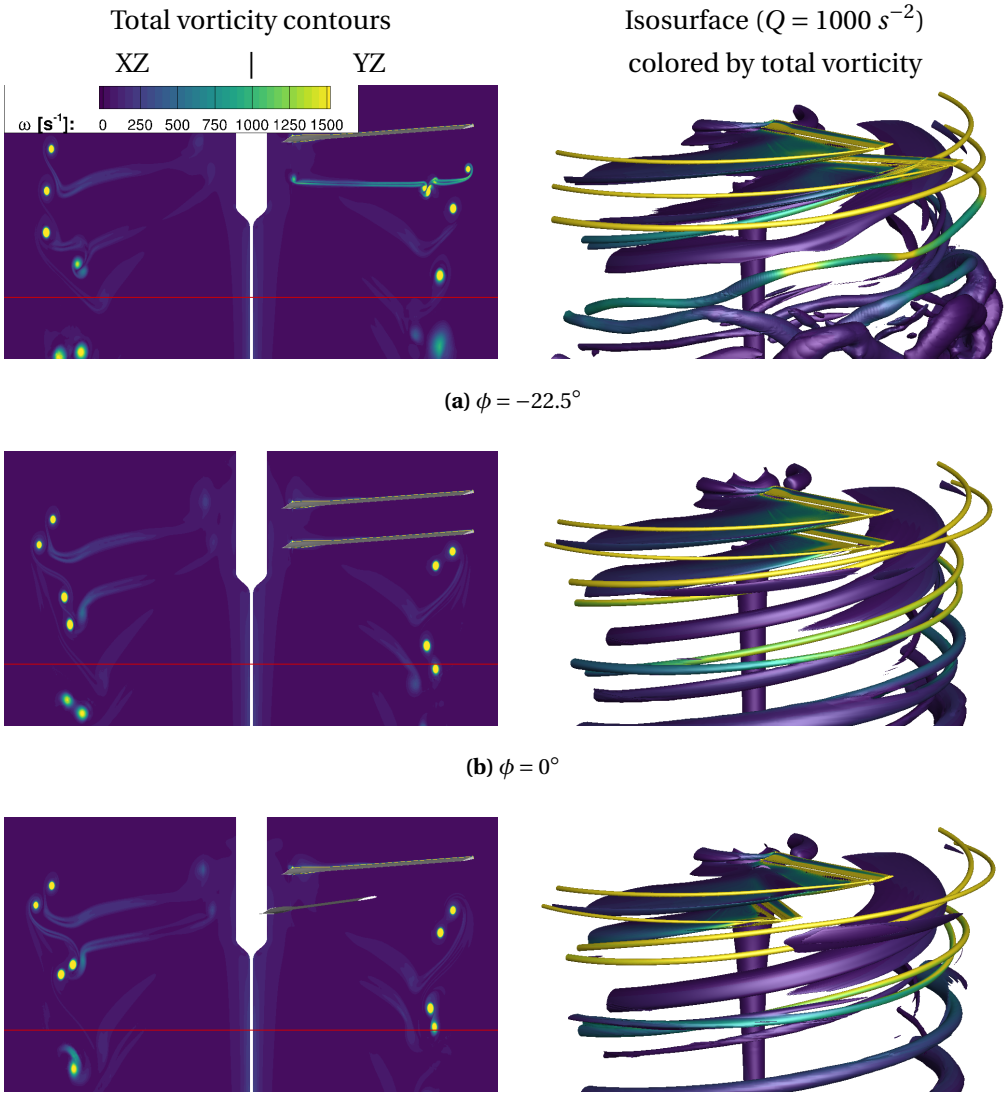

(a) $\phi = -22.5°$

(b) $\phi = 0°$

(c) $\phi = +22.5°$

Figure G.2.: Comparison of total vorticity (ω) contours and vortical structures (Q-criterion isosurfaces) of the UTA stacked rotor at $C_{T,2b}/\sigma = 0.10$ for different index angles ϕ. Corresponding blade loadings for the other configurations are given in Table 6.3 based on the trim strategy defined in chapter 4.6. Red line indicating end of high-resolution grid region for improved vortex preservation; see Fig. 4.22. Vorticity contours shown in two perpendicular vertical planes through the rotor shaft axis (XZ- and YZ-plane).

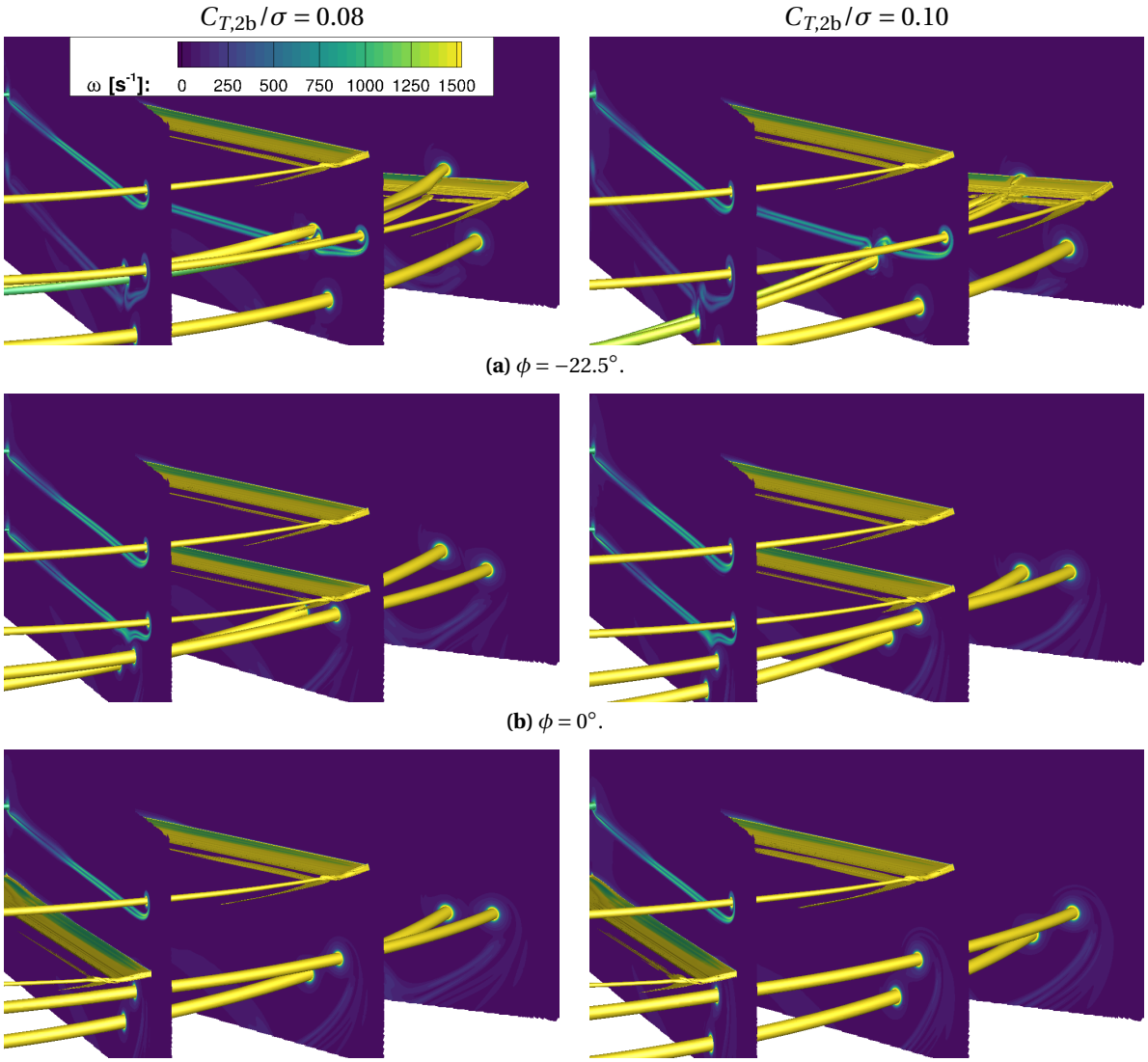

(a) $\phi = -22.5°$.

(b) $\phi = 0°$.

(c) $\phi = +22.5°$.

Figure G.3.: Visualization of computed tip vortices of the UTA stacked rotor at $C_{T,2b}/\sigma = 0.08$[114] and 0.10 using Q-criterion isosurfaces ($Q = 200,000\ s^{-2}$) and total vorticity (ω) contours in three vertical planes ($\psi_b = -22.5°$, 0°, and +22.5°). Isosurfaces colored by total vorticity.

G.2. Tip Vortex Trajectories

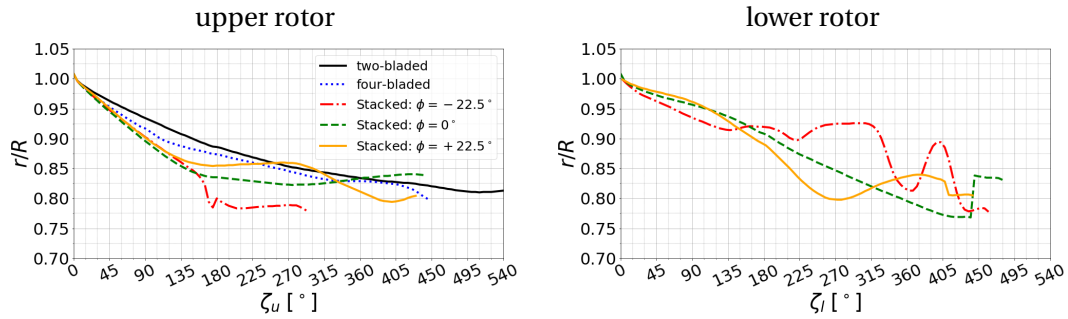

(a) r/R vs. $\zeta_{u,l}$

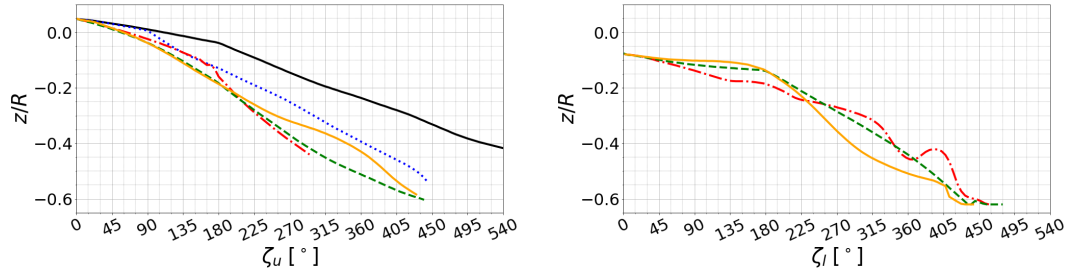

(b) z/R vs. $\zeta_{u,l}$

Figure G.4.: Comparison of computed axial (z/R) and radial (r/R) tip vortex displacements for the UTA stacked rotor test rig at $C_{T,2b}/\sigma = 0.10$. Corresponding blade loadings for the other configurations are given in Table 6.3 based on the trim strategy defined in chapter 4.6.

G.3. Rotor Inflow

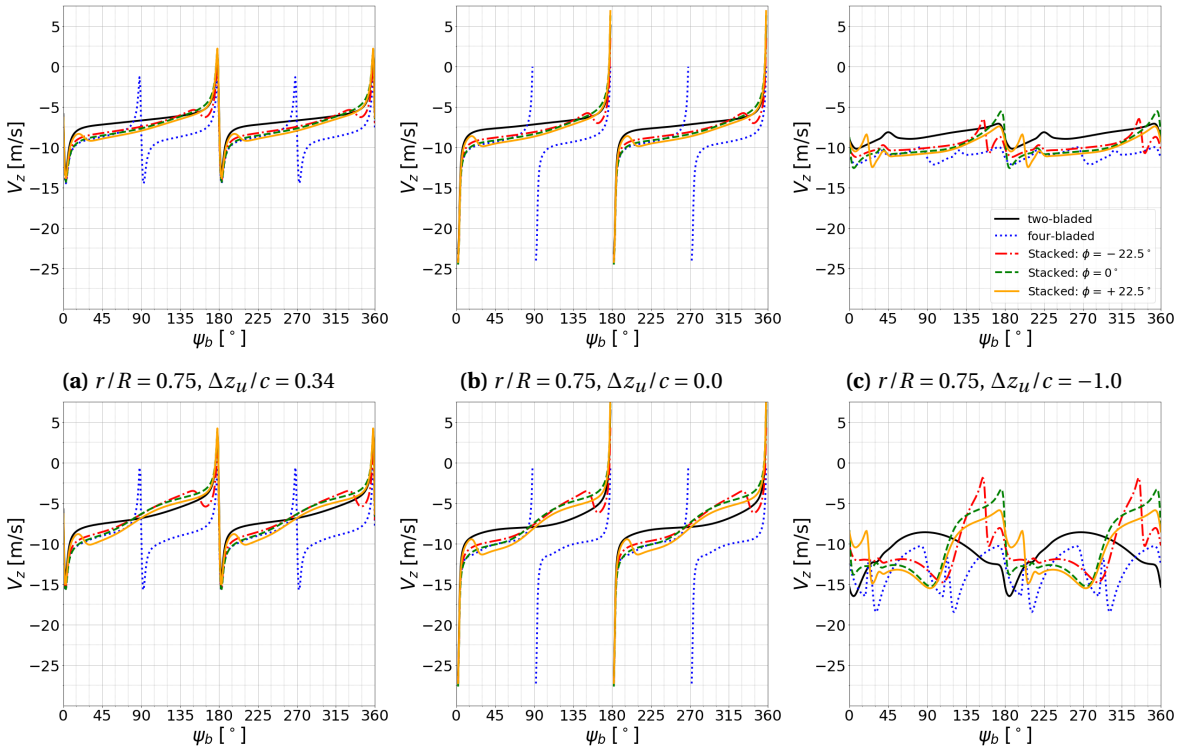

(a) $r/R = 0.75$, $\Delta z_u/c = 0.34$ **(b)** $r/R = 0.75$, $\Delta z_u/c = 0.0$ **(c)** $r/R = 0.75$, $\Delta z_u/c = -1.0$

(d) $r/R = 0.85$, $\Delta z_u/c = 0.34$ **(e)** $r/R = 0.85$, $\Delta z_u/c = 0.0$ **(f)** $r/R = 0.85$, $\Delta z_u/c = -1.0$

Figure G.5.: Comparison of computed axial velocity (v_z) for the stacked rotor with different index angles ϕ. Data shown over one revolution for $C_{T,2b}/\sigma = 0.10$ above, below, and in the upper rotor plane. Blade passage occurred at $\psi_b = 0°$ and 180°.

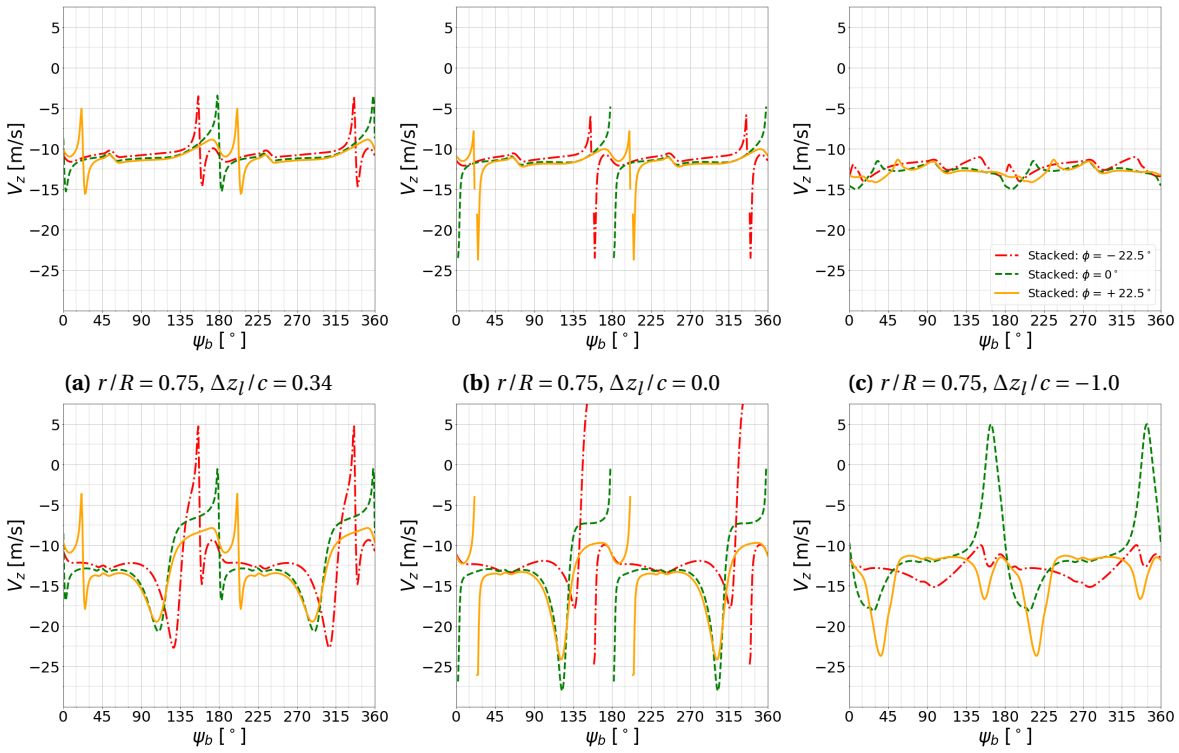

(a) $r/R = 0.75$, $\Delta z_l/c = 0.34$ **(b)** $r/R = 0.75$, $\Delta z_l/c = 0.0$ **(c)** $r/R = 0.75$, $\Delta z_l/c = -1.0$

(d) $r/R = 0.85$, $\Delta z_l/c = 0.34$ **(e)** $r/R = 0.85$, $\Delta z_l/c = 0.0$ **(f)** $r/R = 0.85$, $\Delta z_l/c = -1.0$

Figure G.6.: Comparison of computed axial velocity (v_z) for the stacked rotor with different index angles ϕ. Data shown over one revolution for $C_{T,2b}/\sigma = 0.10$ above, below, and in the lower rotor plane. Blade passage occurred at $\psi_b = 0°$ and 180°.

H. Dynamic Pitch Actuation

H.1. Forces and Moments

H.1.1. Two-Bladed Single Rotor

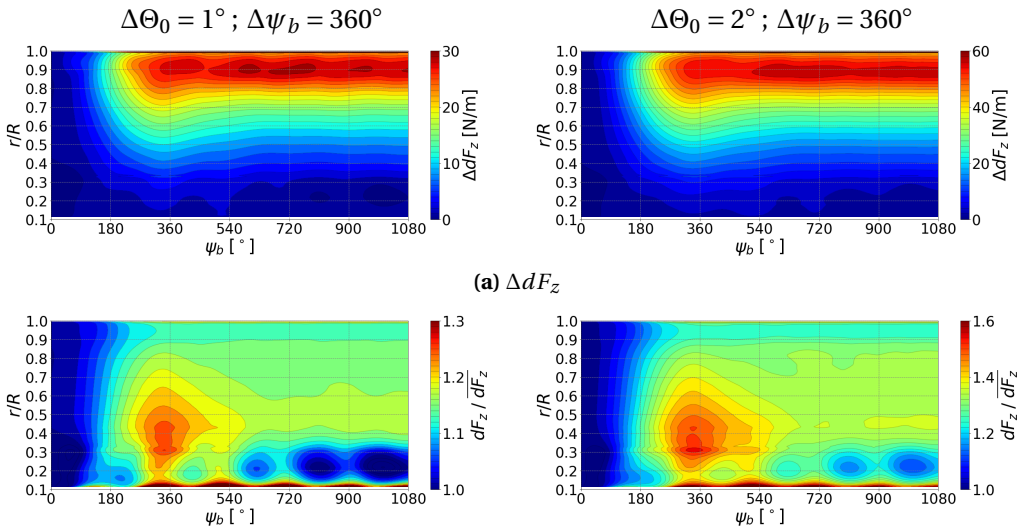

(a) ΔdF_z

(b) $dF_z / \overline{dF_z}$

Figure H.1.: Comparison of computed sectional thrust increase ($\Delta dF_z = dF_z - \overline{dF_z}$) and relative variation ($dF_z / \overline{dF_z}$) during and after collective pitch step inputs for the two-bladed single rotor based on the UTA CCR rotor test rig. Relative data scaled by the sectional thrust before pitch input ($\overline{dF_z}$). Rotor trimmed to $C_T/\sigma = 0.08$ before pitch input. Pitch angle variations are shown in Fig. 7.4a.

H.1.2. Two-by-Two-Bladed CCR Rotor

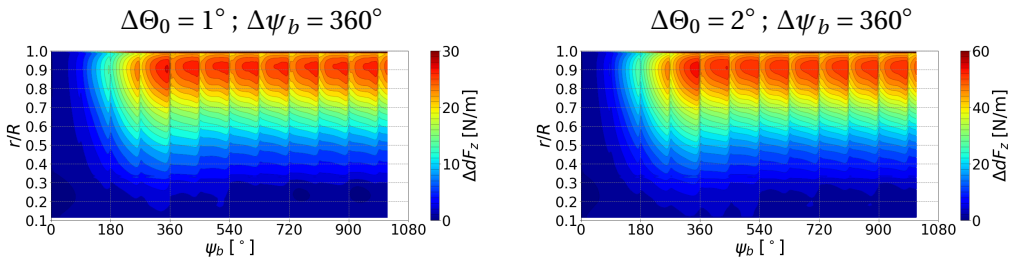

(a) ΔdF_z

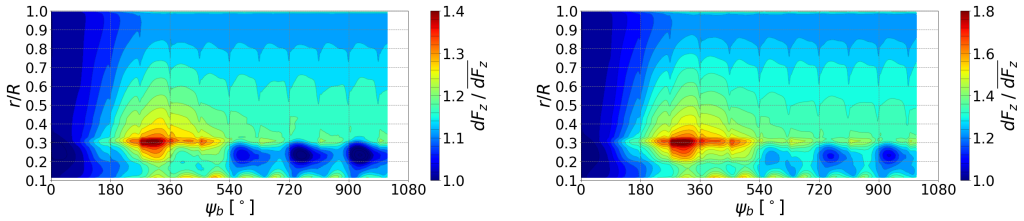

(b) $dF_z/\overline{dF_z}$

Figure H.2.: Comparison of computed sectional thrust increase ($\Delta dF_z = dF_z - \overline{dF_z}$) and relative variation ($\Delta dF_z/\overline{dF_z}$) during and after collective pitch step inputs for the upper rotor of the CCR rotor. Relative data scaled by the sectional thrust before pitch input ($\overline{dF_z}$). Rotor trimmed to $C_T/\sigma = 0.08$ before pitch input. Pitch angle variations are shown in Fig. 7.4a. Data shown up to the maximum wake age computed, before the residual of the turbulence model transport variable $\rho\tilde{\nu}$ diverged.

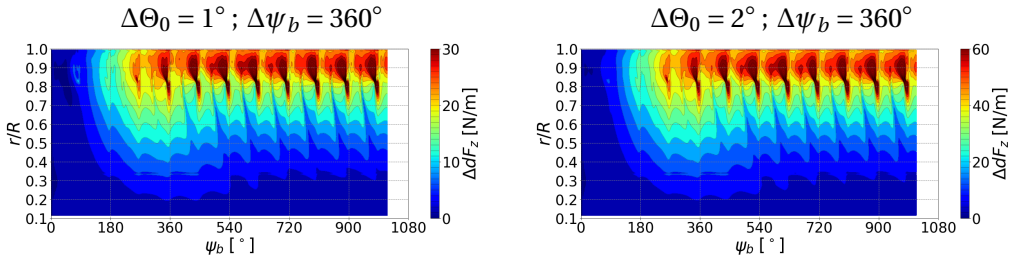

(a) ΔdF_z

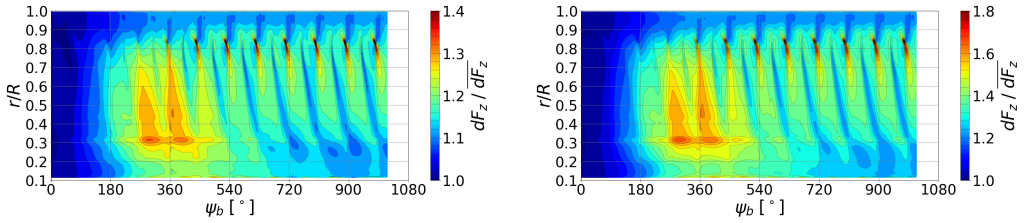

(b) $dF_z/\overline{dF_z}$

Figure H.3.: Comparison of computed sectional thrust increase ($\Delta dF_z = dF_z - \overline{dF_z}$) and relative variation ($\Delta dF_z/\overline{dF_z}$) during and after collective pitch step inputs for the lower rotor of the CCR rotor. Relative data scaled by the sectional thrust before pitch input ($\overline{dF_z}$). Rotor trimmed to $C_T/\sigma = 0.08$ before pitch input. Pitch angle variations are shown in Fig. 7.4a. Data shown up to the maximum wake age computed, before the residual of the turbulence model transport variable $\rho\tilde{\nu}$ diverged.

H.2. Rotor Inflow

H.2.1. Two-Bladed Single Rotor

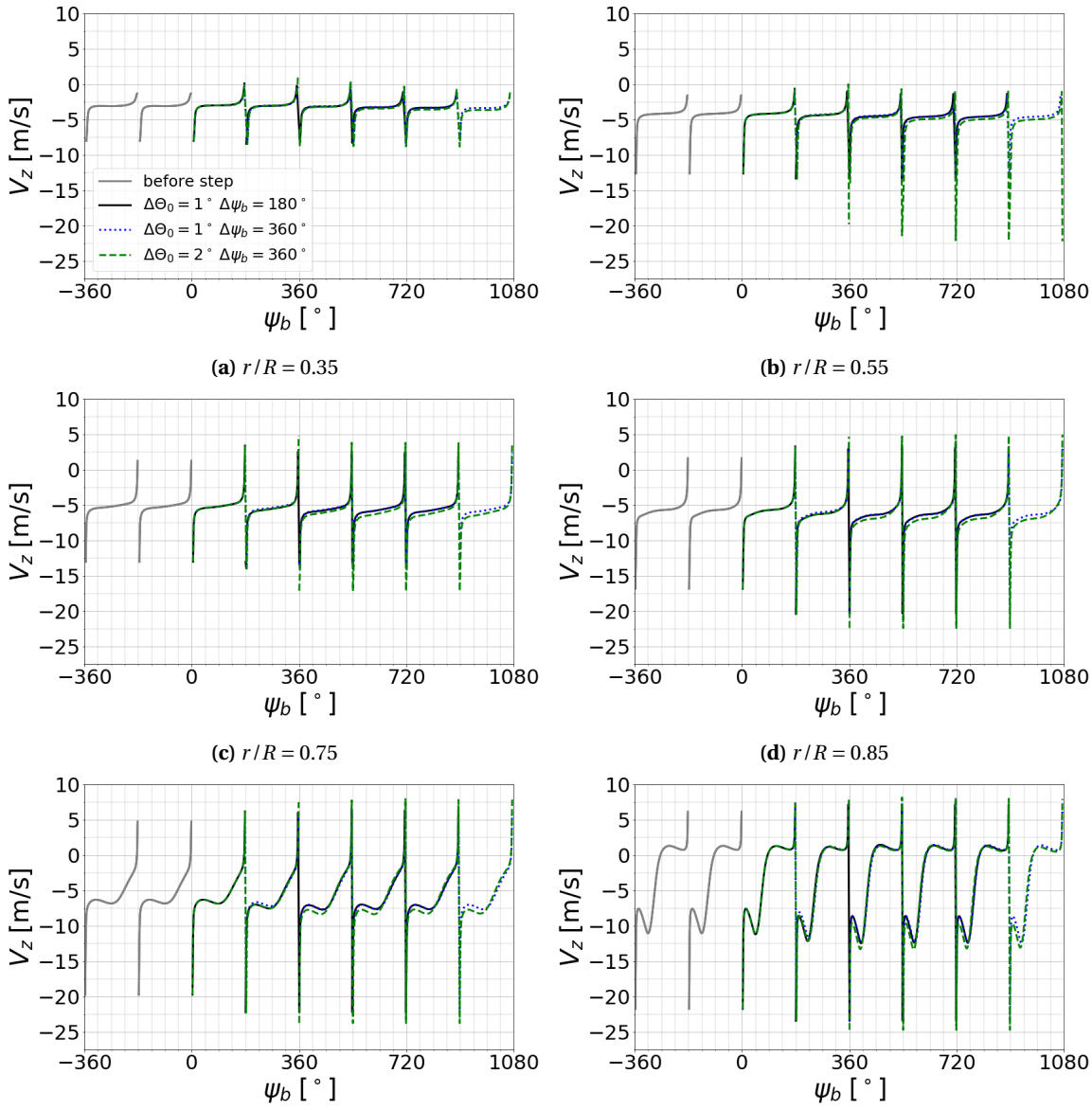

(a) $r/R = 0.35$

(b) $r/R = 0.55$

(c) $r/R = 0.75$

(d) $r/R = 0.85$

(e) $r/R = 0.90$

(f) $r/R = 0.95$

Figure H.4.: Computed variations of axial velocity (v_z) before, during and after collective pitch step inputs for the two-bladed single rotor based on the UTA CCR rotor test rig. Data extracted in the rotor plane ($\Delta z/c = 0$) in plane $\xi = 0°$; see Fig. 6.8. Rotor was trimmed to $C_T/\sigma = 0.06$ before pitch input. Pitch angle variations are shown in Fig. 7.4a.

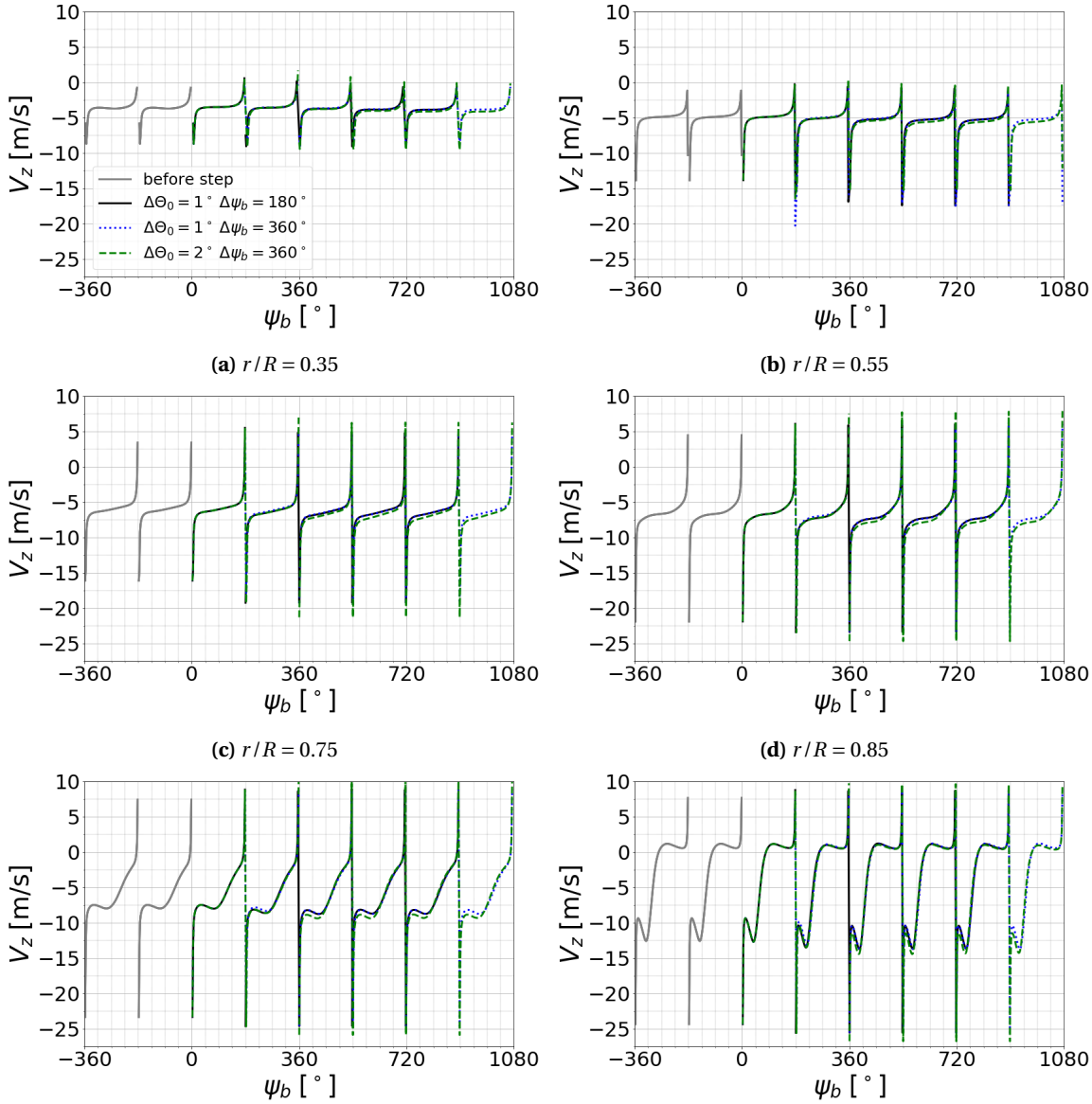

(a) $r/R = 0.35$

(b) $r/R = 0.55$

(c) $r/R = 0.75$

(d) $r/R = 0.85$

(e) $r/R = 0.90$

(f) $r/R = 0.95$

Figure H.5.: Computed variations of axial velocity (v_z) before, during and after collective pitch step inputs for the two-bladed single rotor based on the UTA CCR rotor test rig. Data extracted in the rotor plane ($\Delta z/c = 0$) in plane $\xi = 0°$; see Fig. 6.8. Rotor was trimmed to $C_T/\sigma = 0.08$ before pitch input. Pitch angle variations are shown in Fig. 7.4a.

H.2.2. Two-by-Two-Bladed CCR Rotor

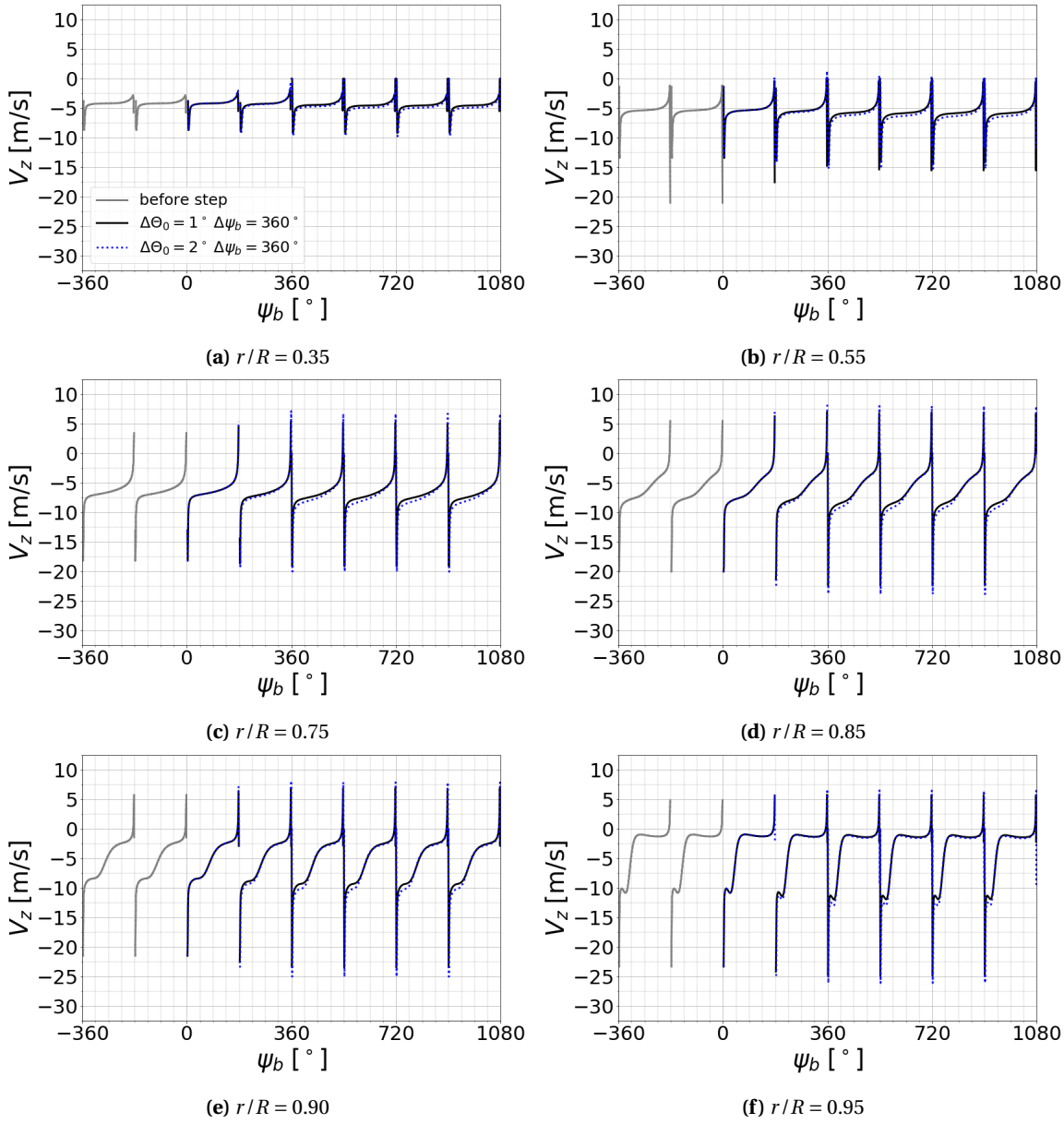

(a) $r/R = 0.35$ **(b)** $r/R = 0.55$

(c) $r/R = 0.75$ **(d)** $r/R = 0.85$

(e) $r/R = 0.90$ **(f)** $r/R = 0.95$

Figure H.6.: Computed variations of axial velocity (v_z) before, during and after collective pitch step inputs of the upper rotor plane of the CCR rotor. Data extracted in the rotor plane ($\Delta z/c = 0$) in plane $\xi = 0°$; see Fig. 6.8. Rotor was trimmed to $C_T/\sigma = 0.06$ before pitch input. Pitch angle variations are shown in Fig. 7.4a.

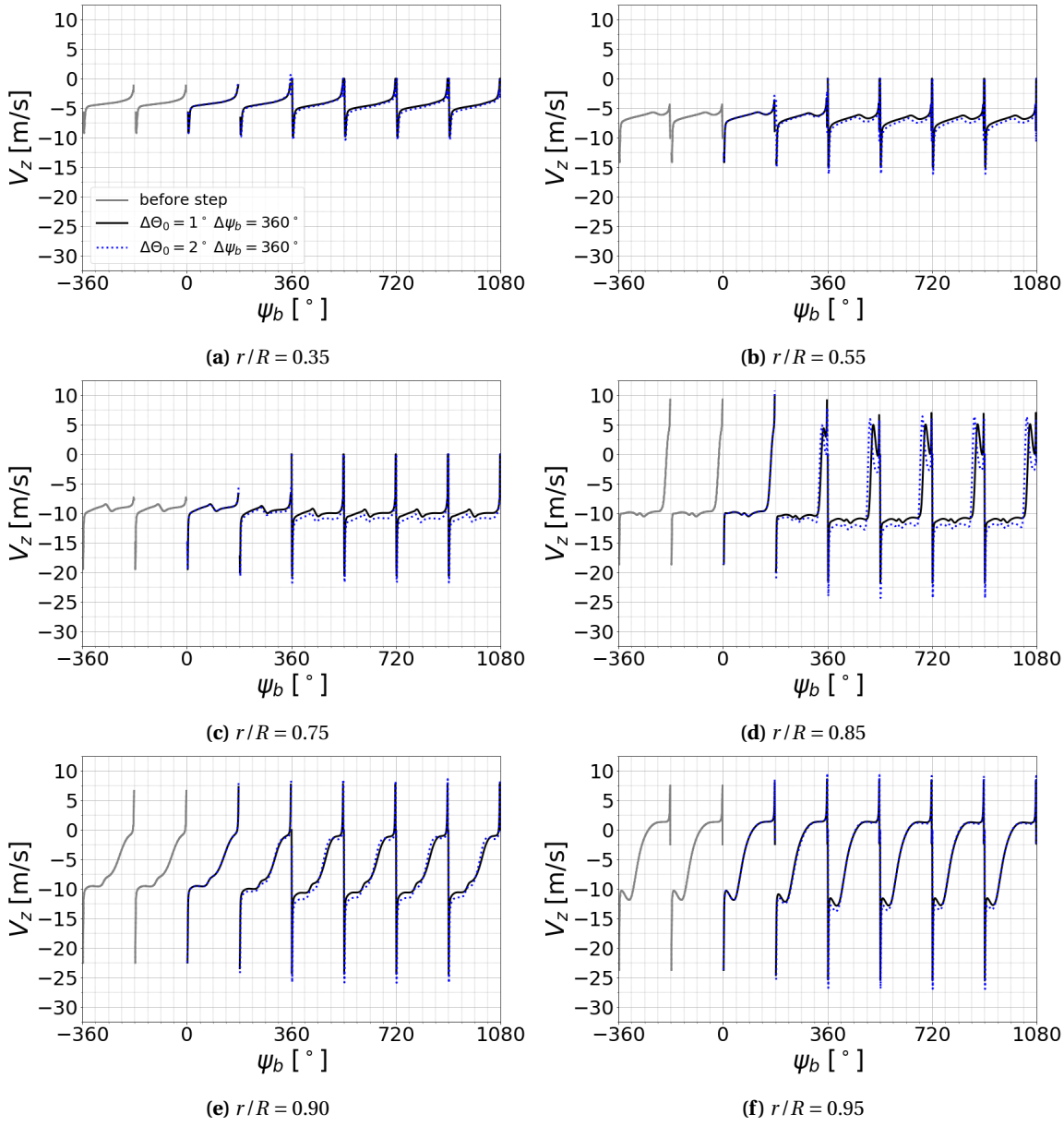

(a) $r/R = 0.35$

(b) $r/R = 0.55$

(c) $r/R = 0.75$

(d) $r/R = 0.85$

(e) $r/R = 0.90$

(f) $r/R = 0.95$

Figure H.7.: Computed variations of axial velocity (v_z) before, during and after collective pitch step inputs of the lower rotor plane of the CCR rotor. Data extracted in the rotor plane ($\Delta z/c = 0$) in plane $\xi = 0°$; see Fig. 6.8. Rotor was trimmed to $C_T/\sigma = 0.06$ before pitch input. Pitch angle variations are shown in Fig. 7.4a.

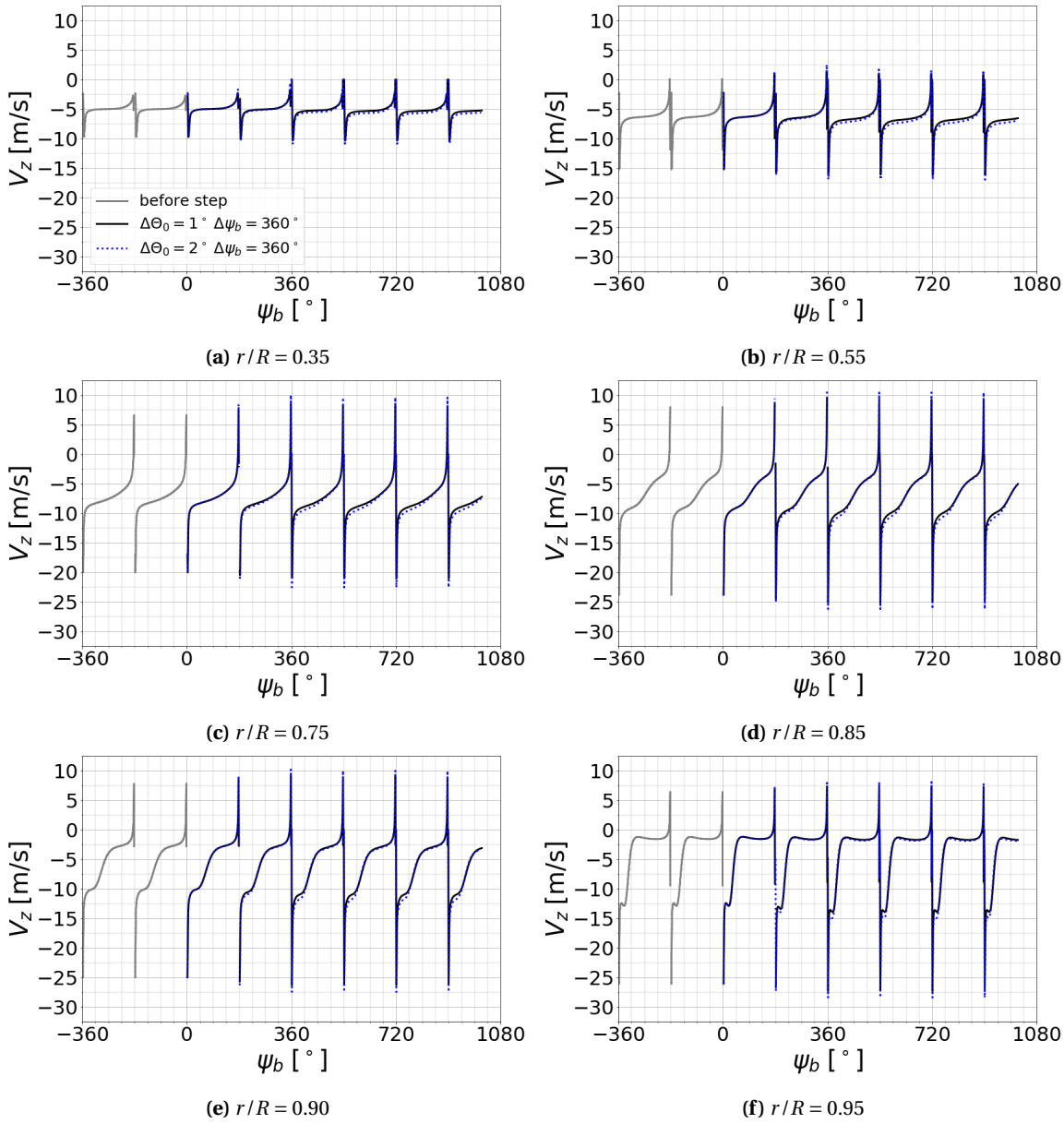

(a) $r/R = 0.35$ **(b)** $r/R = 0.55$

(c) $r/R = 0.75$ **(d)** $r/R = 0.85$

(e) $r/R = 0.90$ **(f)** $r/R = 0.95$

Figure H.8.: Computed variations of axial velocity (v_z) before, during and after collective pitch step inputs of the upper rotor plane of the CCR rotor. Data extracted in the rotor plane ($\Delta z/c = 0$) in plane $\xi = 0°$; see Fig. 6.8. Rotor was trimmed to $C_T/\sigma = 0.08$ before pitch input. Pitch angle variations are shown in Fig. 7.4a. Data shown up to the maximum wake age computed, before the residual of the turbulence model transport variable $\rho\tilde{\nu}$ diverged.

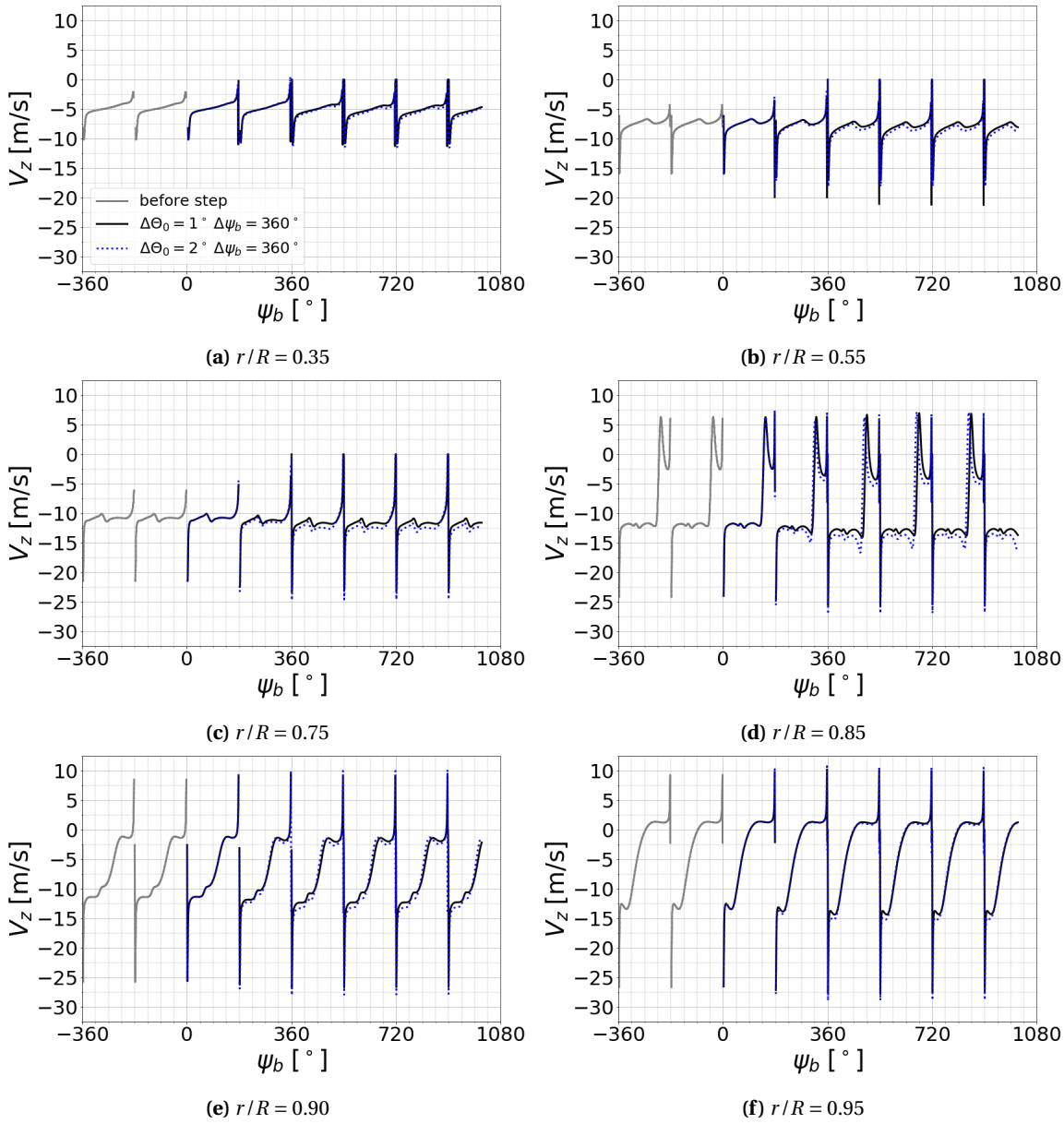

(a) $r/R = 0.35$ **(b)** $r/R = 0.55$

(c) $r/R = 0.75$ **(d)** $r/R = 0.85$

(e) $r/R = 0.90$ **(f)** $r/R = 0.95$

Figure H.9.: Computed variations of axial velocity (v_z) before, during and after collective pitch step inputs of the lower rotor plane of the CCR rotor. Data extracted in the rotor plane ($\Delta z/c = 0$) in plane $\xi = 0°$; see Fig. 6.8. Rotor was trimmed to $C_T/\sigma = 0.08$ before pitch input. Pitch angle variations are shown in Fig. 7.4a. Data shown up to the maximum wake age computed, before the residual of the turbulence model transport variable $\rho\tilde{\nu}$ diverged.

I. Dynamic Rotational Speed Actuation

I.1. Forces and Moments

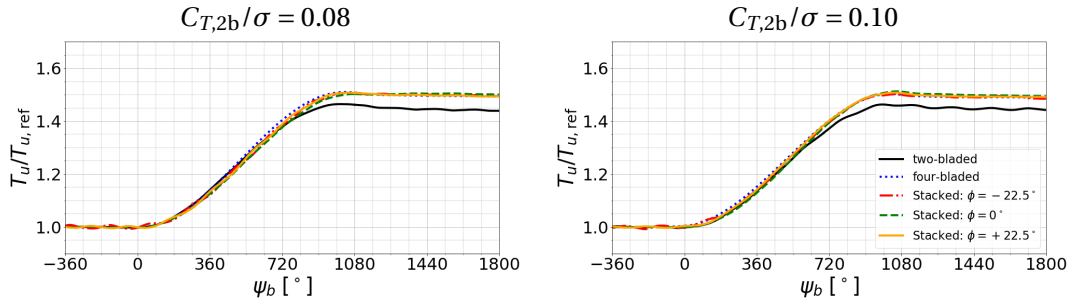

(a) Upper rotor

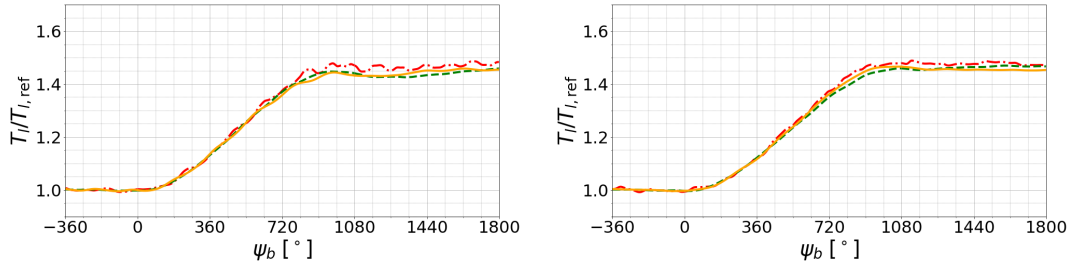

(b) Lower rotor

Figure I.1.: Rotor thrust ($T_{u|l}/T_{u|l,\mathrm{ref}}$) variations of rotors based on the UTA stacked rotor test rig for $\Delta\Omega$ = 20% over $\Delta\psi_b = 1080°$. Rotor trimmed to $C_{T,2b}/\sigma = 0.08$ and 0.10 before pitch input. Thrust and torque were normalized by mean values prior to RPM input. RPM variations shown in Fig. 7.10b.

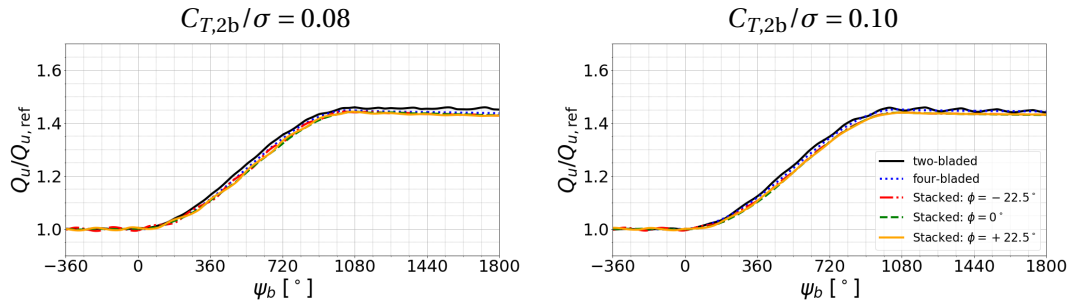

(a) Upper rotor

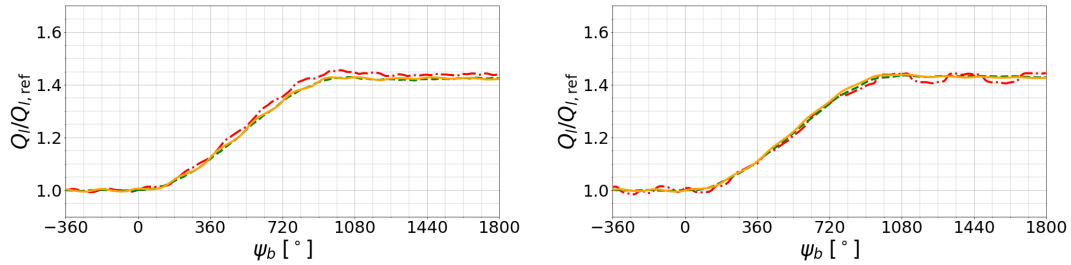

(b) Lower rotor

Figure I.2.: Rotor torque ($Q_{u|l}/Q_{u|l,\mathrm{ref}}$) variations of rotors based on the UTA stacked rotor test rig for $\Delta\Omega$ = 20% over $\Delta\psi_b = 1080°$. Rotor trimmed to $C_{T,2b}/\sigma = 0.08$ and 0.10 before pitch input. Thrust and torque were normalized by mean values prior to RPM input. RPM variations shown in Fig. 7.10b.

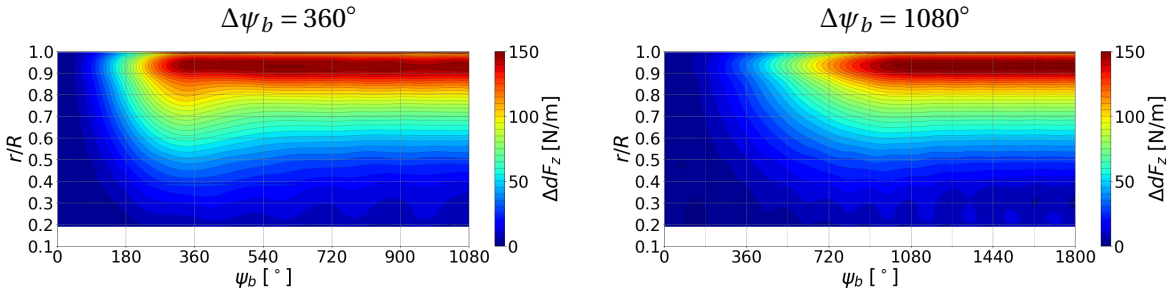

(a) ΔdF_z

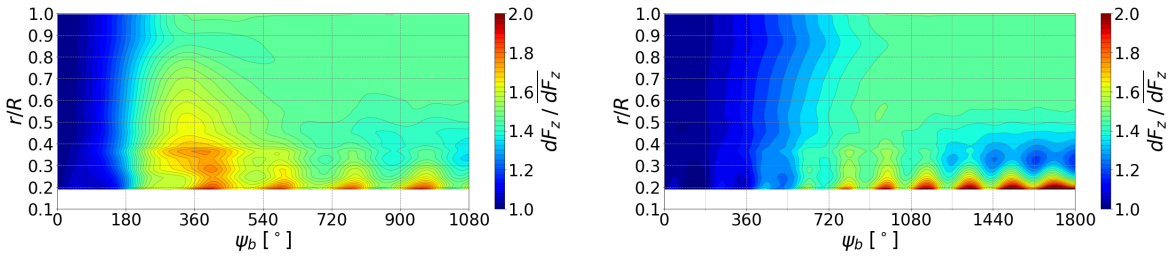

(b) $dF_z/\overline{dF_z}$

Figure I.3.: Comparison of computed sectional thrust increase ($\Delta dF_z = dF_z - \overline{dF_z}$) and relative variation ($\Delta dF_z/\overline{dF_z}$) during and after RPM inputs ($\Delta\Omega$ = 20%) for the two-bladed single rotor based on the UTA stacked rotor test rig. Relative data scaled by the sectional thrust before RPM input ($\overline{dF_z}$). Rotor trimmed to $C_{T,2b}/\sigma = 0.10$ before RPM input. RPM variations are shown in Fig. 7.10b.

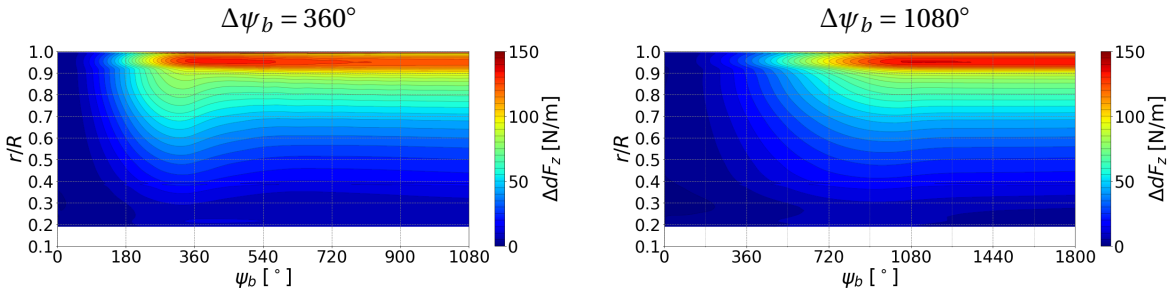

(a) ΔdF_z

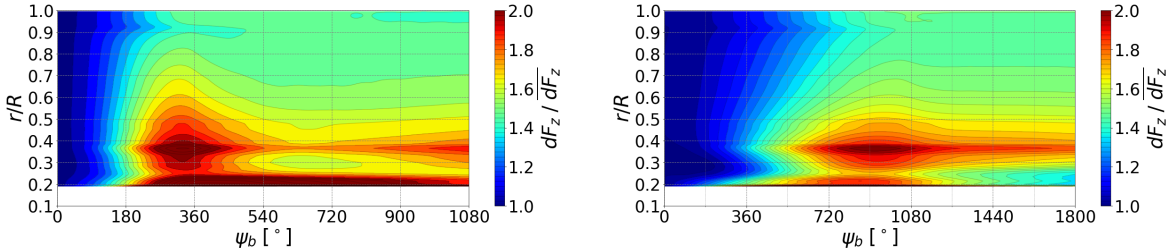

(b) $dF_z/\overline{dF_z}$

Figure I.4.: Comparison of computed sectional thrust increase ($\Delta dF_z = dF_z - \overline{dF_z}$) and relative variation ($\Delta dF_z/\overline{dF_z}$) during and after RPM inputs ($\Delta\Omega = 20\%$) for the four-bladed single rotor based on the UTA stacked rotor test rig. Relative data scaled by the sectional thrust before RPM input ($\overline{dF_z}$). Rotor trimmed to $C_{T,2b}/\sigma = 0.08$ before RPM input. RPM variations are shown in Fig. 7.10b.

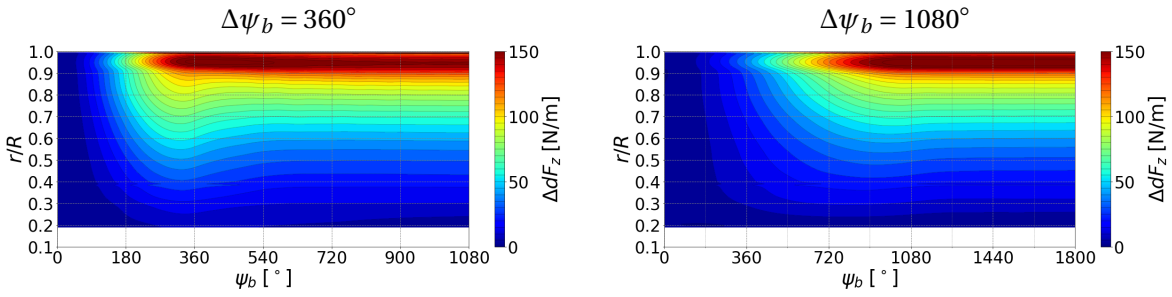

(a) ΔdF_z

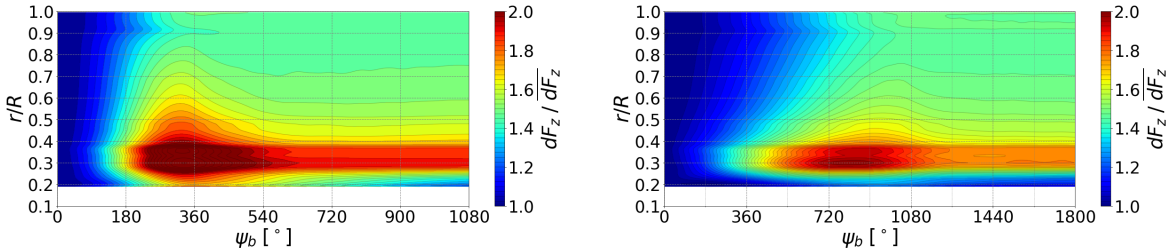

(b) $dF_z/\overline{dF_z}$

Figure I.5.: Comparison of computed sectional thrust increase ($\Delta dF_z = dF_z - \overline{dF_z}$) and relative variation ($\Delta dF_z/\overline{dF_z}$) during and after RPM inputs ($\Delta\Omega = 20\%$) for the four-bladed single rotor based on the UTA stacked rotor test rig. Relative data scaled by the sectional thrust before RPM input ($\overline{dF_z}$). Rotor trimmed to $C_{T,2b}/\sigma = 0.10$ before RPM input. RPM variations are shown in Fig. 7.10b.

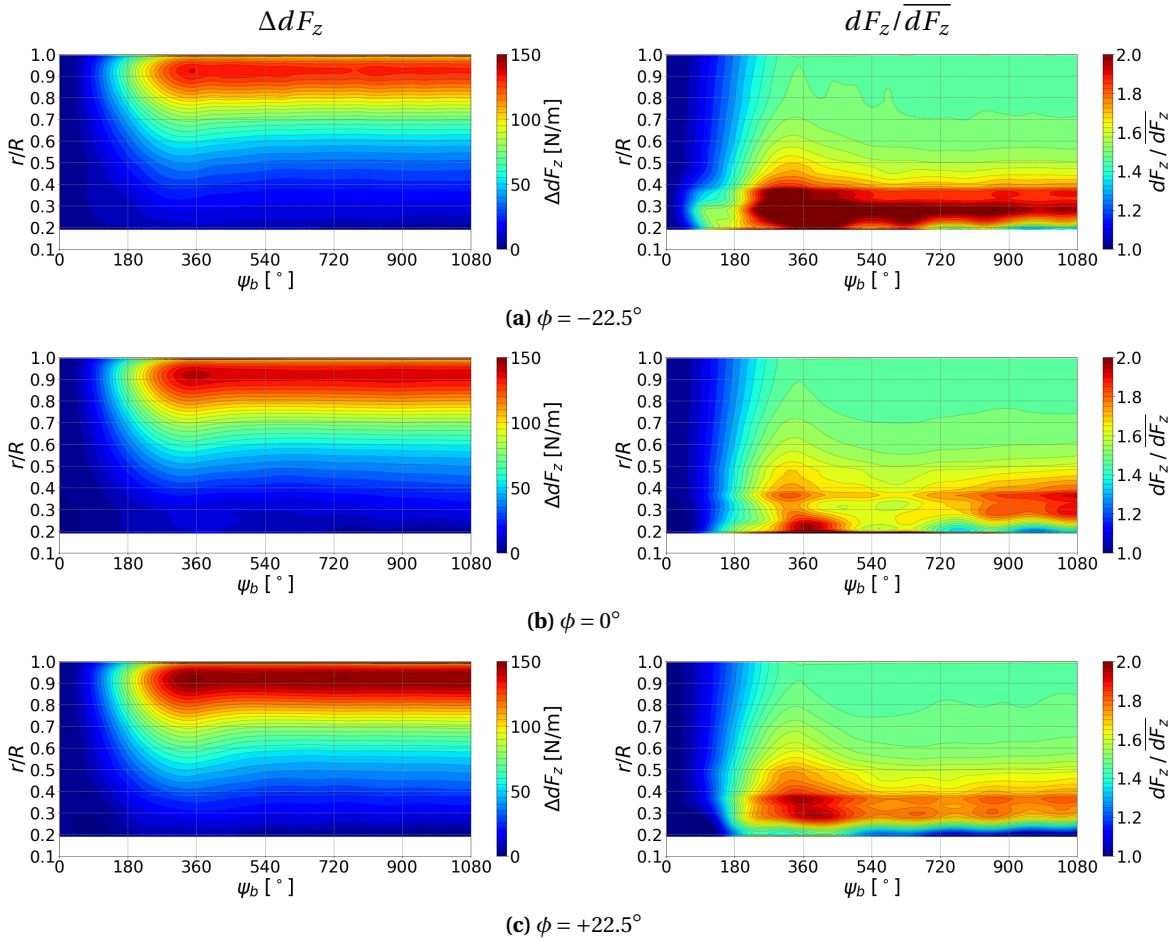

(a) $\phi = -22.5°$

(b) $\phi = 0°$

(c) $\phi = +22.5°$

Figure I.6.: Comparison of computed upper rotor sectional thrust increase ($\Delta dF_z = dF_z - \overline{dF_z}$) and relative variation ($\Delta dF_z/\overline{dF_z}$) during and after RPM inputs for the stacked rotor. Rotor trimmed to $C_{T,2b}/\sigma = 0.10$ before RPM input. Relative data scaled by the sectional thrust before RPM input ($\overline{dF_z}$). Rotor rotational frequency was increased by $\Delta\Omega = 20\%$ over $\Delta\psi_b = 360°$.

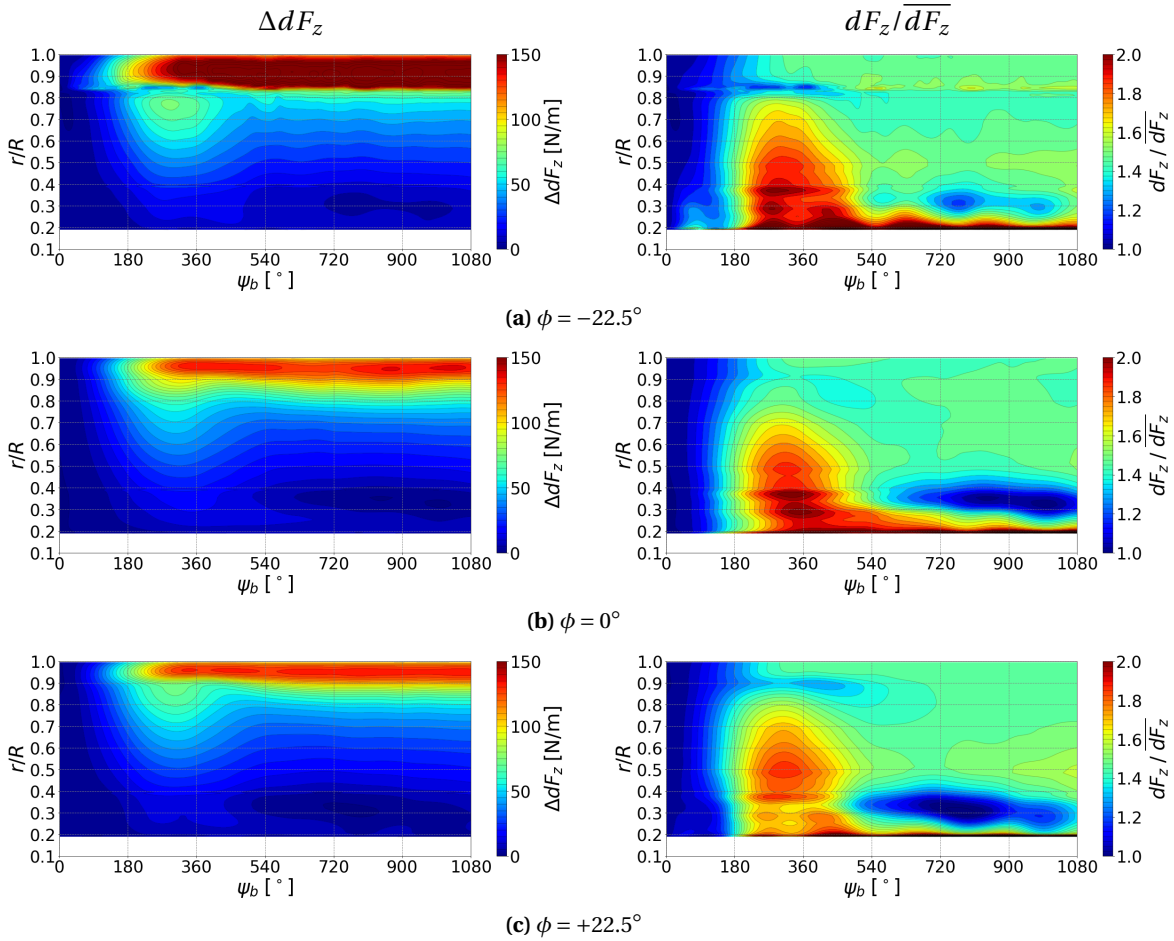

(a) $\phi = -22.5°$

(b) $\phi = 0°$

(c) $\phi = +22.5°$

Figure I.7.: Comparison of computed lower rotor sectional thrust increase ($\Delta dF_z = dF_z - \overline{dF_z}$) and relative variation ($\Delta dF_z/\overline{dF_z}$) during and after RPM inputs for the stacked rotor. Rotor trimmed to $C_{T,2b}/\sigma = 0.10$ before RPM input. Relative data scaled by the sectional thrust before RPM input ($\overline{dF_z}$). Rotor rotational frequency was increased by $\Delta\Omega = 20\%$ over $\Delta\psi_b = 360°$.

I.2. Rotor Inflow

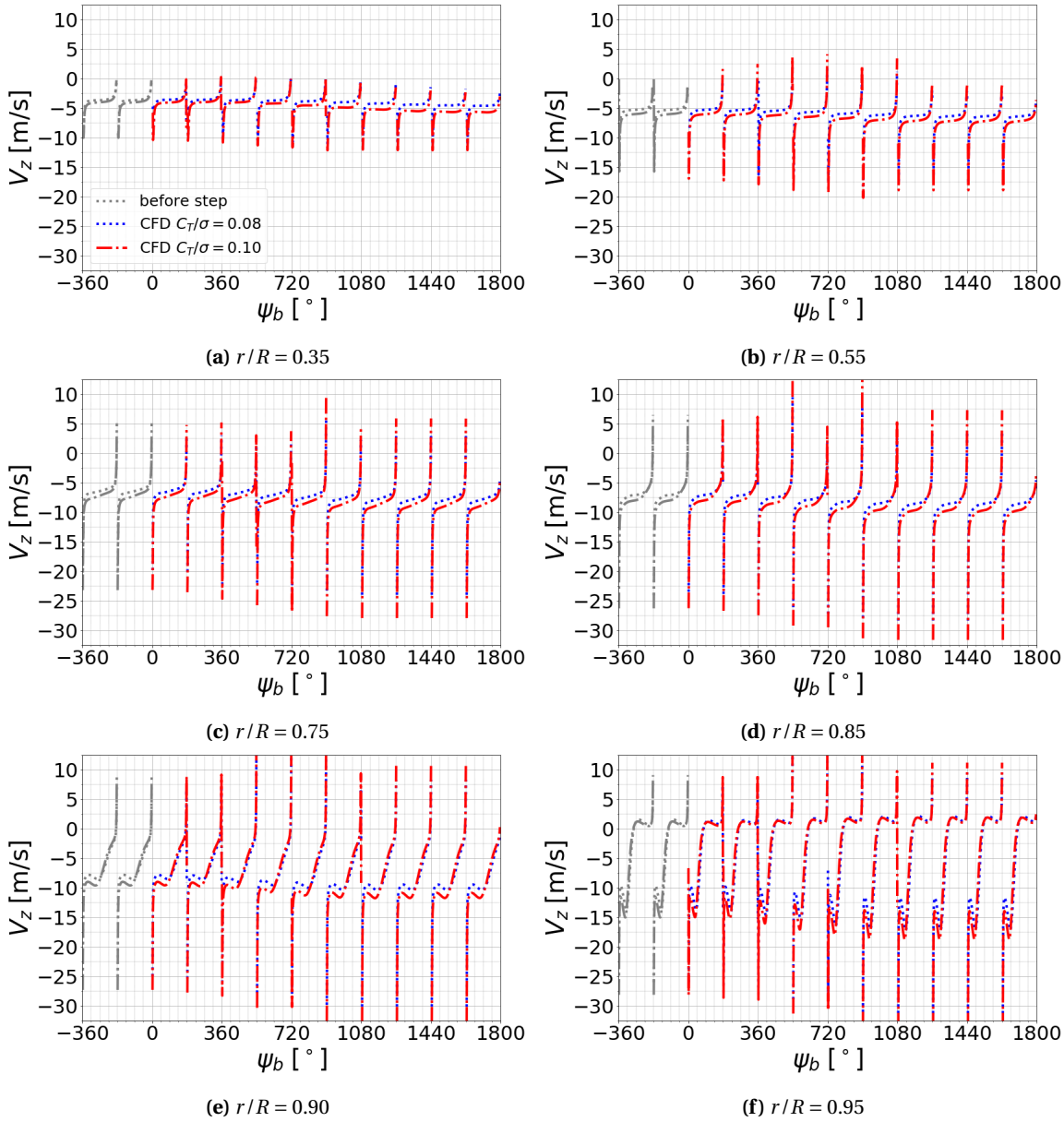

(a) $r/R = 0.35$ **(b)** $r/R = 0.55$

(c) $r/R = 0.75$ **(d)** $r/R = 0.85$

(e) $r/R = 0.90$ **(f)** $r/R = 0.95$

Figure I.8.: Axial velocity (v_z) variations before, during and after RPM inputs in the rotor plane ($\Delta z/c = 0$) of the two-bladed single rotor based on the UTA stacked rotor test rig at $C_T/\sigma = 0.08$ and 0.10 before the input. Data shown for ΔRPM = 20% over $\Delta\psi_b = 1080°$.

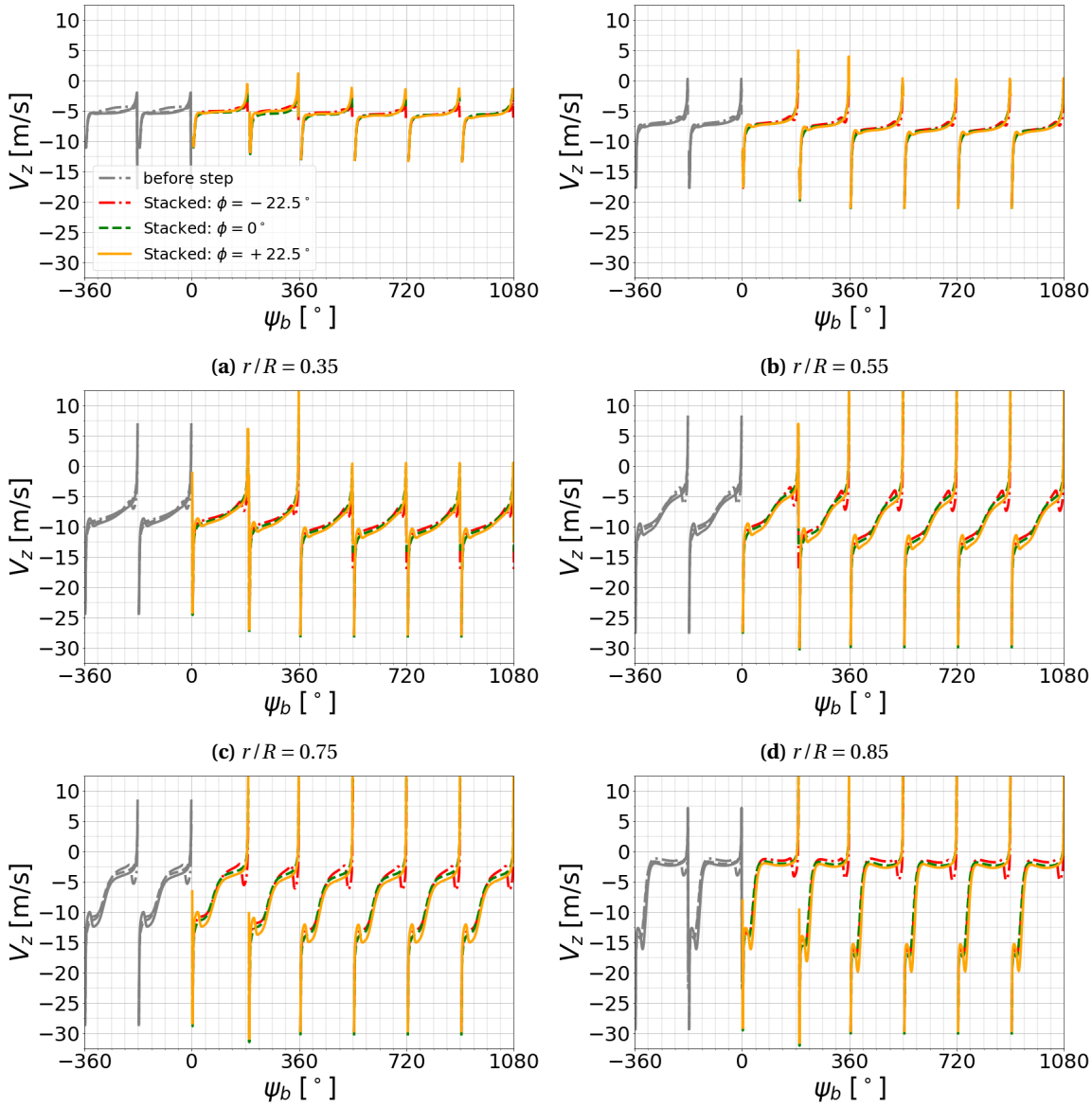

(a) $r/R = 0.35$ **(b)** $r/R = 0.55$

(c) $r/R = 0.75$ **(d)** $r/R = 0.85$

(e) $r/R = 0.90$ **(f)** $r/R = 0.95$

Figure I.9.: Axial velocity (v_z) variations before, during and after RPM inputs in the upper rotor plane ($\Delta z/c = 0$) of the UTA stacked rotor at $C_T/\sigma = 0.10$ before the input. Data shown for three index angles ($\phi = -22.5, 0°$, and $22.5°$) and $\Delta\text{RPM} = 20\%$ over $\Delta\psi_b = 360°$.

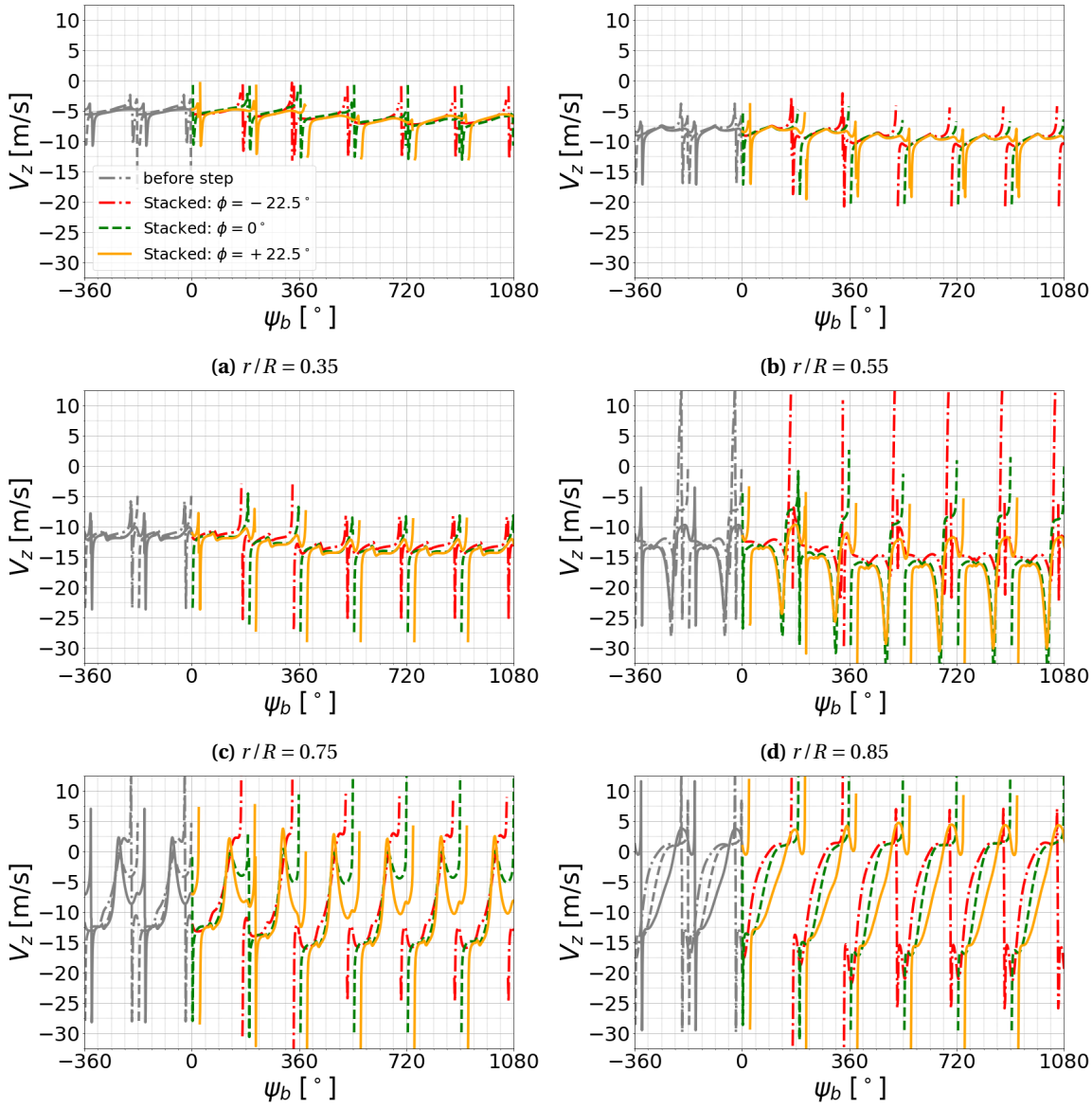

(a) $r/R = 0.35$ **(b)** $r/R = 0.55$

(c) $r/R = 0.75$ **(d)** $r/R = 0.85$

(e) $r/R = 0.90$ **(f)** $r/R = 0.95$

Figure I.10.: Axial velocity (v_z) variations before, during and after RPM inputs in the lower rotor plane ($\Delta z/c = 0$) of the UTA stacked rotor at $C_T/\sigma = 0.10$ before the input. Data shown for three index angles ($\phi = -22.5, 0°$, and $22.5°$) and ΔRPM = 20% over $\Delta\psi_b = 360°$.

Bibliography

[1] *AIAA Rotorcraft Hover Prediction Workshop*. URL: https://aiaahover.wixsite.com/website-6 (visited on 11/28/2020).

[2] *Turbulence Modeling Resource*. URL: https://turbmodels.larc.nasa.gov/ (visited on 08/18/2020).

[3] Allmaras, S. R., Johnson, F. T., and Spalart, P. R. "Modifications and Clarifications for the Implementation of the Spalart-Allmaras Turbulence Model". In: *Seventh International Conference on Computational Fluid Dynamics (ICCFD7)*. 2012, pp. 1–11.

[4] Ananthan, S. and Leishman, J. G. "Transient Helicopter Rotor Wakes in Response to Time-Dependent Blade Pitch Inputs". In: *Journal of Aircraft* 41.5 (2004), pp. 1025–1041.

[5] Andrew, M. J. "Co-Axial Rotor Aerodynamics in Hover". In: *6th European Rotorcraft and Powered Lift Aircraft Forum*. Bristol, England, 1980.

[6] Anikin, V. A. "Aerodynamic Features of a Coaxial Rotor Helicopter". In: *17th European Rotorcraft Forum* (1991), pp. 533–551.

[7] Barbely, N. L., Komerath, N. M., and Novak, L. A. "A Study of Coaxial Rotor Performance and Flow Field Characteristics". In: *AHS Technical Meeting on Aeromechanics Design for Vertical Lift* (2016), pp. 609–623.

[8] Bhagwat, M. J. and Leishman, J. G. "Time-Accurate Free-Vortex Wake Model for Dynamic Rotor Response". In: *American Helicopter Society Specialist Meeting*. 2000.

[9] Bhagwat, M. J., Ormiston, R. A., Saberi, H. A., and Xin, H. "Application of CFD/CSD Coupling for Analysis of Rotorcraft Airloads and Blade Loads in Maneuvering Flight". In: *American Helicopter Society 63rd Annual Forum* 3 (2007), pp. 2171–2200.

[10] Bhagwat, M. J. and Ormiston, R. A. "Examination of Rotor Aerodynamics in Steady and Maneuvering Flight using CFD and Conventional Methods". In: *American Helicopter Society International - AHS Specialists' Conference on Aeromechanics* (2008).

[11] Bhagwat, M. J. "Co-rotating and Counter-Rotating Coaxial Rotor Performance". In: *AHS Aeromechanics Design for Transformative Vertical Flight* (2018).

[12] Blazek, J. *Computational Fluid Dynamics: Principles and Applications*. First Edit. Elsevier Ltd., 2005.

[13] Bludau, J., Rauleder, J., Friedmann, L., and Hajek, M. "Real-Time Simulation of Dynamic Inflow Using Rotorcraft Flight Dynamics Coupled With a Lattice-Boltzmann Based Fluid Simulation". In: *AIAA SciTech 2017 Forum*. Grapevine, TX, USA, 2017.

[14] Bodling, A. and Potsdam, M. "Numerical Investigation of Secondary Vortex Structures in a Rotor Wake". In: *American Helicopter Society 76th Annual Forum*. Virgina Beach, VA, 2020.

[15] Brown, R. E. "Rotor Wake Modeling for Flight Dynamic Simulation of Helicopters". In: *AIAA journal* 38.1 (2000), pp. 57–63.

[16] Cameron, C. G., Uehara, D., and Sirohi, J. “Transient Hub Loads and Blade Deformation of a Mach-Scale Coaxial Rotor in Hover”. In: *AIAA Scitech Forum*. Kissimmmee, Florida, USA, 2015.

[17] Cameron, C. G., Karpatne, A., and Sirohi, J. “Performance of a Mach-Scale Coaxial Counter-Rotating Rotor in Hover”. In: *Journal of Aircraft* 53.3 (2016), pp. 746–755.

[18] Cameron, C., Sirohi, J., Feil, R., and Rauleder, J. “Measurement of Transient Loads and Blade Deformation in a Coaxial Counter-Rotating Rotor”. In: *American Helicopter Society 73rd Annual Forum*. Fort Worth, Texas, USA, 2017.

[19] Carpenter, P. J. and Fridovich, B. *Effect of a Rapid Blade-Pitch Increase on the Thrust and Induced-Velocity Response of a Full-Scale Helicopter Rotor*. Tech. rep. Langley Field, VA, USA: National Advisory Committee for Aeronautics, 1953.

[20] Cheeseman, I. C. and Bennett, W. E. *The Effect of the Ground on a Helicopter Rotor in Forward Flight*. Tech. rep. 1955.

[21] Cheney, M. C. “The ABC Helicopter”. In: *AIAA/AHS VTOL Research, Design and Operations Meeting*. Atlanta, GA, USA, 1969.

[22] Chirico, G., Szubert, D., Vigevano, L., and Barakos, G. N. “Numerical modelling of the aerodynamic interference between helicopter and ground obstacles”. In: *CEAS Aeronautical Journal* 8.4 (2017), pp. 589–611.

[23] Coleman, C. P. *A Survey of Theoretical and Experimental Coaxial Rotor Aerodynamic Research*. Tech. rep. National Aeronautics and Space Administration, 1997.

[24] Costenoble, M., Baeder, J., Singh, R., and Anusonti-Inthra, P. “Simulation of Airfoil Interaction in Co-Rotating Coaxial Rotors with Uncertainty Quantification”. In: *VFS Transformative Vertical Flight*. San Jose, CA, USA, 2020.

[25] Davidson, L. “Evaluation of the SST-SAS Model : Channel Flow , Asymmetric Diffuser and Axi-Symmetric”. In: *ECCOMAS CFD 2006: Proceedings of the European Conference on Computational Fluid Dynamics*. Egmond aan Zee, The Netherlands, 2006.

[26] DLR-Institute of Aerodynamic and Flow Technology. *TAU-Code User Guide Release 2018.1.0*. Tech. rep. Deutsches Zentrum für Luft- und Raumfahrt e.V. - Institute of Aerodynamics and Flow Technology, 2018.

[27] DLR-Institute of Aerodynamic and Flow Technology. *Technical Documentation of the DLR TAU-Code Release 2018.1.0*. Tech. rep. Deutsches Zentrum für Luft- und Raumfahrt e.V. - Institute of Aerodynamics and Flow Technology, 2018.

[28] Duque, E. P. N., Toqoda, A., Burklung, M. D., Hariharan, N., Narducci, R., and Stone, C. P. “Direct Comparison of Hover Prediction Workshop Results”. In: *54th AIAA Aerospace Sciences Meeting*. San Diego, CA, USA, 2016.

[29] Duraisamy, K. and Brown, R. E. “Aerodynamic response of a hovering rotor to ramp changes in pitch input”. In: *64th Annual Forum of the American Helicopter Society*. Montreal, Canada, 2008.

[30] Egorov, Y., Menter, F. R., Lechner, R., and Cokljat, D. “The Scale-Adaptive Simulation Method for Unsteady Turbulent Flow Predictions. Part 2: Application to Complex Flows”. In: *Flow, Turbulence and Combustion* 85 (2010), pp. 139–165.

[31] Eisfeld, B., Rumsey, C., and Togiti, V. “Verification and Validation of a Second-Moment-Closure Model”. In: *AIAA Journal* 54.5 (2016), pp. 1524–1541.

[32] Ellenrieder, T. J. and Brinson, P. R. “The Dynamic Induced Velocity Field of a Model Rotor in Hover Conditions”. In: *Proceedings of the 22nd European Rotorcraft Forum*. Brighton, GBR, 1996.

[33] Feil, R., Rinker, M., and Hajek, M. “Flight Testing of a Coaxial Ultralight Rotorcraft”. In: *American Helicopter Society 73rd Annual Forum*. Fort Worth, Texas, USA, 2017.

[34] Feil, R., Rauleder, J., Cameron, C. G., and Sirohi, J. “Aeromechanics Analysis of a High-Advance-Ratio Lift-Offset Coaxial Rotor System”. In: *Journal of Aircraft* 56.1 (2019).

[35] Fradenburgh, E. A. “The Helicopter as a Ground Effect Machine”. In: *Symposium on Ground Effect Phenomena*. Princeton, NJ, USA, 1959, pp. 203–217.

[36] Gerhold, T. “Overview of the Hybrid RANS Code TAU”. In: *MEGAFLOW - Numerical Flow Simulation for Aircraft Design. Notes on Numerical Fluid Mechanics and Multidisciplinary Design (NNFM)* 89 (2005), pp. 81–92.

[37] Gibertini, G., Grassi, D., Parolini, C., Zagaglia, D., and Zanotti, A. “Experimental investigation on the aerodynamic interaction between a helicopter and ground obstacles”. In: *Proceedings of the Institution of Mechanical Engineers, Part G: Journal of Aerospace Engineering* 229.8 (2014), pp. 1395–1406.

[38] Gilad, M., Chopra, I., and Rand, O. “Performance Evaluation of a Flexible Rotor in Extreme Ground Effect”. In: *37th European Rotorcraft Forum 2011*. Cascina Costa, ITA, 2011.

[39] Gnemmi, P., Meder, K., and Rey, C. “Aerodynamic Performances of a Micro Air Vehicle Based on Two Coaxial Counter-Rotating Rotors”. In: *ANSYS Conference & 29th CADFEM Users’ Meeting*. Stuttgart, GER, 2011.

[40] Goerttler, A., Braukmann, J. N., Schwermer, T., Gardner, A. D., and Raffel, M. “Tip-vortex Investigation on a Rotating and Pitching Rotor Blade”. In: *43rd European Rotorcraft Forum*. Milan, ITA, 2017.

[41] Graftieaux, L., Michard, M., and Grosjean, N. “Combining PIV, POD and vortex identification algorithms for the study of unsteady turbulent swirling flows”. In: *Measurement Science and Technology* 12 (2001), pp. 1422–1429.

[42] Hanjalić, K. *Closure Models for Incompressible Turbulent Flows*. 2004.

[43] Harrington, R. D. *Full-Scale-Tunnel Investigation of the Static-Thrust Performance of a Coaxial Helicopter Rotor*. Tech. rep. Langley Field, VA, USA: National Advisory Committee for Aeronautics, 1951.

[44] Hayden, J. S. “Effect of the Ground on Helicopter Hovering Power Required”. In: *American Helicopter Society 32nd Annual Forum*. Washington, D.C., USA, 1976.

[45] He, C., Xin, H., and Bhagwat, M. “Advanced Rotor Wake Interference Modeling for Multiple Aircraft Shipboard Landing Simulation”. In: *American Helicopter Society 59th Annual Forum*. Baltimore, MD, USA, 2004.

[46] He, C. and Zhao, J. “Modeling Rotor Wake Dynamics with Viscous Vortex Particle Method”. In: *AIAA Journal* 47.4 (2009), pp. 902–915.

[47] He, C., Lee, C. S., and Chen, W. “Rotorcraft Simulation Model Enhancement to Support Design, Testing and Operational Analysis”. In: *American Helicopter Society 55th Annual Forum*. Montreal, Canada, 1999.

[48] He, C.-J. “Finite State Dynamic Wake Interference Modeling for Rotorcraft Simulation”. In: *American Helicopter Society 53rd Annual Forum*. Virgina Beach, VA, USA, 1997.

[49] Heyson, H. H. *Theoretical Study of the Effect of Ground Proximity on the Induced Efficiency of Helicopter Rotors*. Tech. rep. Langley Field, VA, USA: National Aeronautics and Space Administration, 1977.

[50] Ho, J. C., Yeo, H., and Bhagwat, M. “Validation of Rotorcraft Comprehensive Analysis Performance Predictions for Coaxial Rotors in Hover”. In: *Journal of the American Helicopter Society* 62.2 (2017), pp. 1–13.

[51] Iboshi, N., Nagashima, T., and Prasad, J. V. R. “Experimental Validation of an Inclined Ground Effect Model”. In: *American Helicopter Society 57th Annual Forum*. Washington, D.C., USA, 2001.

[52] Iboshi, N., Itoga, N., Nagashima, T., Hayata, Y., and Prasad, J. V. R. “Blade Flapping Motion of a Rotor Hovering above a Finite Inclined Ground Plane for Partial and Full Ground Effect Cases”. In: *Heli Japan*. Tochigi, Japan, 2002.

[53] Iboshi, N., Itoga, N., Prasad, J. V. R., and Sankar, L. N. “Ground Effect of a Rotor Hovering above a Confined Area”. In: *Frontiers in Aerospace Engineering* 3.1 (2014), pp. 7–16.

[54] Itoga, N., Nagashima, T., Yoshizawa, Y., and Prasad, J. V. R. “Numerical Method for Predicting I.G.E. Hover Performance of a Lifting Rotor”. In: *Transactions of the Japan Society for Aeronautical and Space Sciences* 43.141 (2000), pp. 122–129.

[55] Jacobellis, G., Singh, R., Johnson, C., Sirohi, J., and McDonald, R. “Experimental and Computational Investigation of Stacked Rotor Acoustics in Hover”. In: *Vertical Flight Society 76th Annual Forum*. Virtual Conference, 2020.

[56] Jacobellis, G., Singh, R., Johnson, C., Sirohi, J., and McDonald, R. “Investigation of Stacked Rotor Performance in Hover pt . II: Computational Validation”. In: *VFS Aeromechanics for Advanced Vertical Flight Technical Meeting*. San Jose, CA, USA, 2020.

[57] Johnson, C. and Sirohi, J. “Experimental Measurements and Low-Order Modeling of Stacked Rotor Performance in Hover”. In: *Vertical Flight Society 76th Annual Forum*. Virtual Conference, 2020.

[58] Johnson, C., Sirohi, J., Jacobellis, G., Singh, R., and McDonald, R. “Investigation of Stacked Rotor Performance in Hover Part 1: Experimental Measurements”. In: *VFS Aeromechanics for Advanced Vertical Flight Technical Meeting*. San Jose, CA, USA, 2020.

[59] Juhasz, O., Syal, M., Celi, R., Khromov, V., Rand, O., Ruzicka, G. C., and Strawn, R. C. “Comparison of Three Coaxial Aerodynamic Prediction Methods Including Validation with Model Test Data”. In: *Journal of the American Helicopter Society* 59.3 (2014), pp. 1–14.

[60] Kalra, T. S., Lakshminarayan, V. K., and Baeder, J. D. “CFD Validation of Micro Hovering Rotor in Ground Effect”. In: *American Helicopter Society 66th Annual Forum*. Phoenix, AZ, USA, 2010.

[61] Kalra, T. S., Lakshminarayan, V. K., Baeder, J. D., and Thomas, S. “Methodological Improvements for Computational Study of Hovering Micro-Rotor in Ground Effect”. In: *20th AIAA Computational Fluid Dynamics Conference*. Honolulu, HI, USA, 2011.

[62] Kalra, T. S., Lakshminarayan, V. K., and Baeder, J. D. “Effect of Tip Geometry on a Hovering Rotor in Ground effect: A Computational Study”. In: *31st AIAA Applied Aerodynamics Conference*. San Diego, CA, USA, 2013.

[63] Kalra, T. S. and Baeder, J. D. “Modeling Subscale Rotor Wake in Ground Effect with Accurate Turbulent Length Scales”. In: *AIAA Journal* 55.9 (2017), pp. 3085–3094.

[64] Kalra, T. S. “CFD Modeling and Analysis of Rotor Wake in Hover Interacting with a Ground Plane”. PhD thesis. University of Matyland, 2014.

[65] Khier, W. “Numerical Analysis of Hub and Fuselage Interference to Reduce Helicopter Drag”. In: *38h European Rotorcraft Forum*. Amsterdam, The Netherlands, 2012.

[66] Kim, H. W. and Brown, R. E. “Coaxial Rotor Performance and Wake Dynamics in Steady and Manoeuvring Flight”. In: *American Helicopter Society 62nd Annual Forum*. Phoenix, AZ, USA, 2006.

[67] Kim, H. W. and Brown, R. E. “A Comparison of Coaxial and Conventional Rotor Performance”. In: *Journal of the American Helicopter Society* 55.1 (2010), pp. 1–20.

[68] Knight, M. and Hefner, R. A. *Analysis of Ground Effect on the Lifting Airscrew*. Tech. rep. Washington, USA: National Advisory Committee for Aeronautics, 1941.

[69] Kocak, G. “Flow Characterization of Full, Partial, and Inclined Ground Effect”. Master thesis. Middle East Technical University, 2016.

[70] Komerath, N. M., Smith, M. J., and Tung, C. “A Review of Rotor Wake Physics and Modeling”. In: *Journal of the American Helicopter Society* 56.2 (2011), p. 022006.

[71] Konus, M. F. “Vortex Wake of Coaxial Rotors in Hover”. PhD thesis. Univrsity of California, Berkeley, 2017.

[72] Kutz, B. M., Großmann, T., Keßler, M., and Krämer, E. “Experimental and Numerical Examination of a Helicopter Hovering in Ground Effect”. In: *38h European Rotorcraft Forum*. Amsterdam, The Netherlands, 2012.

[73] Lakshminarayan, V. K. and Baeder, J. D. “High-Resolution Computational Investigation of Trimmed Coaxial Rotor Aerodynamics in Hover”. In: *Journal of the American Helicopter Society* 54.4 (2009), pp. 1–21.

[74] Lakshminarayan, V. K. and Baeder, J. D. “Computational Investigation of Microscale Coaxial-Rotor Aerodynamics in Hover”. In: *Journal of Aircraft* 47.3 (2010), pp. 940–955.

[75] Lakshminarayan, V. K., Kalra, T. S., and Baeder, J. D. “Detailed Computational Investigation of a Hovering Microscale Rotor in Ground Effect”. In: *AIAA Journal* 51.4 (2013), pp. 893–909.

[76] Landgrebe, A. J. and Bellinger, E. D. *Experimental Investigation of Model Variable-Geometry and Ogee Tip Rotors*. Tech. rep. Washington, D.C., USA: National Aeronautics and Space Administration, 1974.

[77] Launder, B. E., Reece, G. J., and Rodi, W. “Progress in the development of a Reynolds-stress turbulence closure”. In: *Journal of Fluid Mechanics* 68.3 (1975), pp. 537–566.

[78] Lee, T. E., Leishman, J. G., and Ramasamy, M. “Fluid Dynamics of Interacting Blade Tip Vortices with a Ground Plane”. In: *Journal of the American Helicopter Society* 55.2 (2010).

[79] Leishman, J. G. and Syal, M. “Figure of Merit Definition for Coaxial Rotors”. In: *Journal of the American Helicopter Society* 53.3 (2008), pp. 290–300.

[80] Leishman, J. G., Baker, A., and Coyne, A. “Measurements of rotor tip vortices using three-component laser Doppler velocimetry”. In: *AHS Aeromechanics Specialists’Conference*. Fairfield County, CT, USA, 1995.

[81] Leishman, J. G. *Principles of Helicopter Aerodynamics*. Second Edi. New York, NY, USA: Cambridge University Press, 2006.

[82] Leishman, J. G. “Aerodynamic Performance Considerations in the Design of a Coaxial Proprotor”. In: *Journal of the American Helicopter Society* 54.1 (2009).

[83] Letzgus, J., Gardner, A. D., Schwermer, T., Keßler, M., and Krämer, E. “Numerical Investigations of Dynamic Stall on a Rotor with Cyclic Pitch Control”. In: *Journal of the American Helicopter Society* 64.1 (2019).

[84] Lietzau, Z. T., Ramasamy, M., Jain, R., Leishman, J. G., and Ekaterinaris, J. “Comparison of Advanced RANS Modeling with Dual-Plane PIV Measurements for a Hovering Rotor”. In: *Journal of the American Helicopter Society* 63.2 (2018), pp. 1–14.

[85] Light, J. S. “Tip Vortex Geometry of a Hovering Helicopter Rotor in Ground Effect”. In: *American Helicopter Society 54th Annual Forum*. Boston, MA, USA, 1989.

[86] Lim, J. W., McAlister, K. W., and Johnson, W. “Hover Performance Correlation for Full-Scale and Model-Scale Coaxial Rotors”. In: *Journal of the American Helicopter Society* 54.3 (2009).

[87] Liou, S.-G., Komerath, N. M., and Lal, M. K. “Measurement Around a Rotor Blade Excited in Pitch, Part 1: Dynamic Inflow”. In: *Journal of the American Helicopter Society* 39.2 (1994), pp. 3–12.

[88] Ma, Y., Chen, M., Zhang, X., and Wang, Q. “Scale-model tests of coaxial rotors in water tunnel via particle image velocimetry technique”. In: *Journal of Aerospace Engineering* 230.3 (2016), pp. 426–443.

[89] Martin, P. B., Pugliese, G. J., and Leishman, J. G. “High Resolution Trailing Vortex Measurements in the Wake of a Hovering Rotor”. In: *Journal of the American Helicopter Society* 48.1 (2003), pp. 39–52.

[90] Martinez, A., Milluzzo, J., Drayton, S., and Davids, S. “Performance Measurements on Rotors Hovering above Moving Surfaces”. In: *Vertical Flight Society 75th Annual Forum*. Philadelphia, PS, USA, 2019.

[91] McAlister, K. W. and Tung, C. “Experimental study of a hovering coaxial rotor with highly twisted blades”. In: *Annual Forum Proceedings - AHS International* 3 (2008), pp. 1765–1781.

[92] Menter, F. R., Kuntz, M., and Langtry, R. “Ten Years of Industrial Experience with the SST Turbulence Model”. In: *Proceedings of the Fourth International Symposium on Turbulence, Heat and Mass Transfer*. Antalya, Turkey, 2003.

[93] Menter, F. R. and Egorov, Y. “The Scale-Adaptive Simulation Method for Unsteady Turbulent Flow Predictions. Part 1: Theory and Model Description”. In: *Flow, Turbulence and Combustion* 85 (2010), pp. 113–138.

[94] Menter, F. R. and Rumsey, C. L. “Assessment of Two-Equation Turbulence Models for Transonic Flows”. In: *25th AIAA Fluid Dynamics Conference*. Colorado Springs, CO, USA, 1994.

[95] Menter, F. R. *Improved Two-Equation k-omega Turbulence Models for Aerodynamic Flows*. Tech. rep. Moffett Field, CA, USA: National Aeronautics and Space Administration, 1992.

[96] Michard, M., Graftieaux, L., Lollini, L., and Grosjean, N. “Identification of vortical structures by a non local criterion- Application to PIV measurements and DNS-LES results of turbulent rotating flows”. In: *11th Symposium on Turbulent Shear Flows*. Grenoble, France, 1997, pp. 25–28.

[97] Milluzzo, J., Sydney, A., Rauleder, J., and Leishman, J. G. “In-Ground-Effect Aerodynamics of Rotors with Different Blade Tips”. In: *American Helicopter Society 66th Annual Forum*. Phoenix, AZ, USA, 2010.

[98] Milluzzo, J. I. and Leishman, J. G. “Vortical Sheet Behavior in the Wake of a Rotor in Ground Effect”. In: *AIAA Journal* 55.1 (2017), pp. 24–35.

[99] Milluzzo, J., Martinez, A., Drayton, S., and Davids, S. “PIV and Performance Measurements on Rotors Hovering Above Inclined Surfaces”. In: *American Helicopter Society 74th Annual Forum*. Phoenix, AZ, USA, 2018.

[100] Morillo, J. A. and Peters, D. A. “Velocity Field Above a Rotor Disk by a New Dynamic Inflow Model”. In: *Journal of Aircraft* 39.5 (2002), pp. 731–738.

[101] Mortimer, P., Sirohi, J., Platzer, S., and Rauleder, J. “Coaxial Rotor Wake Measurements in Hover Using Phase-Resolved and Time-Resolved PIV”. In: *Vertical Flight Society 75th Annual Forum*. Philadelphia, PS, USA, 2019.

[102] Mortimer, P., Johnson, C., Sirohi, J., Platzer, S., and Rauleder, J. “Experimental and Numerical Investigation of a Variable-Speed Rotor for Thrust Control”. In: *AIAA AVIATION Forum*. Virtual Conference, 2020.

[103] Mortimer, P., Sirohi, J., Platzer, S., and Rauleder, J. “Single Rotor Inflow and Wake Characterization in Hover with Dynamic Pitch Excitation”. In: *Vertical Flight Society 76th Annual Forum*. Virtual Conference, 2020.

[104] Moukalled, F., Mangani, L., and Darwish, M. *The Finite Volume Method in Computational Fluid Dynamics*. Springer International Publishing, 2016.

[105] Mula, S. M., Stephenson, J. H., Tinney, C. E., and Sirohi, J. “Dynamical characteristics of the tip vortex from a four-bladed rotor in hover”. In: *Experiments in Fluids* 54.10 (2013).

[106] Mula, S. M., Cameron, C. G., Tinney, C. E., and Sirohi, J. “Low-dimensional characteristics of tip vortices from a coaxial rotor in hover”. In: *American Helicopter Society 70th Annual Forum*. Montreal, Canada, 2014.

[107] Passe, B., Sridharan, A., and Baeder, J. “Computational Investigation of Coaxial Rotor Interactional Aerodynamics in Steady Forward Flight”. In: *33rd AIAA Applied Aerodynamics Conference*. Dallas, TX, USA, 2015.

[108] Pasquali, C., Serafini, J., Bernardini, G., Gennaretti, M., Milluzzo, J., and Davids, S. “Numerical-Experimental Correlation of Rotor Flowfield in Ground Effect”. In: *44th European Rotorcraft Forum*. Delft, The Netherlands, 2018.

[109] Pickles, D. J., Green, R. B., and Giuni, M. “Rotor wake interactions with an obstacle on the ground”. In: *The Aeronautical Journal* 122.1251 (2018), pp. 798–820.

[110] Platzer, S., Rauleder, J., and Hajek, M. “Investigation of Centrifugal Pumping Rotor Blades in Hover Using CFD”. In: *34th AIAA Applied Aerodynamics Conference*. Washington, D.C., USA, 2016.

[111] Platzer, S., Rauleder, J., Hajek, M., and Milluzzo, J. “Experimental and Computational Investigation on Rotor Blades with Spanwise Blowing”. In: *42nd European Rotorcraft Forum*. Lille, France, 2016.

[112] Platzer, S., Milluzzo, J., and Rauleder, J. “Investigation on Hovering Rotors over Inclined Ground Planes - a Computational and Experimental Study”. In: *44th European Rotorcraft Forum*. Delft, The Netherlands, 2018.

[113] Platzer, S., Rauleder, J., Hajek, M., Mortimer, P., Jain, P., and Sirohi, J. “Experiments and Computations Towards an Improved Understanding and Modeling of the Dynamic Inflow of Rotors in Hover”. In: *VFS Aeromechanics for Advanced Vertical Flight Technical Meeting*. San Jose, CA, USA, 2020.

[114] Platzer, S., Hajek, M., Rauleder, J., Mortimer, P., and Sirohi, J. “Investigation of the Flow Fields of Coaxial Stacked and Counter-Rotating Rotors Using PIV Measurements and URANS Simulations”. In: *Vertical Flight Society 77th Annual Forum*. Virtual Conference, 2021.

[115] Pölzlbauer, P., Desvigne, D., and Breitsamter, C. “Performance Improvement of a Compound Helicopter Rotor Head by Aerodynamic Design Optimization”. In: *31st Congress of the International Council of the Aeronautical Sciences*. Belo Horizonte, Brazil, 2018.

[116] Pope, S. B. *Turbulent Flows*. Seventh pr. Cambridge, UK: Cambridge University Press, 2010.

[117] Porter, R., Shirinzadeh, B., and Choi, M. H. “Experimental Analysis of Variable Collective-pitch Rotor Systems for Multirotor Helicopter Applications”. In: *Journal of Intelligent and Robotic Systems* 83.2 (2016), pp. 271–288.

[118] Prasad, J. V. R., Nowak, M., and Xin, H. “Finite State Inflow Models for a Coaxial Rotor in Hover”. In: *38th European Rotorcraft Forum*. Amsterdam, The Netherlands, 2012.

[119] Prasad, J. V. R., Kong, Y. B., and Peters, D. “Analytical Methods for Modeling Inflow Dynamics of a Coaxial Rotor System”. In: *42nd European Rotorcraft Forum*. Lille, France, 2016.

[120] Qi, H., Xu, G., Lu, C., and Shi, Y. “A study of coaxial rotor aerodynamic interaction mechanism in hover with high-efficient trim model”. In: *Aerospace Science and Technology* 84 (2019), pp. 1116–1130.

[121] Rajmohan, N., Zhao, J., and He, C. “A Coupled Vortex Particle/CFD Methodology for Studying Coaxial rotor Configurations”. In: *Fifth Decennial AHS Aeromechanics Specialists’ Conference*. San Francisco, CA, USA, 2014.

[122] Ramasamy, M., Gold, N. P., and Bhagwat, M. J. “Flowfield Measurements to Understand Effects of Wake Behavior on Rotor Performance”. In: *28th AIAA Applied Aerodynamics Conference*. Chicago, IL, USA, 2010.

[123] Ramasamy, M. “Hover Performance Measurements Toward Understanding Aerodynamic Interference in Coaxial, Tandem, and Tilt Rotors”. In: *Journal of the American Helicopter Society* 60.3 (2015), pp. 1–17.

[124] Rauleder, J. and Leishman, J. G. “Flow Environment and Organized Turbulence Structures Near a Plane Below a Rotor”. In: *AIAA Journal* 52.1 (2014), pp. 146–161.

[125] Rorke, J. B. *Hover Performance Tests of Full Scale Variable Geometry Rotors*. Tech. rep. Washington, D.C., USA: National Aeronautics and Space Administration, 1976.

[126] Rossow, V. J. *Effect of Ground and/or Ceiling Planes on Thrust of Rotors in Hover*. Tech. rep. Moffett Field, CA, USA: National Aeronautics and Space Administration, 1985.

[127] Rozhdestvensky, M. G. "Essential Results Obtained From Research Involved in Scissors Rotor". In: *21st European Rotorcraft Forum*. Saint-Petersburg, Russia, 1995.

[128] Rubio, R. C., Diaz, P. V., and Yoon, S. "High-Fidelity Computational Analysis of Ducted and Coaxial Rotors for Urban Air Mobility". In: *Vertical Flight Society 75th Annual Forum*. Philadelphia, PS, USA, 2019.

[129] Rung, T., Lübcke, H., Franke, M., Xue, L., Thiele, F., and Fu, S. "Assessment of Explicit Algebraic Stress Models in Transonic Flows". In: *Proceedings of the 4th International Symposium on Engineering Turbulence Modelling and Measurements*. Ajaccio, Corsica, France, 1999, pp. 659–668.

[130] Ruzicka, G. C. and Strawn, R. C. "Computational Fluid Dynamics Analysis of a Coaxial Rotor Using Overset Grids". In: *AHS Specialist's Conference on Aeromechanics*. San Francisco, CA, USA, 2008.

[131] Schwamborn, D., Gerhold, T., and Heinrich, R. "The DLR TAU-Code: Recent Applications in Research and Industry". In: *European Conference on Computational Fluid Dynamics*. Egmond aan Zee, The Netherlands, 2006.

[132] Schwamborn, D., Gardner, A. D., Geyr, H. von, Krumbein, A., Ludecke, H., and Stürmer, A. "Development of the Dlr Tau-Code for Aerospace Applications". In: *International Conference on Aerospace Science and Technology* June (2008), pp. 1–8.

[133] Schneider, S., Mores, S., Edelmann, M., D'Alascio, A., and Schimke, D. "Drag Analysis for an Economic Helicopter". In: *37th European Rotorcraft Forum*. Cascina Costa, ITA, 2011.

[134] Shur, M., Strelets, M., Travin, A., and Spalart, P. R. "Turbulence Modeling in Rotating and Curved Channels: Assessment of the Spalart-Shur Correction Term". In: *36th AIAA Aerospace Sciences Meeting and Exhibit*. Reno, NV, USA, 1998.

[135] Silwal, L. and Raghav, V. "Preliminary study of the near wake vortex interactions of a coaxial rotor in hover". In: *AIAA Scitech 2020 Forum*. Orlando, FL, USA, 2020.

[136] Singh, P. and Friedmann, P. P. "Application of Vortex Methods to Coaxial Rotor Wake and Load Calculations in Hover". In: *Journal of Aircraft* 55.1 (2018), pp. 373–381.

[137] Smirnov, P. E. and Menter, F. R. "Sensitization of the SST Turbulence Model to Rotation and Curvature by Applying the Spalart-Shur Correction Term". In: *Journal of Turbomachinery* 131.4 (2009), pp. 1–8.

[138] Spalart, P. R. and Allmaras, S. R. "A one-equation turbulence Mmodel for aerodynamics flows". In: *La Recherche Aerospatiale* 1 (1994), pp. 5–21.

[139] Spalart, P. R. and Shur, M. "On the Sensitization of Turbulence Models to Rotation and Curvature". In: *Aerospace Science and Technology* 5 (1997), pp. 297–302.

[140] Speziale, C. G., Sarkar, S., and Gatski, T. B. *Modeling the Pressure-Strain Correlation of Turbulence - An Invariant Dynamical Systems Approach*. Tech. rep. Hampton, VA, USA: National Aeronautics and Space Administration, 1990.

[141] Sydney, A., Baharani, A., and Leishman, J. G. “Understanding Brownout using Near-Wall Dual-Phase Flow Measurements”. In: *American Helicopter Society 67th Annual Forum*. Virgina Beach, VA, USA, 2011.

[142] Tanabe, Y., Saito, S., Ooyama, N., and Hiraoka, K. “Study of a Downwash Caused by a Hovering Rotor in Ground Effect”. In: *34th European Rotorcraft Forum*. Liverpool, UK, 2008.

[143] Tanabe, Y., Saito, S., Ooyama, N., and Hiraoka, K. “Investigation of the Downwash Induced by Rotary Wings in Ground Effect”. In: *International Journal of Aeronautical and Space Sciences* 10.1 (2009), pp. 20–29.

[144] Taylor, M. K. *A Balsa-Dust Technique for Air-Flow Visualization and its Application to Flow Through Model Helicopter Rotors in Static Thrust*. Tech. rep. Washington, USA: National Advisory Committee for Aeronautics, 1950.

[145] Thomas, S., Ananthan, S., and Baeder, J. D. “Wake-Coupling CFD-CSD Analysis of Helicopter Rotors in Steady and Maneuvering Flight Conditions”. In: *AHS Specialists’ Conference on Aeromechanics*. San Francisco, CA, USA, 2010.

[146] Tritschler, J. K., Milluzzo, J. I., and Holder, J. M. “Performance Effects of Hover In-Ground-Effect over Sloped Terrain”. In: *Vertical Flight Society 75th Annual Forum*. Philadelphia, PS, USA, 2019.

[147] Uehara, D. and Sirohi, J. “Quantification of Swirl Recovery in a Coaxial Rotor System”. In: *American Helicopter Society 73rd Annual Forum*. Fort Worth, TX, USA, 2017.

[148] Uehara, D., Sirohi, J., Feil, R., and Rauieder, J. “Measurement of Transient Blade Passage Loads of a Coaxial Counter-Rotating Rotor in Hover”. In: *44th European Rotorcraft Forum*. Delft, The Netherlands, 2018.

[149] Uehara, D., Sirohi, J., and Bhagwat, M. J. “Hover Performance of Corotating and Counter-rotating Coaxial Rotors”. In: *Journal of the American Helicopter Society* 65.1 (2020), pp. 1–8.

[150] Wachspress, D. A. and Quackenbush, T. R. “Impact of Rotor Design on Coaxial Rotor Performance, Wake Geometry and Noise”. In: *American Helicopter Society 62nd Annual Forum*. Phoenix, AZ, USA, 2006.

[151] Wallin, S. and Johansson, A. V. “An explicit algebraic Reynolds stress model for incompressible and compressible turbulent flows”. In: *Journal of Fluid Mechanics* 403 (2000), pp. 89–132.

[152] Wallin, S. and Johansson, A. V. “Modelling streamline curvature effects in explicit algebraic Reynolds stress turbulence models”. In: *International Journal of Heat and Fluid Flow* 23 (2002), pp. 721–730.

[153] Wang, G., Schwöppe, A., and Heinrich, R. “Comparison and Evaluation of Cell-Centered and Cell-Vertex Discretization in the Unstructured TAU-Code for Turbulent Viscous Flows”. In: *5th European Conference on Computational Fluid Dynamics*. Lisbon, Portugal, 2010.

[154] Whiteside, S. K., Zawodny, N. S., Fei, X., Pettingill, N. A., Patterson, M. D., and Rothhaar, P. M. “An Exploration of the Performance and Acoustic Characteristics of UAV-Scale Stacked Rotor Configurations”. In: *AIAA Scitech 2019 Forum*. San Diego, CA, USA, 2019.

[155] Wilcox, D. C. *Turbulence Modeling for CFD*. Third Edit. La Canada, CA, USA: DCW Industries, 2006.

[156] Wolf, C. C., Schwarz, C., Kaufmann, K., Gardner, A. D., Michaelis, D., Bosbach, J., Schanz, D., and Schröder, A. “Experimental study of secondary vortex structures in a rotor wake”. In: *Experiments in Fluids* 60.175 (2019), pp. 1–16.

[157] Woodgate, M. A., Fitzgibbon, T. A., Barakos, G. N., Shi, Y., and Li, P. “Simulation of step input in collective pitch for hovering rotor”. In: *Vertical Flight Society 76th Annual Forum*. Virtual Conference, 2020.

[158] Xin, H., Prasad, J. V. R., and Peters, D. A. “An Analysis of Partial Ground Effect on the Aerodynamics of a Helicopetr Rotor”. In: *38th Aerospace Sciences Meeting and Exhibit*. Reno, NV, USA, 2000.

[159] Xin, H., Prasad, J. V. R., Peters, D. A., Iboshi, N., and Nagashima, T. “Correlation of Experimental Measurements with a Finite-State Ground Effect Model”. In: *American Helicopter Society 56th Annual Forum*. Virgina Beach, VA, USA, 2000.

[160] Xin, H., He, C., and Lee, J. “Combined Finite State Rotor Wake and Panel Ship Deck Models for Simulation of Helicopter Shipboard Operations”. In: *American Helicopter Society 57th Annual Forum*. Washington, D.C., USA, 2001.

[161] Xin, H., Prasad, J. V. R., and Peters, D. A. “Unsteady Aerodynamics of Helicopter Rotor Hovering in Dynamic Ground Effect”. In: *23rd Atmospheric Flight Mechanics Conference*. Boston, MA, USA, 1998, pp. 711–720.

[162] Xin, H., Prasad, J. V. R., Peters, D. A., Nagashima, T., and Iboshi, N. “A Finite State Inflow Model for Simulation of Helicopter Hovering in Ground Effect”. In: *American Helicopter Society 54th Annual Forum*. Washington, D.C., USA, 1998.

[163] Xin, H., Prasad, J. V. R., Peters, D. A., Itoga, N., Iboshi, N., and Nagashima, T. “Ground Effect Aerodynamics of Lifting Rotors Hovering above Inclined Ground Plane”. In: *17th AIAA Applied Aerodynamics Conference*. Norfolk, VA, USA, 1999.

[164] Yoon, S., Chaderjian, N. M., Pulliam, T. H., and Holst, T. L. “Effect of Turbulence Modeling on Hovering Rotor Flows”. In: *45th AIAA Fluid Dynamics Conference*. June 2015. Dallas, TX, USA, 2015, pp. 1–12.

[165] Yoon, S., Lee, H. C., and Pulliam, T. H. “Computational Study of Flow Interactions in Coaxial Rotors”. In: *AHS Technical Meeting on Aeromechanics Design for Vertical Lift*. San Francisco, CA, USA, 2016.

[166] Yoon, S., Chan, W. M., and Pulliam, T. H. “Computations of Torque-Balanced Coaxial Rotor Flows”. In: *55th AIAA Aerospace Sciences Meeting*. Grapevine, TX, USA, 2017.

[167] Young, L. a. *Vortex Core Size in the Rotor Near-Wake*. Tech. rep. Moffett Field, CA, USA: National Aeronautics and Space Administration, 2003.

[168] Yu, K. and Peters, D. A. “Nonlinear State-Space Modeling of Dynamic Ground Effect”. In: *Journal of the American Helicopter Society* 50.3 (2005), pp. 259–268.